# Multiphase extensions to ODE models for detonations of non-ideal explosives

Elise Melinda Croft

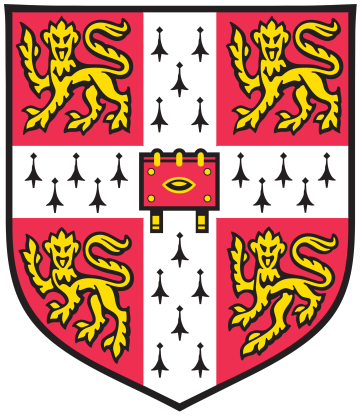

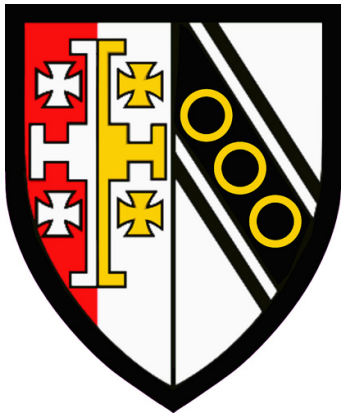

Selwyn College

University of Cambridge

*This dissertation is submitted for the degree of Doctor of Philosophy.*

January 2017

Supervisor: Dr Nikos Nikiforakis

## Abstract

Two streamline, ordinary differential equation (ODE) models for detonation, the Chan-Kirby model[1] and the straight streamline approach of Watt et al.[2], are extended to a multiphase system of equations. These multiphase equations, with realistic equations of state, are used to better capture the heterogeneities in non-ideal explosives used in mining applications.

Streamline ODE multidimensional models are normally obtained by reducing the partial differential equations (PDEs) describing the motion of the material to ODEs by making approximations about some of the physics of the problem. These models are referred to as reduced ODE models in this work and are the primary focus of this research into fast, efficient solutions of non-ideal explosives.

In the development of these reduced order forms, some terms in the full equations have been removed for analytical convenience. Although this is not always the result of a formal order of magnitude analysis, this somewhat empirical approach is justified by simulation studies. In particular, by demonstrating that in a variety of benchmark problems, the reduced order ODEs give similar results to those obtained from the much more complex, full order PDE models. Further support is obtained by comparing the reduced order solution with experimental results.

Comparisons with multiphase direct numerical simulations and experiments are undertaken to investigate the effect of the approximations and assumptions made in the derivation of the models. Both models produce comparable diameter effect curves for two different non-ideal explosives, EM120D and ANFO, in unconfined conditions. Empirical assumptions in the Chan-Kirby model can be eliminated but investigation shows that the straight streamline multiphase extension is based on better approximations for non-ideal explosives. This latter approach also gives better prediction of the diameter effect curve and detonation driving zone shape.

The multiphase straight streamline model is then extended to model confined multiphase detonations, with realistic equations of state for the confining material, and predicts most strong confinement examples well.

Future work of extending to curved streamlines and including confinement other than strong or weak is discussed.


---

[1] S. K. Chan and I. J. Kirby. "Analysis of VOD-Diameter Data Using an Analytical Two-Dimensional Non-Ideal Detonation Model". In: *Shock Compression of Condensed Matter*. Ed. by M. D. Furnish, M. Elert, T. P. Russell, & C. T. White. Vol. 845. American Institute of Physics Conference Series. July 2006, pp. 453–456. DOI: 10.1063/1.2263358. URL: http://adsabs.harvard.edu/abs/2006AIPC..845..453K

[2] Simon Watt, Gary Sharpe, Sam Falle, and Martin Braithwaite. "A streamline approach to two-dimensional steady non-ideal detonation: the straight streamline approximation". In: *Journal of Engineering Mathematics* (2011), pp. 1–14. ISSN: 0022-0833. DOI: 10.1007/s10665-011-9506-0. URL: http://dx.doi.org/10.1007/s10665-011-9506-0

## Related publications

Some of the derivation shown in Appendix A was submitted as part of my MPhil in Scientific Computing:

> E. Croft. *Investigation of a reduced model using parametric studies of a 2-dimensional compliant confinement model.* Cambridge University MPhil Dissertation. M.Phil. Thesis. 2011.

Some of the work in Chapter 7 was presented at the 15th International Detonation Symposium:

> E.M. Croft, S.K. Chan, I.J. Kirby, and N. Nikiforakis. "Modelling multiphase detonation with streamline models". In: *Proc. 15th International Detonation Symposium.* (Grand Hyatt San Francisco, July 13–18, 2014). Office of Naval Research, Arlington, Virginia, 2014, pp. 1096–1106.

## Declaration

This dissertation is the result of my own work and includes nothing which is the outcome of work done in collaboration except as declared.

It is not substantially the same as any that I have submitted, or, is being concurrently submitted for a degree or diploma or other qualification at the University of Cambridge or any other University or similar institution except as declared in the Preface and specified in the text. I further state that no substantial part of my dissertation has already been submitted, or, is being concurrently submitted for any such degree, diploma or other qualification at the University of Cambridge or any other University of similar institution except as declared in the Preface and specified in the text.

It does not exceed the prescribed word limit for the Degree Committee for the Faculty of Physics & Chemistry.

**Acknowledgements**

Firstly, I would like to thank my partner, Jeffrey Salmond, for his continued support and unending patience. He has spent most of his spare time as the person I bounce all of my ideas off and this thesis would not have been possible without his help and our lengthy discussions.

Secondly, I would like to acknowledge my supervisor Dr Nikos Nikiforakis and his work in acquiring funding for this project. I am grateful to Orica Mining Services for their funding of this project and for providing supportive industry expertise. I thank Drs. Jim Chan, Ian Kirby and Alan Minchinton for their continued help, constructive criticism, moral support and fascinating stories. Furthermore, I would like to thank Prof Martin Braithwaite for helpful discussions and feedback on my work.

I would also like to acknowledge the many people who read this work and the very helpful feedback they gave: Dr David Salmond, Dr Deborah Salmond, Dr Oliver Strickson, David Barry and Dr Steve Millmore. I appreciate the many hours spent wading through mismatched notation, unaligned equations and ridiculously long sentences.

Finally, I would like to thank my family for all of their support and the multitude of ways that they have provided it. My parents' motto of 'just do whatever makes you happy' hasn't always been applicable to this thesis but it has constantly reminded me of their love and support. So thank you.

# Contents

# 1. Introduction

Detonation is a fast and violent form of combustion that transfers energy via mass flow in strong compression waves, often initiated by a strong shock wave propagating into an explosive. The propagating shock wave triggers a chemical reaction by compressing the material and thus increasing the temperature. The chemical reaction in turn supports the shock wave and the process propagates until the reactants have been consumed [40].

Detonation modelling is of vital importance in understanding how explosive materials behave in different conditions, given that experiments are costly. However, since the reactions that drive a detonation take place on a microscopic scale, whereas the product of these reactions is a detonation wave moving on a macroscopic scale, modelling of the detonation process presents a computational challenge.

Two main industries maintain a focus on detonation: military and mining. Military explosives have historically been high (ideal) explosives with high pressures, fast detonation waves and fast reaction times. These explosives are developed to optimise energy release but also need a long shelf life.

Conversely, mining explosives, which are the main focus of this thesis, are developed with a focus on cost, efficiency and transport safety [57]. Mining explosives are used to fracture and move rock surrounding a material of interest. For example, open-cut coal mining uses shelf blasting to fracture and heave rock surrounding a coal seam. Given that crushing and transporting the surrounding rock has a surprisingly large energy cost, the detonation needs to be set up so that the surrounding rock is broken into parts that are large enough to be easily moved by large, imprecise machinery but small enough to reduce the cost of further breaking the rock down off-site [52, 65]. This implies that mining explosives need to exert moderate pressures, compared to military explosives, on the surrounding material so that the rock is not pulverised but rather fractured to an optimal size. These moderate pressures are achieved with slower burning detonations which have the added advantage of their slow reactions releasing gasses that help to heave the rock during their expansion [65].

The explosive materials used for mining are typically ammonium nitrate-based and exhibit strongly non-ideal behaviour. This non-ideal behaviour includes lower pressures, slower detonation waves, curved shock fronts and longer reaction zones and means that the detonation performance is strongly coupled to the charge size and the confining material [52, 71]. To sensitise the materials, voids are introduced to create hotspots, introducing complex

heterogeneities in the explosive. It is both the non-ideal behaviour and the heterogeneities in the mining explosives that need to be fully realised in detonation modelling in order to accurately simulate the detonation process.

The required outcome of detonation models for mining explosives is focussed on the interaction between the explosive, typically in a cylindrical borehole, and the confining material, typically rock, as shown in Figure 1.1. The two main questions that arise are: how does the explosive affect the confiner and how does the confiner affect the explosive? The first of these two questions can be investigated by looking at the pressure the explosive exerts on the confiner [72], normally seen as a pressure contour plot of the detonation driving zone (DDZ) where the majority of the reaction takes place and where most of the energy is released. The second question is answered by looking at a diameter effect curve: as the size of the charge is varied, what happens to the speed of the detonation wave and at what diameter does it fail to detonate?

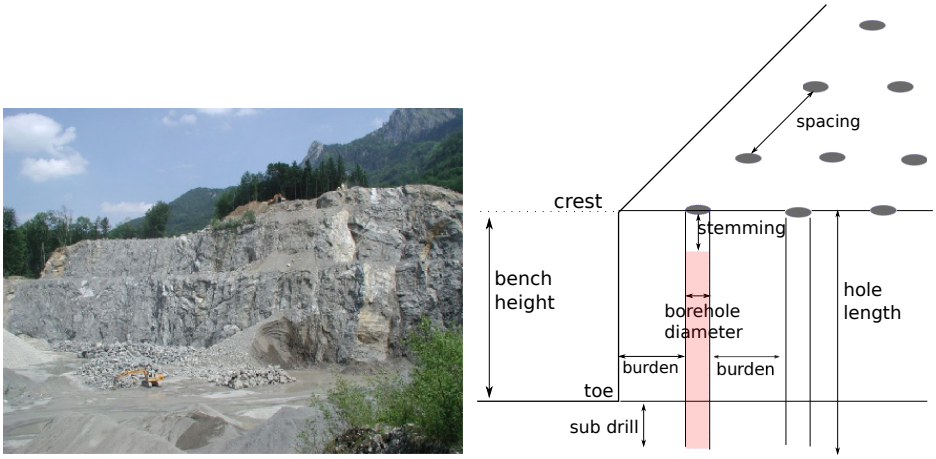


Figure 1.1.: Left: an open cut coal mining operation (photo courtesy of Orica). Right: A diagram of a typical open cut shelf blast set up.

Experiments for mining explosives are usually carried out by firing ratesticks, thin-walled paper tubes filled with the explosive material, with different diameters (see, for example, [14]). These experiments give an indication of the diameter effect for unconfined detonations, where the streamline deflection in the explosive can exceed that possible via a shocked state, but do not answer the question of what happens when the explosive is surrounded by different materials [9, 72]. To obtain this information, numerical simulations of the detonation process need to be undertaken. Typically, these are 'ratestick' simulations (explosive material in a cylinder modelled under an axisymmetric assumption) that are fitted to the unconfined data; the simulations then predict what will happen to the propagation of detonation under different confinement conditions. Ratestick simulations, with

cylindrical geometry, are used for numerical modelling of mining explosives as the explosive in a borehole can be approximated by a cylinder.

Unfortunately, due to the complicated nature of the heterogeneous mining explosive materials, and the difficulty of modelling on such different scales, producing these simulations is too numerically costly for day-to-day use in the mining industry. For practical purposes what is needed is a detonation model that can produce fast but accurate solutions for a range of parametric studies.

Historically, detonation modelling has developed from the simple one-dimensional, homogeneous, single reaction, ideal models to representations that include some two-dimensional effects: quasi-one-dimensional models [40, 69]. With increasing computational performance, full three-dimensional solutions of the detonation problem via the augmented Euler equations have become more feasible.

The Euler equations describe the motion of adiabatic, inviscid flow and the augmented Euler equations include a rate equation which describes the reactive flow of a homogeneous fluid. These equations are given as

$$\frac{D\rho}{Dt} + \rho\nabla\cdot\mathbf{v} = 0, \tag{1.1}$$

$$\rho\frac{D\mathbf{v}}{Dt} = -\nabla p, \tag{1.2}$$

$$\frac{De}{Dt} - \frac{p}{\rho^2}\frac{D\rho}{Dt} = 0, \tag{1.3}$$

$$\frac{D\lambda}{Dt} = W, \tag{1.4}$$

where $\dfrac{D}{Dt} = \dfrac{\partial}{\partial t} + \mathbf{v}\cdot\nabla$ is the time derivative following the motion of the fluid or material derivative, $\rho$ is the density, $\mathbf{v}$ is the velocity vector, $p$ is the pressure, $e$ is the internal energy, $\lambda$ is the mass fraction and $W$ is the reaction progress.

Once multidimensional solutions to the Euler equations became possible, focus shifted toward including complex behaviour at the microscopic level in these problems. The most prevalent complexity is the multimaterial nature of the solution. Multimaterial models can be loosely categorised as either multiphase or multifluid. Multiphase models describe the fluid as a mixture at each spatial point of the fluid. Multifluid models describe boundaries between each fluid so there is only a single fluid at each spatial point [62].

For detonation problems the material is reacting and this implies that in the region of the reaction, the reaction zone, there will be a mixture of reactants and products. In some models, such as those that use a programmed burn (see, for example, [50]), the detonation wave speed is an input parameter and only the pressure wave after an instantaneous reaction, in time and space, is modelled. For these solutions, a resolved reaction zone is unnecessary.

However, these models are not predictive and need input from solutions with resolved reaction zones. The multiphase model is able to resolve the reaction zone where the bulk of energy is transferred from the chemical reactions to the fluid and hence from the explosive to the confining material. The development in this thesis employs a multiphase model.

Multimaterial, and multidimensional, solutions are computationally expensive, so approximate multimaterial models, similar to the quasi-one-dimensional models developed previously for the Euler equations, have been previously developed for faster solutions. This is once again a competitive option for industrial applications.

Such approximate multidimensional models are normally obtained by reducing the partial differential equations (PDEs) describing the motion of the material to ordinary differential equations (ODEs) by making approximations about some of the physics of the problem. These models are referred to as reduced ODE models in this thesis and are the primary focus of this research into fast, efficient solutions of non-ideal explosives.

In the next chapter, an outline of the development of detonation modelling and existing reduced ODE models is given. The underlying equations for all of the reduced ODE models are the augmented Euler equations, which are discussed in detail in Chapter 6. Any previous attempts at multimaterial reduced ODE modelling consist of a homogeneous explosive progressing to a gaseous product.

A novel contribution of this thesis is the development of multiphase reduced ODE models for non-ideal explosives. These have been obtained by manipulating a multiphase mechanical equilibrium model in a similar way to previous work on the augmented Euler equations. Two different manipulations are explored. The models are compared to validated, full direct numerical simulation (DNS) solutions to confirm the viability of reduced ODE models for modelling multiphase detonation. Initially, the unconfined case is investigated. The approximations made in each model and their affect on simulating the propagation of a steady detonation wave in a heterogeneous, non-ideal explosive is assessed with use of DNS solutions. The assessment is then extended to the confined case.

This thesis is in three parts: (I) an introduction to detonation and material modelling, (II) an outline of the approximate models with comparative results including both unconfined and confined detonation and (III) a conclusive discussion on comparisons between the models and the DNS solutions.

Part I illustrates the relevant background information on detonation modelling needed for the rest of the thesis. Part II explores efficient modelling of steady-state, unconfined, multiphase detonation. A two-phase Euler-based model, called the Chan-Kirby model, is derived and implemented in Chapter 6: its shortcomings prompt the introduction of a more realistic multiphase model. Chapter 7 shows how the same techniques can be used on a multiphase system of equations to produce a multiphase reduced model.

However, with this implementation, DNS comparisons reveal defects in the fundamental assumptions of the approach and so an alternative multiphase scheme, based on the straight streamline approximation in [78], is developed and comparisons with DNS results are shown. In §8.3 the straight streamline approximation is extended to include confinement.

Part III of this thesis presents an analysis of the reduced order models that have been developed here. This analysis includes comparison with experiments, DNS results, the efficiency of each model, limitations and possible future extensions.

A small note on notation: variables are labelled according to their original use in the models that have been extended. This means that there are some variables, such as radial velocity, where a different symbol is used when referring to the Chan-Kirby model (where radial velocity is denoted by $\omega$) compared to the straight streamline approach (where radial velocity is denoted by $u$). This has been done so that the reader may easily identify extensions made in this work by referring back to the original papers.

In Part I, some general detonation theory is provided as background for the development of the reduced order models described in Part II. A description of the materials used throughout this work and the equations of state used to describe the behaviour of these materials are given in Chapters 3 and 4, respectively.

# Part I.

# Background theory & materials

# 2. Detonation modelling

The form of a detonation model is strongly influenced by the motivation for developing that model and hence detonation modelling comes in a variety of forms with a range of desired outcomes. Some models focus on the initiation of detonation to gain information about the safety and reliability of materials. These types of models are normally focussed on the transition to detonation, from a state that has been changed in some way by an external force, which can be measured by pressure or temperature evolution profiles or by distinguishing features on a pressure versus volume, $p - v$, plot (see [46, 61] for examples).

Steady-state describe what happens once an explosive has developed a full detonation wave. These models aim to provide information about the impact or performance of certain explosives in a range of environments. The main outputs of interest are the effect of the size of the charge and its confining material on pressure and detonation velocity. This information is normally illustrated by the diameter effect curve (detonation velocity versus inverse radius) and flooded contour plots of the pressure distribution in a detonated charge. This thesis focusses on these steady-state models and outputs.

The first widely used model for detonation was proposed in 1899 by Chapman [31] and was followed by the independent work of Jouguet [48, 49, 47] and is consequently called the Chapman-Jouguet (CJ) model. The CJ model, discussed in the next section, assumes that the flow of detonation is one-dimensional, that the shock front is a discontinuity across which conservation laws for shock waves apply and that the shock front is driven by a reaction that is instantaneous and finishes at the CJ state. The model had success predicting detonation velocities (the speed at which the shock propagates and often denoted by $D$ or VoD) and was thus instantly applicable to the explosive gas industry [40].

The use of experimental photography (see, for example, the smear-camera work of Campbell and Woodhead [24]) in the 1920s revealed that detonation reactions were, for the most part, not instantaneous. Zeldovich (1940) [80], von Neumann (1942) [56] and Döring (1943) [37] independently developed an extension of CJ theory to include a chemical reaction that takes place in a finite amount of time after the shock wave.

The model, called the Zeldovich-von Neumann-Döring (ZND) model, is based on the Euler equations. Like the CJ model, the flow is assumed to be one-dimensional and the shock is treated as a discontinuity. However, in the ZND model the discontinuity is not a result of a chemical reaction – the

chemical reaction is triggered by the shock and it proceeds at a finite rate after the shock until completion at the CJ point. The CJ and ZND theories are outlined in the next section.

## 2.1. One-dimensional detonation theory

This section will explore the most commonly known one-dimensional theories: CJ theory and ZND theory, to complement the development, results and discussions found in the later sections of this thesis.

### 2.1.1. CJ theory

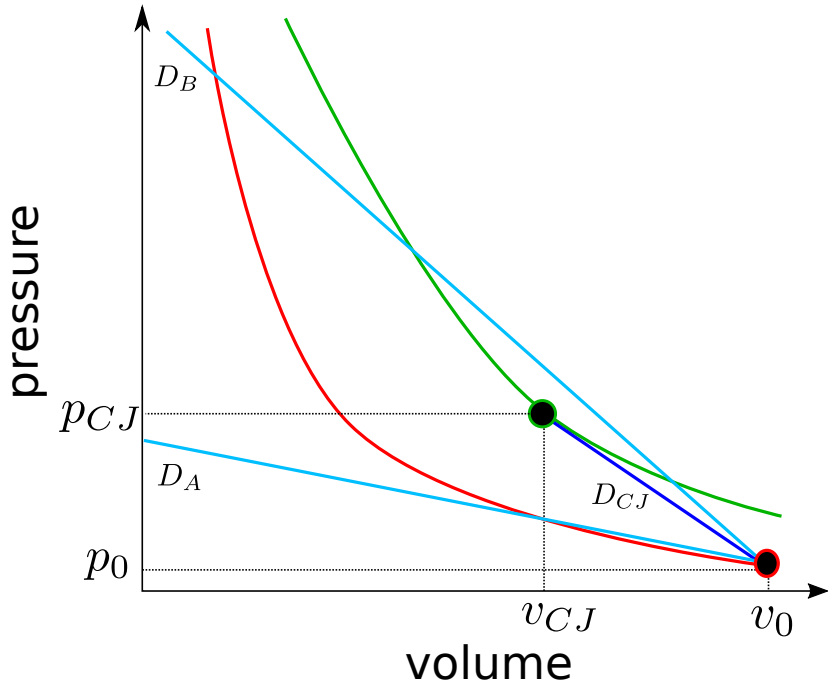


Figure 2.1.: The CJ model assumes that a reactive wave will transition, normally via a shock, from the upstream initial conditions ($v_0$, $p_0$) on the reactant Hugoniot (red) to the final CJ state on the product Hugoniot or final Crussard curve (green). This reactive wave propagates at $D_{\text{CJ}}$ and the slope of the line (dark blue) connecting $(v_0, p_0)$ to $(v_{\text{CJ}}, p_{\text{CJ}})$ is proportional to $D^2_{\text{CJ}}$. The lighter blue lines show reactive waves with lower, $D_A$, or higher, $D_B$, detonation velocities and represent unsteady detonation and overdriven detonation, respectively.

CJ theory is the simplest model for detonation. The detonation wave is assumed to be one-dimensional and caused by a single reaction such that

the products upstream are unreacted and the products downstream are completely reacted. The reactive wave does not have to be discontinuous although often it is represented this way as a shock. The states upstream and downstream are in thermochemical equilibrium. The detonation wave is modelled as independent of time. The upstream particle velocity, in the shock-attached frame, is equal to the detonation velocity.

CJ theory implies that the detonation wave is propagating at a speed such that the reaction in the explosive material reaches completion at the same time the velocity of the material in the frame of the shock reaches sonic velocity. Information behind the CJ point, or sonic locus in two-dimensions, cannot be transferred to in front of the CJ point.

### Conservation laws

Across the shock conservation laws for mass, momentum and energy apply. If the detonation is propagating with speed $D$ then these conservation laws in the shock-attached form are,

$$\rho_0 D = \rho \left(D - u\right), \tag{2.1}$$

$$p - p_0 = \rho_0 u D, \tag{2.2}$$

$$e\left(p, v, \lambda = 1\right) + pv + \frac{1}{2}\left(D - u\right)^2 = e\left(p_0, v_0, \lambda = 0\right) + p_0 v_0 + \frac{1}{2}D^2, \tag{2.3}$$

where $\rho$ is the density (and $v$, its inverse, is the specific volume), $u$ is the particle velocity, $p$ is the pressure, $e$ is the internal energy, $\lambda$ is the reaction progress and is a measure of mass fraction and the subscript 0 represents the unreacted material in front of the shock. Note that upstream (in front of the shock), the particle velocity of the unreacted material in the lab-attached frame is zero.

Note that Equation (2.3) is incomplete without an equation of state that describes how the internal energy is related to the other variables. The equation of state will be discussed below.

### Hugoniot curves and Rayleigh lines

The most convenient diagrams to use for identification of the stages in the detonation process are $p - v$ diagrams that plot the pressure against the specific volume. Using the conservation laws across the shock, two sets of distinctive lines can be extracted to give a complete picture of the detonation process. These curves are called the Rayleigh line and Hugoniot curves.

Elimination of $u$ from (2.1) and (2.2) defines the Rayleigh line (shown in dark blue in Figure 2.1),

$$\mathscr{R} = \rho_0^2 D^2 - \frac{\left(p - p_0\right)}{\left(v_0 - v\right)} = 0. \tag{2.4}$$

This line passes through the point $(p_0, v_0)$ and has a slope $-\rho_0^2 D^2$ so that $D = \infty$ will produce a vertical line, representing an instantaneous detonation of all material, and $D = 0$ will produce a horizontal line, representing no reaction.

The Hugoniot curve is derived in a similar way by using (2.1) and (2.2) to eliminate $u$ and $D$ from (2.3),

$$\mathscr{H} = e\left(p, v, \lambda = 1\right) - e\left(p_0, v_0, \lambda = 0\right) - \frac{1}{2}\left(p + p_0\right)\left(v_0 - v\right) = 0, \qquad (2.5)$$

where the equation of state, which specifies $e(\rho, p, \lambda)$, completes the description of the line. This Hugoniot curve is the locus of all possible shocked states for given initial conditions $(v_0, p_0)$ (shown in red in Figure 2.1).

CJ theory describes a transition from upstream unreacted conditions to downstream fully reacted conditions only. This means that a reacting wave starts at the initial state $(v_0, p_0)$ on the reactant Hugoniot in red in Figure 2.1 and proceeds via the Rayleigh line (dark blue) to the final CJ state as $(v_{\text{CJ}}, p_{\text{CJ}})$ shown on the green curve. This green curve is also a Hugoniot but of the products; that is, when $\lambda = 1$.

The expressions for the conserved variables at the CJ point are called the CJ conditions and they are derived using a combination of the Rayleigh and Hugoniot lines, isentropic thermodynamic laws and the conservation laws. They also depend on the equation of state used.

### Calculating the detonation velocity

The detonation velocity can be calculated from the slope of the Rayleigh line. There are an infinite number of solutions for the Rayleigh line although only one, which corresponds to the CJ detonation velocity, is steady.

Figure 2.1 illustrates a few possibilities for the Rayleigh lines. Note that only the line tangent to the green product Hugoniot curve satisfies the CJ conditions. $D = D_{\text{CJ}}$ is the only line with a unique solution that intersects the Hugoniot just once. This point, the CJ point, represents the final state where the CJ conditions apply.

The Rayleigh line with $D_A$ has a finite, negative slope but does not intersect the green product Hugoniot curve; this implies that there is no steady solution. The Rayleigh line with $D = D_B$, on the other hand, intersects the green product Hugoniot curve twice; this implies there are two solutions: a weak solution close to the initial state and a strong solution further up the $p - v$ diagram. Since there needs to be a unique solution the weak solution is rejected as inconsistent with the model and only the upper solution is recognised [40]. This strong solution represents subsonic flow and the detonation is said to be overdriven at this velocity. This flow will be unsteady but may eventually result in a steady wave. For example, in the case of an overdriven piston, a forward-moving rarefaction is generated

which will overtake the front and eventually produce a steady solution corresponding to the new piston velocity.

### Equation of state

The equation of state plays an important role in closing the systems of equations used to model detonation and in describing the properties of the material being modelled. For inert materials, these equations are normally fitted to experimental Hugoniot data of the different materials when shocked. For reactive materials, the equations of state need to take into account the complicated intermolecular interactions that take place and can include any of entropy, pressure and temperature. The equations of state used in this work will be described in Chapter 4.

The instantaneous chemical reaction in the CJ description of the evolution of detonation is a solid starting point for modelling detonation and was successful at predicting the detonation velocity of ideal explosives at the time of its development. However, the model fails to take into account the change in behaviour of similar products or the dependence of detonation behaviour on parameters such as pressure or temperature. The ZND theory explored in the next section takes some of these ideas to improve on CJ theory.

## 2.1.2. ZND theory

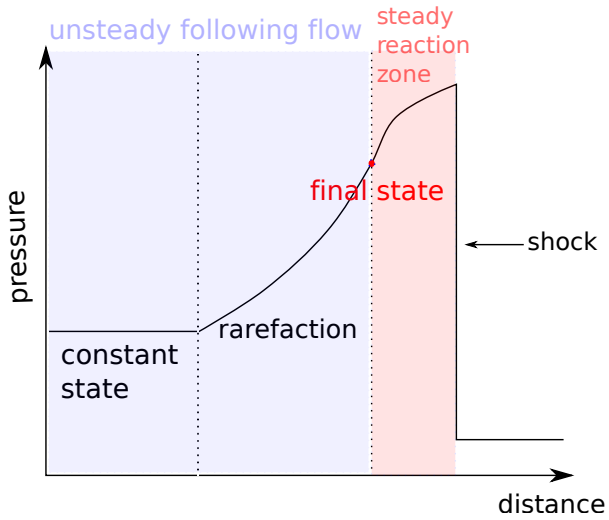


Figure 2.2.: Diagram illustrating the different components of a ZND pressure wave.

ZND theory [37, 56, 80] extends CJ theory to include a finite reaction rate. A shock initiates a single reaction and a finite reaction zone behind the shock

follows. The reactive wave then settles into the final CJ state, as shown in Figure 2.2.

Figure 2.3 illustrates possible solutions with the ZND solution shown in dark blue. The material starts at $(v_0, p_0)$ on the red Hugoniot curve and is then shocked to another point on the Hugoniot, at the intersection with the blue Rayleigh line which represents a wave travelling at velocity $D_{\text{CJ}}$. This pressure peak is called the von Neumann point and is the maximum pressure achieved by a steady-state wave travelling at $D_{\text{CJ}}$. At this point the reaction can be initiated and the state travels via the Rayleigh line to the tangential CJ point on the green fully reacted final Crussard curve.

The lighter blue lines in Figure 2.3 are again unsteady and overdriven detonations. They have the same properties as the lighter blue lines in Figure 2.1 that were discussed in §2.1.1.

Although the ZND theory takes into account the nature of pressure initiated detonation and the finite reaction behind the shock front, it still fails to capture any multidimensional effects.

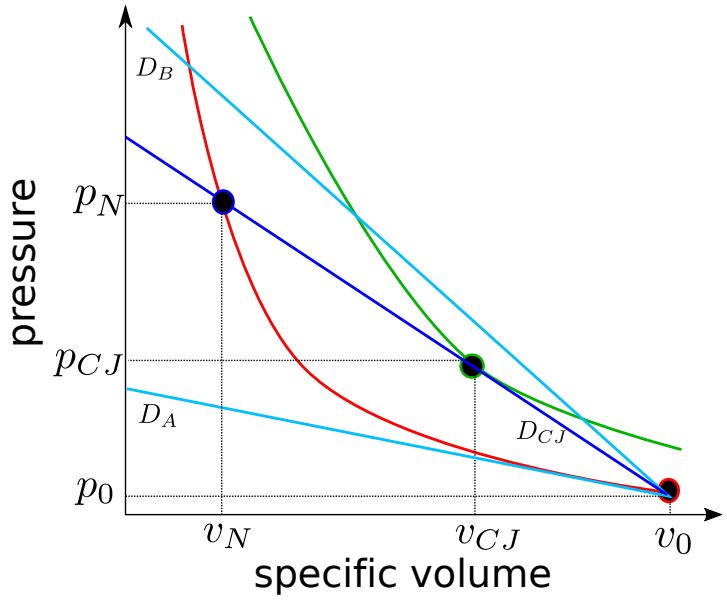


Figure 2.3.: The reactant Hugoniot (red) and product Hugoniot or final Crussard curve (green). The inert shock compresses the material from the initial state $(v_0, p_0)$ to the von Neumann point at $(v_N, p_N)$. The finite reaction then describes an expansion down the Rayleigh line (blue) to the final state. The dark blue line is tangent to the final Crussard curve and the final state here is the CJ state. The two lighter blue lines show unsteady detonation and overdriven detonation travelling at a speed of $D_A$ and $D_B$, respectively.

## 2.2. Multidimensional detonation theory

In reality, detonation is a three-dimensional phenomenon and radial losses of energy have a large impact on the propagation of a detonation wave, particularly in non-ideal explosives. In the past sixty or so years, multidimensional modelling of detonation has been one of the main areas of focus for detonation modellers. Initially, these attempts at multidimensional modelling were analytical attempts at including radial losses into the detonation problem. Some of these theories are briefly outlined in §2.2.1. These first attempts have evolved into more sophisticated analytical or streamline models, such as Detonation Shock Dynamics (see [15] for a comprehensive review) or the straight streamline approximation of [78]. These are outlined in §2.2.2.

Multidimensional models aim to capture the multidimensional aspects of a propagating detonation wave. For ratestick examples, although the propagating wave is three dimensional, assuming axisymmetric geometry implies that a radial slice of the solution will be representative of the whole solution, as shown in Figures 2.4 and 2.5.

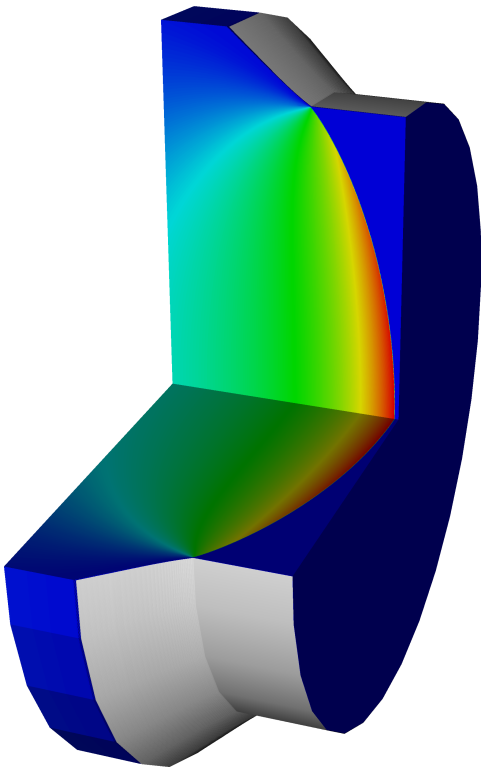

Figure 2.4.: A DNS solution is calculated in two dimensions with axisymmetric geometry on a single radial slice (top facing side). This solution is rotated about the $z$-axis to recover the full three-dimensional solution.

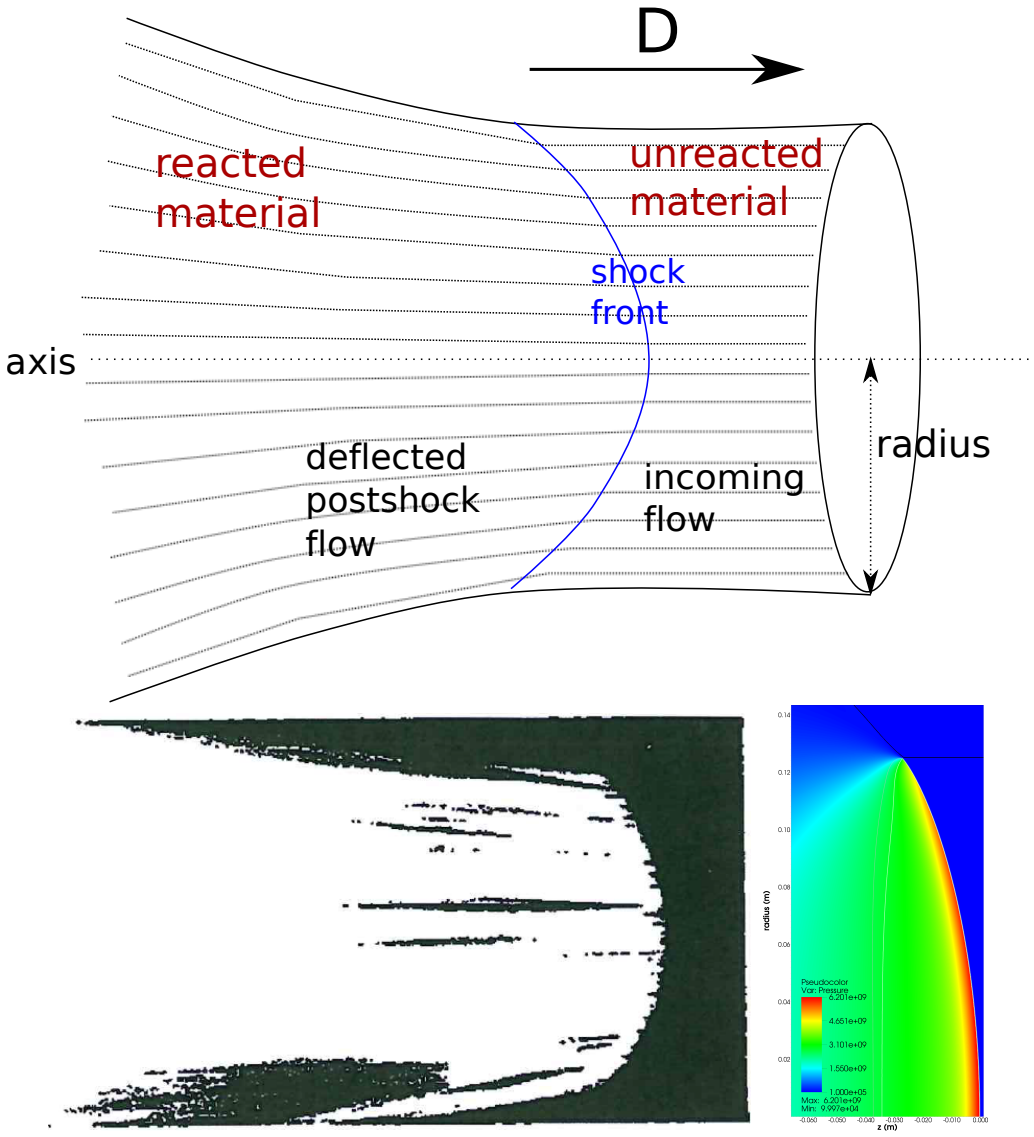


Figure 2.5.: (top) A representation of the three dimensional ratestick problem. A detonation wave passes through a cylinder of unreacted explosive material. Incoming flow is deflected by the curved shock front and behind the shock the flow diverges, pushing outwards into the surrounding material. Experimentally, the shock shape can be captured by streak photography of the propagating shock front (bottom left, taken from [11] with permission from Orica). In modelling, as the flow is axisymmetric, only half of this slice of the ratestick is simulated (bottom right).

Approximate multidimensional models have maintained popularity within the commercial detonation world because they can provide fast solutions to complex problems. However, over the last three or so decades, the numerical efficiency of computers has increased to the point where obtaining a direct numerical simulation (DNS) result, with the right techniques, is almost as fast as obtaining an approximate solution. Although this study focusses on approximate solutions, the different forms of DNS for modelling detonation will be briefly outlined in §2.2.3 and one of these is used for as a benchmark for the reduced order developments.

### 2.2.1. Slightly divergent flow

The first well-cited attempt at including multidimensional effects in detonation modelling was the quasi-one-dimensional model of Wood & Kirkwood [79], and there is a good review of this model in §5G of [40]. In brief, the Wood-Kirkwood model assumes that the detonation can be modelled by the steady, two-dimensional axisymmetric augmented Euler equations, (1.1)-(1.4) with $\frac{\partial}{\partial t} = 0$, but specialised to the axis so that the radial velocity disappears.

The augmented Euler equations are given again below but are written using axisymmetric coordinates to make the radial terms clearer. The radial velocity is now denoted by $\omega$ and the axial velocity is denoted by $u$, with $r$ and $z$ denoting the radial and axial directions. The conservation of mass (1.1) becomes

$$u\frac{\partial \rho}{\partial z} + \omega\frac{\partial \rho}{\partial r} + \rho\left(\frac{\partial \omega}{\partial r} + \frac{\omega}{r} + \frac{\partial u}{\partial z}\right) = 0,$$

with the axial momentum (1.2) given by

$$\omega\frac{\partial u}{\partial r} + u\frac{\partial u}{\partial z} + \frac{1}{\rho}\frac{\partial p}{\partial z} = 0,$$

and the radial momentum (1.2) by

$$\omega\frac{\partial \omega}{\partial r} + u\frac{\partial \omega}{\partial z} + \frac{1}{\rho}\frac{\partial p}{\partial r} = 0.$$

Using the expression for the sound speed,

$$c^2 = \frac{\frac{p}{\rho^2} - \left(\frac{\partial e}{\partial \rho}\right)_{p,\lambda}}{\left(\frac{\partial e}{\partial p}\right)_{\rho,\lambda}},$$

and thermicity,

$$\sigma = -\frac{1}{\rho c^2}\frac{\left(\frac{\partial e}{\partial \lambda}\right)_{\rho,p}}{\left(\frac{\partial e}{\partial p}\right)_{\rho,\lambda}},$$

the conservation of energy is given by (see Appendix A)

$$u^2\left(\frac{\partial u}{\partial z}\right)+\omega^2\left(\frac{\partial \omega}{\partial r}\right)+u\omega\left(\frac{\partial u}{\partial r}+\frac{\partial \omega}{\partial z}\right)-c^2\left(\frac{\partial u}{\partial z}+\frac{\partial \omega}{\partial r}+\frac{\omega}{r}\right)=-c^2\sigma W.$$

From (1.4) the reaction progress is given by

$$u\frac{\partial \lambda}{\partial z}+\omega\frac{\partial \lambda}{\partial r}=W.$$

Specialised to the axis, the only remaining radial term in the resulting ODEs is the radial divergence, $\frac{\partial \omega}{\partial r}$: the PDEs reduce to a set of ODEs which can be integrated. This gives a relationship between the detonation front curvature and the detonation velocity (see Chapter 6).

The Wood-Kirkwood theory was then generalised by many authors for different parameters of non-ideal detonation. See, for example, [12, 13, 53] or for a detailed list and brief history see Chapter 4 of [39]. These models take into account any of: shape of the shock front, effects of confinement, effects of diameter and other two-dimensional properties that can affect the evolution of detonation in explosives. These models are particularly useful for the non-ideal explosives where there are typically lower detonation velocities and greater shock front curvature and the diameter effect or the impact of the detonation on surrounding inert material is of great interest. One of these models is that of Chan & Kirby [30] which is one of the models investigated and extended in this work.

However, there is a limit to validity of this slightly divergent flow approach for significantly non-ideal explosives, especially in determining the diameter effects for unconfined and confined cases [69]. Relationships between the radius of curvature of the shock at the axis, the charge diameter and confinement need to be empirically specified in parts of these methods to obtain the diameter effect relationship. Whether or not the efficiency that these models provide outweighs this limit of validity is a question addressed in this thesis - see Chapters 6 and 7.

Alternative reduced ODE models for detonation that move away from the Wood-Kirkwood slightly divergent flow are discussed in the next section.

### 2.2.2. Detonation shock dynamics

Detonation shock dynamics (DSD) is a growing body of work that describes the dynamics of detonation if the detonation shock front curvature is small compared to the length of the reaction zone, or $D \approx D_{\text{CJ}}$. The theory is based on the two-dimensional augmented Euler equations (partial differential equations (PDEs) for reactive flow) that are then transformed to shock-attached, intrinsic coordinates. A comprehensive review of DSD is available [15] but a brief outline in the context of non-ideal explosives follows.

DSD theory stems from the initial work of Bdzil [13] and was developed primarily for ideal to weakly non-ideal military explosives. The theory is based on a $D_n - \kappa$ relationship where $D_n$ is the shock normal detonation velocity and $\kappa$ is a measurement of the curvature. In the leading order theory, this relationship is determined by analysis under the asymptotic limit when $\kappa$ is small. The relationship determines the shock shape which can then be used to solve the whole steady-state problem.

The leading order DSD model is the most widely used form and has been used to successfully model weakly non-ideal detonations [15] and is fast (calculates within seconds) and efficient. However, the asymptotic analysis used for this leading order theory relies on a large shock front radius of curvature typical of ideal detonation velocities.

Previous attempts to model less ideal explosives [7, 14, 73] are very specific and cannot be used in general for non-ideal explosives without extensive fitting of each explosive [78].

Although successful implementations of DSD for strongly non-ideal explosives has not been reported, it has been suggested that the theory could be extended to a higher order for this purpose, and still possibly find a solution within seconds [8]. Other DSD-like developments, for example Sharpe et al. [69], could be the basis for modelling non-ideal detonations for predictive or comparative uses.

The recent straight streamline theory of Watt et al. appears to give a better fit to direct numerical simulation (DNS) results than leading order DSD (see [78]), although only a simple polytropic 'heavy' gas has been used to model a non-ideal explosive until now. This theory is also based on the two-dimensional axisymmetric augmented Euler equations, transformed to streamline-attached coordinates where the streamlines are assumed to be straight but divergent. In Chapter 8, this approach is extended to a multiphase system to provide more realistic modelling of the non-ideal explosives of interest.

### 2.2.3. Direct numerical solutions

All of the results in this study will be compared with direct numerical simulation (DNS) results. Direct numerical simulations are, as the name suggests, numerical solutions of the underlying PDEs that describe the fluid dynamics of the problem.

To solve the PDEs that describe a fluid dynamics problem several things need to be considered. Firstly, the size of the domain needs to be large enough to capture any macroscopic features of interest. For example, for rate stick simulations, if one was interested in the diameter effect relationship, the domain would need to be wide enough to capture the width of the charge and long enough so that, after an initial pressure boost, the reactive wave front can settle into a steady state. Within this domain, however, the grid

needs to be fine enough to capture the important small-scale features of the problem. For detonation modelling, the shock and reaction zone need to have as many cells in them as possible to capture the underlying physics accurately. The problem is that a large domain with small cells necessarily implies more cells and lots of calculations, which of course adds to the computational time.

To navigate this problem in detonation modelling many numerical techniques have been developed. A few of these are discussed below.

### Shock-capturing DNS

Most detonation problems involve a shock followed by a reactive wave. However, a shock is a sharp, discontinuous change in the flow variables and this discontinuity is difficult to represent numerically. Shock capturing methods diffuse the shock to avoid numerical instabilities. However, if the nature of the problem is changed then the solution will be changed and so a set of methods have been developed that can diffuse the shock front while preserving speed and strength (see [75]).

One of these techniques, the monotonic upstream-centered scheme for conservation laws (MUSCL), was used by Schoch et al. to produce DNS of non-ideal detonations in various confinements [66, 67, 68]. However, because the mechanical equilibrium multiphase equations used by Schoch et al. are non-conservative, the speed and strength of the shock is not preserved. To combat this, level sets are used to track the progress of the shock and to update the state behind the shock with a corrected set of values. This is akin to shock-fitting, as described below. The DNS developed by Schoch et al. in [68] is used for the DNS comparisons in this work.

### Efficiency in shock-capturing DNS

Shock capturing methods address the problem of resolving the shock front but do not necessarily address the problem of resolving the reaction zone while at the same time solving the equations on a domain that captures the macroscopic behaviour of the problem. One approach is to use adaptive mesh refinement (AMR) where a larger mesh (fewer cells) is used on areas where there are no changes in any of the flow variables and more cells are used around the areas of great change, such as the shock front.

An alternative approach used in [68] is to only simulate the area around the detonation driving zone (DDZ). The DDZ can be tracked via the steep gradients in the flow variables at the shock front and the CJ conditions at the sonic locus. Anything outside this region is ignored and so computational time is focussed on the area of interest only. This can provide the same solution for the DDZ as would be achieved with a full domain but is much more efficient. Simulations with 200 cells in the DDZ take roughly 5 hours on 1-2 cores to solve. While this is much more efficient than shock-capturing on

a full domain, even with AMR, a faster solution is possible with shock-fitting.

### Shock-fitting DNS

Shock-fitting locates and tracks the motion of the shock. However, instead of diffusing the shock and implementing a method that preserves the flow variables at the shock, the shock is instead treated as a boundary between the upstream and downstream regions. Advantageously, in these regions the governing equations have smooth solutions. The appropriate shock conditions are then used to approximate the space-time evolution of the shock. This means that the shock is no longer diffused and the solution is therefore potentially more accurate.

Shock-fitting in detonation modelling has recently surged in popularity and the initial work of Henrick on idealised gaseous and condensed phase one- and two-dimensional explosives [44] has been extended to more accurate schemes with a growing range of explosives, such as in [60]. Although these shock-fitting schemes can provide highly accurate detonation solutions at relatively small computational cost, the models explored so far have all been for slab geometry with mostly idealised equations of state. The implementation of a more realistic equation of state in [60] proved unsuccessful without adjustment of the rate parameters and even then the diameter effect or failure diameter was not predicted well. This implementation also only relied on an augmented Euler system that would require closure conditions (discussed in §6.2.4). So although shock-fitting provides a model that is competitive in efficiency with shock-capturing methods, it is still not as efficient as the reduced ODE models explored in this work; nor does it truly capture the heterogeneities of the explosive material with its underlying system of equations.

As the focus of this work is unconfined, heterogeneous explosives, the next chapter looks at the two explosives used throughout this study and outlines classifications for different types of confiners.

# 3. Materials

Due to the complicated nature of the detonation process, there is no strict definition of when an explosive is classified as ideal or non-ideal. Broadly speaking, a non-ideal explosive can be defined as one that releases some of its energy behind the detonation front. However, there are many explosives that are considered to be ideal that also display this behaviour.

There are further guidelines that may be helpful in identifying whether or not an explosive is illustrating non-ideal behaviour. A non-ideal explosive is expected to have a CJ pressure or velocity that is significantly different (50 kbar and 500 $ms^{-1}$, respectively) from the CJ pressure or velocity obtained from a steady-state, ideal, CJ detonation calculation for that same explosive. The expansion isentrope may also be used as a measure and any differences above 0.1 $cm\mu s^{-1}$ would be considered significant.

Interestingly, adding non-explosive materials to an ideal explosive will not necessarily make it non-ideal. For example, there are some cases where the addition of metals to an ideal explosive allows the explosive to retain and sometimes even improve upon its ideal nature. For example, the addition of aluminium as this metal is most often completely reacted near the CJ plane. However, there are some inert metal-loaded explosives and mixtures of explosives with ammonium salts, such as ammonium nitrate, that do display non-ideal behaviour [55].

Mining explosives tend to be non-ideal. They are relatively cheap to manufacture and are typically more stable. However, low cost and stability are not their only advantage. The focus of most blasting for mining purposes is to fracture the surrounding rock into a size that will make transportation and further breakdown easier. This means that the rock needs to be large enough to be moved by large-scale machinery, but not so large as to raise the costs of breaking down the material at an off-site location. The blast also needs to be limited so that the material of interest is not damaged.

Ideal explosives are not suitable for mining purposes. Not only are they much more expensive to manufacture, they are often highly unstable and tend to release their energy too quickly. The resulting high detonation pressures pulverise the surrounding rock into a small powder which is then difficult to gather and move from the area surrounding the material of interest. The late release of energy behind the detonation front in non-ideal explosives make them much better candidates for use in mining applications.

Another distinguishing feature of non-ideal explosives is that their behaviour can be strongly dependent on the diameter of the charge. Determin-

ing this behaviour, most often characterised by the detonation velocity as a function of the radius or diameter, is often the focus of non-ideal detonation codes used for practical mining purposes. This relationship results in a smooth curve often called the diameter effect curve.

This study focusses on two types of non-ideal explosives often used in mining applications: ammonium nitrate/fuel oil (ANFO) and emulsion explosives, in particular EM120D. In the following chapters their behaviour as a function of the charge diameter in different confinements will be a focus for simulations. The following sections give a brief outline of these two types of non-ideal explosives and the confining materials that will be used.

## 3.1. ANFO

Figure 3.1.: (left) ANFO prills [41]. (right) Filling a borehole with ANFO prills in preparation for rock blasting [43].

ANFO is a dry, free-flowing non-ideal explosive usually composed of about 6% fuel oil and 94% ammonium nitrate (AN) prills, as shown in Figure 3.1. It is the most commonly used blasting explosive mixture due to its low cost and high stability: under most conditions ANFO is a tertiary explosive so is insensitive to shocks and requires an intermediate explosive booster of secondary explosive such as pentolite or PETN to achieve a reliable detonation wave.

The AN prills for ANFO are normally produced in the form of a solution, by a reaction of anhydrous ammonia gas and concentrated nitric acid. The concentration of this solution is then increased by evaporation of nearly all of the excess water. This AN solution is then turned into a prill and the

small percentage of water left in the prill leaves voids when it is dried. This leaves the prill porous to allow for the absorption of the fuel oil. The AN prills can be further sensitised with the addition of air, aluminium, perlite, chemical gassing agents or glass microballoons. These sensitising additions are most often added to allow greater absorption of the fuel oil or to create hotspots in the unreacted explosive. The porous nature of the AN prills in ANFO make it distinct from the AN fertiliser prills.

Despite its popularity, ANFO has some disadvantages. AN is highly hygroscopic and so any humidity in the air or any water in a borehole can make ANFO dangerous, unreliable or both. Furthermore, the correct fuel to AN ratio needs to be maintained for consistent performance and to ensure that only nitrogen, carbon dioxide and water are the by-products of the reaction. Since mixing of the AN and fuel in a borehole can be inconsistent and unreliable, ANFO is often overloaded with fuel so that consistent blasting performance can be maintained. However, changing the fuel to AN ratio results in an oxygen imbalance with excessive post-blast fumes. In practice, moderate amounts of toxic gases such as carbon monoxide and nitrogen oxides are produced depending on if the oxygen balance is negative (CO) or positive ($NO_x$).

## 3.2. Emulsion explosives

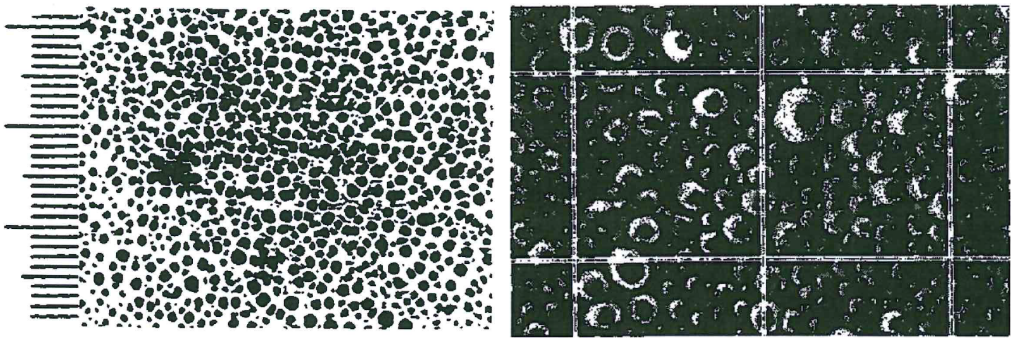

Figure 3.2.: (left) Microphotograph of emulsion mono layer from [11]. One point on the scale to the left is 10 $\mu$m. (right) Typical photograph of an emulsion's surface taken from [38]. A square size is equal to $20 \times 20 \mu m^2$. Both photographs are reproduced with permission from ORICA.

An emulsion is a mixture of two or more liquids, normally immiscible, that are able to be mixed with the use of a stabilising emulsifier. An emulsion explosive, therefore, is normally a solution of oxidiser salts, such as AN, dispersed as microdroplets into a continuous fuel phase. This means that the chemistry of an emulsion can be quite similar to that of ANFO but with

the advantage that the emulsion, unlike ANFO, is water-resistant so can be used in wet boreholes and is not affected by humid environments.

The droplet size of the oxidiser is normally many orders of magnitude less than that of AN prills, as shown in Figure 3.2, but the emulsion can also be sensitised with the addition of air, chemical gassing agents, glass microballoons or blending with ANFO.

The bulk density of an emulsion is also typically higher than that of ANFO but one advantage of emulsions is that the addition of inert materials can allow for variable density. These bulking agents then determine and control the sensitivity of the emulsion and high detonation velocities can be obtained. Furthermore, because of the intimate mixture of oxidiser and fuel, emulsion explosives can have a much higher detonation energy than ANFO but the greater control on oxygen-balance means that fewer toxic gases are produced.

#### EM120D

The specific emulsion investigated in this work is the research emulsion EM120D, with use of experimental results of Dremin [38] which were obtained under contract with ICI Explosives Canada.

EM120D is a mixture of ammonium nitrate, water, fuel and emulsifier with a condensed phase density of $\rho_c = 1400$ kgm$^{-3}$. Sensitised with glass microballoons (hollow glass spheres), EM120D has an average mixture density of $\rho_0 = 1200 \pm 10$ kgm$^{-3}$. The ideal detonation velocity, determined with the ideal chemical equilibrium program IDEX, is $D_{\text{ideal}} = 6385.35$ ms$^{-1}$.

## 3.3. Confiners

The confinement of an explosive by inert materials can affect the propagation of the detonation in the explosive [9]. The most noticeable effect is a change in shock front shape, as shown in Figure 3.3. A curved shock front implies larger radial losses of energy and hence lower detonation velocities. To counteract these radial losses, larger charge diameters must be used to achieve the same detonation velocities. Therefore, the type of confinement can affect the diameter effect curve.

An unconfined detonation occurs when there is no confinement except for air. Unconfined detonations can be of interest to those looking at safety aspects of transporting explosive materials where accidents can result in unconfined detonations. Improvised explosive devices (IEDs) are also usually detonated in mostly unconfined conditions and so unconfined explosive studies can give an overview of expected impact of IEDs in a variety of situations. In terms of commercial explosives, data for cylindrical unconfined detonations is collected experimentally so that detonation models can be

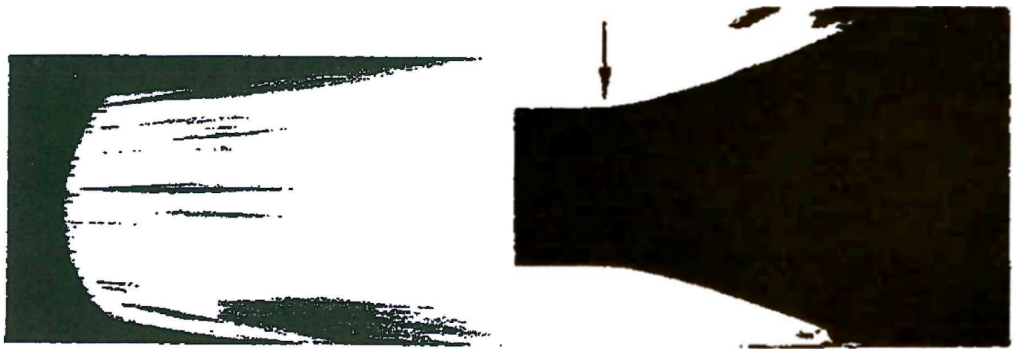

Figure 3.3.: (left) Photoscanning picture of EM120D in concrete confinement. (right) Photogram of the same emulsion in copper confinement. The arrow points to the start of the motion of the confiner. The same emulsion explosive affects the surrounding confiner differently due to the properties of the confining material. Although not shown for the copper confinement, the confiner in turn also impacts on the shape of the shock front and hence the detonation speed for a given radius. Both images are reproduced from [11] with permission from ORICA.

validated and then used to predict the explosive's behaviour under confined conditions. These cylindrical unconfined detonations are normally not truly unconfined as the explosive material must be initially held by some material such as paper or cardboard. However, DNS simulations of commercial explosives in paper and air confinement show minimal, if any, difference in the diameter effect curves [65].

Confinement can be modelled in a variety of ways with differing accuracy. Models can take into account the elastic-plastic nature of the surrounding materials (see, for example, [67]) or use shock Hugoniot data for the confining material and simulate the confiner as a liquid (see, for example, [68]) or use shock polars for a prediction of confiner-explosive interaction (see, for example, [9, 29, 78]).

Due to the nature of reduced ODE models, in this work the confining material is modelled using the intersection of shock polars, the theory for which is outlined in Appendix B. The intersection point is parametrised by the angle that an incoming particle makes with the shock front at the charge edge. This angle is used as a restriction on the shock front shape in the ODE models. This theory is explored further in §7.4 and is used as part of modelling confined detonation in §8.3.

In this study, two confining materials are investigated: steel and concrete. Although none of these materials are expected to be found surrounding a borehole on a mining site, they are have been investigated with a DNS solution in [65, 66, 67, 68] and some experimental data is available. These materials also represent two different types of classic explosive-confiner interactions

that ODE models should be able to model.

There are some explosive-confiner interactions that shock polar analysis cannot be used for. Along with steel and concrete, these materials are also briefly discussed below.

### 3.3.1. Steel

Steel is a metal alloy used widely in construction due to its high tensile strength (capacity to withstand loads tending to elongate). Since it is an alloy, there is no universal steel composition and so its properties and behaviour depend on the constituents of the alloy. The density of steel can range from about 7750 $\text{kgm}^{-3}$ to 8050 $\text{kgm}^{-3}$, with varying degrees of tensile strength. In general, it can be classed as a very strong confinement for most explosives which means that shock polar analysis will result in a solution for the explosive–confiner interaction.

The steel simulated in this work represents experimental data from the EM120D experiments of Dremin [38], with the parameters taken from [65]. This steel has an ambient density of 7840 $\text{kgm}^{-3}$ and a bulk sound speed of 3670 $\text{ms}^{-1}$. Two sets of experimental data appear as one in the results of this work. In the experiment, the steel confinement tubes for the small diameters (7-10 mm) were machined from cylindrical steel rods with a stated tensile strength of $\sigma_{\text{UTS}} = 0.48$ GPa. Larger diameter experiments (14-75 mm) used weld free steel tubes with a stated tensile strength of $\sigma_{\text{UTS}} = 0.56$ GPa. This difference in tensile strength is suggested to affect the diameter effect curve for the EM120D confined in steel DNS solutions presented in [65, 67] and so would also be expected in any reduced ODE simulations.

### 3.3.2. Concrete

In the same EM120D experiments, the emulsion's performance was also tested in concrete confinement. Concrete confinement tubes were produced by pouring the cement (10 parts), quartz sand (20 parts) and water (7 parts) mixture into steel moulds to produce $30 \pm 0.5$ mm thick cylinders. Once dried, strength tests of samples were carried out to find consistent samples.

Like steel, concrete is strong confinement so a solution for the explosive–confiner interaction can be found using shock polar analysis and hence can be used in a reduced ODE simulation. However, unlike steel, it has a high compressive strength (capacity to withstand loads tending to compress) but lower tensile strength and is therefore useful to study as another form of classic confinement.

There are materials, however, that cannot be explored using shock polar analysis that still may be of interest to mining applications. These are not

investigated in this work as they cannot be modelled using the ODE models investigated but a discussion of these materials is warranted.

### 3.3.3. Unrepresented materials

As discussed in [66] and [71], it has been estimated that approximately half of the current rock blasting situations involve confining materials that have sound speeds greater than or equal to the detonation velocity of the explosive. Due to high sound speed in these materials, detonation energy is transported via acoustic waves in the confining material ahead of the detonation front. Schoch [65] showed that, especially for low velocity detonations, the movement both inward and outward of aluminium confining EM120D contributed to higher than expected detonation velocities. This has also been shown for aluminium confining ANFO [45].

If this phenomenon is observed both experimentally and in DNS solutions then it should be a part of a confined reduced ODE model. However, confined reduced ODE models typically use shock polars to determine the explosive-confiner interaction. In confining materials where the sound speed is greater than the detonation velocity, the explosive-confiner interaction is shock-free. Instead, a pressure gradient is found in the confining materials which moves with the detonation velocity. This type of confinement is called unsteady.

The second type of confinement that is not represented in this work is stiff confinement. Stiff confiners also have high ambient sound speeds but they are typically lower than the detonation speed of the explosive. Unlike unsteady confinement, there is a shock in the material but it is a low-pressure shock and the only possible shock polar match is via an intervening expansion fan in the confiner [6]. This expansion fan represents a low-pressure shock driven from the confiner into the explosive which implies a negative, inward, streamline deflection.

Both of these types of explosive-confiner interaction are outside the scope of the reduced ODE models explored in this work. However, to complete the discussion on confining materials and shock polars, these unrepresented types are further explored in §7.4 on shock polars.

To describe any of the materials mentioned in this chapter, equations of state need to be chosen and fitted for each material. Different equations of state suit different materials and this is explored in the next chapter.

# 4. Equations of state

All of the models investigated in this work require the declaration of an equation of state for each phase or material in order to close the system of equations used to describe the detonation process.

Chapter 6 explores the use of an Euler-equation-based two material model. Only a single equation of state for each phase, unreacted and reacted, describes detonation in the explosive material. This is unrealistic for heterogeneous non-ideal explosives and so the alternative mechanical equilibrium model is utilised in Chapter 7 to include a void phase in the unreacted material. Shock polar theory is then included in the calculations in §7.4 so that the edge of the charge can be more accurately determined and this includes the use of an equation of state to describe the confining material.

For all models it is assumed that the equation of state chosen for the components of the detonation can be cast in Mie-Grüneisen form,

$$e_k\left(p, v_k\right) = e_{k,\mathrm{ref}}\left(v_k\right) + \frac{v_k}{\Gamma_k\left(v_k\right)}\left(p - p_{k,\mathrm{ref}}\left(v_k\right)\right), \tag{4.1}$$

where $\Gamma_k\left(v_k\right)$ is the Grüneisen coefficient, $e$ is the internal energy, $p$ is the pressure and $\left(p_{k,\mathrm{ref}}\left(v_k\right), e_{\mathrm{ref}}\left(v_k\right)\right)$ is the reference curve for pressure and energy. The subscript $k$ is the index of a specific material; for example it may represent the unreacted, void or reacted material.

Three different equations of state are used in this work. The polytropic, or ideal gas (IG), equation of state is used in both states of two-fluid simulations as a tool for validation. It is also used to model the unreactive void phases in the unreacted ANFO and emulsion explosives and air confinement. The Linear Mie-Grüneisen (LMG) equation of state is used in the unreacted condensed phase of the explosives and for some examples of confinement when illustrating the use of shock polar theory. The Williamsburg (WMBG) equation of state is employed for the reacted phase of both ANFO and the emulsion explosive.

The forms for these equations of state are outlined in Table 4.1, and the values for the parameters used are given in Tables 4.2–4.4. The following sections outline each equation of state, its benefits for modelling non-ideal detonation in the context of streamline models and the parameters used for the materials investigated in this work.

| EOS | $e_{\text{ref}}(v_k)$ | $p_{\text{ref}}(v_k)$ | $\Gamma_k(v_k)$ |
|---|---|---|---|
| IG | $-Q$ | 0 | $\gamma_k - 1$ |
| LMG | $\frac{1}{2}p_{\text{ref}}(v_k^c - v_k)$ | $\frac{c_0^2(v_k^c - v_k)}{(v_k^c - s(v_k^c - v_k))^2}$ | $\Gamma\frac{v_k}{v_k^c}$ |
| WMBG | $-Q$ | 0 | $\frac{A(v_k/v_k^0)}{B(v_k/v_k^0)}$ |

Table 4.1.: Equations of state used in this study with (4.1). Note that for the WMBG equation of state, the variables $A(v_k/v_k^0)$ and $B(v_k/v_k^0)$ denote polynomials of order $N$.

| | Unreacted | Reacted | Air | Void |
|---|---|---|---|---|
| $\rho_0$ [kg/m$^3$] | 1600 | 1600 | 10 | 10 |
| $\gamma$ | 3.0 | 1.4 | 1.4 | 1.22 |
| $p_0$ [Pa] | 1.0E5 | 1.0E5 | 1.0E5 | 1.0E5 |
| $Q$ [J] | 0 | 3.822E6 | 0 | 0 |

Table 4.2.: Parameters for the constant gamma polytropic equations of state used for the unreacted and reacted phase of a simple test problem and for air and voids. Air is used as the confining material in the unconfined shock polar calculations. The void material is used as the inert void material in both ANFO and the emulsion.

## 4.1. Polytropic equation of state

The constant gamma polytropic, or classic ideal gas, equation of state is a simple equation of state used to model gases and is roughly accurate for low pressure and moderate temperature simulations. It is given by

$$e = \frac{p}{\rho(\gamma - 1)} - Q, \tag{4.2}$$

where $\gamma$ is the ratio of specific heats, $\gamma = \frac{C_p}{C_v}$, known as the adiabatic gamma.

The ideal gas equation has historically been used to model unreacted non-ideal explosives as 'heavy gases' with $\gamma = 3$. The popularity of this equation of state is due to its simple form which is easy to work with and so the pressure is easily extracted. Given that this equation of state was designed for low pressure and moderate temperatures and that the $\gamma$ is constant, it is unrealistic to use for detonation simulations.

Since the polytropic equation of state is historically used as a test case for most published work, it will be used in parts of this work for validation and comparative purposes. A sample of parameters used are given in Table 4.2.

| | EM120D | ANFO | Steel | Concrete |
|---|---|---|---|---|
| $\rho_k^c$ [kg/m$^3$] | 1400 | 1641.1 | 7840.0 | 2340.0 |
| $\Gamma_0$ | 0.937 | 1.1095 | 2.0 | 2.0 |
| $s$ | 1.82 | 1.71 | 1.645 | 1.745 |
| $c_0$ [m/s] | 2259.0 | 2809.0 | 3670.0 | 2235.0 |

Table 4.3.: Parameters for the LMG equation of state, for the condensed phase of EM120D and ANFO and for steel and concrete.

## 4.2. Linear Mie-Grüneisen (LMG) equation of state

For simulations of compressible flows involving shocks it is convenient to use shock Hugoniots for the reference state curves in (4.1). For many solids of interest, starting from state $(\rho_0, p_0)$, experimental data indicates that over a large range of shock strengths the relationship between shock and particle speed is adequately approximated by a simple linear fit,

$$u_s = c_0 + s u_p, \tag{4.3}$$

where $u_s$ is the shock's speed, $u_p$ is the postshock particle speed, $c_0$ is the upstream speed of sound, and $s$ is related to the isentropic derivative of the bulk modulus $K_s$ of the upstream flow,

$$K_s = \left.\frac{\partial \ln(\rho)}{\partial \rho}\right|_s, \tag{4.4}$$

$$s = \frac{1}{4}\left(\left.\frac{\partial K_s}{\partial p}\right|_s + 1\right). \tag{4.5}$$

Coupled with the Rankine-Hugoniot jump conditions, the internal energy and pressure can be expressed as functions of the density along the Hugoniot. The form of this equation is specified in Table 4.1. The values for the parameters used in the LMG equation of state in this study for EM120D and ANFO are given in Table 4.3. These values are taken from [65] where an in-depth discussion on how they were achieved can be found (see, in particular, Appendix G).

## 4.3. Williamsburg equation of state

The Williamsburg (WMBG) equation of state is a complete equation of state, developed by Byers Brown et al. [18, 19, 20, 21, 22, 77], used to describe the gaseous products of a detonation. Complete in this context implies that the specific energy is a function of both specific volume and entropy. The

form of the WMBG is motivated by molecular interactions to more accurately describe entropy and temperature changes.

Other forms of equation of state used for gaseous products include the polytropic, discussed in §4.1, and the Jones-Wilkins-Lee (JWL) formulations. The polytropic equation of state, however, fails to accurately describe the asymptotic behaviour of gaseous detonation products in the high and low pressure regimes. The JWL equation of state does a better job with parameters based on the isentrope that passes through the CJ state. However, both of these equations of state rely on a constant Grüneisen gamma coefficient $\Gamma$, so that temperature or entropy can only be calculated via crude approximations, such as constant heat capacity [16]. Although the main focus of non-ideal detonation modelling is in pressure distribution and the diameter effect, it is important that the behaviour and interaction of the unreacted explosive and gaseous products is captured accurately as it contributes to the structure and propagation of the detonation wave.

The WMBG equation of state is also based on a fit to the isentrope through the CJ state, the principal isentrope, but due to the inclusion of the molecular interactions it is expected to have a greater range of validity than the data used to fit the equation of state parameters.

The most recent formulation of WMBG, from [16], defines the equation of state in terms of two basis functions $f = f(z)$ and $g = g(z)$ where $z = v/v_{\text{CJ}}$. These basis functions are used to define the relationship between the thermodynamic quantities on the principal isentrope,

$$p_k = \left( g\Big(\frac{v_k}{v_{\text{CJ}}}\Big) - 1 \right) \frac{e_k}{v_k}, \tag{4.6}$$

$$T_k = f\Big(\frac{v_k}{v_{\text{CJ}}}\Big) \frac{e_k}{n\mathcal{R}}, \tag{4.7}$$

where the standard notation for volume $v$, pressure $p$, temperature $T$, specific internal energy $e$ and the gas constant $\mathcal{R}$ has been used. The value $v_{\text{CJ}}$ is the volume of the CJ state.

To represent gaseous detonation products, the parameters are found via a fit to results from an ideal detonation code. The ideal detonation code produces a single isentrope through the CJ state. Along the isentrope values of $v$, $p$, $e$ and $T$ are determined. A linear regression process can then be used to fit approximations to $f(v)$ and $g(v)$.

If the Mie-Grüneisen form is applied, the pressure and specific internal energies are

$$p\,(v, e) = p_{\text{ref}}(v) + \frac{\Gamma(v)}{v}\,(e - e_{\text{ref}}(v))\,, \tag{4.8}$$

$$e\,(v, p) = e_{\text{ref}}(v) + \frac{v}{\Gamma(v)}\,(p - p_{\text{ref}}(v))\,. \tag{4.9}$$

For this equation of state, the reference curves $p_{\text{ref}}(v)$ and $e_{\text{ref}}(v)$ are the values of pressure and internal energy on the principal isentrope:

$$p_{\text{ref}}(v) = p_k(v), \tag{4.10}$$
$$e_{\text{ref}}(v) = e_k(v). \tag{4.11}$$

The form of the Grüneisen parameter $\Gamma$ can be derived as

$$\Gamma = v \left.\frac{\partial p}{\partial e}\right|_v \tag{4.12}$$
$$= (g-1) - \left.\frac{\partial \log f}{\partial \log v}\right|_S, \tag{4.13}$$

where $S$ is the entropy. The pressure and internal energy are then related via

$$p\,(v,e) = \frac{\Gamma(v)}{v}e + \frac{e_0 I(v)}{v}\left((g-1) - \Gamma\right), \tag{4.14}$$

where

$$(g-1) - \Gamma = \left.\frac{\log f}{\log v}\right|_S, \tag{4.15}$$

and

$$I(v) = \exp \int_{v_0}^{v} \frac{(1-g)}{v} \mathrm{d}v. \tag{4.16}$$

To fit the equation of state to the isentrope, $f$ and $g$ are approximated by arbitrary polynomials. For this work the polynomials are of order $n$ in $z = v/v_{\text{CJ}}$:

$$f(z) = A_0 + A_1 z + A_2 z^2 + A_3 z^3 + \ldots + A_n z^n, \tag{4.17}$$

and

$$g(z) = B_0 + B_1 z + B_2 z^2 + B_3 z^3 + \ldots + B_n z^n. \tag{4.18}$$

The WMBG equation of state is used to model the gaseous products of the non-ideal mining explosives modelled in this work. The values used for the polynomials for both EM120D and ANFO are given in Table 4.4 and again these were taken from [65]. In brief, the process of fitting the parameters involves the use of an ideal detonation code to produce isentrope data for the product material. The WMBG equation of state is then fit to this data. For more discussion of how these particular parameters were found, see Appendix G of [65].

These equations of state, with the same parameters, are used in all of the models that follow to provide accurate comparison between models.

| EM120D | | | |
|---|---|---|---|
| $\rho_0$ [kg/m$^3$] | 1600.4 | $Q$ [J] | 3.29341E6 |
| $A_1$ | -0.9289 | $B_1$ | 0.9225 |
| $A_2$ | 9.0615 | $B_2$ | 2.6724 |
| $A_3$ | -1.0607 | $B_3$ | -1.6394 |
| $A_4$ | 1.0 | $B_4$ | 2.8818 |
| ANFO | | | |
| $\rho_0$ [kg/m$^3$] | 1100.4 | $Q$ [J] | 4.9E6 |
| $A_1$ | 2.3228 | $B_1$ | 0.8263 |
| $A_2$ | 0.5956 | $B_2$ | 0.3355 |
| $A_3$ | 1.0 | $B_3$ | 3.1155 |

Table 4.4.: Parameters for WMBG equation of state for the reacted, gaseous phase of EM120D for use in (4.17) and (4.18).

# 5. Reaction rates

With the equation of state, the reaction rate closes the system of equations used to model reactive flow. While the equation of state describes the behaviour of a material with changes in pressure or temperature, the reaction rate describes the transfer of chemical bond energy into heat energy and bulk motion [40]. With the same initial and boundary conditions, a material with reaction can behave vastly differently to the same material without reaction.

The chemical bond energy in an explosive is complicated and difficult to describe via a simple ODE. Furthermore, reaction rates normally need to be fitted to experimental data for a specific explosive and adding in extra terms to account for complex behaviour normally implies more parameters. However, too many parameters can result in 'over-fitting' to data which can be more forgiving to approximations in a model than is strictly realistic. Ideally, a reaction rate model should have as few parameters as possible [78].

Realistically a reaction rate is a function of both temperature and pressure. However, modelling with a complete equation of state, that includes both temperature and pressure, is difficult. Therefore, reaction rates are often functions of either pressure or temperature and the mass fraction, $\lambda$. A temperature reaction rate may be more physically realistic but there is more pressure data available to calibrate pressure-based reaction rates and so they are used as a sufficient approximation.

A simple reaction rate is used for validation to avoid the introduction of error-fixing via parameter-fitting. A more complicated two-stage reaction rate, developed to mimic hotspot behaviour in porous non-ideal explosives, is used in the simulations for EM120D and ANFO.

Both reaction rates used in this study are of the form

$$\frac{\mathrm{d}\lambda}{\mathrm{d}t} = (1-\lambda)^m f(p)\,. \tag{5.1}$$

where $\lambda_k$ is the mass fraction for a specific material with index $k$, $m$ is a parameter and $f(p)$ is an arbitrary function of pressure only.

## 5.1. Single-stage reaction rate

For validation purposes, the same simple, single-stage reaction rate found in [78] is used:

$$f(p) = \frac{p^n}{\tau_H}. \tag{5.2}$$

where $\tau_H$ and $n$ are model parameters.

## 5.2. Two-stage reaction rate

The two-stage reaction rate incorporates the contribution of hotspots created by voids in the unreacted non-ideal explosive. The form of the reaction rate is taken from [30] and is given by

$$f(p) = H(p - p_H)\frac{a_H}{\tau_H}p^n + \left(\frac{1 - a_H}{\tau_S}\right)p, \tag{5.3}$$

where $a_H = \exp\left(-(\lambda/W_H)^N\right)$ and $W_H$, $p_H$, $\tau_H$, $\tau_S$, $N$ and $n$ are fitted parameters to unconfined diameter curve data.

This reaction rate was developed to mimic the hotspot behaviour in ammonium nitrate emulsions. The first term represents the hotspot reaction, with a Heaviside function to indicate that the reaction fails below a certain critical pressure, $p_H$. This hotspot burning dominates at ignition when $a_H$ is close to 1. The value of $n$ allows for some flexibility in the hotspot behaviour but the burn time of the hotspot is prescribed by $\tau_H$.

The second term represents the bulk burning term which is directly proportional to the pressure and which dominates toward the end of the reaction when $a_h$ is close to zero. Like the hotspot term, the burn time of the bulk burning is prescribed by $\tau_S$.

The parameter $a_H$ is a function of $W_H$, the fraction of explosive that burns in the hotspot process, and $N$, which governs the rate of the switch between the hotspot burning and bulk burning [30, 65].

Using an appropriate reaction rate and equation of state for each material, the system of equations to describe reactive flow is closed. This work explores and implements different models for reactive flows, in both confined and unconfined simulations, using these equations of state and reaction rates. These different models are explored in the following part of the thesis.

# Part II.

# Approximate models for steady multiphase detonation

# 6. Euler-based two-phase Chan-Kirby model

The Chan-Kirby model improves the Wood-Kirkwood style quasi-one-dimensional (Q1D) theories by moving away from finding a solution only on the axis. This is done through a series of geometric manipulations, some first-order approximations and some empiricism.

A further improvement to the Wood-Kirkwood style model is the change in the approximated relationship between the radial velocity, $\omega$, and the radius, $r$. This is known as the divergence term, $d\omega/dr = \omega_r$, and some of the original approximations are shown in [40]. The Chan-Kirby model also improves upon the assumed empirical relationship between radius of curvature, diameter and reaction zone length, which was shown to be a poor approximation in [33].

The Chan-Kirby model is described by the authors as a first-order, analytical, two-dimensional (2D) detonation model [30]. The model is based on the 2D axisymmetric augmented Euler equations that are reduced to a system of ODEs via the approximations that $\omega/u$ (radial velocity divided by axial velocity) and terms in shock front angle squared are small enough to be neglected. The resulting ODEs contain more 2D terms than traditional Wood-Kirkwood approaches although most are still neglected in the reduction.

Instead of solving differential equations in all directions, the model uses differential equations for the direction where most change is seen (the axial direction) and makes approximations for the values of the variables in the other direction (radial) by neglecting the small changes and using simple discrete updates. The streamlines produced are straight and parallel to the axis but, with trigonometry, can be manipulated to build a diverging streamline profile.

It can be argued that, since the Chan-Kirby model neglects many of the 2D effects, it is still only a Q1D theory. Although the Chan-Kirby model solves the ODEs for each streamline to build up a 2D solution, strictly this solution is not a 2D solution as no information is passed between streamlines. The solution is instead a finite number of neighbouring 1D-manifolds, not a 2D-manifold. It would be more correct to call this approach a 'decoupled 2D model'. The model is also not strictly analytical since it cannot be solved (or certainly has not been solved to date) without the use of numerical solvers and discretised approximations for some of the boundary conditions (see

Section 6.1.1). However, it has been argued that the Chan-Kirby approach is an improvement on the Wood-Kirkwood type models for non-ideal explosives, while maintaining the faster simulation time of the simpler model [30, 29]. For this reason, the Chan-Kirby model is explored as a basis for further developments for a non-ideal detonation ODE model.

Initially, the single-phase Chan-Kirby model is explored with respect to another ODE model; the straight streamline approximation of Watt et al. [78]. This is another ODE detonation model for non-ideal explosives but only solutions for a single phase have been published to date. This model will be analysed and extended in Chapter 8. Of course, realistic detonation modelling includes multiple phases and so the two-phase augmented Euler version of the Chan-Kirby model is outlined in §6.2. However, exploration of the thermal closure conditions reveal that a move towards a true multiphase model, with a multiphase system of equations underlying the ODE model, would provide a better solution to the non-ideal detonation problem.

## 6.1. Single-phase Chan-Kirby model

The following section outlines the single-phase Chan-Kirby model. The ODEs that describe the motion are given in the next section and the algebraic expressions needed to close the system of equations are given in the following sections. The accompanying oblique shock conditions used as one set of boundary conditions are then listed and the methods used to determine the final boundary condition at the sonic locus are outlined. The approximation for the edge of charge is also discussed in the final part of this section.

### 6.1.1. Model

#### Equations of motion

The ODEs that describe the motion of the explosive are given below. These equations were previously derived in [28] but have been independently derived in Appendix A to highlight the neglected terms. The equations of motion

are

$$\frac{d\omega_r}{dz} = -\left(\frac{\omega_r^2}{u} + C\frac{du}{dz}\right), \tag{6.1}$$

$$\frac{d\rho}{dz} = -\frac{\rho}{u}\left(\omega_r + \frac{\omega}{r} + \frac{du}{dz}\right), \tag{6.2}$$

$$\frac{dt}{dz} = \frac{1}{u}, \tag{6.3}$$

$$\frac{du}{dz} = \frac{\left(\sigma\dot{\lambda} - \omega_r - \frac{\omega}{r}\right)}{\left(1 - \frac{|\mathbf{u}|^2}{c^2}\right)} = \frac{\psi}{\eta}, \tag{6.4}$$

where $u$ and $\omega$ are the axial and radial velocities, so that the radial velocity divergence term is $\omega_r = \dfrac{\partial\omega}{\partial r}$, hereafter referred to as radial divergence. The density is given as $\rho$ and $t$ is the time. The rate of reaction is $\dot{\lambda} = \dfrac{\mathrm{d}\lambda}{\mathrm{d}t}$. The variables $\psi$ and $\eta$ are the numerator and denominator of the right hand side of (6.4); they have no notable physical relevance but are used for convenience. The numerator, $\psi$, has dimensions of 1/time and the denominator, $\eta$, is dimensionless.

### Isobar curvature

The isobar curvature is a measure of the change in slope between points on adjacent streamlines with equal pressure. It describes the distribution of the pressure throughout the DDZ and how the isobars are shaped. As shown in Figure 6.1, near the axis the isobars are flatter than near the charge edge. The value of the isobar curvature $C$ at each point on a streamline is unknown.

If the slope of an isobar at a point is denoted by $\epsilon = \dfrac{dz}{dr}$ then the curvature of the isobar is related to the arc lengths by

$$C = \frac{d\epsilon}{ds} = \frac{d\epsilon}{dr}\frac{dr}{ds},$$

where the incremental arc length can be expressed as

$$ds = \sqrt{dr^2 + dz^2},$$

so that

$$\frac{ds}{dr} = \sqrt{1 + \left(\frac{dz}{dr}\right)^2} = \sqrt{1 + \epsilon^2},$$

and

$$C = \frac{d\epsilon}{dr}\frac{1}{\sqrt{1+\epsilon^2}} \approx \frac{d\epsilon}{dr},$$

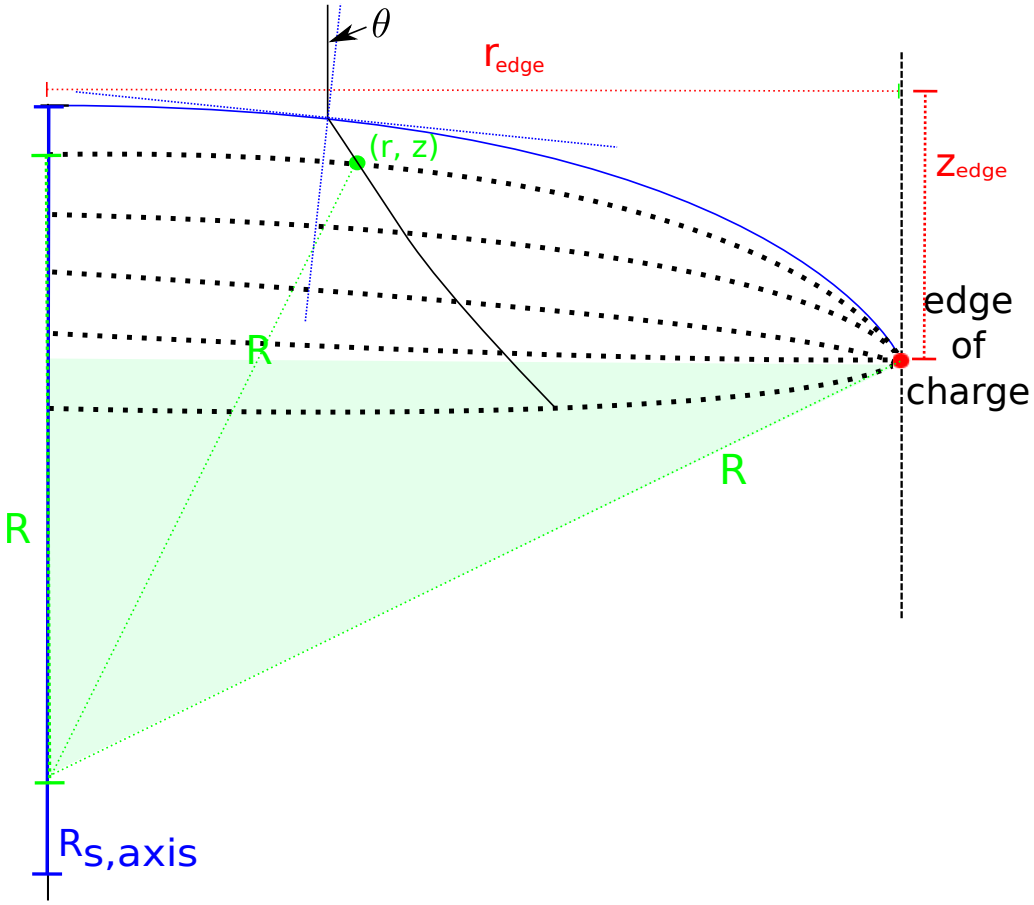


Figure 6.1.: A graphical representation of the DDZ with shock front (blue solid curve) and isobars (dotted curves). A streamline approaches the shock at an angle $\theta$ to the normal at the shock. The shock shape is approximated as a circular arc and so the radius of curvature of the shock front, $R_s$, is the same on the axis as at the charge edge. Each isobar is also approximated as a circular arc with radius $R$. The example shown in green highlights that the radius of curvature of the isobar at the axis is identical to that at the charge edge.

since $\epsilon$ is small. Note, however, that this approximation is more relevant close to the axis than at the charge edge.

From Figure 6.1 it can be seen that a right angle triangle can be formed from the radius of the isobar at the charge edge and the perpendicular line from the axis to the charge edge. Using Pythagoras' theorem this can be expressed as

$$r_{\text{edge}}^2 = (z_{\text{edge}} - z)\,(2R - (z_{\text{edge}} - z))\,,$$

so that

$$C = \frac{1}{R} = \frac{2\,(z_{\text{edge}} - z)}{r_{\text{edge}}^2 + (z_{\text{edge}} - z)^2}, \tag{6.5}$$

where $R$ is the radius of curvature of the isobar and $C$ is the isobar curvature.

The radius of the charge, $r_{\text{edge}}$, can be approximated with simple trigonometry,

$$r_{\text{edge}} = R_s \sin\theta. \tag{6.6}$$

Chan & Kirby [30] replace this relationship with

$$r_{\text{edge}} = \beta R_s, \tag{6.7}$$

where $\beta$ is an empirical constant found from a narrow range of explosives and is taken to always be 0.5. This empirical constant implies that the incoming shock angle is the same at each point along the shock front. This is a reasonable assumption if the shock front is relatively flat and gives reasonable results for the range of explosives explored by Chan & Kirby in [30]. However, the shock front and isobars for non-ideal explosives are much more curved at the edge than at the axis and so there is room for improvement in this approach. A discussion on an alternative approach is presented in §7.3.

The isobar curvature throughout the DDZ is then approximated using the isobar curvature at the shock front, $C_s$, and (6.5),

$$C = C_s - \frac{2z}{(\beta R)^2}. \tag{6.8}$$

However, as mentioned, this expression is empirical and was determined from a narrow range of commercial explosives. An improvement to this empirical relation is explored in §7.3 after the introduction of the multiphase mechanical equilibrium model so that direct comparisons between the Chan-Kirby approximations and a DNS solution can be made.

### Algebraic Expressions

To close the system of equations, an equation of state needs to be specified. This equation of state is a function of pressure so an expression for pressure, in terms of the integrated variables, also needs to be specified. All simulations

in this section use the polytropic equation of state for all phases. This is a very simple equation of state and although it is unrealistic to use it for both phases it is helpful for validation. It is also widely used by others in the detonation community and therefore is an ideal choice for comparative purposes.

**Pressure**

The pressure can be calculated from the integrated variables using Bernoulli's equation:

$$e + \frac{p}{\rho} + \frac{1}{2}|\mathbf{u}|^2 = \frac{1}{2}D_0^2 + e_0 + \frac{p_0}{\rho_0}, \tag{6.9}$$

where $e = e(p, \rho, \lambda)$ is the internal energy given by the equation of state and $|\mathbf{u}|^2 = u^2 + \omega^2$. If the standard assumption is made that $u \gg \omega$ this reduces to

$$e + \frac{p}{\rho} + \frac{1}{2}u^2 = \frac{1}{2}D_0^2 + e_0 + \frac{p_0}{\rho_0}. \tag{6.10}$$

However, this assumption becomes increasingly inaccurate as the streamline calculations move away from the charge axis and towards the charge edge. It is for this reason that the $\omega$ has been included in this formulation of the Chan-Kirby model despite it being neglected in the original formulation.

With the polytropic equation of state this can be easily rearranged to obtain the pressure as a function of the other variables. For more complex equations of state, the equation cannot be rearranged and a numerical root finder has been implemented.

**Radial velocity**

Unlike the radial momentum equation in the Euler equations, the equations of motion for the Chan-Kirby model are in terms of the radial divergence and not the radial velocity. In more traditional Wood-Kirkwood-style quasi-one-dimensional models, the radial divergence is described via an algebraic expression and not a differential equation. There are many expressions available for radial divergence in quasi-one-dimensional models, each with their advantages and disadvantages, and these are outlined in Section 5G of [40].

Since the Chan-Kirby model determines the radial divergence via a differential equation, the radial velocity must then be determined via an approximation. The approximation used is that the ratio of radial velocity to radial divergence is proportional to the radius,

$$\omega = \chi r \omega_r. \tag{6.11}$$

The constant of proportionality, $\chi$, is assumed to be constant along a streamline and can be determined at the shock front. This is illustrated in a following section on boundary conditions.

Although the linear relationship (6.11) is not exact, the relatively small size of the radial velocity compared to the axial velocity is once again used as a justification for the approximation. However, this is inappropriate for large shock front curvatures and for streamlines away from the charge axis.

**Sound Speed**

The speed of sound for each material needs to be specified in order to close the equations. The sound speed for a material can be expressed as

$$c^2 = \frac{\frac{p}{\rho^2} - \left(\frac{\partial e}{\partial \rho}\right)_{p,\lambda}}{\left(\frac{\partial e}{\partial p}\right)_{\rho,\lambda}} \tag{6.12}$$

and is calculated from each equation of state.

**Thermicity**

The thermicity describes the effective rate of energy release and appears in the ODE for axial velocity (6.4) and so is needed to close the system of equations. It is expressed as

$$\sigma = -\frac{1}{\rho c^2} \frac{(\partial e/\partial \lambda)_{\rho,p}}{(\partial e/\partial p)_{\rho,\lambda}}. \tag{6.13}$$

Like the sound speed, the thermicity is calculated from each equation of state.

### Determination of $\frac{du}{dz}$ at the sonic locus

To determine the correct solution along each streamline, the boundary conditions at the front are given and a shooting method (outlined in §6.1.2) is carried out to determine the correct boundary conditions at the sonic locus. The sonic locus is the locus of points at the end of the DDZ where the particle velocity is equal to sound speed of the material. This locus of points separates the flow; no information can reach inside the DDZ from beyond the sonic locus.

To determine the final boundary condition, $du/dz = \psi/\eta$ must be zero at the sonic locus: both $\psi$ and $\eta$ must reach zero at the same time. If the starting boundary conditions are ill-posed, and $\eta$ reaches zero first, $du/dz$ becomes singular. An alternative approach, using the second derivative, was outlined in [17] and was used by Chan and Kirby for their simulations. This approach is outlined below as it is used for the Euler-based simulations. However, the singularity problem is easily overcome by a change of coordinates and this is outlined on the next page.

**Continuity of the second derivative**

Given that $du/dz = \psi/\eta$, the second derivative of $u$ with respect to $z$ is determined by

$$\eta \frac{d^2u}{dz^2} + \frac{d\eta}{dz}\frac{du}{dz} = \frac{d\psi}{dz}. \tag{6.14}$$

Since both $\psi$ and $\eta$ are monotonic (in $z$), continuous functions it is assumed that their derivatives are also continuous.

At the sonic locus $\eta = 0$ so this expression goes to

$$\frac{du}{dz} = \frac{d\psi/dz}{d\eta/dz}, \tag{6.15}$$

where

$$\frac{d\psi}{dz} = \frac{\partial\psi}{\partial\lambda}\frac{d\lambda}{dz} + \frac{\partial\psi}{\partial u}\frac{du}{dz} + \frac{\partial\psi}{\partial\rho}\frac{d\rho}{dz} + \frac{\partial\psi}{\partial \mathrm{w}}\frac{d\mathrm{w}}{dz} + \frac{\partial\psi}{\partial\omega_r}\frac{d\omega_r}{dz}, \tag{6.16}$$

$$\frac{d\eta}{dz} = \frac{\partial\eta}{\partial\lambda}\frac{d\lambda}{dz} + \frac{\partial\eta}{\partial u}\frac{du}{dz} + \frac{\partial\eta}{\partial\rho}\frac{d\rho}{dz} + \frac{\partial\eta}{\partial \mathrm{w}}\frac{d\mathrm{w}}{dz} + \frac{\partial\eta}{\partial\omega_r}\frac{d\omega_r}{dz}, \tag{6.17}$$

where $\mathrm{w} = \dfrac{\omega}{r}$. The right hand sides of these expressions are explicitly functions of $du/dz$, so the equation for $du/dz$ is actually quadratic. One of the roots is unphysical and is neglected. The other root gives the solution. This method follows directly from [17].

**Change of coordinates**

The ODE for axial velocity (6.4), where the singularity can occur, can be written as

$$\frac{du}{dz} = \frac{c^2\left(\sigma\dot{\lambda} - \omega_r - \frac{\omega}{r}\right)}{c^2 - |\mathbf{u}|^2} \tag{6.18}$$

$$= \frac{c^2\left(\sigma\dot{\lambda} - \omega_r - \frac{\omega}{r}\right)}{(c - |\mathbf{u}|)(c + |\mathbf{u}|)}. \tag{6.19}$$

The singularity still occurs when $|\mathbf{u}| = c$ but if a coordinate transformation is made such that

$$\frac{dz}{d\bar{z}} = \frac{c - |\mathbf{u}|}{c} \tag{6.20}$$

then the transformed ODE for axial velocity is given by

$$\frac{du}{d\bar{z}} = \frac{c\left(\sigma\dot{\lambda} - \omega_r - \frac{\omega}{r}\right)}{(c + |\mathbf{u}|)}. \tag{6.21}$$

A singularity only occurs in this equation if $|\mathbf{u}| = -c$. As long as $|\mathbf{u}|$ and $c$ remain positive, as they should, this coordinate transformation avoids the

problem of the singularity at the sonic locus. Each of the remaining ODEs is also transformed.

As this latter method does not involve any derivatives that are either algebraically complex or numerically expensive, it is the preferred method for evolving the equations. However, for all Euler-based solutions in this work, the former method of derivatives is used to more closely resemble the original theory of Chan & Kirby.

### Boundary conditions

The first set of boundary conditions are the oblique shock conditions (see, for example, [32]). For the polytropic equation of state they are as follows:

$$p_s = \frac{2\rho_0 D^2 \cos^2\theta}{\gamma+1}, \tag{6.22}$$

$$\rho_s = \frac{\rho_0^2 D^2 \cos^2\theta}{\rho_0 D^2 \cos^2\theta - (p_s - p_0)}, \tag{6.23}$$

$$u_s = D\left(1 - \cos^2\theta\left(1 - \frac{\rho_0}{\rho_s}\right)\right), \tag{6.24}$$

where $\theta$ is the incoming shock angle measured as the angle between the incoming streamline and the normal to the shock front at that point, $\gamma$ is the ratio of specific heats, $p_s$ is the pressure, $\rho$ is the density and $u_s$ is the particle velocity. The subscript 0 denotes the upstream value of a variable before the shock and the subscript $s$ denotes the downstream value of a variable after the shock. The detonation velocity, $D$, is chosen and the unknown apriori radius of curvature of the shock for a streamline is then determined using the a shooting problem, outlined in the next section, and the conditions at the sonic locus.

The boundary condition for the radial divergence, $\partial\omega/\partial r$, is found by differentiating the oblique shock condition for the radial velocity, $\omega$,

$$\omega_s = \frac{D}{2}\sin 2\theta\left(1 - \frac{\rho_0}{\rho_s}\right). \tag{6.25}$$

This implies that the radial divergence is

$$\begin{aligned}\left(\frac{\partial\omega}{\partial r}\right)_s &= \frac{\partial\omega}{\partial\theta}\frac{\partial\theta}{\partial r} \\ &= \frac{\partial\omega}{\partial\theta}\frac{1}{R_s\cos\theta} \\ &= \frac{1}{R_s\cos\theta}\frac{\partial}{\partial\theta}\left(\frac{D}{2}\sin 2\theta\left(1-\frac{\rho_0}{\rho_s}\right)\right) \\ &= \frac{D}{R_s}\left[\left(\frac{\cos 2\theta}{\cos\theta}\left(1-\frac{\rho_0}{\rho_s}\right)\right) + \sin\theta\frac{\rho_0}{\rho_s^2}\frac{\partial\rho_s}{\partial\theta}\right],\end{aligned} \tag{6.26}$$

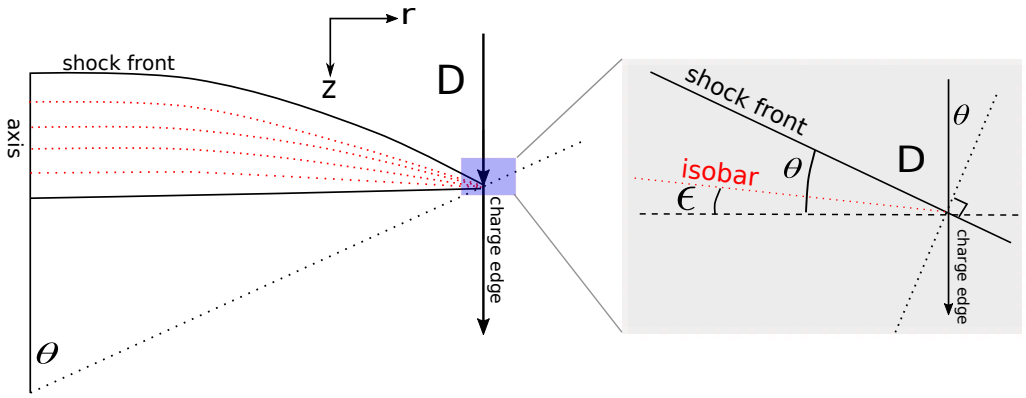


Figure 6.2.: This graphical representation of the detonation front shows that the incoming shock angle $\theta$ is also the angle that the normal to the shock front makes with the axis and the angle between the shock front and the normal to the axis. Similarly, the angle that the isobar makes at the same point is denoted by $\epsilon$.

where the derivative of density with respect to the shock angle is determined numerically,

$$\frac{\partial \rho_s}{\partial \theta} = \rho_s(\theta[i]) - \rho_s(\theta[i-1])/\delta\theta, \tag{6.27}$$

where $i$ denotes the index of the current streamline.

The value for $\chi$ at the shock front is determined from its definition (6.11) as the ratio of radial velocity per radial distance and the radial divergence,

$$\chi = \frac{\omega}{r}\left(\frac{\partial \omega}{\partial r}\right)^{-1}. \tag{6.28}$$

Combining (6.25) and (6.26),

$$\chi = \begin{cases} 1 & \text{(on axis)}, \\ \dfrac{R_s \sin 2\theta}{2r}\left(\dfrac{\cos 2\theta}{\cos\theta} + \sin\theta \dfrac{\rho_0}{(\rho_s - \rho_0)}\dfrac{\partial \rho_s}{\partial \theta}\right)^{-1} & \text{(off axis)}, \end{cases} \tag{6.29}$$

where the radius is determined numerically,

$$r[i] = \begin{cases} R_s[i]\sin\theta & \text{(on axis)}, \\ r[i-1] + R_s[i]\left(\sin(\theta[i]) - \sin(\theta[i-1])\right) & \text{(off axis)}. \end{cases}$$

Figure 6.2 shows the angle between the shock front and an isobar as $\theta - \epsilon$, where $\epsilon$ is the angle between the isobar and the normal to the axis at a point $(r, z)$. Therefore, at any point $(r, z)$, the incremental axial length $\Delta z$ between the shock front and the isobar, for incremental change in the radial direction $\Delta r$, can be approximated as

$$\begin{aligned} \Delta z &= \Delta r \tan\theta - \Delta r \tan\epsilon, \\ &\approx \Delta r\,(\theta - \epsilon)\,. \end{aligned}$$

The change in pressure along a isobar is then

$$\frac{dp}{dr}\Delta r = \frac{dp}{dz}\Delta z = \frac{dp}{dz}\Delta r\left(\theta - \epsilon\right),$$

which implies

$$\theta - \epsilon = \frac{\left(\frac{dp}{dr}\right)_s}{\frac{dp}{dz}},$$

where the subscript $s$ refers to the shock. Substituting this into the axial momentum equation (see Appendix A.2),

$$\frac{dp}{dz} = -u\rho\frac{du}{dz}, \tag{6.30}$$

and using the chain rule, the expression becomes

$$\epsilon = \theta + \frac{\frac{dp}{d\theta}\frac{d\theta}{dr}}{\rho u\frac{du}{dz}}.$$

Using the approximation $\left(\frac{dr}{d\theta}\right)_s \approx R_s\cos\theta$, the expression becomes

$$\epsilon \approx \theta + \frac{\frac{dp}{d\theta}}{\rho u\frac{du}{dz}R_s\cos\theta}.$$

The derivative of the expression for the pressure at the shock front, (6.22), with respect to $\theta$ is used to obtain

$$\epsilon \approx \theta - \frac{\rho_0 D}{\rho u R_s\cos\theta}\frac{\left(\frac{du}{d\theta}\right)_s}{\frac{du}{dz}}. \tag{6.31}$$

The derivative of axial velocity at the shock front with respect to $\theta$; that is, the derivative of (6.24), is then substituted to obtain

$$\epsilon \approx \theta - \frac{\rho_0 D^2}{\rho R_s u\cos\theta\frac{du}{dz}}\left(\sin 2\theta\left(1-\frac{\rho_0}{\rho}\right) - \frac{\rho_0}{\rho^2}\cos^2\theta\frac{d\rho}{d\theta}\right).$$

Finally, the axial velocity at the shock front $u_s$, (6.24), is substituted to obtain,

$$\epsilon \approx \theta - \frac{\rho_0 D}{\rho R_s\cos\theta\frac{du}{dz}}\frac{1}{\left(1-\cos^2\theta\left(1-\frac{\rho_0}{\rho}\right)\right)}\left(\sin 2\theta\left(1-\frac{\rho_0}{\rho}\right) - \frac{\rho_0}{\rho^2}\cos^2\theta\frac{d\rho}{d\theta}\right). \tag{6.32}$$

The curvature, $C_s \approx \dfrac{d\epsilon}{dr} = \dfrac{d\epsilon}{d\theta}\dfrac{d\theta}{dr}$, is then equal to the derivative of (6.32) with respect to the $\theta$ multiplied by $1/R_s\cos\theta$. This introduces derivatives

in $\rho$ and $R_s$ with respect to $\theta$, but it is assumed that these variables do not change significantly with small changes in $\theta$. This is justified by the fact that the isobar curvature term only has a small impact on the total evolution of the variables; an approximated value at the shock front has only a small effect on the results. It is also assumed that the second term in the parentheses of (6.32) is negligible for the same reason.

The final expression for $C_s$ is

$$C_s = \frac{1}{R_s \cos\theta}\left(1 - \frac{2D\cos 2\theta}{R_s \frac{du}{dz}}\left(1 - \frac{\rho_0}{\rho}\right)\right). \tag{6.33}$$

**Edge of charge assumption**

The Chan-Kirby model is a streamline theory that builds a 2D picture with 1D information from individual streamlines. In the Chan-Kirby model, these streamlines are chosen using constant increments in the shock angle $\theta$. On axis $\theta = 0$ and the increments are chosen so that

$$\delta\theta = \frac{\theta_{\max}}{\text{number of streamlines}}, \tag{6.34}$$

where $\theta_{\max}$ is the maximum deflection angle at the charge edge. This value is not known a priori.

Chan [26] has proposed that, using the Chan-Kirby equations and the oblique shock conditions, $\theta_{\max} = \frac{\pi}{6}$ when the flow is sonic. The simulations of the Chan-Kirby model in this study use this value of $\theta_{\max} = \frac{\pi}{6}$ for the maximum incoming shock angle. However, it is shown in §7.4 that this is an inaccurate assumption and a new theory for inhomogeneous explosives using shock polars is formulated to calculate $\theta_{\max}$ at the charge edge.

The equations shown above fully describe the single-phase system with the exception that the radius of curvature is unknown a priori. However, these equations cannot be integrated analytically and so numerical techniques to integrate and then iterate to a solution for the radius of curvature are needed. These are outlined in the following section.

## 6.1.2. Numerical methods for the single-phase model

To find a solution for a single-phase detonation using the Chan-Kirby model, a shooting method needs to be implemented to determine the unknown radius of curvature, $R_s$. Within this shooting method, the equations of motion (6.2) to (6.4) need to be numerically integrated from the shock front to the sonic locus. At the sonic locus, the second boundary condition needs to be satisfied and this is how the shooting method determines a solution for the radius of curvature. This method and the numerical integrator used are outlined below.

### Shooting method

The shooting method is a common numerical method used to solve two-point boundary value problems [59]; systems of ODEs where the exact initial conditions of the system are not known but where there are certain constraints (boundary conditions) on the system at more than one value of the independent variable. These constraints can be anywhere in the system. This means that the boundary values at the starting point do not determine a unique solution to the system and so a range of starting boundary values must be iterated over in order to satisfy all constraints. Below, the shooting method is outlined, in very general terms and along with how it is applied to this model.

#### General outline of the shooting method

The shooting method aims to obtain the solution to a set of $N$ coupled first-order ODEs,

$$\frac{dy_i(x)}{dx} = g_i\left(x, y_1, y_1, y_2, \ldots, y_N\right) \quad i = 1, 2, \ldots N, \tag{6.35}$$

satisfying $n_1$ boundary conditions at the starting value $x_1$,

$$B_{1j}\left(x_1, y_1, y_2, \ldots, y_N\right) = 0 \quad j = 1, \ldots, n_1 \tag{6.36}$$

and a remaining set of $n_2 = N - n_1$ boundary conditions at the end value $x_2$,

$$B_{2k}\left(x_2, y_1, y_2, \ldots, y_N\right) = 0 \quad k = 1, \ldots, n_2. \tag{6.37}$$

The integration of the ODEs proceeds from $x_1$ to $x_2$. At $x_1$, there are $N$ starting values $y_i$ subject to $n_1$ conditions which leaves $n_2 = N - n_1$ values to be specified freely. These $n_2$ values are the values that need to be guessed and iterated over to meet the correct boundary values at $x_2$. Figure 6.3 shows a schematic illustration of the shooting method.

A complete set of $N$ $y_i$ can be generated from an arbitrary vector $\mathbf{V}$ of dimension $n_2$, that satisfies the boundary conditions at $x_1$ while maintaining complete freedom of all $n_2$ component values:

$$y_i(x_1) = y_i\left(x_1; V_1, \ldots, V_{n_2}\right) \quad i = 1, \ldots, N. \tag{6.38}$$

Once $\mathbf{V}$ has been chosen, $\mathbf{y}(x_1)$ can be integrated to $\mathbf{y}(x_2)$. The distance between the solution and the $n_2$ boundary conditions at this point can be measured by a discrepancy vector $\mathbf{F}$. For example,

$$F_k = B_{2k}\left(x_2, \mathbf{y}\right) \quad k = 1, \ldots, n_2. \tag{6.39}$$

The final step is to find a vector value of $\mathbf{V}$ that zeros the vector value of $\mathbf{F}$ and to adjust $\mathbf{V}$ accordingly. An appropriate root finding method should be chosen to do this.

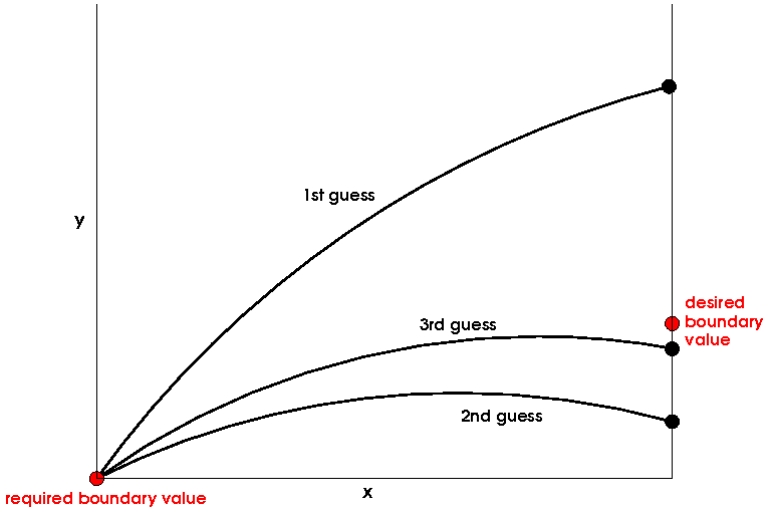


Figure 6.3.: A graphical interpretation of the shooting method. The solution must satisfy both boundary conditions. In this form of the shooting method, the left-hand boundary conditions are given and the system is integrated to the right-hand side. The distance from the desired boundary condition is then measured and the left-hand boundary conditions are then adjusted accordingly and the integration is carried out again (and again...) until the the desired right-hand boundary condition is reached.

The most appropriate method for most systems is Newton-Raphson and further discussion about the implementation of the shooting method combined with Newton-Raphson can be found in [59]. However, the use of this method requires that each component of the Jacobian matrix is calculated to solve the set of $n_2$ linear equations to find the root. This requires separate integration of all $N$ ODEs and this is numerically costly. Fortunately, due to the nature of the Chan-Kirby model, Newton-Raphson is avoidable and an alternative method adopted, the bisection method, is outlined in the next section.

### Determination of radius of curvature using bisection

For the numerical simulation of detonation using the Chan-Kirby model, most of the boundary values of the variables at the shock front are known through the oblique shock conditions, given in Section 6.1.1, but the radius of curvature at the shock front, $R_s$, which determines some of these shock boundary values, is not known.

At the other boundary, the sonic locus, the only constraint is that the

flow satisfies the first and second CJ conditions,

$$\eta = \left(1 - \frac{u^2}{c^2}\right) = 0, \tag{6.40}$$

$$\psi = \left(\sigma\dot{\lambda} - \frac{\partial\omega}{\partial r} - \frac{\omega}{r}\right) = 0. \tag{6.41}$$

A simple bisection method to find $R_s$ is adopted since some arbitrary, positive small number can be chosen as the minimum value since $R_s > 0$ for unconfined detonation.

Furthermore, if the detonation is assumed to be convex in shape, the radius of curvature at the shock front of the current streamline is always going to be less than the radius of curvature at the shock front of the previous streamline. Including some allowance for error in the calculation of the previous $R_s$, this gives a specific range to find the correct $R_s$ of the current streamline. Therefore, the bisection method is given a very specific range over which the solution must exist and, as convergence is guaranteed, the shooting method can converge to a solution quickly.

Initial implementations of the Chan-Kirby model, including work presented by this author in [34, 35], added a further restriction on the iteration method by specifying a minimum $R_s$. The theory, developed from comments in [27], argues that at the shock front at the charge edge, $R_s$ will be at a minimum. At the charge edge the shock front will also meet that sonic locus and so the CJ conditions must be satisfied. Asserting that the second CJ condition, $\psi = 0$, must be satisfied and substituting in the boundary conditions for the variables in $\psi$ gives

$$R_{\text{edge}} = \frac{2R_s\left(\frac{\partial\omega}{\partial r}\right)_s}{\sigma\dot{\lambda}} \qquad \theta = 0, \tag{6.42}$$

$$= \frac{R_s\left(\frac{\partial\omega}{\partial r}\right)_s}{\sigma\dot{\lambda} - \chi\left(\frac{\partial\omega}{\partial r}\right)_s} \qquad \theta > 0, \tag{6.43}$$

where $R_s\omega_s$ can be evaluated without $R_s$ by multiplying both sides of (6.26) by $R_s$. However, as will be shown in §7.3, the $R_s$ value with the minimum error is always $R_{\text{edge}}$ and as a result the shock front is artificially flattened and hence the radius is artificially extended. This implies that (6.43) is invalid, most probably due to the approximations used in developing the expressions and the numerical approximations used in determining them in practice. To overcome this, later developments returned to the use of a small, arbitrary number as a minimum value and a numerical check is made to make sure that the optimised solution is always within the bisection bracket.

This implementation of the bisection method relies on a convex shock front. If the detonation shock front is not convex, which can happen in some

confined non-ideal detonations, then this method is no longer valid and the algorithm would not be able to converge to a valid solution. If confined non-ideal detonations are considered in future work for this method, this technique will need to be revisited.

### Integration techniques

To integrate the ODEs between boundary values, a fourth-order Runge-Kutta scheme is implemented with an adaptive stepsize control.

An adaptive stepsize exerts control over the progress of the integrator in order to achieve some greater accuracy with minimum computational effort. As the main aim of reduced models is to reduce computational time, this adaptive stepsize control is a desirable feature.

There are many well-known adaptive stepsize methods available. The most obvious choice for solving these type of ODEs is the Runge-Kutta-Fehlberg method, outlined in [59]. However, it was shown in [33] that an easier-to-implement method used by Chan [28] was just as accurate for this specific problem and this is the adaptive stepsize method used for the simulations of the Chan-Kirby model.

The general concept for the simpler method is that the behaviour of $\eta$ is of the most concern since its presence in the denominator will make the $\frac{du}{dz}$ function singular if it reaches zero before $\psi$. The stepsize is consequently changed according to the behaviour of $\eta$. Knowing that $\eta$ will approach zero faster as it gets closer to it, an arbitrary point is chosen where it is likely that this has not yet happened but will soon occur. Until this point, the stepsize is taken to be a function of the difference between $\eta[j-1]$ and $\eta[j-2]$, where $j$ denotes the index of the current point, $(r, z)$, on the streamline. Once the chosen point has been passed, the stepsize is still a function of this difference but is reduced by at least a factor of a half.

The combination of the shooting method and the fourth-order Runge-Kutta scheme complete the numerical methods used to solve the system of equations. The remaining algorithms used are to manipulate the discrete streamline solution into visually-accessible contour plots. These processes are outlined in the following sections.

### Determination of the DDZ skeleton

The Chan-Kirby model gives discrete streamline solutions to the detonation problem. Each streamline is solved separately, with no dependence on the previous streamline, so the solution is a finite number of parallel streamlines with different lengths. All variables are known along the streamline but the exact location of each streamline, and how it diverges, needs to be extracted from the information determined about the radius of curvature. Once the location of each point on each streamline is determined, the skeleton of the

detonation driving zone (DDZ) is built and flooded contour plots can be produced using the discrete information on each streamline.

The method originally used in [28] to build the DDZ is outlined below along with a new approach that simplifies the calculation. Note, however, that while the solution for each streamline is not independent of the location of each point on the streamline, the streamlines are virtually straight for the explosives of interest and the inclusion of the new method makes no significant difference.

**Chan's streamline skeleton**

The method outlined in [28] determines the distance between the streamlines at the shock front by using the radius of curvature determined on the previous streamline $R_s[i-1]$ and simple trigonometry:

$$r_s[i] = r_s[i-1] + R_s[i-1]\left(\sin(\theta[i]) - \sin(\theta[i-1])\right). \tag{6.44}$$

Theoretically, each streamline could start in the same place without the calculation being changed, so that the result would look something like Figure 6.4a. However, each streamline has an iteratively determined radius of curvature value so trigonometry is again used to build up the curved shock front and sonic locus skeleton of the DDZ can be found as

$$z_s[i] = z_s[i-1] + R_s[i-1]\left(\cos(\theta[i]) - \cos(\theta[i-1])\right), \tag{6.45}$$

$$R_{s,av} = \frac{(R_s[i-1] + R_s[i])}{2}, \tag{6.46}$$

$$\theta_{av} = \frac{(\theta[i-1] + \theta[i])}{2}, \tag{6.47}$$

$$r[i] = r[i-1] + R_{s,av}\delta\theta\cos(\theta_{av}), \tag{6.48}$$

$$z[i] = z[i-1] + R_{s,av}\delta\theta\sin(\theta_{av}), \tag{6.49}$$

where $\delta\theta = \theta[i] - \theta[i-1]$.

In order to calculate how the streamlines diverge, each $(r, z)$ point calculated during the integration of the ODEs needs to be recalculated to reflect how the streamline diverges as a result of the curved shock front and consequent shock deflection angle. From the oblique shock conditions, (6.22) to (6.26),

$$\tan(\phi) = \frac{\omega_s}{u_s} = \frac{D\sin(\theta[i])\cos(\theta[i])\left(1 - \dfrac{\rho_0}{\rho_s}\right)}{D\left(\sin^2(\theta[i]) + \dfrac{\rho_0}{\rho_s}\cos^2(\theta[i])\right)}, \tag{6.50}$$

and further simple trigonometry,

$$r = r_s[i] + z\tan(\phi). \tag{6.51}$$

The resulting changed streamlines can be seen in Figure 6.4b.

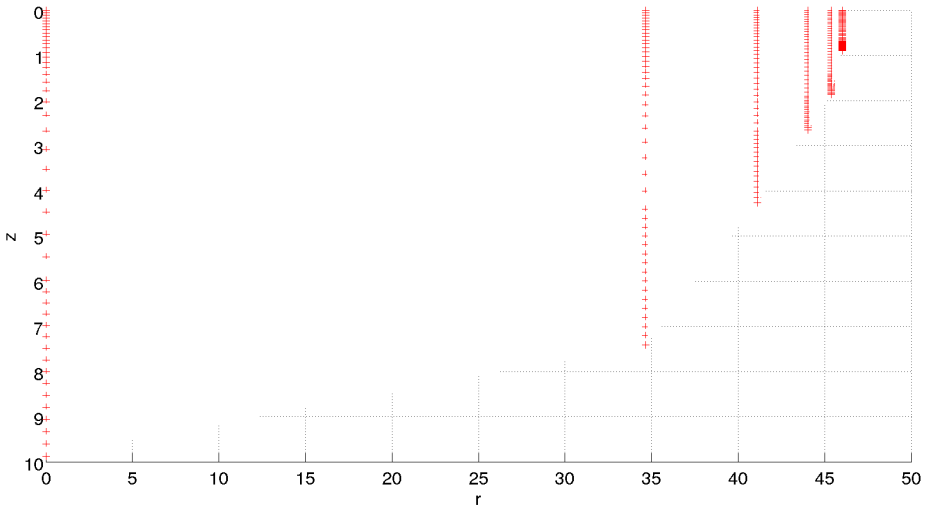


(a)

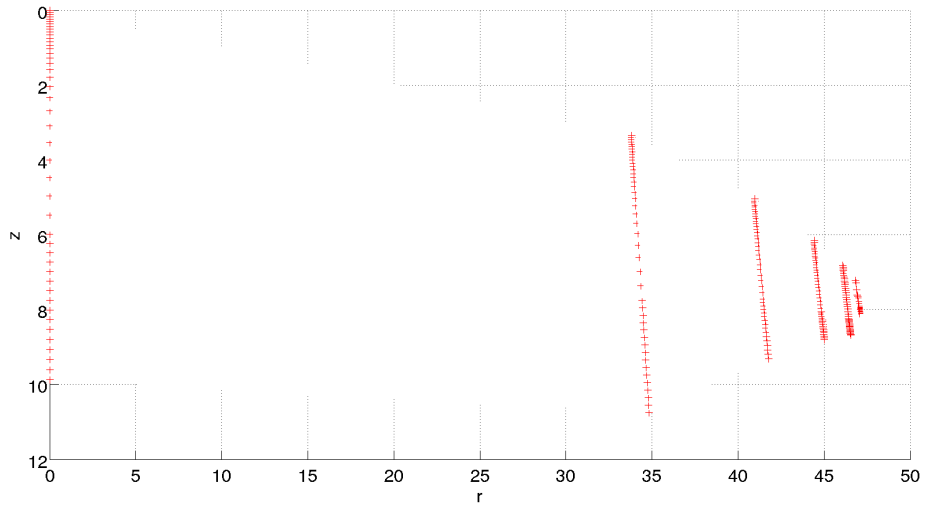


(b)

Figure 6.4.: a) The unaltered DDZ skeleton of the streamline problem. The red lines are the streamlines, all starting at the same point in $z$ and finishing at different points depending on when the CJ conditions are met. Each streamline has a set of data for each variable that changes with respect to $z$. Any changes in variables with respect to $r$ need to be calculated separately and discretely. b) Using some simple trigonometry and averaging of calculating radius of curvature values, the streamlines show features of the expected curved shock front and diverging streamlines.

**New streamline skeleton**

As above, to calculate how the streamlines diverge, each $(r, z)$ on the streamline needs to be determined. If the ODEs are derivatives with respect to $z$, then $z$ is determined by the integration step. This leaves $r$ unknown. However, the value of $r$ at the shock front, $r_s$, can be approximated using (6.44) and so a boundary condition for $r$ is given.

Noting that the change in $r$ with respect to $z$ is just the ratio of the radial and axial velocities,

$$\frac{dr}{dz} = \frac{\omega}{u}, \tag{6.52}$$

an ODE, with a suitable boundary condition, is determined for $r$. This can then be included in the system of ODEs so that at each step in $z$ a corresponding value for $r$ is determined. This eliminates any complicated post-integration processing of the variables and more accurately describes the change in $r$. However, even with the more accurate value of $r$, the structure of the DDZ remains virtually unchanged from the structure given by the method above.

## 6.1.3. Single-phase results

The combination of the above numerical methods, with the given ODEs and algebraic expressions, can be used to calculate any steady-state, unconfined, single-phase detonation problem. Although single-phase results are of little practical interest because they lack the sophistication to refine the complexities of non-ideal detonation behaviour, the provide a useful benchmark. This section compares the results of the single-phase Chan-Kirby model with the single-phase results of the straight streamline approximation (SSA) in [78]. The first part of this section looks at the general setup for all of the results. The single-phase Chan-Kirby model is then compared to the SSA published in [78]. Finally, the Chan-Kirby model is compared to solutions of a mechanical equilibrium DNS code with the caveat that the comparison is being made between solutions of two different systems of equations.

**Problem setup**

The Chan-Kirby model assumes steady-state detonation and simulates the evolution of the variables between the shock front and the sonic locus.

For the comparisons with the SSA, the equations are non-dimensionalised,

$$\rho = \frac{\tilde{\rho}}{\tilde{\rho}_0}, \quad \mathbf{u} = \frac{\tilde{\mathbf{u}}}{\tilde{D}_{CJ}}, \quad p = \frac{\tilde{p}}{\tilde{D}_{CJ}^2 \tilde{\rho}_0}, \quad e = \frac{\tilde{e}}{\tilde{D}_{CJ}^2}, \quad t = \frac{\tilde{t}\tilde{D}_{CJ}}{\tilde{z}_{\frac{1}{2}}}, \quad \mathbf{x} = \frac{\tilde{\mathbf{x}}}{\tilde{z}_{\frac{1}{2}}},$$

where $\tilde{z}_{\frac{1}{2}}$ is the half-reaction length calculated from the ideal 1D solution (for example, see Figure 6.5). The other simulations use dimensional units.

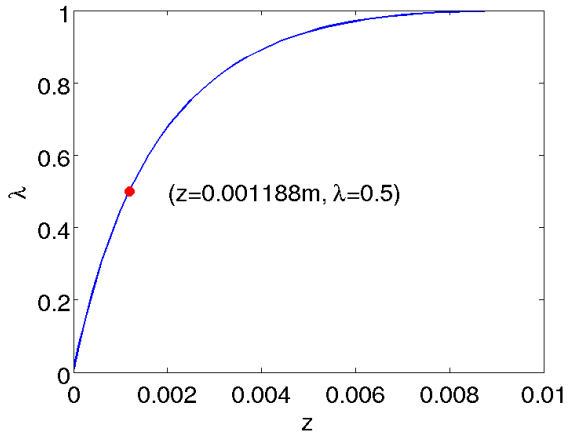


Figure 6.5.: The 1D ideal solution for $\lambda$ as a function of $z$ in the single phase problem with $k = 3.3 \times 10^4$ s$^{-1}$, in the simple pressure dependent reaction rate, with $m = 0.5$ and $n = 1.0$. The red point is the half-reaction point, $\tilde{z}_{\frac{1}{2}}$, (that is, the $z$ for which $\lambda = 0.5$). This $\tilde{z}_{\frac{1}{2}}$ value is used in the non-dimensionalisation.

The polytropic equation of state is used with the parameters

$$\gamma = 3.0, \quad Q = \frac{D_{\text{CJ}}^2}{2\left(\gamma^2 - 1\right)} = 0.0625,$$

and a simple pressure-dependent reaction rate is used,

$$\dot{\lambda} = \frac{d\lambda}{dt} = kp^n \left(1 - \lambda\right)^m,$$

where $k$, $n$ and $m$ are fitted parameters and are given for each result.

### Flooded contour solutions

As outlined in Section 6.1.2, it is helpful to be able to present solutions of 2D simulations in a visually-accessible format. If this is not done, it is particularly difficult to visualise a 2D solution, especially with models like the Chan-Kirby model when the solution is determined on discrete streamlines. It is for this reason that the algorithm outlined in Section 6.1.2 was developed. This section illustrates these results.

Figures 6.6a and 6.6b show pressure contour plots from solutions of the Chan-Kirby model of the same problem but solved for a different number of streamlines. Both give essentially the same radius, DDZ length, maximum pressure, minimum pressure and pressure distribution. The greatest differences are that the contour plot in Figure 6.6a, with 300 streamlines, looks a lot smoother than that in Figure 6.6b. The greater number of streamlines in Figure 6.6a also resolves a small tail on the right edge of the DDZ. It is

surmised that this is a numerical error associated with the edge of charge problem discussed in Section 7.4.

### Comparison to single-phase straight streamline approach

A comparison to the results given in [78] is undertaken for $D = 0.8$, $m = 0.5$, $n = 1$ and $k = 0.680991$. Unfortunately, there are no unconfined axisymmetric examples of the detonation driving zone given in the paper. However, a single comparison of the DDZ is shown in Figure 6.7, with data from [70], and shows that the single-phase Chan-Kirby model underestimates the width of the charge. Due to the neglected radial terms, this underestimation is not a surprising feature. However, the comment is made in [78] that the straight streamline approach, when compared to DNS results in slab geometry, underpredicts the shock lag at the charge edge, pushing the shock front and sonic locus ahead of the same curves for the DNS results. As there are no axisymmetric results presented, it is difficult to say if this problem is more prevalent with axisymmetric coordinates or not. Thus, the discrepancy between the Chan-Kirby and straight-streamline approach for the DDZ could be a combination of the loss of information in the neglected radial terms in the Chan-Kirby model and the underprediction of the shock lag in the straight-streamline model.

Figure 6.7a also shows a discrepancy in the DDZ lengths between the two compared models. On axis, the straight-streamline model is shown in [78] to consistently underestimate the length of the DDZ when compared to DNS results. The Chan-Kirby model, however, is developed so that, on axis, the equations reduce to a one-dimensional solution and so a more accurate position for the sonic locus is given.

The comparisons clearly show that a more accurate on-axis solution does not guarantee that an accurate solution is maintained away from the axis. However, despite the underestimation of the charge radius, the Chan-Kirby model gives a surprisingly accurate shape of the diameter effect curve, as shown in Figure 6.7b; the Chan-Kirby model matches the results of [78] closely. There is some divergence at lower detonation velocities due to the instability of solutions at detonation velocities far from $D_{CJ}$. These instabilities were addressed during later developments of the multiphase implementation of the Chan-Kirby model.

These results show that the Chan-Kirby model needs improvement with respect to radial losses and how these affect the desired outcomes. However, the advantage of the Chan-Kirby model over the straight streamline approach is that it has been extended to a two-phase model and is arguably more useful for non-ideal detonation simulations. This two-phase model is implemented in the following section to compare the effect of an additional phase in comparison to a multiphase DNS solution.

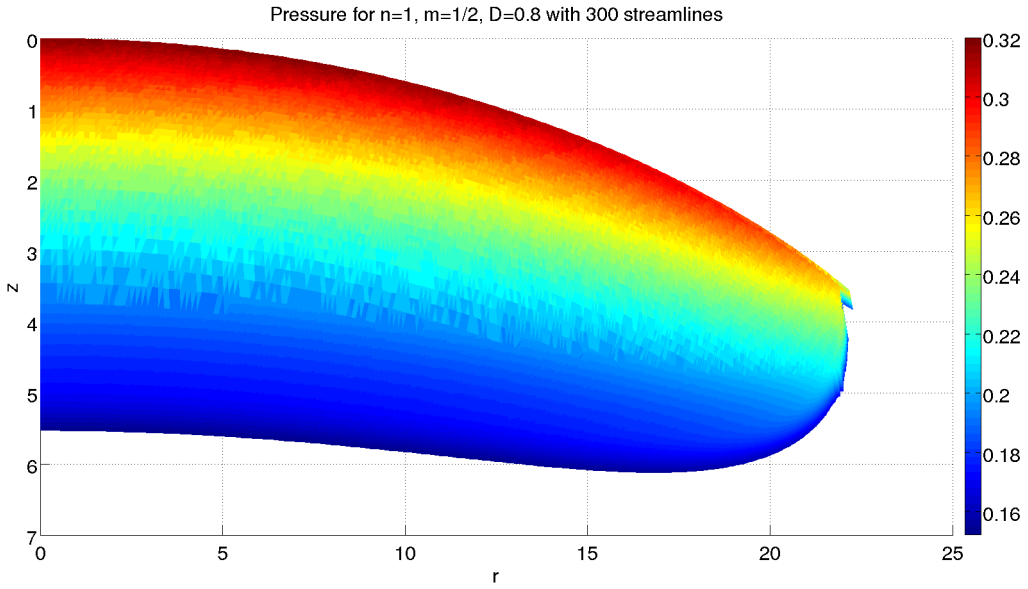


(a)

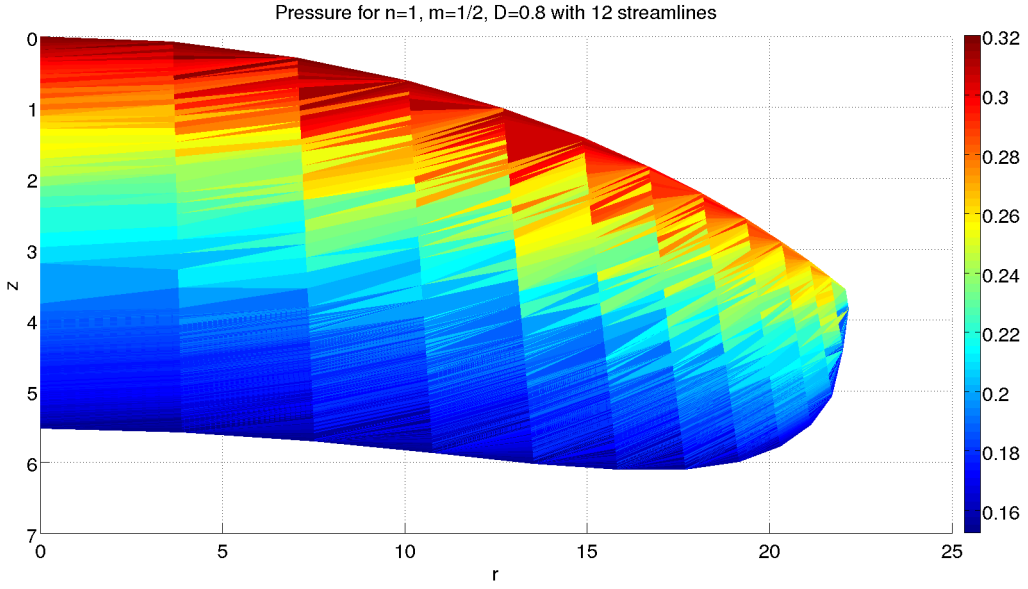


(b)

Figure 6.6.: Flooded contour plots with a) 300 streamlines and b) 12 streamlines. For use in the field, 12 streamlines is sufficient and runs in less than a second on a single processor. For comparison with detonation hydrocodes the addition of many more streamlines provides a comparable flooded contour plot. The increase of streamlines to 300 increases the run time to about 20 seconds.

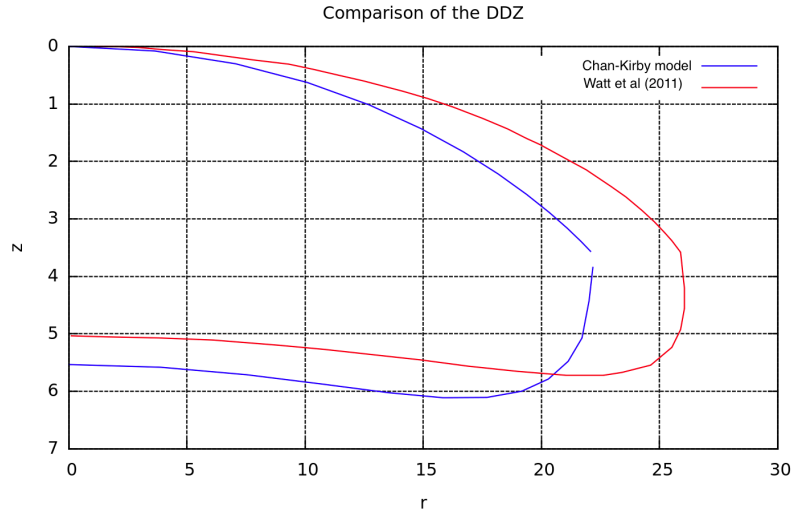


(a)

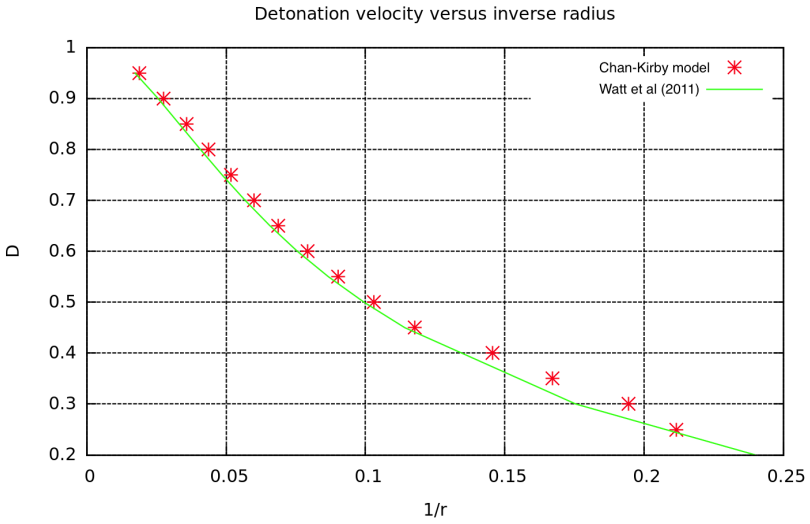


(b)

Figure 6.7.: Comparison of the Chan-Kirby model with [78] for reaction rate parameters $m = 0.5$, $n = 1$ and $k = 0.680991$. a) A comparison with the DDZ shows that there is a discrepancy between the length of the DDZ and the radius. b) Comparison of the detonation versus inverse radius curve. There is an underestimation of the charge radius by the Chan-Kirby model but the general shape is correct.

## 6.2. Two-phase Chan-Kirby model

The two-phase Chan-Kirby model describes unconfined detonation in steady state as the unreacted condensed explosive transitions to a reacted gaseous product. Two equations of state are used, one for each material, and a simple rule governs the mixture of the two states,

$$e = (1 - \lambda)e_u(p, \rho_u) + \lambda e_r(p, \rho_r). \tag{6.53}$$

Here the subscript $u$ indicates the unreacted phase and the subscript $r$ denotes the reacted phase. Although this by no means captures the inhomogeneity of a non-ideal explosive, it is a more realistic model than a single phase.

The two-phase Chan-Kirby model is identical to the single-phase model, as outlined in Section 6.1, except that the expressions for the two different densities need to be specified. An extra ODE to track the evolution of the unreacted density is added and an expression to calculate the reacted density from the unreacted density and mixture density completes the system.

### 6.2.1. Unreacted density ODE

The underlying two-phase equations of the Chan-Kirby model require a closure condition to relate the volumes of the two phases. The Chan-Kirby model makes the assumption that the unreacted phase expands isentropically; that is, on the isentrope,

$$c_u^2 = \frac{dp}{d\rho_u}. \tag{6.54}$$

This equation can then be rearranged to obtain an ODE for the unreacted density:

$$d\rho_u = \frac{dp}{c_u^2}, \tag{6.55}$$

$$\frac{d\rho_u}{dz} = \frac{1}{c_u^2}\frac{dp}{dz}. \tag{6.56}$$

Using the expression obtained for the axial momentum (6.30):

$$\boxed{\frac{d\rho_u}{dz} = -\frac{\rho u}{c_u^2}\left(\frac{du}{dz}\right).} \tag{6.57}$$

The equation, the isentropic closure condition, has been boxed to indicate that this is an additional ODE, along with those derived in Appendix A.

There is further discussion on this closure condition in Section 6.2.4.

### 6.2.2. Algebraic Expressions

As with the single-phase system, there are several algebraic expressions needed to close the system of equations. These are slightly different for the two-phase system and are outlined in the following paragraphs.

### Reacted density

Since the reacted density is undetermined at the shock front, it makes more sense to determine $\rho_r$ algebraically from $\rho$ and $\rho_u$, as they can be explicitly defined via the conservation of mass, (6.2), and the isentropic expansion closure condition, (6.57).

The assumed mixture rules between the densities,

$$\frac{1}{\rho} = \frac{1-\lambda}{\rho_u} + \frac{\lambda}{\rho_r}, \tag{6.58}$$

can be rearranged to obtain an expression for the reacted density,

$$\rho_r = \frac{\lambda \rho \rho_u}{\rho_u - (1-\lambda)\,\rho}, \tag{6.59}$$

where $\lambda$ is the mass fraction of the reacted material. For the simulations in this section, it is assumed that the Chan-Kirby model is a true mixture model - the mass fraction $\lambda$ is given a small, finite value at $t = 0$.

### Sound Speed

The speed of sound in each material, and the two-material mixture speed of sound, also need to be specified to close the equations. The speeds of sound in the two materials are given by (compare to (6.12)),

$$c_u^2 = \frac{p/\rho_u - \left(\partial e_u/\partial \rho_u^2\right)_{p,\lambda}}{\left(\partial e_u/\partial p\right)_{\rho_u,\lambda}},$$
$$c_r^2 = \frac{p/\rho_r - \left(\partial e_r/\partial \rho_r^2\right)_{p,\lambda}}{\left(\partial e_r/\partial p\right)_{\rho_r,\lambda}},$$

and the two-material mixture sound speed,

$$\frac{1}{c^2\rho^2} = \frac{1-\lambda}{c_u^2\rho_u^2} + \frac{\lambda}{c_r^2\rho_r^2}, \tag{6.60}$$

$$c^2 = \frac{c_r^2\rho_r^2 c_u^2\rho_u^2}{\rho^2\left((1-\lambda)\,c_r^2\rho_r^2 + \lambda c_u^2\rho_u^2\right)}, \tag{6.61}$$

is the two-material case of the mechanical equilibrium sound speed, (7.7), and is discussed further in §7.1.

### Thermicity

The thermicity is also needed to close the system of equations. It is expressed as

$$\begin{aligned}\sigma &= -\frac{1}{\rho c^2}\frac{\frac{\partial e}{\partial \lambda}}{\frac{\partial e}{\partial p}} \\ &= -\frac{1}{\rho c^2}\frac{\frac{\partial e}{\partial \lambda}}{\frac{\partial e}{\partial e_u}\frac{\partial e_u}{\partial p} + \frac{\partial e}{\partial e_r}\frac{\partial e_r}{\partial p}}.\end{aligned} \tag{6.62}$$

Using the assumed mixture equation (6.53) gives

$$\sigma = -\frac{1}{\rho c^2}\frac{e_r - e_u - Q}{(1-\lambda)\frac{\partial e_u}{\partial p} + \lambda\frac{\partial e_r}{\partial p}}. \tag{6.63}$$

### Pressure

Like the single-phase model, the pressure can be calculated from the integrated variables using Bernoulli's equation. The equation is identical to (6.9) except that the internal energy is now a function of both the unreacted and reacted internal energies according to the mixture rule given by (6.53).

### Boundary conditions

The boundary conditions for the two-phase model are identical to the single-phase model except that the unreacted density needs to be specified. This is taken to equal the initial mixture density (6.23),

$$\rho_s = \rho_{u,s} = \frac{\rho_0^2 D^2 \cos^2(\theta)}{\rho_0 D^2 \cos^2(\theta) - (p_s - p_0)}. \tag{6.64}$$

With the model defined, comparisons are made to a DNS solution in the following section.

## 6.2.3. Results

Comparisons between solutions of the two-phase augmented Euler Chan-Kirby model and the multiphase mechanical equilibrium DNS are made for an explosive modelled with a polytropic ideal gas with $\gamma_u = 3.0$ in the unreacted phase and $\gamma_r = 1.4$ in the reacted phase. The simple reaction rate (5.2) is used with $\tau_H = 3.18126869$, taken from [70] for later comparisons of this work with [78]. The unconfined DNS results are achieved by confining the ratestick in air confinement of very large thickness to mimic an infinitely unconfined charge.

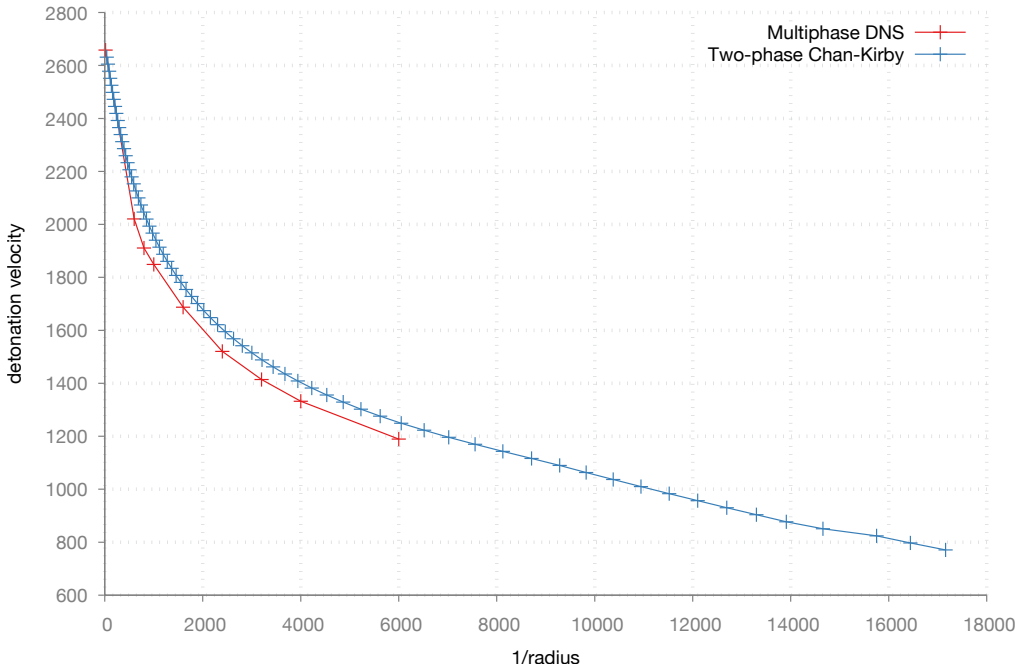


Figure 6.8.: Diameter effect curve for a two-phase ideal gas with $\gamma_u = 3$ and $\gamma_r = 1.4$. The results from the two-phase Chan-Kirby model are shown in blue and compare well to the unconfined results from the multiphase DNS, shown in red.

The diameter effect curve, shown in Figure 6.8, shows good agreement between the two-phase augmented Euler Chan-Kirby model and the multiphase DNS with some underestimation of the radius in the Chan-Kirby model, as expected from the neglected radial terms.

The solution at $1/r = 0$ is a theoretical solution for the material chosen [40]. Towards this limit, very small changes in radius have a big effect on the resulting detonation velocity. The lack of the data from the DNS near this limit is due to the fact that the code was designed for non-ideal multiphase detonation, and not near-ideal explosives at large diameters, and solutions were not able to be obtained.

These initial comparisons are useful but in order to adequately assess the effects of the neglected radial terms, the underlying models of the two implementations should be the same. The DNS solution shown in Figure 6.8 uses a different underlying system of equations to the Chan-Kirby model. The following section will outline how these two implementations differ and why an alternative for multiphase modelling is preferred.

### 6.2.4. Homogeneous mixture closure assumption: isentropic pressure expansion

To close the system of equations for a homogeneous mixture simulation, an assumption needs to be made about the mixture. There are three possibilities: thermal isolation, thermal equilibrium ($T_u = T_r$) or that the ratio of product volumes is constant ($\phi = v_u/v_r = \text{constant}$).

The Chan-Kirby model assumes that the pressure expansion of the gaseous, reacted products stays on the isentrope of the unreacted material:

$$p_{\text{isentrope}}(v_u) = p_r(e_r, v_r). \tag{6.65}$$

This is equivalent to thermal isolation.

The thermal equilibrium and thermal isolation interphase conditions are extreme cases and the physical reality of the situation would be somewhere between these two [23]. The constant ratio of product volumes assumption does not have any real physical meaning but produces results very similar to those of thermal equilibrium and simplifies the system significantly. Temperature equilibrium mixture models have been illustrated to give unphysical results [58]. Despite this, temperature equilibrium models still appear to be the more popular choice for homogeneous mixture simulations.

The Chan-Kirby model uses the more physically realistic isentropic expansion closure condition. With this isothermal closure condition, for certain equations of state, an analytical solution to the 1D problem can be calculated and is most useful for validation purposes. The next section outlines how this solution can be obtained for the polytropic equation of state.

#### Analytical solution from Hugoniot, Crussard curves and Rayleigh lines

The first law of thermodynamics relates internal energy to temperature, entropy, pressure and volume,

$$de = TdS - pdv, \tag{6.66}$$

where $S$ is the entropy per unit mass.

For an isentropic process, the equation becomes:

$$de = -pdv \Rightarrow p = -\left(\frac{de}{dv}\right)_S. \tag{6.67}$$

Substituting in an appropriate equation of state will give a non-homogeneous ODE for internal energy on an isentrope and the solution to this ODE will then give the isentropic pressure. Closed-form solutions for pressure are not available for all equations of state [5]. Fortunately, a closed-form solution can be determined for the polytropic equation of state.

Substituting the polytropic equation of state for the unreacted phase into (6.67),

$$\frac{de_u}{dv_u} = -\frac{e_u(\gamma_u - 1)}{v_u}, \tag{6.68}$$

and taking the integral,

$$\int \frac{de_u}{e_u} = -\left(\gamma_u - 1\right) \int \frac{dv_u}{v_u}, \tag{6.69}$$

the solution, passing through the reference state $(e_{\text{ref}}, v_{\text{ref}})$, is determined as

$$e_u = e_{\text{ref}} \left(\frac{v_u}{v_{ref}}\right)^{-(\gamma_u - 1)}. \tag{6.70}$$

Substituting the equation of state back into this equation, an expression for the isentropic pressure is obtained,

$$p_{\text{isentrope}} = \frac{e_{\text{ref}}\left(\gamma_u - 1\right)}{v_u} \left(\frac{v_u}{v_{\text{ref}}}\right)^{-(\gamma_u - 1)}. \tag{6.71}$$

Now that the isentropic pressure has been determined, it can be substituted into (6.65) so that the pressure can be eliminated and a relationship between the volumes of the two phases can be obtained:

$$\frac{e_{\text{ref}}\left(\gamma_u - 1\right)}{v_u} \left(\frac{v_u}{v_{\text{ref}}}\right)^{-(\gamma_u - 1)} = \frac{e_r\left(\gamma_r - 1\right)}{v_r} - q\lambda, \tag{6.72}$$

$$\text{so that} \quad v_u = \left(\frac{e_r}{v_r} \frac{\left(\gamma_r - 1\right)}{\left(\gamma_u - 1\right) e_{\text{ref}} v_{\text{ref}}^{(\gamma_u - 1)}}\right)^{-\frac{1}{\gamma_u}}$$

$$= \left(\frac{p}{\left(\gamma_u - 1\right) e_{\text{ref}} v_{\text{ref}}^{(\gamma_u - 1)}}\right)^{-\frac{1}{\gamma_u}}, \tag{6.73}$$

that is, $v_u = v_u\left(p\right)$.

The internal energy is then defined by

$$e\left(p, v_u, v_r, \lambda\right) = \left(1 - \lambda\right) e_u\left(p, v_u\right) + \lambda e_r\left(p, v_r\right), \tag{6.74}$$

$$= \left(1 - \lambda\right) e_u\left(p\right) + \lambda e_r\left(p, v_r\right). \tag{6.75}$$

Given the mixture rule for the volume,

$$v = \left(1 - \lambda\right) v_u + \lambda v_r, \tag{6.76}$$

that is, $v = v\left(v_u, v_r\right) = v\left(p, v_r\right)$, the internal energy can be expressed as

$$e\left(p, v_u, v_r, \lambda\right) = e\left(p, v, \lambda\right) = \left(1 - \lambda\right) e_u\left(p, v\right) + \lambda e_r\left(p, v\right). \tag{6.77}$$

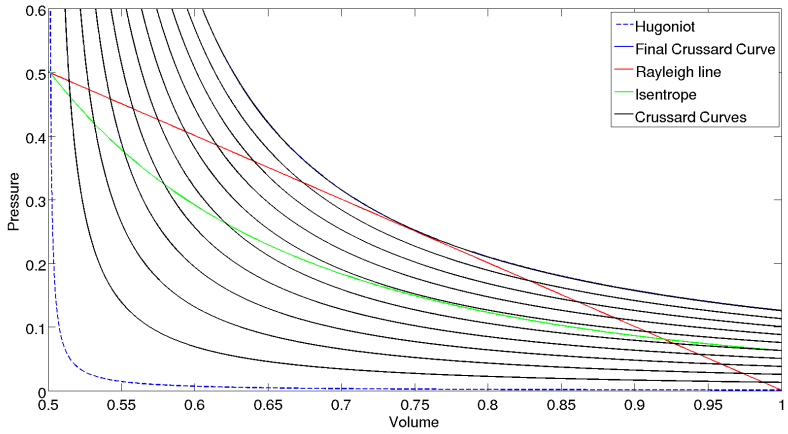


Figure 6.9.: Hugoniot, Rayleigh line, Crussard curves and isentrope for the two-phase reaction between two polytropic materials with $\gamma = 3.0$ in both.

The importance of this expression becomes apparent when addressing the issue of how to solve the 1D homogeneous mixture system of conservation equations analytically using the Hugoniot, the Crussard curves and the Rayleigh lines.

The Hugoniot curve

$$e\left(p, v, \lambda = 0\right) - e_0 = \frac{1}{2}\left(p + p_0\right)\left(v_0 - v\right) \tag{6.78}$$

gives the locus of all possible final states for any shock in the $(p, v)$ plane. Similarly, the Crussard curves

$$e\left(p, v, \lambda\right) - e_0 = \frac{1}{2}\left(p + p_0\right)\left(v_0 - v\right) \tag{6.79}$$

give the locus of all possible states in the $(p, v)$ plane, but for $0 < \lambda \leq 1$ where each curve is constant $\lambda$.

The Rayleigh line

$$p - p_0 = \left(\frac{D}{v_0}\right)^2 \left(v_0 - v\right) \tag{6.80}$$

gives another set of $(p, v)$ values, valid for a specific detonation velocity and set of initial conditions $(p_0, v_0)$. The intersection of the Rayleigh line with the Hugoniot curve is the von Neumann (VN) point. The intersection of the Rayleigh line with the final Crussard curve ($\lambda = 1$) gives the CJ point.

Between the CJ and VN points one can solve the CJ Rayleigh line and the Crussard curves to find an expression for $(p - v - \lambda)$. All of these curves are illustrated in Figure 6.9.

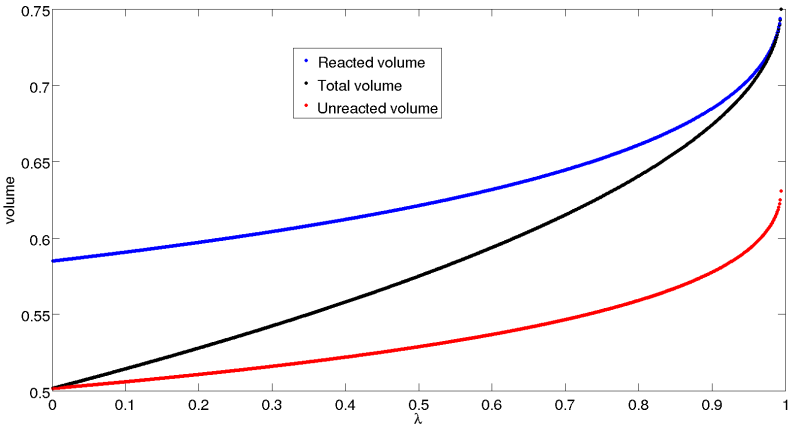


Figure 6.10.: Despite the fact that the gaseous products (blue line) and the explosive products (red line) are modelled with the exact same polytropic equation of state and with $\gamma = 3.0$ in both materials, the evolution of the volumes with respect to mass fraction is very different. This is due to the isentropic closure condition.

For a homogeneous mixture system (that is, $\gamma = k$ in both phases), the equations are complicated by the multiple phases. The following outlines the derivation of the equations for a two-phase system.

Firstly, the final Crussard curve is defined for the fully reacted state only, so will be a function of $e = e_r$ and $v = v_r$. Similarly, the Hugoniot will be a function of the unreacted phase; that is, $e = e_u$ and $v = v_u$. All of the Crussard curves between these two curves will be a mixture of the two phases,

$$e\left(p, v_u, v_r, \lambda\right) - e_0 = \frac{1}{2}\left(p + p_0\right)\left(v_0 - v\right), \tag{6.81}$$

where $e\left(p, v_u, v_r, \lambda\right)$ is defined by (6.74). This expression illustrates why it is important to be able to derive the relationship between the two volumes, shown in (6.73), and to be able to express the equation of state in the form shown in (6.77): pressure needs to be defined as a function of $v$ only, and the separate phase volumes, $v_u$ and $v_r$, can be calculated using a combination of (6.73) and (6.76).

Apart from the obvious comparisons that can be made with this analytical solution and any numerical solutions along the axis, this analytical model is also useful because it illustrates that any comparisons between single-phase and two-phase models need to be done carefully.

A two-phase model, with identical materials in each phase, compared with a single-phase model, with the same material in the single phase, could be thought to give results with the same volume in all phases of all models. However, due to the closure condition outlined above, this is not

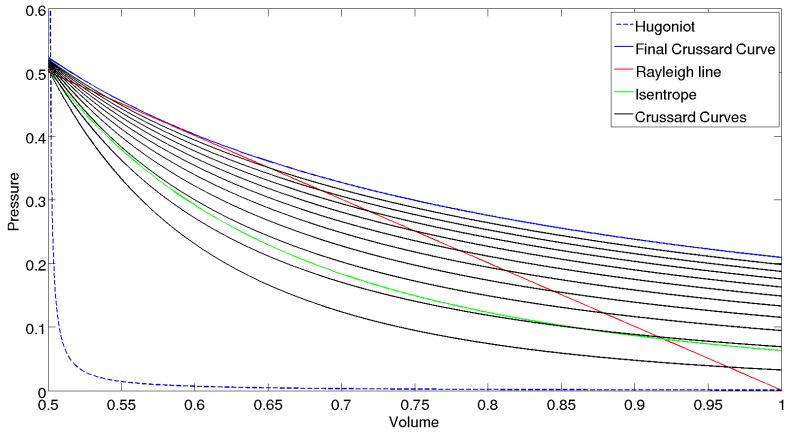


Figure 6.11.: Hugoniot, Rayleigh line, Crussard curves and isentrope for a two-phase system with a condensed explosive modelled with a polytropic gas with $\gamma = 3.0$ that converts to a gaseous product modelled by a polytropic gas with $\gamma = 1.4$. The bottom Crussard curve is the Hugoniot produced with the mixture rule.

a capability of homogeneous mixture models. This is illustrated in Figure 6.10; the mixture volume and material volumes of the two-phase system are plotted against reaction extent $\lambda$. The two phases have identical, polytropic equations of state with $\gamma = 3$. The volumes of the different phases, however, expand very differently as a function of reaction extent.

For a two-phase system with both phases still modelled by the polytropic gas but with a different $\gamma$ in each phase, the reacted isentrope resembles the final Crussard curve but is quite unlike the Hugoniot, as shown in Figure 6.11. In fact, there is a large gap between the Hugoniot and the first Crussard curve. This means that the assumption that the pressure expansion of the reacted products remains along the unreacted isentrope is a poor one.

In condensed explosives, with more realistic equations of state, this is less of a problem since the Hugoniot and the reacted isentrope lie much closer in the $p - v$ plane. For the polytropic gas, the Hugoniot is not well behaved as Figure 6.11 illustrates. The corresponding evolution of the different volumes is shown in Figure 6.12.

In conclusion, the isentropic closure condition, while probably the best of the mixture closure conditions, is not well-suited to the polytropic equation of state. Although more complex equations of state are used to model non-ideal explosives, the isentropic closure condition is still an approximation that may or may not be appropriate depending on the materials being modelled. It would be better to use a system of equations that does not rely on any closure condition.

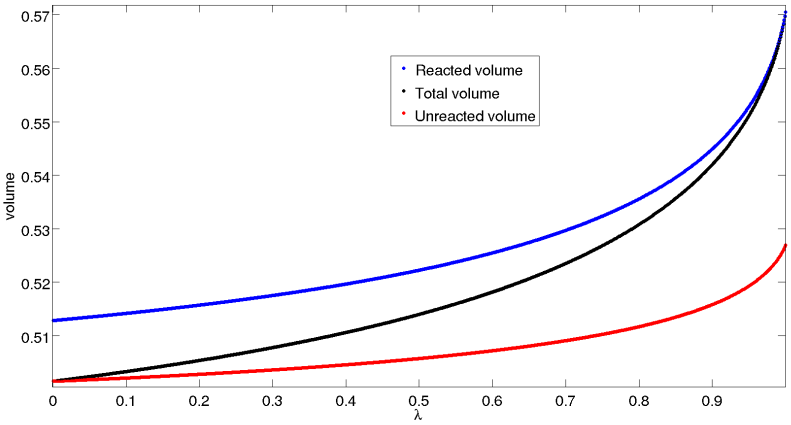


Figure 6.12.: Evolution of the mixture, unreacted and reacted volumes for a two-phase system with a condensed explosive modelled with a polytropic gas with $\gamma = 3.0$ that converts to a gaseous product modelled by a polytropic gas with $\gamma = 1.4$.

Furthermore, most non-ideal explosives are inhomogeneous: in an unreacted non-ideal explosive there are often voids or additives that create hotspots when compressed. Although previous implementations of the Chan-Kirby model have endeavoured to take this into account with a multi-stage reaction rate, it would arguably be better to model these inhomogeneities using a multiphase model.

One multiphase model that eliminates the need for a mixture closure condition, and can capture the inhomogeneous nature of non-ideal explosives with a multiphase system of equations, is the multiphase mechanical equilibrium model. Chapter 7 will explore the origins of this model and how the Chan-Kirby approximations can be applied to it in order to make sensible comparisons with DNS solutions.

# 7. Multiphase mechanical equilibrium Chan-Kirby model

Mining explosives can display highly non-ideal behaviour. At a minimum, a suitable post-ignition model needs to be multidimensional, reactive and multiphase. Ideally, the multiphase components of the model should capture the heterogeneity of the unreacted explosive satisfactorily.

A suitable formulation for modelling the multiphase structure of non-ideal explosives is a reduction of the Baer-Nunziato (BN) model proposed in [51].

The BN model is a multiphase, disequilibrium model - none of the variables are in equilibrium so heuristic closure conditions are not needed. However, the BN model cannot be written in conservation form and so utilising standard finite volume methods to solve the governing equations numerically is problematic.

This work develops a reduction of the BN model initially proposed in [51]. This mechanical equilibrium multiphase model eliminates the heuristic thermal closure conditions needed in an augmented Euler-equation-based model without the overhead costs associated with the full BN model. The model's mechanical relaxation assumption is suitable for the fast mechanical relaxation between the explosive's components and has been shown to accurately predict unconfined and confined non-ideal explosive behaviour [68].

As illustrated in the previous section, it is evident that augmented Euler-equation-based multiphase models have their shortcomings, stemming from the need to make a closure condition assumption. Taking into consideration that reduced models make further approximations, it is to be expected that the final, reduced model solution will not be an exact match to experimental results.

There is some debate among the detonation community about the best system of equations to use to model multiphase detonation. Augmented Euler-equation-based multiphase models, with their approximate closure conditions, are the simplest while the BN model is the most complicated. The more complicated the system gets, the more difficult and economically challenging it is to solve. Therefore, the best system to use is often defined by the user's objectives.

If accuracy and economy are both a consideration then there is a middle ground between these two extremes that is less complicated than the BN model but does not require the approximate closure condition of the

augmented Euler-equation-based multiphase approach. This middle ground is the group of mechanical equilibrium models. The system that will be explored in this thesis is the *single-pressure and single-velocity multiphase model* of [65] that, for brevity's sake, will here be referred to as the mechanical equilibrium model.

The mechanical equilibrium model was developed to address the large gap in the development of detonation codes of non-ideal detonation modelling capabilities; in particular, being able to represent the type of behaviour displayed by strongly heterogeneous mining explosives. This benefit is coupled with the fact that it is more economical than the BN model and more physically accurate than multifluid approaches.

For these reasons, if it is able to be reduced to a system of ODEs that produces extremely fast solutions with reasonable accuracy, the reduced mechanical equilibrium model will be an invaluable tool to the mining industry.

The following sections outline the mechanical equilibrium model and show the derivation of the mechanical equilibrium reduced model.

## 7.1. The mechanical equilibrium model

The mechanical equilibrium model with mass transfer, as presented in [65], is:

$$\frac{\partial \alpha_k}{\partial t} + \mathbf{u} \cdot \nabla \alpha_k - \alpha_k \left( \frac{\rho c^2}{\rho_k c_k^2} - 1 \right) \nabla \cdot \mathbf{u} = \dot{\alpha_k}, \tag{7.1}$$

$$\frac{\partial \alpha_k \rho_k}{\partial t} + \nabla \cdot (\alpha_k \rho_k \mathbf{u}) = \rho \dot{\lambda}_k, \tag{7.2}$$

$$\frac{\partial \rho \mathbf{u}}{\partial t} + \nabla \cdot (\rho \mathbf{u} \otimes \mathbf{u}) + \nabla p = 0, \tag{7.3}$$

$$\frac{\partial \rho E}{\partial t} + \nabla \cdot ((\rho E + p)\, \mathbf{u}) = 0, \tag{7.4}$$

where the subscript $\cdot_k$ refers to the relevant material, $\alpha_k$ is the volume fraction of the material, $\rho$ is the total density, $\mathbf{u}$ is the velocity vector and $E$ is the total energy. Note that the total density $\rho$ is different from the density of the individual phases $\rho_k$:

$$\rho = \sum_k \alpha_k \rho_k, \tag{7.5}$$

where $\sum_k \alpha_k = 1$ and the mass fraction of an individual material is given by

$$\lambda_k = \frac{\alpha_k \rho_k}{\rho}, \tag{7.6}$$

and where $\sum_k \lambda_k = 1$. The sound speed $c$ is given by the mechanical equilibrium (also known as Wood) sound speed:

$$\frac{1}{\rho c^2} = \sum_k \frac{\alpha_k}{\rho_k c_k^2}. \tag{7.7}$$

For derivation and further discussion of this sound speed for the mechanical equilibrium model see [63]. Note that this reference also considers pressure disequilibrium which has a different sound speed. For the mechanical equilibrium model given by equations (7.1)-(7.4), the characteristics speeds or eigenvalues are $u$, $u + c$ and $u - c$ where $c$ is the sound speed given above in (7.7).

The total specific energy

$$E = e + \frac{\mathbf{u}^2}{2} \tag{7.8}$$

is a function of the specific internal energy,

$$e = \sum_k \lambda_k \, e_k(\rho_k, p). \tag{7.9}$$

The model neglects heat transfer between the phases due to their small interfacial area [58].

The volume fraction source term, $\dot{\alpha}_k$, is taken from [58] and is based on the assumption that a pressure disequilibrium between the different components, which is mechanically relaxed by means of emission of acoustic waves, affects the volume fractions of the mixture:

$$\dot{\alpha}_k = \frac{\rho \dot{\lambda}_k}{\rho_k} - \frac{\alpha_k}{\rho_k c_k^2} \rho c^2 \sum_j \frac{\rho \dot{\lambda}_j}{\rho_j}. \tag{7.10}$$

This model is used for all DNS simulations in this work unless otherwise stated. The validation of this model, and an outline of the numerical methods used for the simulations, can be found in [65].

The following section reduces this mechanical equilibrium model to a set of ODEs.

## 7.2. Reduction of the mechanical equilibrium model to a set of ODEs

The conservation of mass and conservation of momentum (axial and radial) equations are identical to those for the Chan-Kirby model derived in Chapter 6; equations (6.1) to (6.4) with (6.57). The additional equations that need to be derived are equations for the mass fraction and the volume fraction. The

conservation of energy equation also needs to be derived and is calculated in a similar way to that in Chapter 6 but with much added complication because the model tracks both mass and volume fractions. All of these additional equations are derived below. The terms that are crossed out are terms that are neglected in this reduction of the equations. The terms are neglected either because they are small or that it is convenient to do so. In the latter case, the neglected term may not actually be small in all cases, and in this work simulation results are relied upon for justification.

The ODE for the evolution of the mass fraction is derived from the conservation of the individual masses, (7.2). Rearranging the equation for the mass fraction, (7.6), gives

$$\alpha_k \rho_k = \rho \lambda_k,$$

so the mass fraction differential equation may be written

$$\frac{\partial}{\partial t}\left(\rho \lambda_k\right) + \nabla \cdot \left(\rho \mathbf{u} \lambda_k\right) = \rho \dot{\lambda}_k,$$

which can be rearranged to give

$$\rho \frac{\partial \lambda_k}{\partial t} + \lambda_k \frac{\partial \rho}{\partial t} + \rho \mathbf{u} \cdot \nabla \lambda_k + \lambda_k \nabla \cdot \left(\rho \mathbf{u}\right) = \rho \dot{\lambda}_k.$$

Noting that, from (1.1),

$$\lambda_k \left( \frac{\partial \rho}{\partial t} + \nabla \cdot \left(\rho \mathbf{u}\right) \right) = 0,$$

and dividing through by the density gives

$$\frac{\partial \lambda_k}{\partial t} + \mathbf{u} \cdot \nabla \lambda_k = \dot{\lambda}_k, \tag{7.11}$$

which is the same as (1.4) for each material.

Under the assumption of steady state the equation becomes

$$\mathbf{u} \cdot \nabla \lambda_k = \dot{\lambda}_k. \tag{7.12}$$

Transforming the system to axisymmetric coordinates, the system becomes:

$$(u, \omega) \cdot \left( \frac{\partial}{\partial z}, \frac{\partial}{\partial r} \right) \lambda_k = \dot{\lambda}_k.$$

Taking the dot product and assuming that the radial velocity multiplied by the change in mass fraction with respect to the radius is negligible,

$$u \frac{\partial \lambda_k}{\partial z} + \cancel{\omega \frac{\partial \lambda_k}{\partial r}} = \dot{\lambda}_k,$$

gives the final equation:

$$\boxed{\frac{d\lambda_k}{dz} = \frac{\dot{\lambda}_k}{u}.} \tag{7.13}$$

The PDE for the evolution of the volume fraction, (7.1), is given by

$$\frac{\partial \alpha_k}{\partial t} + \mathbf{u} \cdot \nabla \alpha_k - K_k \nabla \cdot \mathbf{u} = M_k, \tag{7.14}$$

where,

$$K_k = \alpha_k \left( \frac{\rho c^2}{\rho_k c_k^2} - 1 \right), \tag{7.15}$$

is the multiphase term and $M_k = \dot{\alpha_k}$ is the mass transfer term. This equation can be reduced to an ODE under the assumption that it is steady state,

$$\mathbf{u} \cdot \nabla \alpha_k - K_k \nabla \cdot \mathbf{u} = M_k, \tag{7.16}$$

and axisymmetric,

$$(u, \omega) \cdot \left( \frac{\partial}{\partial z}, \frac{\partial}{\partial r} \right) \alpha_k - K_k \left( \frac{\partial}{\partial z}, \frac{1}{r} \frac{\partial}{\partial r} \right) \cdot (u, r\omega) = M_k.$$

Taking the dot product the equation becomes

$$u \frac{\partial \alpha_k}{\partial z} + \omega \frac{\partial \alpha_k}{\partial r} - K_k \frac{\partial u}{\partial z} - K_k \frac{\partial \omega}{\partial r} - K_k \frac{\omega}{r} = M_k.$$

Neglecting any terms multiplied by $\dfrac{\omega}{u}$,

$$\frac{\partial \alpha_k}{\partial z} = \cancel{-\frac{\omega}{u} \frac{\partial \alpha_k}{\partial r}} + \frac{K_k}{u} \left( \frac{\partial u}{\partial z} + \frac{\partial \omega}{\partial r} + \frac{\omega}{r} \right) + \frac{M_k}{u},$$

gives the final equation for the volume fraction:

$$\boxed{\frac{d\alpha_k}{dz} = \frac{K_k}{u} \left( \frac{du}{dz} + \frac{\partial \omega}{\partial r} + \frac{\omega}{r} \right) + \frac{M_k}{u},} \tag{7.17}$$

where it is assumed that $u$ is a function of $z$ so that the partial derivatives can be replaced by ordinary derivatives.

The ODE for the evolution of particle velocity is derived from the conservation of energy equation, (7.4). For brevity's sake, some steps have been omitted.

Using the definition of total energy,

$$E = \frac{1}{2} \rho \mathbf{u}^2 + \rho e,$$

with equations for conservation of mass (7.2) and momentum (7.3). This can be reduced to

$$\rho\left(\frac{\partial e}{\partial t}+\mathbf{u}\cdot\nabla e\right)+p\left(\nabla\cdot\mathbf{u}\right)=0.$$

Assuming that the system is steady-state,

$$\rho\mathbf{u}\cdot\nabla e+p\left(\nabla\cdot\mathbf{u}\right)=0.$$

Rearranging the steady state equation for the conservation of mass gives

$$\nabla\cdot\mathbf{u}=\rho\mathbf{u}\cdot\nabla v,$$

which can be substituted back into the energy equation to give

$$\mathbf{u}\cdot\nabla e=-p\left(\mathbf{u}\cdot\nabla v\right)=\frac{p}{\rho^2}\mathbf{u}\cdot\nabla\rho.$$

Note that $v=1/\rho$.

Introducing multiple phases,

$$\begin{aligned}e&=\sum_k\lambda_k e_k\left(p,\rho_k\right),\\ v&=\sum_k\lambda_k v_k,\end{aligned}$$

the energy equation becomes

$$\begin{aligned}\mathbf{u}\cdot\nabla e+p\mathbf{u}\cdot\nabla v&=\sum_k\lambda_k\mathbf{u}\cdot\left(\nabla e_k+p\nabla v_k\right)+\sum_k\left(e_k+pv_k\right)\mathbf{u}\cdot\nabla\lambda_k\\&=\sum_k\lambda_k\mathbf{u}\cdot\left(\nabla p\frac{\partial e_k}{\partial p}-\nabla\rho_k\left(\frac{p}{\rho_k^2}-\frac{\partial e_k}{\partial\rho_k}\right)\right)+\sum_k h_k\mathbf{u}\cdot\nabla\lambda_k\\&=\sum_k\lambda_k\frac{\partial e_k}{\partial p}\mathbf{u}\cdot\left(\nabla p-c_k^2\nabla\rho_k\right)+\sum_k h_k\mathbf{u}\cdot\nabla\lambda_k=0,\end{aligned}$$

with use of the sound speed definition, (6.12).

Let $\dfrac{\partial e_k}{\partial p}=\dfrac{1}{\rho_k\Gamma_k}$ where $\Gamma$ is the Grüneisen parameter (see (4.12)). From (7.6),

$$\frac{\lambda_k}{\rho_k\Gamma_k}=\frac{\alpha_k}{\rho\Gamma_k}. \tag{7.18}$$

This is holds if the equation of state is in Mie-Grüneisen form. Hence, the energy equation is

$$0=\sum_k\frac{\alpha_k}{\Gamma_k}\mathbf{u}\cdot\left(\nabla p-c_k^2\nabla\rho_k\right)+\rho\sum_k h_k\mathbf{u}\cdot\nabla\lambda_k. \tag{7.19}$$

From the steady state equation for mass fraction, (7.2),

$$\nabla \cdot (\alpha_k \rho_k \mathbf{u}) = \rho \dot{\lambda}_k,$$

it follows that

$$\mathbf{u} \cdot \nabla \rho_k = \frac{\rho \dot{\lambda}_k}{\alpha_k} - \rho_k (\nabla \cdot \mathbf{u}) - \frac{\rho_k}{\alpha_k} \mathbf{u} \cdot \nabla \alpha_k. \tag{7.20}$$

From the ODE for the mass fraction, (7.12), $\mathbf{u} \cdot \nabla \lambda_k = \dot{\lambda}_k$, the above equation becomes

$$\mathbf{u} \cdot \nabla \rho_k = \frac{\rho \mathbf{u} \cdot \nabla \lambda_k}{\alpha_k} - \rho_k (\nabla \cdot \mathbf{u}) - \frac{\rho_k \mathbf{u} \cdot \nabla \alpha_k}{\alpha_k}. \tag{7.21}$$

Substituting this and (7.20) back into the equation for energy (7.19) gives

$$\begin{aligned} 0 &= \sum_k \frac{\alpha_k}{\Gamma_k} \left( \mathbf{u} \cdot \nabla p - c_k^2 \left[ \frac{\rho \dot{\lambda}_k}{\alpha_k} - \rho_k (\nabla \cdot \mathbf{u}) - \frac{\rho_k \mathbf{u} \cdot \nabla \alpha_k}{\alpha_k} \right] \right) + \rho \sum_k h_k \dot{\lambda}_k \\ &= \rho \sum_k \left( h_k - \frac{c_k^2}{\Gamma_k} \right) \dot{\lambda}_k + \sum_k \frac{\alpha_k}{\Gamma_k} \mathbf{u} \cdot \nabla p + \sum_k \frac{c_k^2 \rho_k}{\Gamma_k} \mathbf{u} \cdot \nabla \alpha_k + \sum_k \frac{\alpha_k \rho_k c_k^2}{\Gamma_k} (\nabla \cdot \mathbf{u}). \end{aligned} \tag{7.22}$$

From the conservation of momentum, (1.2),

$$\nabla p = -\rho (\mathbf{u} \cdot \nabla) \mathbf{u}, \tag{7.23}$$

and from the volume fraction equation, (7.16),

$$\mathbf{u} \cdot \nabla \alpha_k = K_k (\nabla \cdot \mathbf{u}) + H_k + M_k, \tag{7.24}$$

where $H_k$ is the heat exchange term that has been reintroduced for generality but is taken to be $H_k = 0$ in this work. The energy equation is then

$$\begin{aligned} 0 = \rho \sum_k \left( h_k - \frac{c_k^2}{\Gamma_k} \right) \dot{\lambda}_k - \sum_k \frac{\alpha_k}{\Gamma_k} \rho \mathbf{u} \cdot (\mathbf{u} \cdot \nabla) \mathbf{u} \\ + \sum_k \frac{c_k^2 \rho_k}{\Gamma_k} [K_k (\nabla \cdot \mathbf{u}) + H_k + M_k] + \sum_k \frac{\alpha_k \rho_k c_k^2}{\Gamma_k} (\nabla \cdot \mathbf{u}). \end{aligned} \tag{7.25}$$

In axisymmetric coordinates,

$$\mathbf{u} \cdot \nabla = u \frac{\partial}{\partial z} + \omega \frac{\partial}{\partial r},$$

and

$$\begin{aligned} \nabla \cdot \mathbf{u} &= \left( \frac{\partial}{\partial z}, \frac{1}{r} \frac{\partial}{\partial r} \right) \cdot (u, r\omega) \\ &= \frac{\partial u}{\partial z} + \frac{\partial \omega}{\partial r} + \frac{\omega}{r}. \end{aligned}$$

Hence,

$$\begin{aligned}0 =&\rho\sum_k\left(h_k-\frac{c_k^2}{\Gamma_k}\right)\dot{\lambda}_k-\sum_k\frac{\alpha_k}{\Gamma_k}\rho\left[\left(u^2\frac{\partial u}{\partial z}+\omega^2\frac{\partial\omega}{\partial r}\right)+u\omega\left(\frac{\partial u}{\partial r}+\frac{\partial\omega}{\partial z}\right)\right]\\&+\sum_k\frac{c_k^2\rho_k}{\Gamma_k}\left[K_k\left(\frac{\partial u}{\partial z}+\frac{\partial\omega}{\partial r}+\frac{\omega}{r}\right)+H_k+M_k\right]\\&+\sum_k\frac{\alpha_k\rho_k c_k^2}{\Gamma_k}\left(\frac{\partial u}{\partial z}+\frac{\partial\omega}{\partial r}+\frac{\omega}{r}\right).\end{aligned}$$

An expression for the evolution of the particle velocity in the axial direction is obtained by isolating terms multiplying $\dfrac{\partial u}{\partial z}$; these terms are

$$\begin{aligned}&\sum_k\frac{\alpha_k\rho_k c_k^2}{\Gamma_k}+\sum_k\frac{c_k^2\rho_k K_k}{\Gamma_k}-\sum_k\frac{\alpha_k\rho u^2}{\Gamma_k}\\=&\sum_k\frac{\alpha_k\rho_k c_k^2}{\Gamma_k}+\sum_k\frac{c_k^2\rho_k\alpha_k\rho c^2}{\Gamma_k\rho_k c_k^2}-\sum_k\frac{c^2\rho_k\alpha_k}{\Gamma_k}-\sum_k\frac{\alpha_k\rho u^2}{\Gamma_k}\\=&\sum_k\left(\frac{\alpha_k\rho c^2}{\Gamma_k}-\frac{\alpha_k\rho u^2}{\Gamma_k}\right).\end{aligned}$$

Note that $\displaystyle\sum_k\frac{\alpha_k}{\Gamma_k}=\frac{1}{\Gamma}$, so that the coefficient of $\dfrac{\partial u}{\partial z}$ is

$$\frac{\rho}{\Gamma}\left(c^2-u^2\right). \tag{7.26}$$

The factor of $\dfrac{\rho}{\Gamma}$ will be taken to the other side in a step below so that all that is left is the 1D CJ condition,

$$\left(c^2-u^2\right). \tag{7.27}$$

The terms not associated with $\dfrac{\partial u}{\partial z}$ are

$$\begin{aligned}&\rho\sum_k\left(h_k-\frac{c_k^2}{\Gamma_k}\right)\dot{\lambda}+\sum_k\frac{c_k^2\rho_k}{\Gamma_k}\left[K_k\left(\frac{\partial\omega}{\partial r}+\frac{\omega}{r}\right)+H_k+M_k\right]\\&+\sum_k\frac{\alpha_k\rho_k c_k^2}{\Gamma_k}\left(\frac{\partial\omega}{\partial r}+\frac{\omega}{r}\right)-\sum_k\frac{\alpha_k}{\Gamma_k}\rho\left(\omega^2\frac{\partial\omega}{\partial r}\right).\end{aligned}$$

Multiplying by the factor of $\dfrac{\Gamma}{\rho}$, and recalling that $\lambda_k=\dfrac{\alpha_k\rho_k}{\rho}$, gives

$$\Gamma\left[\sum_k\left(h_k-\frac{c_k^2}{\Gamma_k}\right)\dot{\lambda}_k+\sum_k\frac{c_k^2\rho_k}{\rho\Gamma_k}\left(K_k\left(\frac{\partial\omega}{\partial r}+\frac{\omega}{r}\right)+H_k+M_k\right)\right. \tag{7.28}$$

$$\left.+\sum_k\frac{\lambda_k c_k^2}{\Gamma_k}\left(\frac{\partial\omega}{\partial r}+\frac{\omega}{r}\right)-\cancel{\sum_k\frac{\alpha_k u\omega}{\Gamma_k}\left(\frac{\partial u}{\partial r}+\frac{\partial\omega}{\partial z}\right)-\sum_k\frac{\alpha_k}{\Gamma_k}\omega^2\frac{\partial\omega}{\partial r}}\right]. \tag{7.29}$$

The coefficients of the $\left(\frac{\partial\omega}{\partial r}+\frac{\omega}{r}\right)$ term reduce to

$$\begin{aligned}&\Gamma\sum_k\left[\frac{\alpha_k c^2}{\rho\Gamma_k}-\frac{c_k^2\rho_k\alpha_k}{\rho\Gamma_k}+\frac{\lambda_k c_k^2}{\Gamma_k}\right]\\&=\Gamma\sum_k\left[\frac{\alpha_k c^2}{\rho\Gamma_k}-\frac{c_k^2\rho_k\alpha_k}{\rho\Gamma_k}+\frac{\alpha_k\rho_k c_k^2}{\rho\Gamma_k}\right]\\&=\Gamma c^2\sum_k\frac{\alpha_k}{\Gamma_k}.\end{aligned}\tag{7.30}$$

Recalling that $\frac{1}{\Gamma}=\sum_k\frac{\alpha_k}{\Gamma_k}$, the coefficient of $\left(\frac{\partial\omega}{\partial r}+\frac{\omega}{r}\right)$ reduces to $c^2$.

The terms not associated with $\frac{\partial u}{\partial z}$ are now

$$c^2\left(\frac{\partial\omega}{\partial r}+\frac{\omega}{r}\right)+\Gamma\left[\sum_k\left(h_k-\frac{c_k^2}{\Gamma_k}\right)\dot{\lambda}_k+\sum_k\frac{c_k^2\rho_k}{\rho\Gamma_k}\left(H_k+M_k\right)\right],\tag{7.31}$$

so that

$$\boxed{\frac{du}{dz}=\frac{c^2\left(\frac{\partial\omega}{\partial r}+\frac{\omega}{r}\right)+\Gamma\left[\sum_k\left(h_k-\frac{c_k^2}{\Gamma_k}\right)\dot{\lambda}_k+\sum_k\frac{c_k^2\rho_k}{\rho\Gamma_k}\left(H_k+M_k\right)\right]}{c^2-u^2}},\tag{7.32}$$

where the heat transfer term can be expressed as

$$H_k=\left(\frac{Q_k\Gamma_k}{\rho_k c_k^2}-\alpha_k\frac{\rho c^2}{\rho_k c_k^2}\sum_j\frac{Q_j\Gamma_j}{\rho_j c_j^2}\right),\tag{7.33}$$

but is taken to be $H_k=0$ in this work.

Compared to the Chan-Kirby model, the most obvious advantage is that the augmented Euler-equation-based multiphase closure condition is no longer needed. Additionally, the mechanical equilibrium model introduces a mass transfer term which may give improved results.

There still remain two empirically determined parts of the Chan-Kirby model: locating the edge of the charge and the isobar curvature expression. The former of these will be explored in §7.4 and the latter will be investigated in the next section.

## 7.3. Isobar curvature

This section investigates the use of the empirical isobar curvature term in the radial divergence expression in the Chan-Kirby model equation (6.1). Comparisons between the empirical expression from [30], a new isobar expression and DNS solutions are made. Initial results show that the inclusion of the new isobar expression shows limited improvement. The iteration procedure, outlined in §6.1.2, that artificially increases the radius and flattens the shock front is then removed and the advantage of the new isobar expression is more obvious.

As outlined in §6.1.1, the isobar curvature describes the distribution of the pressure throughout the DDZ and how the curves of constant pressure, isobars, are shaped. These curves cannot be described a priori as the shape of the isobars is determined by the value of the pressure at each point and the pressure is described by the evolution of the variables.

An approximation for the shape of the isobars needs to be made to complete the system of equations that describe the flow variables. To calculate the isobar curvature at a point, the Chan-Kirby model uses an empirical constant $\beta$ with the isobar curvature at the shock front of that streamline, $C_s$, and the distance between the point and the shock front, $z$. In §6.1.1, in (6.8), the empirical expression was given as

$$C = C_s - \frac{2z}{(\beta R)^2}.$$

Figure 7.1 shows a parametric study on the use of a constant $\beta$ in the multiphase, mechanical equilibrium reduced ODE model, with 100 streamlines, compared to the DNS simulations of the same underlying model. It is clear that the correct choice for $\beta$ has a substantial effect on the results but the Chan-Kirby model takes $\beta = 0.5$ which from Figure 7.1 is clearly seen to be a poor fit to the two-phase polytropic explosive simulated. Chan & Kirby state that $\beta = 0.5$ gives the best fit for the range of explosives that were investigated in [30]. However, this range of explosives is limited and the shape of the isobars will change with each detonation velocity for each new explosive material. Since this would mean fitting a new $\beta$ for every new explosive, an alternative approach is needed.

Through examination of the isobar curvature expression, a new expression for the isobar curvature term in the radial divergence ODE is derived and implemented based on the curvature of an ellipse. The ammonium nitrate–based explosives EM120D and ANFO are used to illustrate any improvements via unconfined ratestick DNS results. The next section outlines the new elliptical expression.

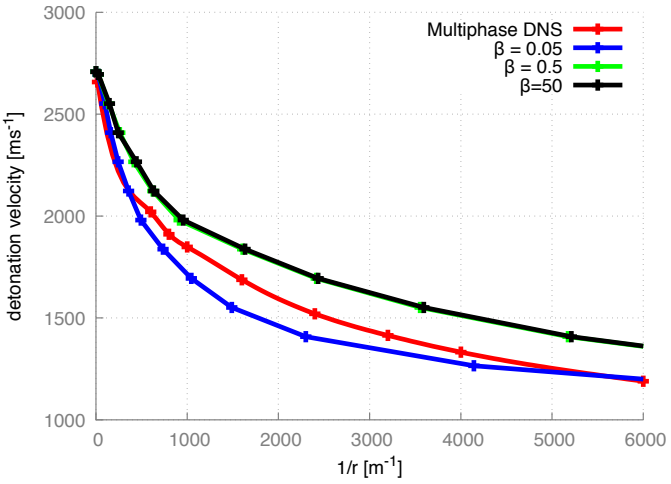


Figure 7.1.: Comparison of different $\beta$ with 100 streamlines for two-phase polytropic explosive with $\gamma = 1.4$ and $\gamma = 3.0$ and with (5.2) with the parameters given in Table 7.1. The diameter effect curves for $\beta = 0.5$ (green) and $\beta = 50$ (black) are very similar, despite there being two orders of magnitude difference. However, decreasing the value of $\beta$ by a factor of 10 made a large difference to the diameter effect curve but is a better fit to the DNS for most detonation velocities. This suggests that the isobar curvature has a substantial effect on the solution.

### 7.3.1. Elliptical isobar curvature

The shock front boundary conditions for the reduced ODE model are determined with use of the oblique shock relations to find expressions for density, $\rho_s$, and axial particle velocity, $u_s$, at the shock front. These oblique shock relations are then differentiated to determine values for the remaining variables: the conservation of momentum is used to determine the shock front isobar curvature $C_s$, the radial particle velocity is used to determine the flow divergence $\omega_{r,s}$, and the ratio of flow divergence and radial velocity is used to determine the constant $\chi_s$. This was shown in §6.1.1.

After the shock front, the isobar curvature $C$ is unknown but is needed in order to calculate the radial divergence, as discussed in §6.1.1. The equation used in the Chan-Kirby model is motivated by considering an isobar as a circular arc passing through the intersection of the isobar and the charge edge. Under this assumption, the isobar curvature can be obtained with simple geometry. It is a function of the location of the edge of the charge $(r_{\text{edge}}, z_{\text{sl,edge}})$ and the position the current point $(r, z)$ (see Figure 7.2 for detail).

$$C = \frac{1}{R} = \frac{2\left(z_{\text{sl,edge}} - z\right)}{r_{\text{edge}}^2 + \left(_{\text{sl,edge}} - z\right)^2}. \tag{7.34}$$

The radius of the charge, $r_{\text{edge}}$, can be approximated as

$$r_{\text{edge}} = R_{s,\text{edge}} \sin\theta, \tag{7.35}$$

where $R_{s,\text{edge}}$ is the radius of curvature of the shock front at the charge edge and $\theta$ is the angle between the incoming shock velocity vector $\mathbf{D}$ and the normal at the shock (see Figure 7.3).

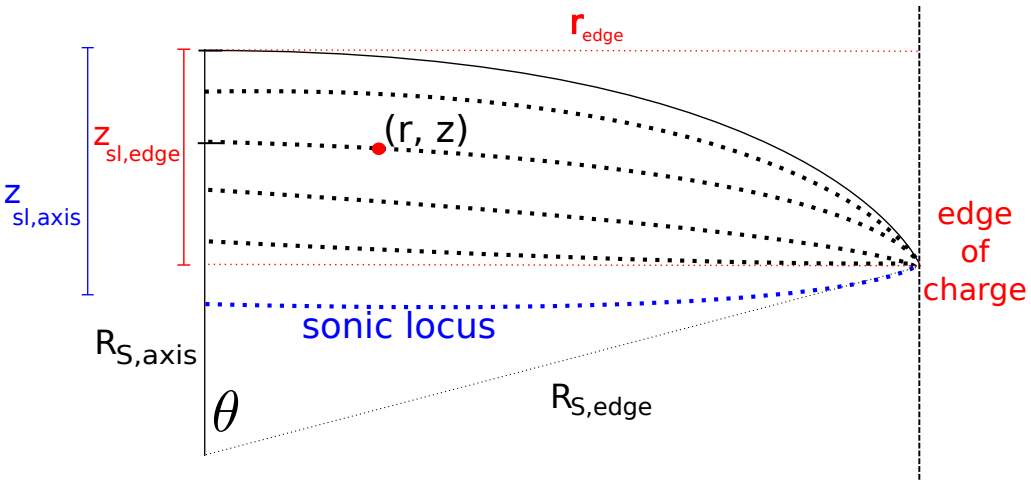


Figure 7.2.: Representation of the isobars in the DDZ and how the curvature at a point (indicated) on an isobar can be determined. Note that (7.34) assumes that the arc used to derive the expression is circular so $R_{\text{s,axis}} = R_{\text{s,edge}}$. This will not be the case for most explosives modelled.

Given that $r_{\text{edge}}$ is not known prior to a calculation, the Chan-Kirby model simplifies this equation by using the expression for the isobar curvature at the shock front:

$$C \approx C_s - 2z\left(\frac{1}{r_{\text{edge}}}\right)^2 = C_s - 2z\left(\frac{1}{\beta R_s}\right)^2, \tag{7.36}$$

where $\beta = \sin\theta$.

For numerical efficiency, the Chan-Kirby model takes $\beta$ to be an empirically determined constant. However, over a range of decreasing detonation velocities the value of $\theta$, and hence $\beta$, should decrease as the radius of the charge decreases. Furthermore, the curvature of an isobar at the edge of the charge will be greater than the curvature of the same isobar at a point closer to the axis due to the fact that the isobars are not circular. This is only partly taken into account with the inclusion of the radius of curvature of that streamline, $R_s$.

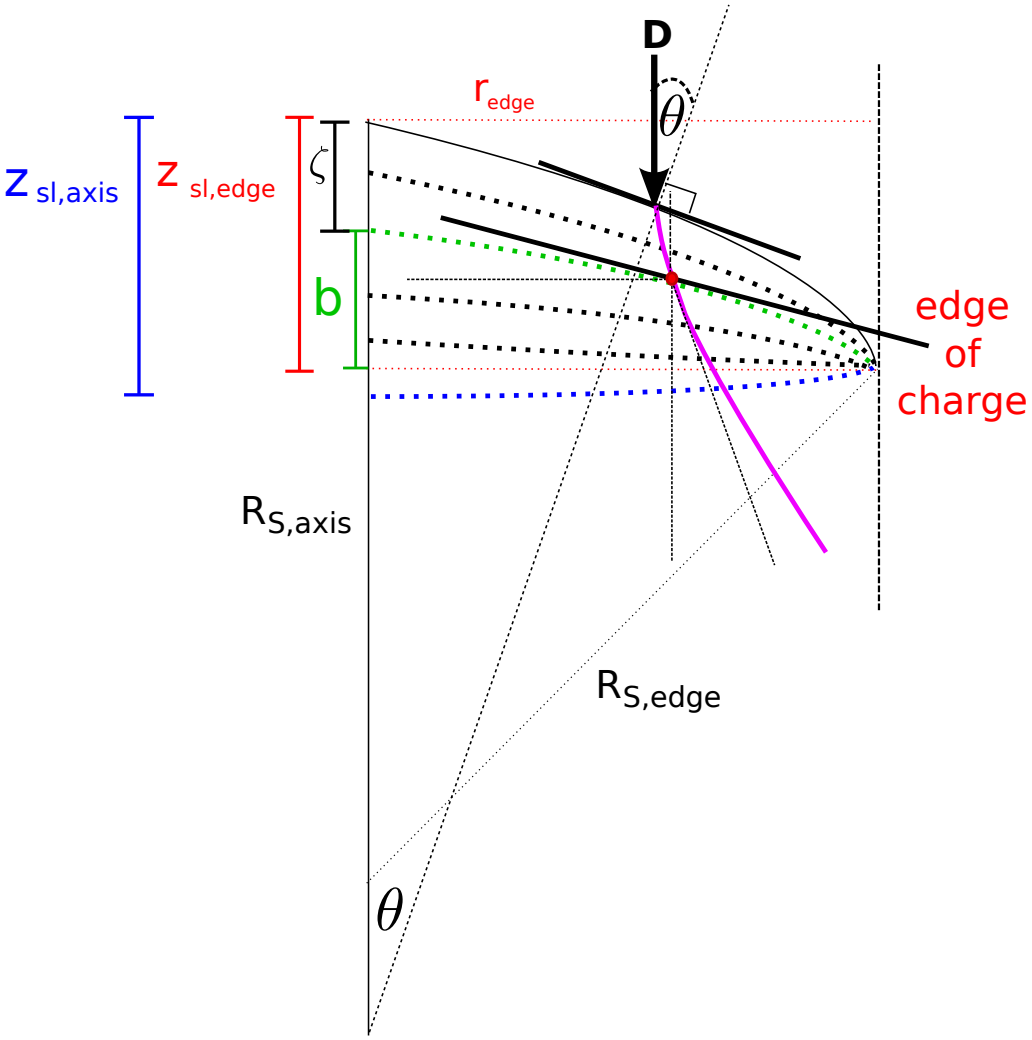


Figure 7.3.: A representation of the DDZ. The incoming detonation velocity vector, **D**, makes an angle $\theta$ with the normal to the shock. The streamline is deflected at each isobar. The red point illustrates how the streamline is deflected at the green isobar. This isobar is modelled as an ellipse with a semiminor axis of $b$.

An alternative to this empirical isobar curvature is found by approximating each isobar as an ellipse. The equation for an ellipse, centred at $(r_0, z_0)$ is

$$\frac{(r - r_0)^2}{a^2} + \frac{(z - z_0)^2}{b^2} = 1, \tag{7.37}$$

where $a$ is the semimajor axis and $b$ is the semiminor axis. For an isobar which starts on the axis at a distance of $\zeta$ behind the shock front, approximating it with an ellipse implies

$$\begin{aligned} a =& r_{\text{edge}}, \\ b =& z_{\text{sl,edge}} - \zeta, \\ (r_0, z_0) =& \left(0, -\left(\frac{z_{\text{sl,axis}} - \zeta}{2}\right)\right). \end{aligned}$$

The curvature of this ellipse is calculated with

$$C = \frac{\frac{d^2 z}{dr^2}}{\left(1 + \left(\frac{dz}{dr}\right)^2\right)^{\frac{3}{2}}}. \tag{7.38}$$

The advantage of this elliptical formulation is that, while there is assumption made about the shape of the isobars (ellipses), there is no longer a fitting parameter involved.

This new expression removes the empirical components of the previous expression used in the Chan-Kirby model. The assumptions made are that the isobars are elliptical and that the values for $r_{\text{edge}}$ and $z_{sl,\text{edge}}$ can be extrapolated from solutions of previous detonation velocities. It does need initial values for the first detonation velocity but large values taken for a detonation velocity close to the ideal detonation velocity suffice.

The use of an ellipse to model the DDZ is more physically reasonable than a circle but only for unconfined detonations. In strong confinement, the detonation driving zone can form a drastically different shape. This investigation shows that there are alternative motivations and forms for the isobar expression available. These new expressions may give better fits but, importantly, do not rely on an empirically derived constant that needs to be changed for each explosive.

The following sections look at validation of the elliptical isobar expression and then at results for the non-ideal explosives for which the constant $\beta$ expression that was developed. The values for the rate parameters of the explosives used in the simulations are given in Table 7.1. The reaction rate used for validation with the polytropic gas is that given by (5.2) and for the non-ideal explosives is (5.3).

| | Polytropic Validation | EM120D | ANFO |
|---|---|---|---|
| $n$ | 0.0 | 1.51 | 1.38 |
| $m$ | 0.5 | 0.667 | 0.667 |
| $p_H$ | 0.0 | 0.1 | 0.4 |
| $\tau_H$ | 1/2.0E6 | 22.0E-6 | 31.0E-6 |
| $\tau_S$ | - | 20.0E-6 | 60.0E-6 |
| $W_h$ | - | 0.95 | 0.7 |
| $N$ | - | 9.0 | 9.0 |

Table 7.1.: Parameters for reaction rates used in this study.

### 7.3.2. Validation

A simple two-phase detonation with 12 streamlines with each phase modelled as an ideal gas ($\gamma_u = 3.0$, $\gamma_r = 1.4$) is simulated to compare with several full DNS calculations. The new elliptical expression and the previous constant $\beta$ expression for the isobar curvature are used in separate simulations. The diameter effect curve resulting from these simulations illustrates the discrepancies between solving the governing PDEs, compared to the reduced ODE system of equations, as well as the difference between the two isobar curvature expressions.

The results of the comparison between the two ODE models with different isobar curvature expressions and the DNS calculations is shown in Figure 7.4. The ODE model underestimates the radius in both implementations due to the first order approximations in the reduction of the governing equations. It appears that the new elliptical expression does not provide an improvement to the previous empirical constant $\beta$ expression. For most of the detonation velocity range the difference between the different isobar curvature equations is very small, especially considering the very small radii involved. However, to see no improvement at all is surprising.

A convergence study is undertaken to see how the diameter effect curve, for each isobar curvature assumption, changes with an increasing number of streamlines, with more streamlines giving a more accurate representation of the underlying equations. This convergence study is shown in Figure 7.5 with the constant $\beta$ expression results at the left and the elliptical expression results on the right.

It is seen that although the constant $\beta$ isobar curvature expression gives a surprisingly good fit for 12 streamlines, the solution quickly diverges from the DNS results for 100 and 300 streamlines. This suggests that $\beta$ may have been fit in [30] using simulations with 12 streamlines.

The elliptical isobar expression appears to quickly converge to a solution that, although not exactly matching the DNS solution, is the same as the converged constant $\beta$ isobar expression, as shown in Figure 7.6.

The comparison illustrates that the only advantage of the newly imple-

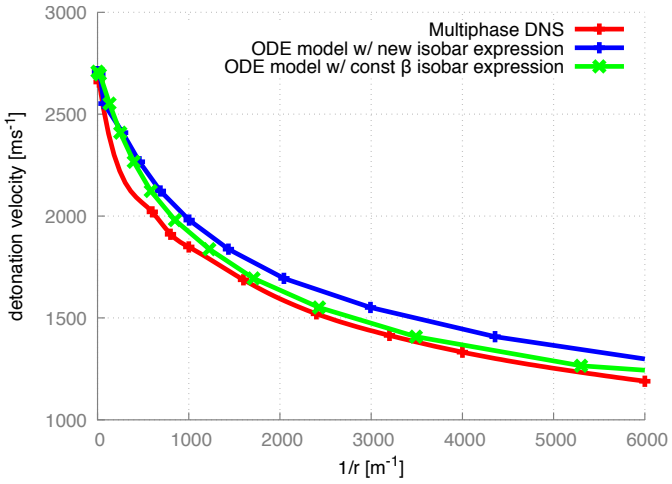


Figure 7.4.: Diameter effect for the multiphase mixture of two ideal materials with $\gamma_u = 3.0$ and $\gamma_r = 1.4$ with 12 streamlines, as used by Chan & Kirby in [30]. The green line shows the reduced ODE approach with the underlying mechanical equilibrium multiphase model with the empirical isobar curvature expression. The blue line shows the same model with the elliptical isobar curvature expression. The red line is a fit to DNS results. For the ideal gas, the elliptical isobar curvature diverges from the DNS solution more than the constant $\beta$ isobar curvature expression for lower detonation velocities. The constant $\beta$ expression is a surprisingly good fit.

mented elliptical isobar expression is that it converges to a solution with less streamlines so will be faster to solve. Figure 7.1 shows that there is some sensitivity in the model to changes in the isobar curvature. It can be concluded then that the constant $\beta$ expression, with an appropriately chosen $\beta$, is a reasonable approximation. Therefore, the only argument for use of the the elliptical expression is that it is not empirical and does not require the use of a parameter that can be changed to give a better fit.

Despite the convergence of both isobar curvature equations to the same diameter effect curve, there is still some discrepancy between the ODE approach and the DNS results. It could be argued that these discrepancies would be expected due to the first order approximations in the equations.

### 7.3.3. Results

The ammonium nitrate–based, non-ideal explosives EM120D and ANFO are simulated to compare the mechanical equilibrium multiphase ODE model with its parent PDE model. A full DNS calculation is used as a benchmark

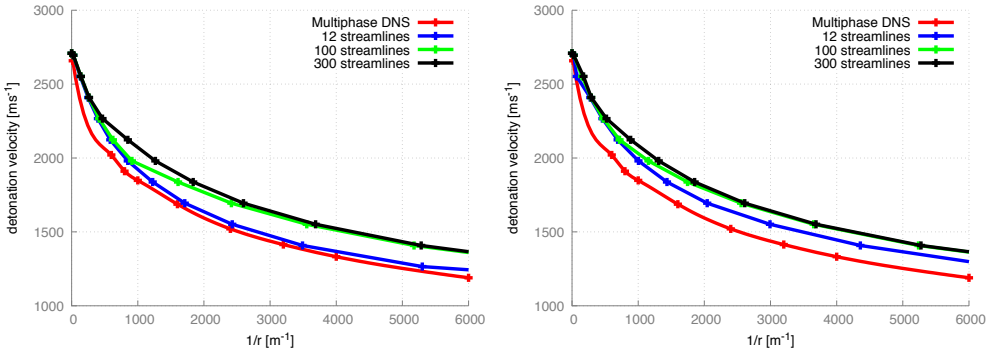


Figure 7.5.: Streamline convergence study for the constant $\beta$ isobar expression (left) and the elliptical isobar expression (right) for the multiphase mixture of two ideal materials with $\gamma_u = 3.0$ and $\gamma_r = 1.4$. Although the constant $\beta$ expression gives a closer fit for 12 streamlines, with more streamlines the solution diverges from the DNS results.

for the solution with the introduction of the first order approximations and empirical assumptions about the isobar curvature.

The emulsion EM120D is described by a linear Mie-Grüneisen equation of state for the condensed phase with air added as a void phase in the unreacted explosive. The reacted phase is modelled with the Williamsburg equation of state. A two-stage reaction rate is used, given by (5.3), that includes a sub-grid scale model for hotspot burning. The values for the parameters for the reaction rate and equations of state are given in Tables 4.2 and 7.1. The values for the initial volume fractions are given in Table 7.2.

| | ANFO | EM120D |
|---|---|---|
| $\alpha_{\text{unreacted}}$ | 0.495 | 0.864 |
| $\alpha_{\text{gas}}$ | $10^{-6}$ | $10^{-6}$ |
| $\alpha_{\text{void}}$ | $1 - (\alpha_{\text{unreacted}} + \alpha_{\text{gas}})$ | $1 - (\alpha_{\text{unreacted}} + \alpha_{\text{gas}})$ |

Table 7.2.: Values for initial volume fraction of the two non-ideal explosives ANFO and EM120D.

A comparison between the previous constant $\beta$ isobar expression and the new elliptical isobar expression is made in Figure 7.9 with the DNS and experimental results given for reference. The elliptical isobar expression gives a consistently better fit to the DNS results and experimental points for the full range of detonation velocities. The constant $\beta$ expression gives a comparable fit for the higher detonation velocities but crosses the DNS results and overestimates the radius for lower detonation velocities. This is due to the fact that the relationship between the detonation velocity and the length

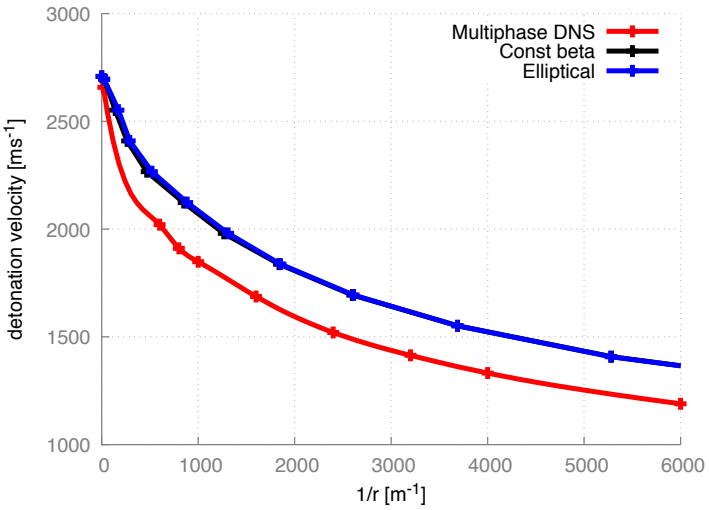


Figure 7.6.: Converged solutions (300 streamlines) for the constant $\beta$ isobar expression (black) and the elliptical isobar expression (blue) for the multiphase mixture of two ideal materials with $\gamma_u = 3.0$ and $\gamma_r = 1.4$. The solutions are almost identical.

of the detonation driving zone (DDZ) is non-linear. The constant $\beta$ isobar expression does not take this into account whereas the new formulation does.

The left-hand side of Figure 7.7 shows a contour plot for a single detonation velocity from the ODE model with the new isobar curvature expression. This is compared to DNS output shown on the right-hand side of Figure 7.7. Figure 7.8 shows contour plots for the same detonation velocity but the left-hand side illustrates the pressure contours obtained when the empirical constant $\beta$ expression for the isobar curvature is used. The empirical isobar curvature expression predicts a larger radius than the new expression but the underestimation of the DDZ and radius of curvature is similar for both expressions.

These contour plots illustrate that the ODE model is providing useful information about the physics of the problem but that it provides imperfect information about the geometry. That is, the values for the pressure are comparable throughout the DDZ but the length of the DDZ and the radius of the charge are underestimated by both implementations of the ODE model.

The DNS results highlight that an elliptical fit of the isobar curvature is only advantageous for part of the DDZ. Towards the sonic locus and the charge edge, the isobars show more complex behaviour as the curvature changes sign. This is overestimated when the elliptical isobar curvature expression is used and underestimated when the constant $\beta$ empirical expression for the isobar is used. Note that use of an elliptical expression for the isobars does not guarantee that the isobars will end up as ellipses; as mentioned previously, the expression for the isobar plays only a small role in the determination of

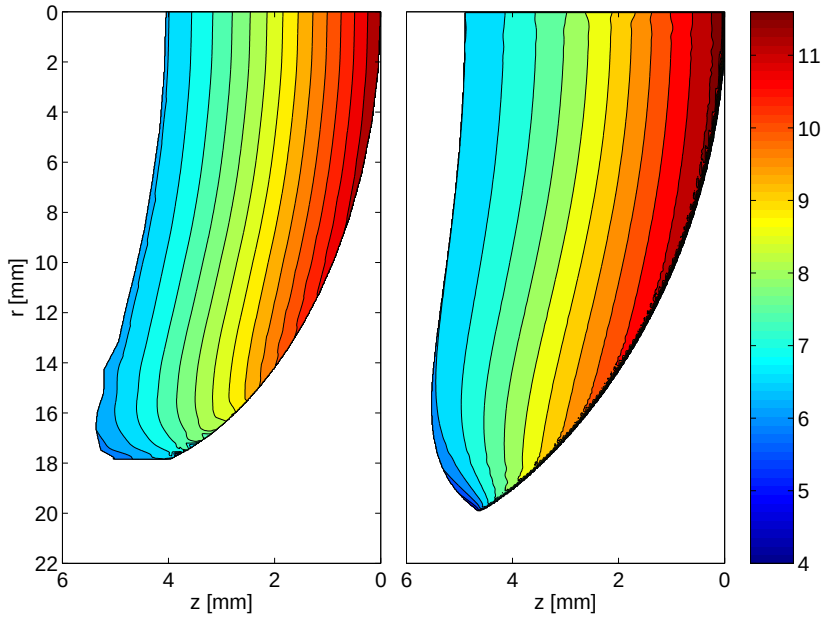


Figure 7.7.: Pressure [GPa] contour plot showing the isobars for EM120D for $D = 4920$ ms$^{-1}$ obtained using the ODE model with the elliptical isobar expression (left) and a DNS simulation (right).

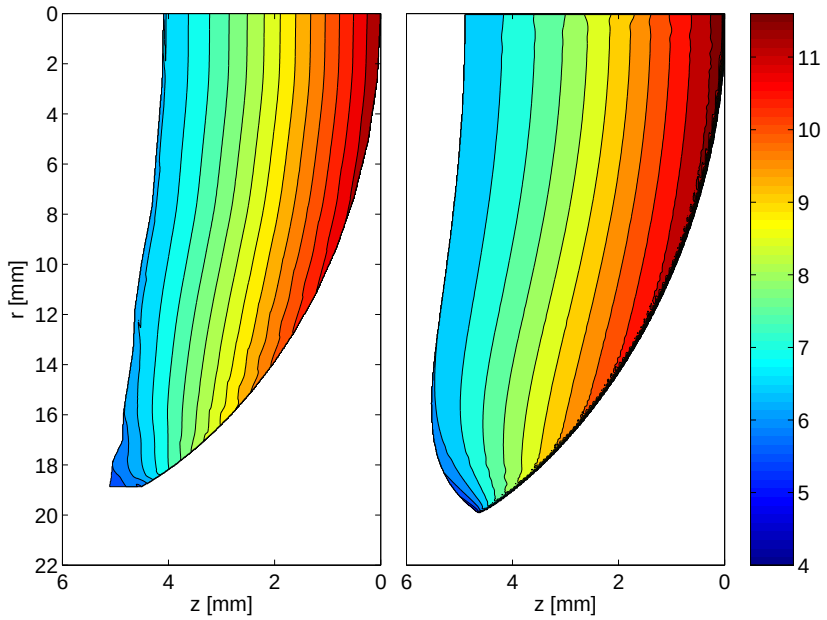


Figure 7.8.: Pressure [GPa] contour plot showing the isobars for EM120D for $D = 4920$ ms$^{-1}$ obtained using the ODE model with the empirical constant $\beta$ isobar expression (left) and a DNS simulation (right).

the flow variables.

The ODE implementations also show that there is a problem with the model at the charge edge. The irregularity in the sonic locus in this region illustrates that the model is not finding consistent solutions on the streamlines so the radius of curvature, which would typically decrease toward the edge, might increase from one streamline to the next so that the shooting problem can converge on a solution. This might be rectified with a more appropriate isobar curvature expression or it could be that the importance of the radial terms near the edge mean that the model, having neglected a lot of them, will not be able find appropriate solutions.

The flat edge on the DDZ of the ODE model results in 7.7 and 7.8 is caused by the algorithm stopping because the curvature of the shock has reached the predicted value for unconfined detonation of this explosive at this detonation velocity. However, as the model does not truly represent the flow in the DDZ, the shock front curves faster than expected and this value is reached before the correct radius is achieved.

Figure 7.9 illustrates the expected underestimation of the radius. With the use of a more general isobar curvature term it is clearer that this discrepancy is caused by the assumptions in the reduction of the equations and not in the empirical isobar curvature term.

All implementations still give detonation velocities within 10% of the DNS solution or experimental points. The empirical isobar curvature expression implementation underpredicts the failure diameter for EM120D although does find solutions up to the experimental points with a comparable failure diameter. The elliptical curvature expression maintains a comparable shape with respect to the experimental and DNS points and finds solutions up to and beyond these results. Although the results for the elliptical expression do have a slightly larger error, it is helpful to keep in mind that these differences in radius are small: 1/50 m compared to 1/60 m.

Similar results are seen for ANFO, as shown in Figure 7.10. The empirical constant $\beta$ expression again shows comparable results for the higher detonation velocities but crosses the experimental and DNS results for the lower detonation velocities. The elliptical expression again does not match the experimental and DNS results but does show the same shape and successfully predicts the failure diameter of the last experimental result. It also produces a smoother curve than the empirical $\beta$ scheme although the curve is still quite wavy. ANFO has a much smaller range of detonation velocities and diameters and so more points are taken in this smaller range. Furthermore, ANFO typically has shock fronts with more curvature than, say for example, EM120D. This means that using the Chan-Kirby model, which appears to overestimate the rate at which the shock front curves due to the neglected radial terms, for ANFO could produce more inconsistent results.

Figure 7.11 shows a comparison of the DDZ and the pressure distribution for the empirical isobar expression and the elliptical expression for both ANFO

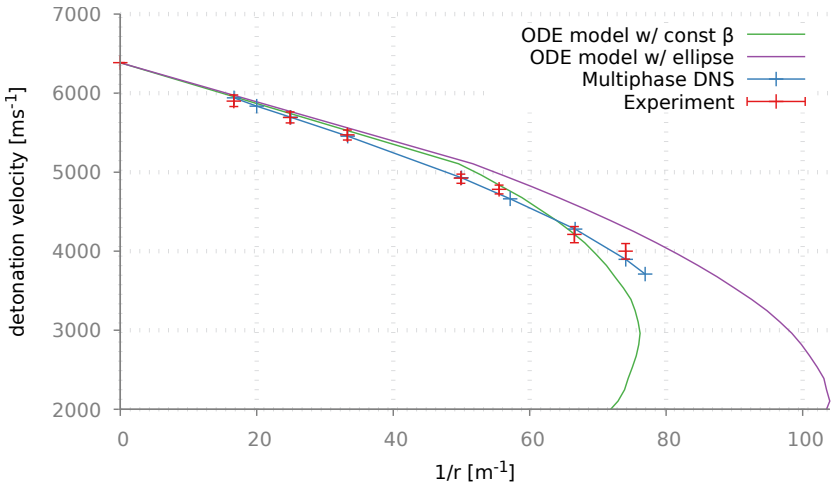


Figure 7.9.: Diameter effect curve for EM120D with different approaches to estimating the isobar curvature with 100 streamlines. Comparison is made to DNS results (blue cross), the fitted curve from these DNS points (blue line) and experimental points (red cross). The green line shows the reduced ODE approach with the empirical expression for the isobar curvature and the purple line shows the result with the new expression. Below $D = 2000$ $\mathrm{ms}^{-1}$ more solutions are obtained but they are ignored since they are outside the range of interest and would fail to detonate in reality.

and EM120D at two different detonation velocities. Both show reasonable pressure distribution despite the underestimation of the radius and DDZ length in all cases. It could be argued that the constant empirical expression gives better results for EM120D but as it was fit to this explosive this is to be expected.

Given these results, it is hard to argue that the elliptical expression gives better results than the previously used empirical expression. However, any reduction in the number of fit parameters always makes a model more robust and applicable to a wider range of explosives. The elliptical expression also converges with fewer streamlines so an accurate representation of the underlying equations is more quickly obtained.

The generalisation of the ODE model to include a less empirical expression for isobar curvature also provides a more robust basis for investigation of the effect of the reduction of the PDEs to ODEs. It is given that the previously used constant $\beta$ expression was fitted to the emulsion with the use of a small number of streamlines. As the number of streamlines are increased or when the empirical expression is changed, there remains a discrepancy in the diameter effect curve between the ODE model and the DNS solution.

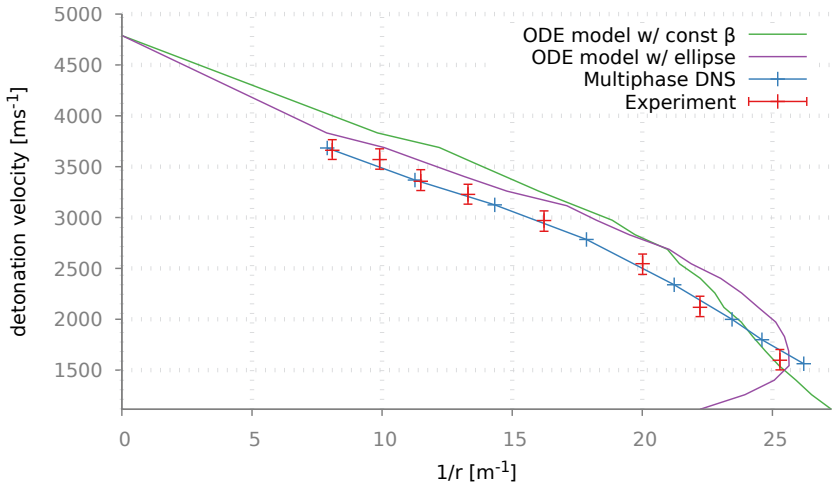


Figure 7.10.: Diameter effect curve for ANFO with different approaches to estimating the isobar curvature with 100 streamlines. Comparison is made to DNS results (blue cross), the fitted curve from these DNS points (blue line) and experimental points (red cross). The green line shows the reduced ODE approach with the empirical expression for the isobar curvature and the purple line shows the result with the new expression.

All of these simulations assumed that at the edge of the charge the slope of the shock front was identical for all detonation velocities for all materials. While this is true of the ideal gas, it is not true of any realistic non-ideal explosive model. To more accurately model the slope of the shock front at the charge edge, and hence the location of the edge of the charge, the explosive-confiner interaction at the charge edge must be simulated. The next section looks at using shock polar analysis combined with multimaterial shock theory to develop and investigate the effect of including this explosive-confiner interaction in the Chan-Kirby model.

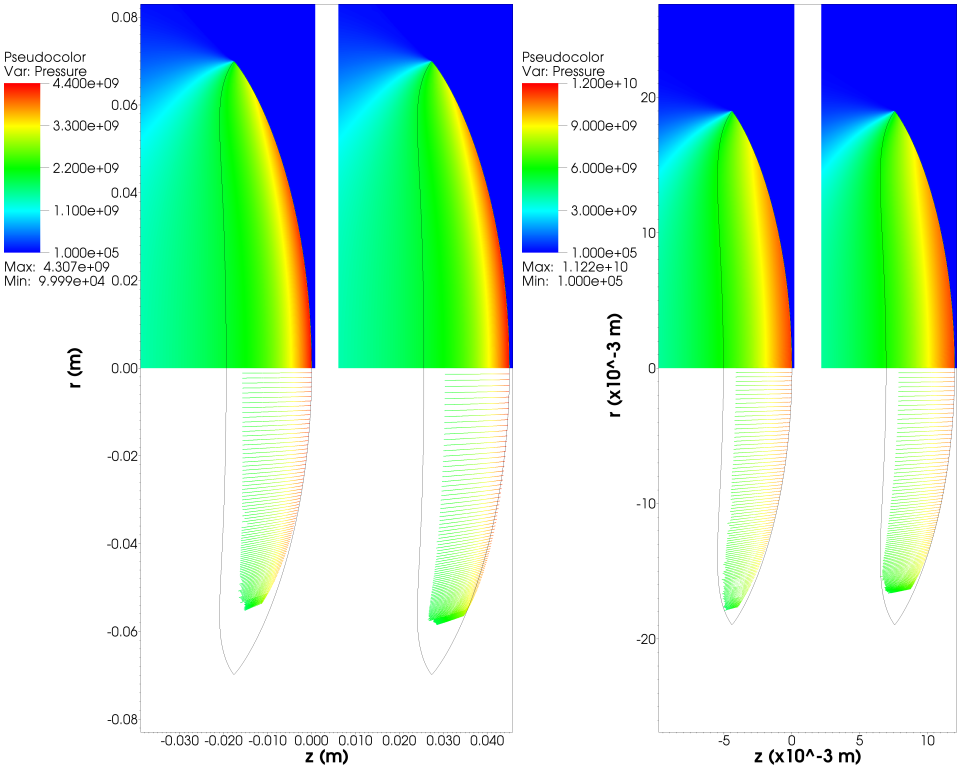


Figure 7.11.: Comparison between the pressure in the DDZ of the DNS solution (above) and the multiphase Chan-Kirby model (below) with the constant isobar approximation (1st & 3rd) and the new elliptical expression (2nd & 4th). Both ANFO at $D = 3116$ ms$^{-1}$ (left) and EM120D at $D = 4800$ ms$^{-1}$ (right) are shown.

## 7.4. Determining the charge edge

The Chan-Kirby model uses a constant, approximate value for the maximum incoming shock angle for all explosives and detonation velocities. Therefore, even assuming all other approximations in the model to be negligible, the value for the location of the edge of the charge is inaccurate. As the relationship between the size of the charge and the detonation velocity is of interest as an output, it is of benefit to develop a better understanding of how the maximum incoming shock angle affects the diameter effect and the DDZ profile. To do this, a theoretical maximum incoming shock angle is obtained via shock polar analysis and results with the new maximum are compared to results with the constant approximate value.

To obtain the relevant information about the charge edge, the pressure and flow deflection immediately behind the leading shock must be matched at the interface separating the explosive and the confiner. Shock polar analysis provides a description of the local interaction of detonation products with the confiner for a given detonation speed, $D$.

This section outlines how shock polar analysis, coupled with the mechanical equilibrium multiphase model, is used to determine the edge for porous non-ideal heterogeneous explosives under different confinement conditions for specific detonation velocities. This theory will then be used in later chapters as an input into streamline simulations of the detonation driving zone.

### 7.4.1. Shock polar analysis

A shock polar relates the postshock pressure $p$ of a material with the streamline deflection $\phi$, caused by an oblique shock, parameterised by the incoming shock angle $\theta$. Oblique shock theory is used as part of shock polar analysis to determine the flow conditions immediately behind the leading shock. An overview of shock polar theory is given in Appendix B and a related discussion on characteristic curves is found in Appendix C.

Initially, the focus for this work is using shock polar analysis to determine the conditions at the charge edge for unconfined charges. However, there are several types of interaction between confiner and explosive, and only some of these can use shock polar analysis to determine information about the charge edge. To gain an understanding of how shock polar analysis is used in confinement, some of these typical types of interactions between confiner and explosive are explored and will be discussed again when confinement is introduced in §8.3.

Below is a discussion of different types of confinement. It may be helpful for the reader to refer to the following section on the ideal gas case, and in particular Figures 7.13a - 7.13f, to gain more insight into what these types of confinement imply for shock polars.

### Weak or no confinement

For no confinement or sufficiently weak confinement, the streamline deflection in the explosive can exceed that obtained from oblique shock theory. Under these conditions, an intervening Prandtl-Meyer fan, centred at the sonic point at the charge edge, allows the streamline angle to increase further and pressure to drop to a match point on the shock polar of the confiner, typically at a very low pressure compared to the shock pressure of the explosive. This type of confinement is seen for any high explosive in most confinements, ranging from air to copper, and for non-ideal explosives in thin paper cylinders or air.

### Strong (classic) confinement

For the classic strong confinement case, a lead shock in the explosive is transmitted into the confining inert material. There is a subsonic region behind the detonation shock and a supersonic region behind the inert shock. This means that the two shock polars will meet at a point on the upper, strong shock branch of the explosive's shock polar and the lower, weak shock branch of the confiner's shock polar. There will be no reflected wave travelling back into the explosive so this is typical of confiners such as steel at large thicknesses.

The two cases of weak and strong confinement are used in this work via shock polar analysis and it has been shown that this gives a good representation of these types of explosive-confiner interaction [9].

There are also many types of interaction that cannot be explored. In this work, the assumption is made that the interactions between confiner and explosive will not include reflected shocks, 'stiff' confinement and 'unsteady' confinement. These types of confinements are briefly outlined below. For more discussion on interactions of inert confiners with explosives see [72].

### Reflected shocks in finite confinement

Reflected shocks occur if a shock wave is driven from the explosive into finite confinement and is then reflected from the free outer boundary. This reflected wave then induces alternating tension and compression regions within the confining material, which in turn induces pressure waves into the explosive. This effect, known as ringing, can affect the DDZ and hence the propagation of detonation. For more information on EM120D and ANFO in this type of confinement see [65, 72].

**Stiff confinement**

Stiff confiners have an ambient sound speed lower than the detonation speed of the explosive ($c_0 < D$) so that the only possible match in the $p - \theta$ plane is a Prandtl-Meyer expansion fan in the confiner [6, 65]. The key feature is that the confiner drives a low-pressure shock, via the expansion fan, into the explosive which can cause negative streamline deflection and hence a locally concave shock front (this does not occur in weak confinement). Military explosives confined by light metals with high sound speeds [6] or ANFO confined by kimberlite [71] are both considered stiff confinement interactions. Stiff confiners are still classed as high sound speed confiners.

Given that Prandtl-Meyer expansion fans are used in weakly confined cases, the use of it here in the confiner is not outside the scope of shock polar theory. However, the Chan-Kirby model assumes that the shock front is convex and this type of explosive-confiner interaction is not currently able to be modelled. It could, however, be a possibility in the straight streamline approach.

**Unsteady confinement**

Another explosive-confiner interaction is the case of 'unsteady' confinement. This occurs when the ambient sound speed in the confiner is greater than the detonation velocity of the explosive ($c_0 > D$). An acoustic wave will then propagate in the inert confiner faster than the detonation in the explosive. This implies that the flow in the confiner becomes subsonic and there will be no shock in the confiner and hence a shock polar analysis between the two materials is impossible [6]. This could, however, occur in mining operations; for example, when ANFO is confined by hard rocks such as granite [71].

There are further cases of explosive-confiner interactions; for example, when there are two or more matches on a shock polar. Aslam & Bdzil [9] showed that in some instances these corresponded to different solutions depending on the thickness of the confining material. However, this has only been shown for a single-phase polytropic example for both materials, and it is unclear if it applies to a greater range of examples. These homogeneous test cases are replicated below to illustrate the different types of confinement. The later parts in this section then extend shock polar theory to heterogeneous explosives.

## 7.4.2. Homogeneous materials

Most shock polar analysis found in supporting literature is for homogeneous materials. The case for the ideal (polytropic) gas is the example used most

often to illustrate oblique shock theory in textbooks. In research papers it is also the material used most frequently to illustrate different confining effects using shock polar analysis, probably due to the simplicity of the equations. The following section will outline these simple equations and reproduce some shock polar plots for comparison with published explosive-confiner investigations for an ideal gas.

The ideal gas equation of state is often used to model materials that are far from ideal. For example, by simply increasing the initial density and the adiabatic constant $\gamma$, it is often hoped that these changes will be sufficient to model solids or liquids. While using the polytropic equation of state is a good starting point because it is straightforward to solve, it does not capture the properties of non-gaseous materials adequately, especially if that material is actually heterogeneous. Despite this, the use of other equations of state in shock polar analysis is not common. Modelling a material as a heterogeneous material is even more uncommon, especially for unconfined shock polar analysis where an intervening expansion fan needs to be calculated to obtain a solution. A theory to approximate this behaviour is introduced and investigated in §7.4.3.

### Ideal gas (polytropic) equation of state

The nature of the ideal gas equation of state makes it very easy to work with. The flow variables conveniently cancel out of most equations and so equations for the postshock flow in terms of just the upstream flow conditions and the incoming shock angle are readily obtained. In the next section, the general equations from Appendix B are simplified with the specification of an ideal gas equation of state.

### Shock deflection angle in an ideal gas

Substituting the unreactive ideal gas equation of state,

$$e = \frac{p}{\rho(\gamma - 1)},$$

into Bernoulli's equation gives

$$\left(\frac{\gamma}{\gamma - 1}\right)\frac{p}{\rho} + \frac{1}{2}u^2 = \text{const} = k.$$

Given that the speed of sound in an ideal gas is $c^2 = \dfrac{p\gamma}{\rho}$ this becomes

$$\frac{c^2}{\gamma - 1} + \frac{1}{2}u^2 = k.$$

Since the Mach number is defined as $M = \frac{u}{c}$, this can be written as

$$\frac{1}{(\gamma-1)M^2} + \frac{1}{2} = \frac{k}{u^2}.$$

Differentiating,

$$\begin{aligned}\frac{-2}{(\gamma-1)M^3}dM &= \frac{-2k}{u^3}du \\ &= \frac{-2du}{u}\left(\frac{1}{(\gamma-1)M^2} + \frac{1}{2}\right).\end{aligned}$$

Assuming that $\theta = 0$ when $M = 1$, this can be manipulated into the Prandtl-Meyer function (B.4) and then integrated to obtain an expression for the shock deflection angle:

$$\theta = \left(\frac{\gamma+1}{\gamma-1}\right)^{\frac{1}{2}} \arctan\left(\left(\frac{\gamma-1}{\gamma+1}(M^2-1)\right)^{\frac{1}{2}}\right) - \arctan(M^2-1)^{\frac{1}{2}}.$$

The relationship between the deflection angle and the other variables is greatly simplified and reduces down to a relationship between the deflection angle $\phi$, the incoming shock angle $\theta$, and the upstream Mach number $M_0$.

The $\phi$–$\theta$–$M$ relationship is shown in Figure 7.12 to highlight how the deflection angle changes with the shock angle for different $M_0$. Two different choices for $\gamma$ are shown to highlight the changes in the behaviour of the $\phi$–$\theta$–$M$ relationship.

### Shock polar analysis for homogeneous polytropic materials

Since the derivations for the flow variables are found in most books on supersonic flow or shock waves (for example, [10]), they have not been reproduced here. However, the ideal gas case is still illustrative to investigate for two reasons. Firstly, it validates that the algorithm is working correctly since there is a plethora of examples of shock polars and expansion fans to compare against for the ideal gas equation of state. Secondly, since solutions for the flow variables and the deflection angle can be obtained algebraically the algorithm does not rely on (often) sensitive root finding algorithms. This means that we can look at a variety of explosive-confiner interactions without having to worry about the reliability of the solution from the root finding algorithms.

A first approximation for modelling a homogeneous condensed explosive is to model it as a 'heavy' gas; that is, as an ideal gas with $\gamma_u = 3.0$. This is done to explore a range of explosive-confiner interactions using shock polar analysis and the results are shown in Figures 7.13a to 7.13f.

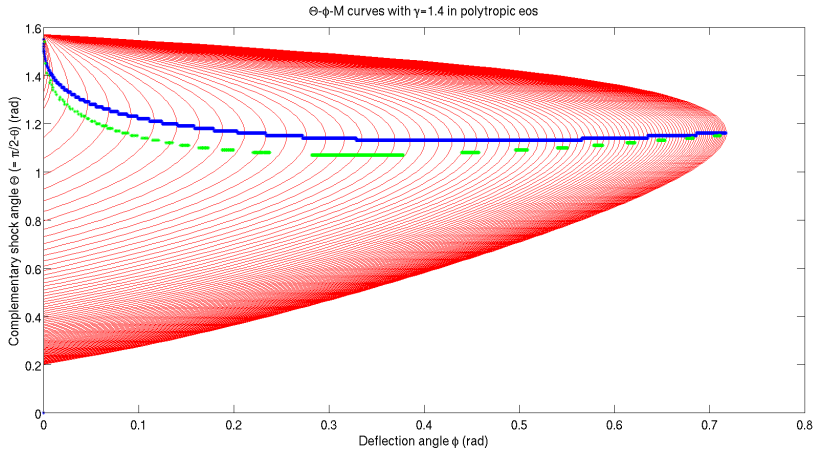


(a)

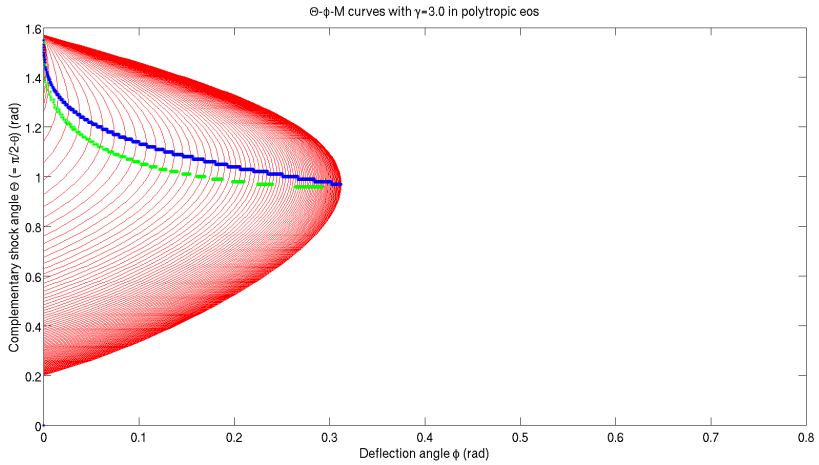


(b)

Figure 7.12.: The relationship between the incoming shock angle $\theta$ and the shock deflection $\phi$ are shown in red for a range of Mach numbers ($M_0 = 1.01$ to 5.0). The maximum $\theta$ obtained for each $M_0$ is shown in blue so that solutions above the blue line are strong shock solutions and solutions below are weak shock solutions. The green line corresponds to $M_s = 1.0$. These plots are for a polytropic equation of state with (a) $\gamma = 1.4$ and (b) $\gamma = 3.0$.

If both $\gamma_{\text{inert}}$ and $\rho_{0,\text{inert}}$ are increased substantially the confiner can change from weak, as shown in Figure 7.13a with $\gamma_{\text{inert}} = 1.4$ and $\rho_{0,\text{inert}} = 2000$ kgm$^{-3}$, to strong, as shown in Figure 7.13b with $\gamma_{\text{inert}} = 7.0$ and $\rho_{0,\text{inert}} = 9000$ kgm$^{-3}$. In the case of weak confinement, the only intersection is via the intervening Prandtl-Meyer expansion fan from the explosive. For strong confinement, there is a match on the subsonic branch of the explosive and supersonic branch of the inert confiner.

For more moderate values of $\gamma_{\text{inert}}$ or $\rho_{0,\text{inert}}$, we see different interactions. Confinement modelled by $\gamma_{\text{inert}} = 2.0$ and $\rho_{0,\text{inert}} = 1465$ kgm$^{-3}$ in Figure 7.13c gives two possible explosive-confiner matches: one on the subsonic branch (strong) and one via an expansion fan (weak). This was shown in [9] to correspond to two different situations: finite and infinite confinement. Somewhat counter-intuitively, the strong solution corresponds to finite confinement when the confinement is thin enough that there is a subsonic region behind both detonation and inert shock. The weak solution corresponds to both infinite and thick confinement when the confinement is thick enough that the subsonic flow behind the detonation front is surrounded by supersonic flow in the confiner.

Lowering the density to $\rho_{0,\text{inert}} = 500$ kgm$^{-3}$ gives three possible explosive-confiner interactions, all weak, as shown in Figure 7.13d. Increasing $\gamma_{\text{inert}}$ to 4.0 and $\rho_{0,\text{inert}} = 1000$ kgm$^{-3}$ gives an explosive-confiner match only on the supersonic branch of the explosive, as shown in Figure 7.13e. A further increase in $\gamma_{\text{inert}}$ to 4.0 with an increase in initial density to $\rho_{0,\text{inert}} = 3000$ kgm$^{-3}$ gives no match at all, as shown in Figure 7.13f. If the ambient sound speed in the confiner is less than the detonation velocity then this latter case would represent stiff confinement.

Although using an ideal gas equation of state to model the explosive is a good initial approximation, more complex equations of state are preferable. The most interesting, and realistic, form for shock polar analysis for a non-ideal explosive is a multimaterial analysis that includes the porous nature of the non-ideal explosive by coupling a realistic equation of state, like the linear Mie-Grüneisen (LMG) equation of state, for the condensed phase of the explosive to another equation of state for the void phase of the explosive. These two equations of state are coupled via a multimaterial model such as the mechanical equilibrium model. This is explored in the next section on inhomogeneous materials.

### 7.4.3. Inhomogeneous materials

A better representation of the porous, inhomogeneous characteristics of non-ideal explosives is obtained from the inclusion of inert materials, such as gas bubbles. These inert materials, despite only making up a small fraction of the volume, can have a distinct effect on the initiation and propagation of a detonation wave [76].

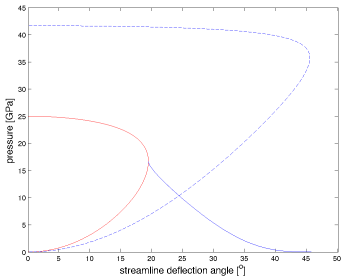


(a) Weak confinement: $\gamma_{\text{inert}} = 1.4$, $\rho_{0,\text{inert}} = 2000$ kgm$^{-3}$.

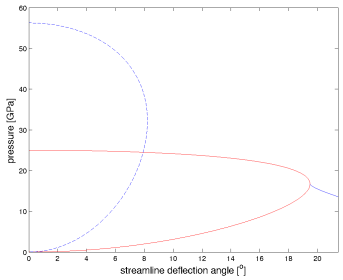


(b) Strong confinement: $\gamma_{\text{inert}} = 7.0$, $\rho_{0,\text{inert}} = 9000$ kgm$^{-3}$.

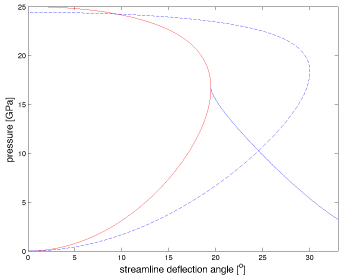


(c) Two possible matches: $\gamma_{\text{inert}} = 2.0$, $\rho_{0,\text{inert}} = 1465$ kgm$^{-3}$.

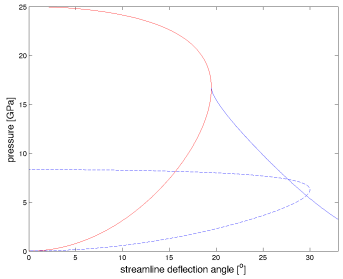


(d) Three possible weak matches: $\gamma_{\text{inert}} = 2.0$, $\rho_{0,\text{inert}} = 500$ kgm$^{-3}$.

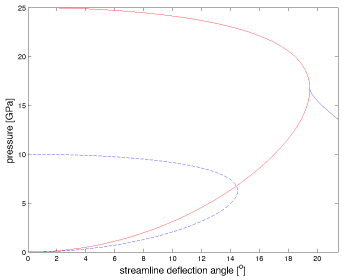


(e) Supersonic match: $\gamma_{\text{inert}} = 4.0$, $\rho_{0,\text{inert}} = 1000$ kgm$^{-3}$.

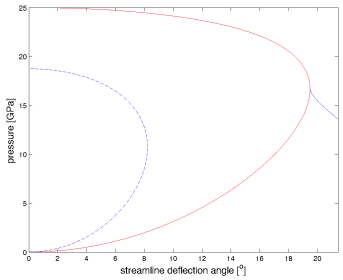


(f) No match: $\gamma_{\text{inert}} = 7.0$, $\rho_{0,\text{inert}} = 3000$ kgm$^{-3}$.

Figure 7.13.: An ideal explosive (solid lines) with $\gamma_u = 3.0$ and $\rho_{0,\text{u}} = 2000$ kgm$^{-3}$ is simulated under different types of confinement (dashed lines) to illustrate the different explosive-confiner interactions.

The non-ideal explosives explored in this work are all inhomogeneous. The unreacted explosives will be modelled with two different equations of state: for the homogeneous condensed material a linear Mie-Grüneisen (LMG) equation of state is used and for the inclusion of inert air bubbles a polytropic equation of state is used. This explosive is then confined with a single, homogeneous inert material.

The condensed and inert components that make up the unreacted explosive need to be modelled in a way that captures the behaviour of these two components as the shock wave moves over the porous material. As a shock wave passes, the material is compressed and the gas bubbles collapse. This causes the substance in the bubbles (normally air) to heat up, often to very high temperatures, which then heats the surrounding material. The gas inside the bubble then rapidly cools, causing further volume decrease of the material [76].

This process is an important mechanism in the reaction and detonation processes and needs to be included for realistic non-ideal detonation modelling. However, since the inert material often makes up only a small fraction of the unreacted explosive material, and is randomly distributed throughout the material, resolving each gas bubble individually is computationally expensive and infeasible.

Throughout the late 1960s and early 1970s, Afanasenkov et al. [1, 76] developed a theory for approximating a generalised Hugoniot of condensed substances using as few of the initial state parameters as possible. This theory included a generalised Hugoniot for heterogeneous materials (mixtures of two solids where each component is present in the form of small particles), solutions (a mixture of two mutually soluble liquids modelled as a homogeneous system with molecular mixing of the components) and porous materials (liquid containing air bubbles or a powder).

Another alternative is to use the multiphase Rankine-Hugoniot relations from the underlying mechanical equilibrium model used to simulate the detonation process. These were formulated by Saurel et al. [64] and showed excellent agreement with experimental data for a range of mixtures of high density materials using a stiffened gas equation of state.

In the following sections the generalised Afanasenkov theory for porous substances is outlined. Hugoniots for the two porous explosives of interest are simulated using the mixture rules from the mechanical equilibrium model. The Rankine-Hugoniot relations for the mechanical equilibrium model are outlined and are then implemented for the same two explosives. The results in [64] are extended by application to a low density material with gaseous voids. The LMG equation of state is used to model the first material instead of the over-simplified stiffened gas equation of state.

### Afanasenkov theory for generalised Hugoniots of porous substances

A shock Hugoniot of a non-porous mixture of two substances (liquid or solid) can be constructed if the pressure in both components at the wave front is the same ($p = p_0 = p_s$) and, at a given pressure, the specific volume of each component satisfies the equation of its shock Hugoniot, or there is no heat transfer between the components.

For pressed or liquid explosives, Afanasenkov et al. [2] surmised that the pressure in the detonation wave is equalised two orders of magnitude more slowly than the temperature and concluded that for liquid explosives with a mean particle size $\mu < 0.05$mm, it is reasonable to assume pressure equilibrium but not reasonable to assume temperature equilibrium between the components. Not only is this then the base for the following theory for generalised Hugoniots for shock polar analysis for mixtures, it also reiterates the justification for moving away from the isentropic or temperature equilibrium closure conditions in Euler-based models for the streamline simulation of detonation propagation for mixtures.

The mechanical equilibrium model describes the total specific volume, $v$, of a mixture which can then be applied to a condensed explosive and an inert gas,

$$v = \lambda v_c + (1 - \lambda)\, v_g, \tag{7.39}$$

where $\lambda$ is the mass fraction of condensed explosive, $v_c$ is the specific volume of the condensed material and $v_g$ is the specific volume of the gaseous material. This expression is valid both before and after the shock since the mass fraction does not change across the shock.

The mass fraction is not known initially and must be calculated. However, the total volume of the mixed material, the volume of the condensed material and the volume of the voids are all known. From this we can calculate the volume fraction of the condensed material,

$$\alpha = \frac{v_{c,0}}{v_0},$$

and hence the total density as a function of the volume fraction,

$$\rho_0 = \frac{\alpha}{v_{c,0}} + \frac{1 - \alpha}{v_{g,0}}.$$

This expression cannot be used since the volume fraction changes across the shock. Therefore, the mass fraction is calculated,

$$\lambda = \frac{\alpha}{v_{c,0}\rho_0},$$

to be used in (7.39). These latter two expressions follow from the mixture conditions for the mechanical equilibrium model.

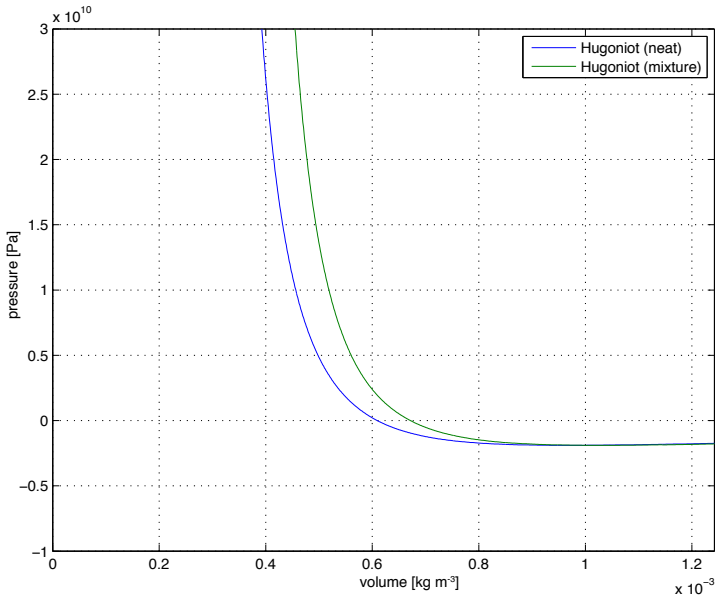


Figure 7.14.: Hugoniots for the neat ANFO and the porous ANFO with added voids with $\alpha_{\text{condensed}} = 0.4905$. The Hugoniot for the porous ANFO is calculated using Afanasenkov theory. The neat ANFO is modelled using LMG equation of state.

The final parameter to be determined is how the volume of the voids changes across the shock. It is assumed that the homogeneous, condensed explosive of the porous material is compressed as it would be if it was a single, homogeneous substance. As the shock moves through the material, the voids in the condensed explosive are then compressed by an experimentally measured, constant factor. According to Afanasenkov theory [1], the shocked gas volume is given by

$$v_g = \frac{\gamma - 1}{\gamma + 1} v_{g,0},$$

where $\gamma = C_p/C_v$ for the gaseous void.

An illustration of how the Hugoniot of the condensed, pure material compares with the Afanasenkov Hugoniot of a porous version of the material is shown in Figure 7.14. Neat ANFO and porous ANFO are compared with parameters taken from Tables 4.3 and 4.2 and with $\alpha_{\text{condensed}} = 0.4905$. It is seen that for very low pressure (equating to low detonation velocities), Afanasenkov theory predicts that the Hugoniot will remain very close to the Hugoniot of the neat, condensed material. It is only when the pressure is increased that the effect of the voids is apparent. After a certain threshold pressure, the effect of the voids is relatively constant.

**Multiphase Rankine-Hugoniot relations**

The multiphase mechanical equilibrium Rankine-Hugoniot relations were formulated by Saurel et al. [64] and describe the postshock state variables in terms of the initial state variables. Heat transfers in the shock layer are assumed negligible. The relations are similar to the normal Rankine-Hugoniot shock relations but with additional equations to describe the state of each material. For $k$ materials the shock relations are [64]:

$$\begin{aligned} \lambda_k &= \lambda_{0,k}, \\ \rho\,(u - D) &= \rho_0\,(u_0 - D) = m, \\ p - p_0 + m^2\,(v - v_0) &= 0, \\ e - e_0 + \frac{p + p_0}{2}\,(v - v_0) &= 0, \\ e_k - e_{0,k} + \frac{p + p_0}{2}\,(v_k - v_{0,k}) &= 0, \end{aligned}$$

where the mixture internal energy is defined by $e = \sum_k \lambda_k e_k$, the mixture specific volume is defined by

$$v = \sum_k \lambda_k v_k, \tag{7.40}$$

the mass fraction is given by $\lambda_k = \dfrac{\alpha_k \rho_k}{\rho}$, the saturation constraint is $\sum_k \alpha_k = 1$ and the mixture mass conservation is given by $\sum_k \lambda_k = 1$. These are the same equations are those outlined in 7.1. Note that the mass fraction $\lambda_k$ does not change over the shock but the volume fraction $\alpha_k$ does. These latter expressions close the system of equations and allow for the shocked state variables to be calculated from the initial state variables. However, the calculation itself is not as straightforward as it may seem.

The results of [64] show excellent agreement with experimental data for a range of mixtures. However, all of the materials illustrated are high density materials and are modelled using a stiffened gas equation of state with well-behaved Hugoniots. Furthermore, the shocked state variables are obtained by assuming that the shocked state pressure is given. For full CFD simulations this is a practical assumption. For streamline or shock polar simulations this assumption is also fine as long as the equation of state is simple enough to be easily rearranged so that the volume of each material on its Hugoniot can be expressed as a function of pressure. However, for more complicated equations of state this becomes impractical.

Ideally, the postshock pressure needs to be obtained for a range of volumes. The caveat to this is that these volumes are functions of the individual volumes of the materials, which are unknown at a given pressure. What is

known is that due to the mechanical equilibrium, the pressure of materials in the mixture is the same for each material. For the example of a two material mixture, the Hugoniots are equated,

$$p = \mathscr{H}_1(v_1) = \mathscr{H}_2(v_2). \tag{7.41}$$

From (7.40), one material's volume can be expressed as a function of the other, recalling that $\lambda_k$ is constant:

$$\mathscr{H}_1(v_1(v_2)) - \mathscr{H}_2(v_2) = 0. \tag{7.42}$$

This equation can then be solved to find $v_2$ and then all subsequent postshock variables can be found.

The difficulty is that the Hugoniots of the two materials are often defined by two different equations of state that are not simple to rearrange and solve. Numerical root finding is a possible solution although these techniques are often very sensitive and unreliable. It was found that this alternative could reproduce all of the well-behaved, high density materials in [64] but could not model any gas, such as air, unless unphysical higher densities were used or the air was 'stiffened' through the use of a relatively large $p_{\text{inf}}$ constant in the stiffened gas equation of state. This meant that the original formulation that assumes that the postshock pressure is known had to be used. Expressions for the specific volumes of each material on the Hugoniot, $v_1^H(p)$ and $v_2^H(p)$, were determined for the specific equations of state being used.

This latter approach is not general and therefore not convenient for less specific use. A more convenient approach is to use the Afanasenkov theory outlined in the previous section as it can be used generally for any equation of state and is much faster to compute. A comparison of the two approaches was undertaken for the two porous explosives under consideration.

An illustration of how the Hugoniot of the condensed, pure ANFO compares with both the Afanasenkov Hugoniot of porous ANFO and the multiphase mixture Hugoniot of the porous ANFO is shown in Figure 7.15a. The parameters are again taken from Tables 4.2 and 4.3 and with $\alpha_{\text{condensed}} = 0.4905$. It is shown that for the pressure in most regimes, Afanasenkov theory predicts that the Hugoniot is almost identical to that of the multiphase mixture theory. It is only when the pressure goes below a certain very low threshold pressure that the two theories deviate. These low pressures equate to very low detonation velocities. This is shown more clearly in Figure 7.16. As these pressures are only relevant to detonation velocities well below those of interest, the Afanasenkov theory can be confidently used for the porous explosives and the same comparison for the emulsion EM120D is shown in Figure 7.15b with similar results despite the fact that the emulsion is distinctly different to ANFO with a much lower porosity.

Afanasenkov theory can only be used for porous materials. As shown in Figure 7.17, using the theory to try to model two materials where neither is a gas produces inadequate results. This is not surprising considering the formulation was specific to compression of gaseous voids.

Afanasenkov theory is used in this work to determine the value for the slope of the shock front at the charge edge only; it is not used to solve for the flow variables along the streamline. It does not need to be used but does eliminate the need for root finders with the more complicated equations of state where the pressure is not easily analytically extracted.

### Prandtl-Meyer expansion fan for inhomogeneous explosives

The equations for the Prandtl-Meyer pressure expansion of a homogeneous material can be extended to include multiple materials within the framework of the mechanical equilibrium model. The ODEs outlined in §B.1.1 can be updated to include the multiple materials when coupled with an equation for the mechanical equilibrium sound speed. These ODEs are then coupled with the equation for the Prandtl-Meyer fan (B.4) with the initial values specified via Afanasenkov's postshock theory as outlined in §7.4.3.

An alternative to this is to only consider the expansion of the condensed explosive and to assume that the voids remain at the same volume. All of these assumptions are explored in the results in the following section.

### Shock polar analysis for inhomogeneous explosives

A comparison between the shock polar for the homogeneous explosive of ANFO without voids, with the parameters as listed in in Table 4.3, and the inhomogeneous explosive ANFO mixture with a porous density of $\rho_0 = 810.0$ kgm$^{-3}$ for $D = 4060$ ms$^{-1}$ is shown in Figure 7.18c, with the neat material represented by the red curve and the inhomogeneous material represented by the blue curve. The green curve is the confining air shock polar. This provides very weak confinement and the only valid match between the two materials is via an intervening Prandtl-Meyer expansion fan in the explosive.

The mechanical equilibrium sound speed (Figure 7.18c) shows a gradual expansion to lower pressures and a larger expansion angle that gives a good match to DNS results. This was tested for a range of detonation velocities for both the porous ANFO and the emulsion EM120D.

The expansion angle at the match point between the Prandtl-Meyer expansion fan and the inert confiner shock polar are not actually used in the unconfined streamline calculation. However, it will be of use if the streamline theory is extended to confined calculations and also helps validate the use of shock polar theory. This result also implies that shock polar theory needs to necessarily include the voids in a porous material if the shock deflection angle is to be comparable to DNS simulations and experimental results, particularly

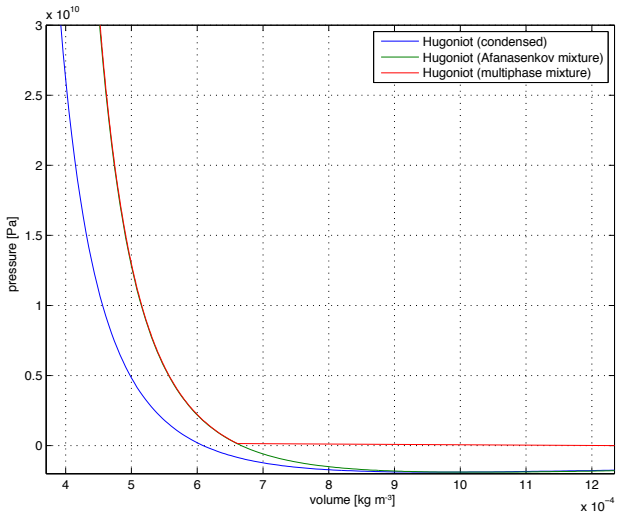


(a) Neat ANFO and the porous ANFO with added voids with $\alpha_{\text{condensed}} = 0.4905$.

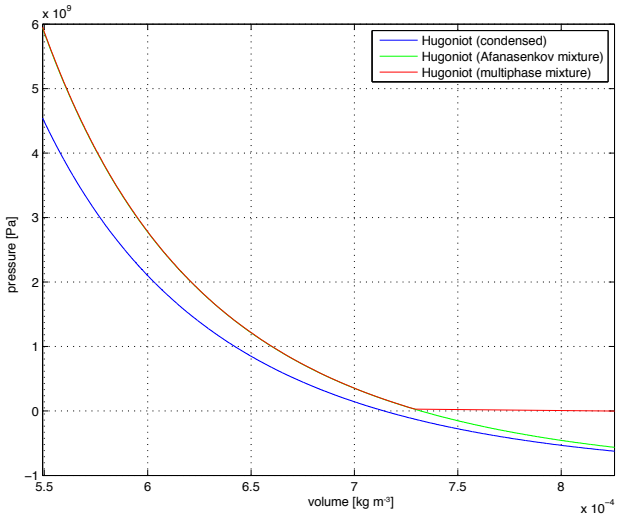


(b) Neat condensed emulsion EM120D and the porous EM120D with added voids with $\alpha_{\text{condensed}} = 0.864$.

Figure 7.15.: Neat Hugoniots and mixture Hugoniots calculated using both Afanasenkov theory and the multiphase mixture conditions given in [64]. Very little difference is seen in the Hugoniots for the pressure regimes of interest, despite the approximations in Afanasenkov's theory. The condensed phases are modelled with a LMG equation of state and the void phases in the mixture is modelled with ideal gas.

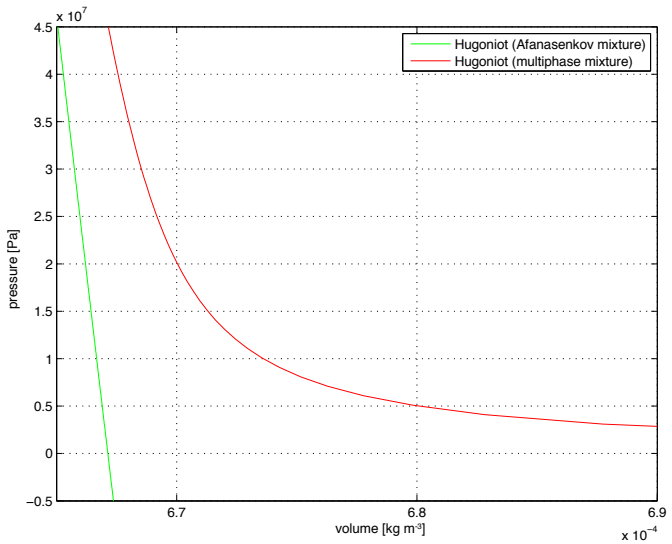


Figure 7.16.: Mixture Hugoniots for ANFO with $\alpha_{\text{condensed}} = 0.4905$ using both Afanasenkov theory and the multiphase mixture conditions given in [64]. At very low shock pressures the Afanasenkov approximation and the mixture Hugoniot diverge.

for materials with high porosity such as ANFO. To further illustrate this, these multiphase, steady-state DNS simulations are compared with shock polar theory for the two explosives of interest for the maximum and minimum detonation velocities for which there is experimental data available.

Figures 7.19a to 7.19d show the comparison for the emulsion explosive EM120D. Within the range of detonation velocities for which there is experimental data available, there is only a small decrease in shock deflection angle $\theta$. The incoming shock angle is not shown on the shock polar plot but is calculated from the deflection angle at the sonic point, denoted by the blue circle. Since there is only a small difference in $\theta$ for these two extreme cases, we expect only a small difference in incoming shock angle as well. This is shown in Figure 7.19. For reference, the condensed shock polar plot for neat EM120D is also shown. However, since EM120D has a relatively low porosity ($\alpha_{\text{voids}} = 0.136$), there is not much difference between the curves for the porous material and the neat material.

ANFO, however, has quite a high relative porosity ($\alpha_{\text{voids}} = 0.5095$) and so the voids have a greater impact on the incoming shock angle. Within the range of detonation velocities for which there is experimental data available, there is only a small decrease in shock deflection angle but a significant increase in incoming shock angle. The shock polar plots show a definite increase in the deflection angle for the higher detonation velocities and this is seen in the DNS results as well. Again, the incoming shock angle is not shown on the shock polar plot but is calculated from the deflection angle at

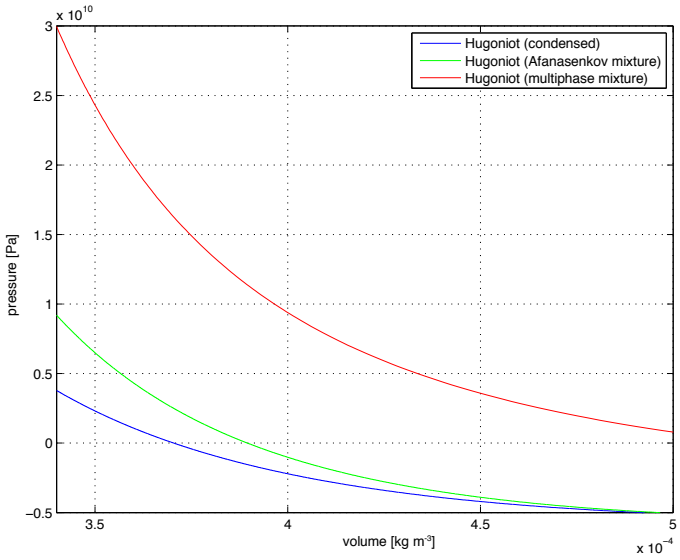


(a)

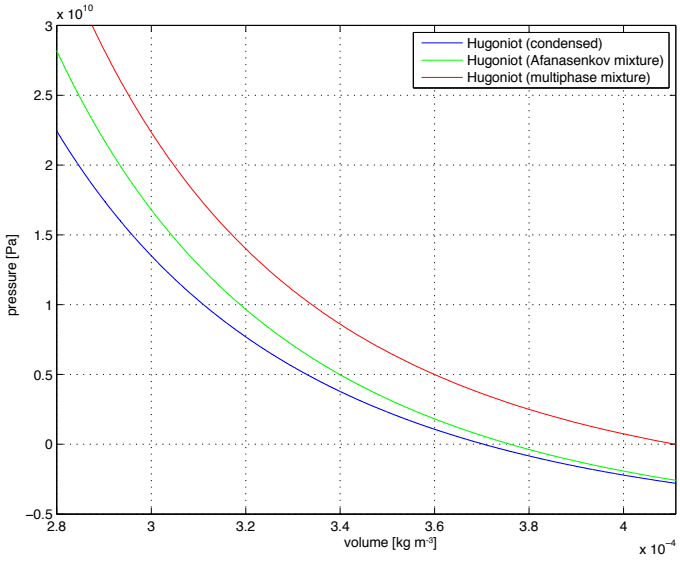


(b)

Figure 7.17.: a) The mixture Hugoniot for paraffin-marble with $\alpha_{\text{paraffin}} = 0.56$ from [64]. b) Hugoniots for paraffin-marble with $\alpha_{\text{paraffin}} = 0.85$ from [64]. Afanasenkov theory is suitable for porous materials only and does a poor job at imitating the multiphase behaviour of two materials if the second material is anything other than a gas. As the volume fraction of the condensed phase approaches 1 the theory appears to be more valid but this is only because there is less of the second material to affect the shock variables.

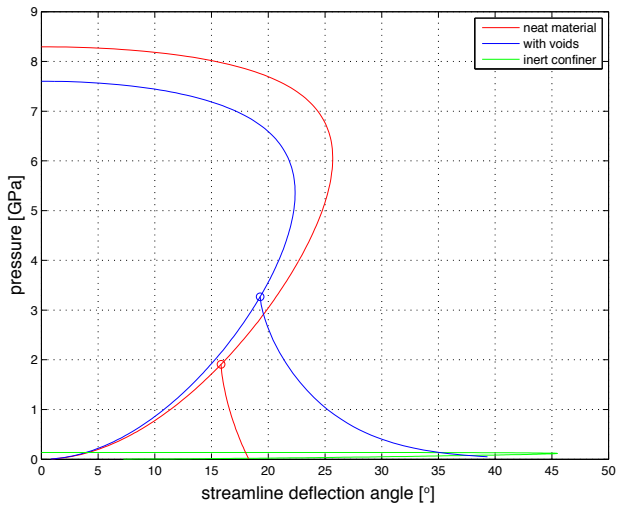


Figure 7.18.: A comparison of different neat and void material calculations in the expansion fan for EM120D. The inclusion of voids is achieved with use of Afanasenkov theory.

the sonic point. This is shown clearly in Figures 7.21 & 7.22 as the black line on the surface plot of the shock polars for EM120D and ANFO, respectively. As there is small but distinct difference in $\theta$, we expect there to be a small difference in incoming shock angle as well. This is shown in the bottom of Figures 7.21 & 7.22.

These comparisons reiterate the importance of including the porous nature of the explosive in calculations and simulations. The inclusion of voids in the calculation of the shock polars makes a difference in the location of the sonic point. In fact, the greater the volume fraction of the voids, the more influential the inclusion of voids is for a material and the location of the sonic point. This sonic point on the shock polar curve, shown by a circle in Figure 7.18c, is at the angle of deflection at the charge edge. From this deflection angle and the oblique shock conditions, the corresponding incoming shock angle can be calculated. This will be the maximum incoming shock angle obtained by that explosive at that detonation velocity. This angle is then used as the indicator of where the edge is for that explosive at that detonation velocity in the Chan-Kirby streamline model.

### 7.4.4. Results

With the use of shock polar analysis, the new approach for determining the incoming shock angle, determined for each detonation velocity using each explosive's individual properties, is implemented.

Figure 7.23 shows the difference in the diameter effect curve with the new charge edge determination for both ANFO and EM120D and Figure 7.24 illustrates the DDZ and pressure distribution within it for two sample

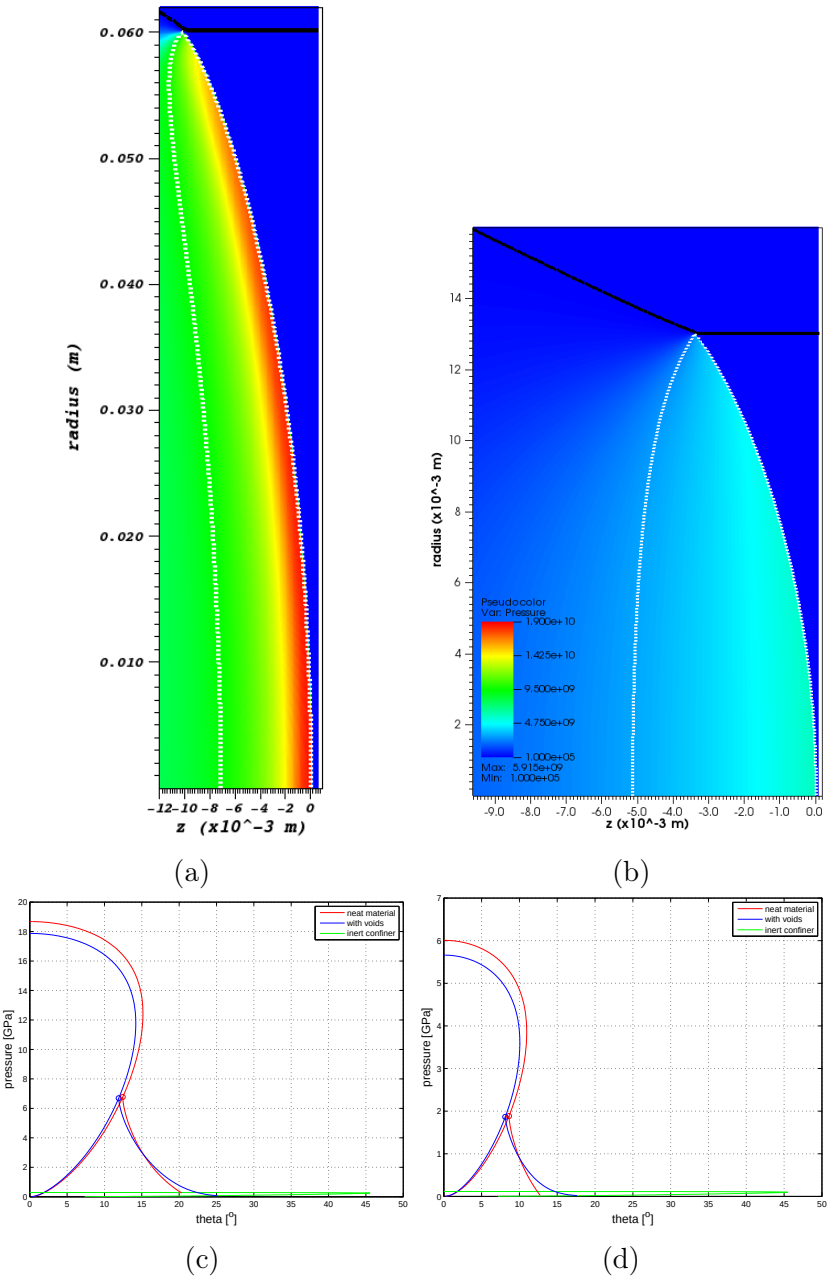


Figure 7.19.: DNS simulations of EM120D with (a) $r = 0.06$m and $D = 5900\text{ms}^{-1}$ and (b) $r = 0.013$m and $D = 3710\text{ms}^{-1}$. The black line shows the inert confiner boundary and the white dotted line shows the Wood sound speed for $M = 1$. The cell size on both is $r \times \frac{9}{16000}$. The expected shock deflection angle is shown in the shock polar plots in (c) and (d) at the point where the expansion wave from the porous material (blue line) intersects the inert shock polar (green). The condensed shock polar for EM120D is shown in red.

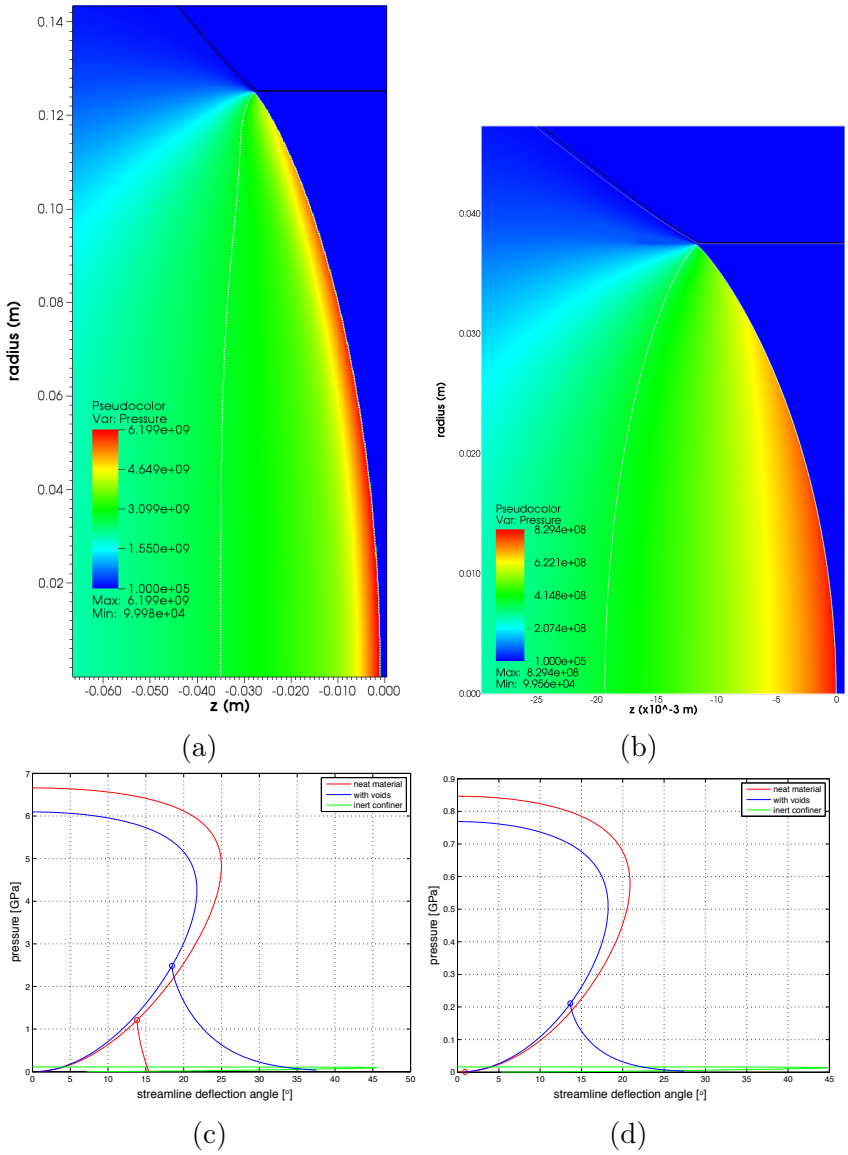


Figure 7.20.: DNS simulations of ANFO with $r = 0.125$m and $D = 3670\text{ms}^{-1}$ (a) and $r = 0.0375$m and $D = 1400\text{ms}^{-1}$ (b). The black line denotes the inert confiner boundary and the white dotted line shows the Wood sound speed for $M = 1$. The expected shock deflection angle is shown in the shock polar plots in (c) and (d) at the point where the expansion wave from the porous material (blue line) intersects the inert shock polar (green). The condensed shock polar for ANFO is shown in red.

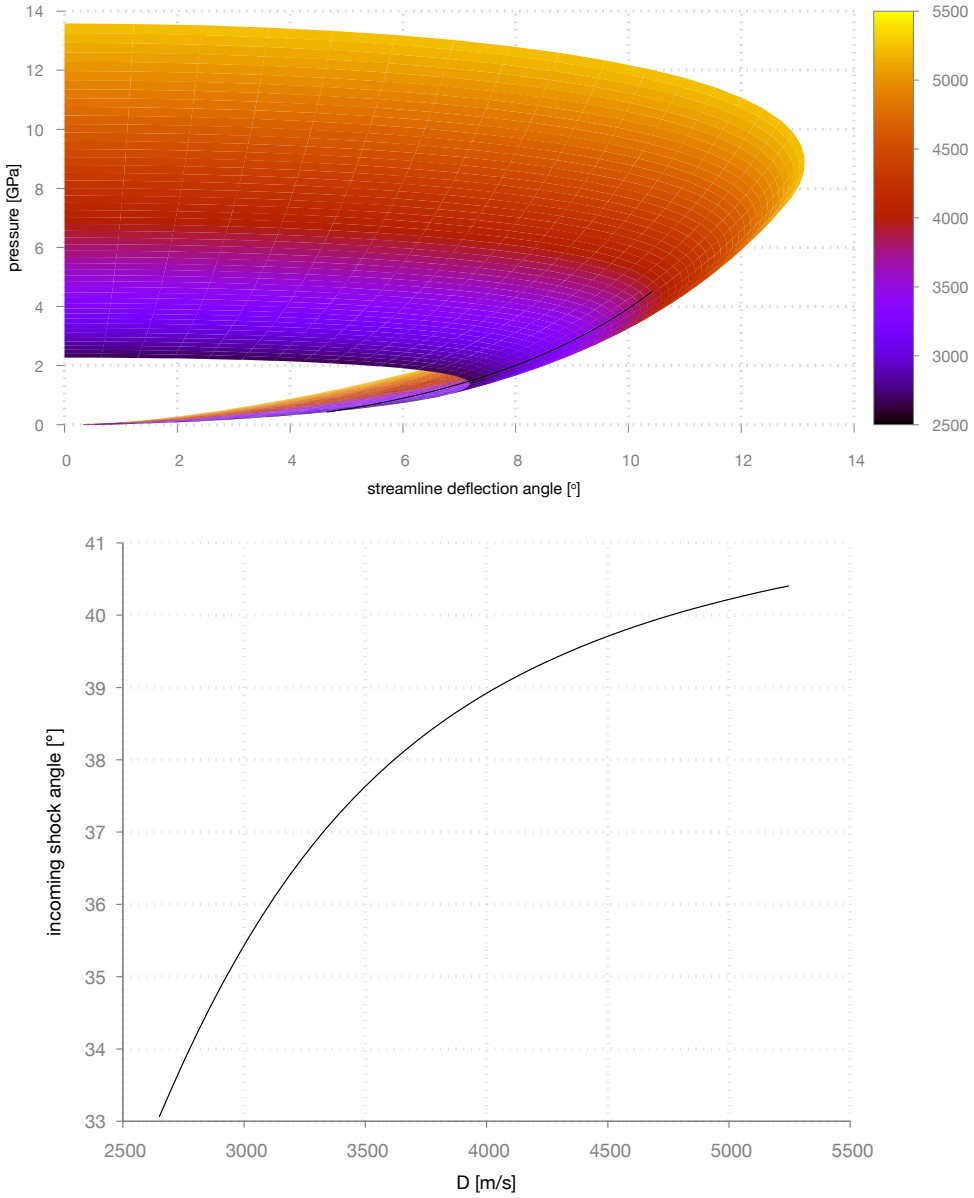


Figure 7.21.: (top) A surface plot of EM120D shock polars, with varying the detonation velocity indicated by the colour scale. The black line is the locus of sonic points for different detonation velocities. These different sonic points correspond to the charge edge. (bottom) Incoming shock angle as a function of the detonation velocity. These points are taken from the black line in the top figure.

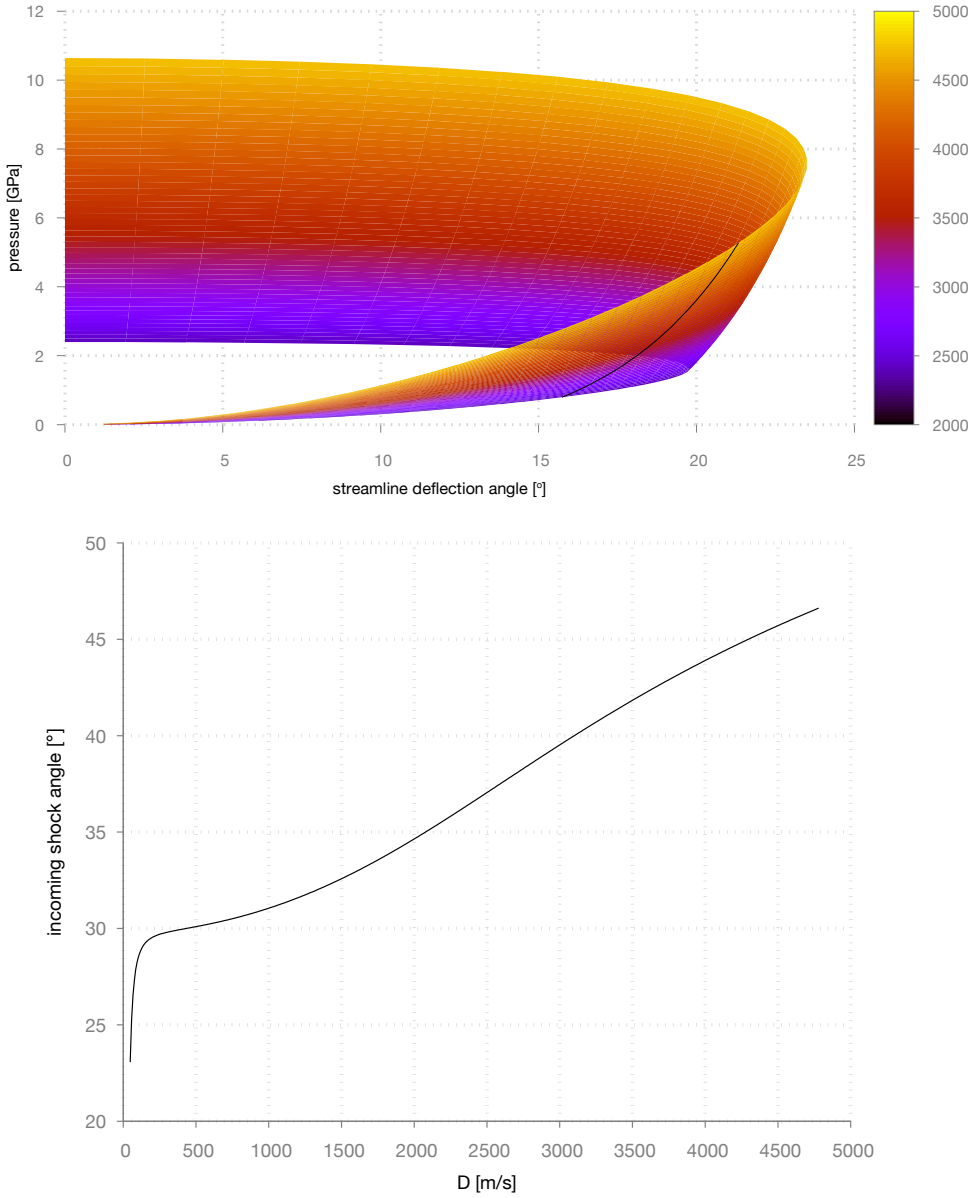


Figure 7.22.: (top) A surface plot of ANFO shock polars, with varying the detonation velocity indicated by the colour scale. The black line is the locus of sonic points for different detonation velocities. These different sonic points correspond to the charge edge. (bottom) Incoming shock angle as a function of the detonation velocity. These points are taken from the black line in the top figure.

detonation velocities for the two different explosives.

Given Figures 7.21 and 7.22, it is unsurprising to see that the the elimination of the empirical constant edge angle has a very small effect. For example, the values calculated for the diameter effect curve for ANFO range from $1500\text{ms}^{-1} \lessapprox D \lessapprox 3500\text{ms}^{-1}$. Results from shock polar analysis, shown in Figure 7.22, show that in this range the incoming shock angle varies from about 32° to 42° only. The corresponding shock slope is the tangent of this value and the difference in slope is very small. This also applies for EM120D even though the range of detonation velocities and angles are slightly larger.

Despite there being very little difference in the results it must once again be argued that the elimination of another empirical parameter in the model can only be advantageous in terms of applying or extending the model to a wider range of applications. However, even with the elimination of the empirical isobar and edge terms, the Chan-Kirby model's underlying approximations with respect to radial velocity mean that it consistently underestimates the radius. For this reason the single-phase work of Watt et al. [78] is extended to multiphase in Chapter 8 to investigate whether an alternative to the Chan-Kirby model is available for multiphase modelling of non-ideal explosives.

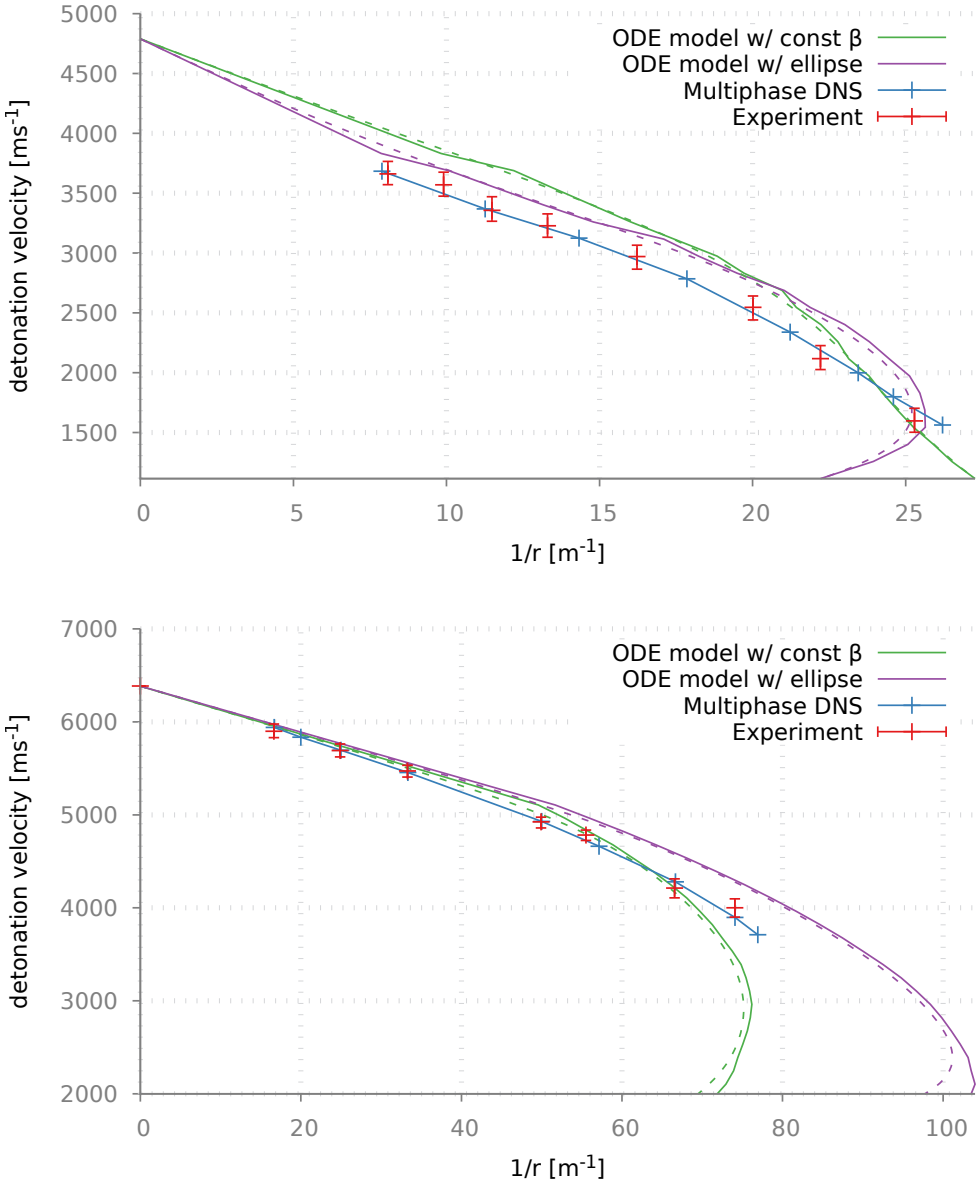


Figure 7.23.: Diameter effect plots for ANFO (top) and EM120D (bottom) showing the use of shock polar theory to determine the edge of the charge (dashed lines) compared to the constant, empirical value of 0.6 (solid lines). Only a small difference is made but the solutions are smoother.

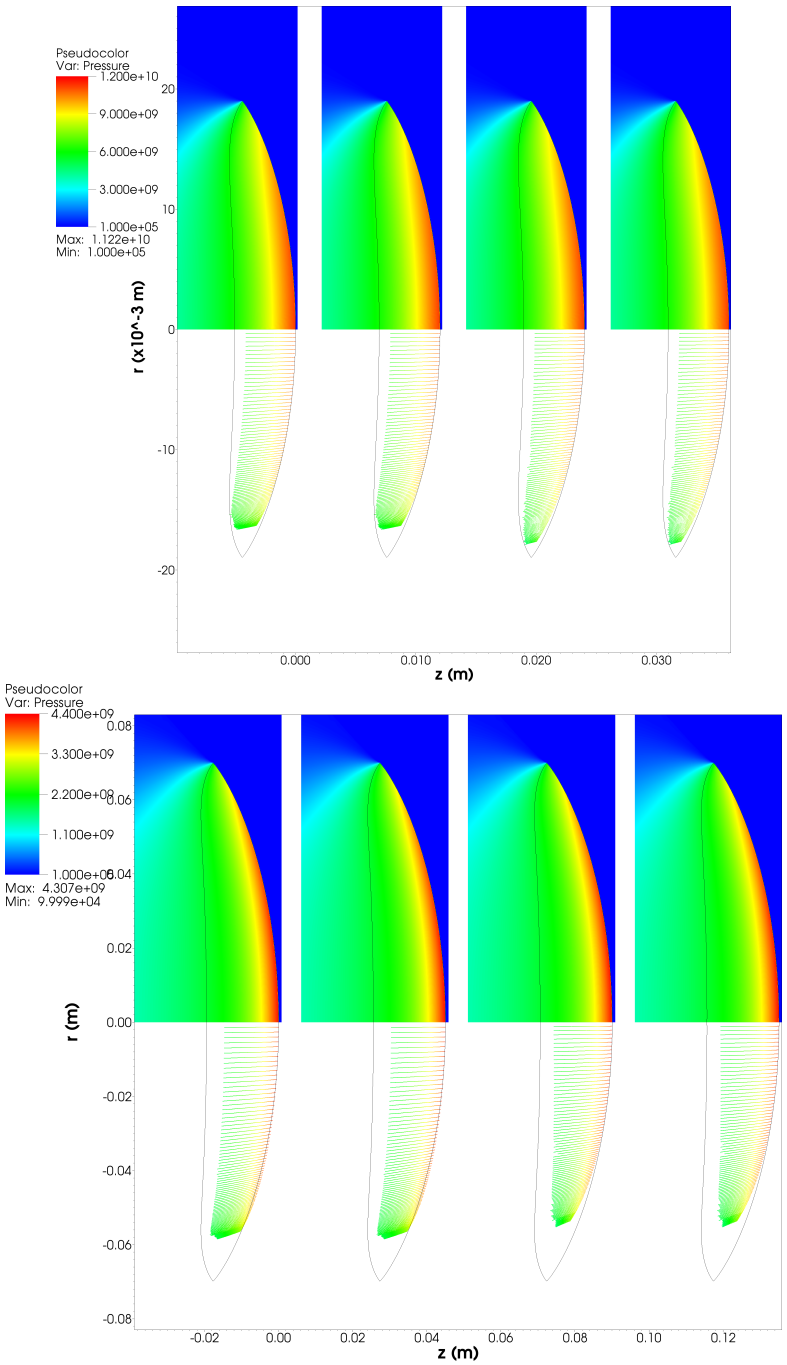


Figure 7.24.: Pressure in the DDZ from a DNS (blue background) and the multiphase Chan-Kirby model. Both ANFO at $D = 3120$ ms$^{-1}$ (top) and EM120D at $D = 3120$ ms$^{-1}$ (bottom) are shown. The effect of shock polar theory to determine the edge of the charge (2nd & 4th) is compared to the constant, empirical value of 0.6 (1st & 3rd). Results for both the constant isobar approximation (3rd & 4th) and the new elliptical expression (1st & 2nd) are shown.

# 8. Multiphase straight streamline approach

The Chan-Kirby model provides a method for modelling two-dimensional, unconfined, steady non-ideal detonation via a shock-attached frame. However, as indicated in the previous chapters, a reduced ODE model is only possible through first order approximations of the equations and an empirical relationship for the shape of the isobars. An alternative approach is a reduction of the governing equations of motion PDEs to ODEs via a change of frame from shock-attached to streamline-attached.

The use of a streamline frame of reference for modelling steady confined detonation was first suggested by Bdzil [12, 13] and was later to become detonation shock dynamics (DSD), widely used to model detonations where the shock front curvature is small. Later developments included time-dependence and some non-ideal detonation modelling.

More recently, Watt et al. [78] used the streamline-attached equations with no limitations on the shock front curvature to successfully model a hypothetical non-ideal detonation. This approach utilises the same theory proposed by Bdzil in [13] with the caveat that there is no curvature of the streamlines despite the substantially curved shock front. Like Bdzil, Watt et al. modelled only a single phase with an underlying Euler model using a polytropic equation of state and simple reaction rate as an analogue for a non-ideal explosive. Comparisons between DNS calculations and the straight streamline approach (SSA) showed a good match between the detonation velocity versus inverse radius curve (VoD curve) for a range of reaction rate parameter values and for both confined and unconfined simulations in both slab and cylindrical geometry. Comparisons were also made to a DSD implementation and these illustrated that a better match to DNS solutions are found with use of the straight streamline approach compared to DSD. Furthermore, the authors claim that the straight streamline VoD curves are calculated in minutes.

With the success of the straight streamline approach for a single phase, this chapter explores the derivation, implementation and solutions of a multiphase straight streamline approach with the addition of general Mie-Grüneisen equations of state and reaction rates that include hotspot formation. The justification for these extensions are much the same as for the Chan-Kirby model: it is hoped that the multiple phases, realistic equations of state and hotspot reaction rate will better mimic the behaviour of non-ideal detonation.

As the straight streamline approach is a relatively new approach, and there is a minimal amount of literature currently available about it, the next section, §8.1, outlines a derivation of the original theory. As this work aims to move away from the ideal gas equation of state, the derivation is shown for a general equation of state. This was previously unavailable. Comparisons to published results from the original theory are made to validate the derivation and implementation.

Section 8.2 outlines the derivation of the multiphase mechanical equilibrium extension. This section also includes a discussion on the use of shock polar theory in the straight streamline approximation model to determine the shock front curvature. A brief discussion of the numerical methods used in the implementation of the extension is also made.

Finally, §8.2.4 illustrates comparisons between the multiphase mechanical equilibrium streamline approximation and multiphase mechanical equilibrium DNS simulations where the same equations of state and reaction rates have been used. The two non-ideal explosives EM120D and ANFO are used for the comparisons.

## 8.1. Single-phase Euler model

The straight streamline approach outlined by Watt et al. [78] is an Euler-based model. The model builds on Bdzil's preliminary use of streamlines [13]. The derivations given in both works are specific to the ideal gas equation of state. Furthermore, the details of these equations are only given for slab geometry. In order to extend the theory to more realistic simulations, the theory is derived for a general equation of state in axisymmetric coordinates.

The underlying equations are given by the augmented Euler equations, (1.1) to (1.4). These are repeated here for convenience:

$$\frac{D\rho}{Dt} + \rho\nabla\cdot\mathbf{v} = 0, \tag{8.1}$$

$$\rho\frac{D\mathbf{v}}{Dt} = -\nabla p, \tag{8.2}$$

$$\frac{De}{Dt} - \frac{p}{\rho^2}\frac{D\rho}{Dt} = 0, \tag{8.3}$$

$$\frac{D\lambda}{Dt} = W, \tag{8.4}$$

where $\dfrac{D}{Dt} = \dfrac{\partial}{\partial t} + \mathbf{v}\cdot\nabla$ is the time derivative following the motion of the fluid, or material derivative, and $W$ is the reaction rate. The partial time derivatives then are the time derivative in the rest frame of the fluid. For the steady state problem, these partial time derivatives are zero. Note that the notation for the velocity vector, $v$, has changed from the earlier parts of this work (previously $u$).

The SSA transforms the equations of motion from a Cartesian coordinate system to a streamline coordinate system via a new variable called the streamline function. The conservation of mass (8.1) is used to replace the two dependent variables for particle velocity, $u$ and $v$, with a single dependent variable $\psi$. This new dependent variable is the streamline function and can be interpreted as both a measure of volume flux and as one component of a vector potential.

In the case of steady state flow, the mass conservation equation (8.1) reduces to

$$\nabla \cdot (\rho \mathbf{v}) = 0. \tag{8.5}$$

With the further restriction that the flow field is axisymmetric, this vector divergence is the sum of only two derivatives. Therefore, the equation for the conservation of mass can be regarded as defining a scalar function from which the components of $\rho\mathbf{v}$ are obtained by differentiation.

If the flow field is axisymmetric with coordinates $(r, z, \phi)$, then $\mathbf{v} = (u, v, 0)$ where $u$ is the radial velocity and $v$ is the axial velocity and both are independent of $\phi$. Note again that this notation is different to the notation used in earlier chapters but is consistent with the original theory of Watt et al. [78]. The mass conservation equation then has the form

$$\frac{1}{r}\frac{\partial(r\rho u)}{\partial r} + \frac{\partial(\rho v)}{\partial z} = 0, \tag{8.6}$$

from which it follows that $rv\rho\delta r - ru\rho\delta z$ is an exact differential (see, for example, Chapter 2 of [10]). If this is equal to, say, $\delta\psi$ then

$$u = \frac{1}{r\rho}\left(\frac{\partial\psi}{\partial z}\right)_r, \tag{8.7}$$

$$v = -\frac{1}{r\rho}\left(\frac{\partial\psi}{\partial r}\right)_z, \tag{8.8}$$

where the unknown scalar function $\psi(r, z, t)$ is defined by

$$\psi - \psi_0 = \int r\rho\,(u dz - v dr), \tag{8.9}$$

where $\psi_0$ is constant and the line integral is taken along an arbitrary curve in an axial plane joining some reference point $O$ to the point $P$ with coordinates $(r, z)$. This is illustrated in Figure 8.1.

To show that this quantity is independent of the path, consider two different paths joining points $O$ and $P$. If the region between the two paths is occupied by compressible flow, and if this flow is steady, the flux of volume across the closed curve formed is necessarily zero due to the conservation of mass. The flux is therefore independent of the choice of the path joining $O$ to $P$. This implies that $\psi$ has only one value at $P$ and is therefore a function of position $(r, z)$ only.

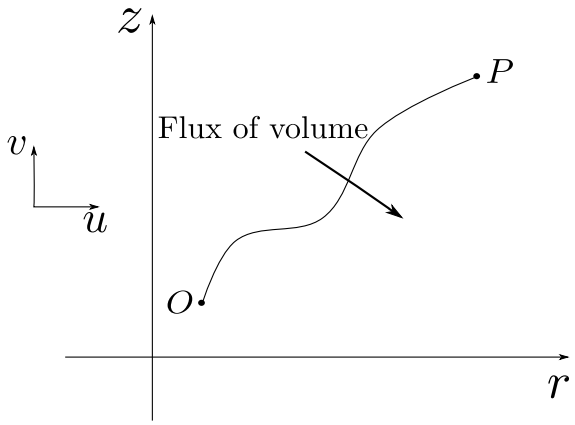


Figure 8.1.: Calculation of the flux of fluid volume across a curve joining the point $O$ to $P(r, z)$ is given by (8.9).

If the arbitrary curve joining $O$ and $P$ in an axial plane is rotated about the axis of symmetry to form a surface, the flux of the fluid across this surface is $2\pi$ times the right-hand side of (8.9). The lines in the axial plane on which $\psi$ is constant, called the streamlines, are everywhere parallel to the vector $(u, v, 0)$. If these lines are chosen so that the values on neighbouring streamlines differ by the same amount then we can build up a visual representation of how the velocity changes, in both magnitude and direction, over the field.

It is not immediately obvious that the result for the ratio of particle velocities,

$$\left(\frac{\partial r}{\partial z}\right)_{\psi} = \frac{u}{v}, \tag{8.10}$$

follows from (8.7) and (8.8) so this should be noted.

The following sections look at how the change from spatial coordinates to streamline coordinates changes the operators and hence the equations of motion.

### 8.1.1. Operators in axisymmetric streamline coordinates

Under the coordinate transformation from $(r, z)$ to $(\psi(r, z), z)$, the derivatives are given as

$$\left(\frac{\partial}{\partial r}\right)_z = \left(\frac{\partial \psi}{\partial r}\frac{\partial}{\partial \psi}\right)_z, \tag{8.11}$$

$$\left(\frac{\partial}{\partial z}\right)_r = \left(\frac{\partial \psi}{\partial z}\frac{\partial}{\partial \psi}\right)_r + \left(\frac{\partial}{\partial z}\right)_{r,\psi}. \tag{8.12}$$

The operators for streamline coordinates are defined as follows.

### Gradient operator

The gradient operator is

$$\begin{aligned}\nabla &= \left(\frac{\partial}{\partial r}, \frac{\partial}{\partial z}\right), \\ &= \left(-r\rho v\frac{\partial}{\partial \psi}, r\rho u\frac{\partial}{\partial \psi} + \frac{\partial}{\partial z}\right),\end{aligned}$$

with use of (8.7) and (8.8).

### Divergence operator

The divergence operator is as follows.

$$\begin{aligned}\nabla \cdot \mathbf{b} &= \frac{1}{r}\frac{\partial}{\partial r}\left(r b_r\right) + \frac{\partial b_z}{\partial z} \\ &= \frac{b_r}{r} + \frac{\partial b_r}{\partial r} + \frac{\partial b_z}{\partial z} \\ &= \frac{b_r}{r} + \frac{\partial \psi}{\partial r}\frac{\partial b_r}{\partial \psi} + \frac{\partial b_z}{\partial z} + \frac{\partial \psi}{\partial z}\frac{\partial b_z}{\partial \psi} \\ &= \frac{b_r}{r} - r\rho v\frac{\partial b_r}{\partial \psi} + \frac{\partial b_z}{\partial z} + r\rho u\frac{\partial b_z}{\partial \psi} \\ &= \frac{b_r}{r} - r\rho v^2\left(\frac{1}{v}\frac{\partial b_r}{\partial \psi} - \frac{u}{v^2}\frac{\partial b_z}{\partial \psi}\right) + \frac{\partial b_z}{\partial z}\end{aligned}$$

### Divergence of velocity

Following from above,

$$\begin{aligned}\nabla \cdot \mathbf{v} &= \frac{u}{r} - r\rho v^2\left(\frac{1}{v}\frac{\partial u}{\partial \psi} - \frac{u}{v^2}\frac{\partial v}{\partial \psi}\right) + \frac{\partial v}{\partial z} \\ &= \frac{u}{r} - r\rho v^2\frac{\partial}{\partial \psi}\left(\frac{u}{v}\right) + \frac{\partial v}{\partial z}.\end{aligned}$$

### Material derivative

$$\begin{aligned}\frac{D}{Dt} &= \frac{\partial}{\partial t} + \mathbf{v}\cdot\nabla \\ &= \cancelto{0}{\frac{\partial}{\partial t}} - r\rho u v\frac{\partial}{\partial \psi} + v\frac{\partial}{\partial z} + r\rho u v\frac{\partial}{\partial \psi} \\ &= v\frac{\partial}{\partial z}\end{aligned}$$

## 8.1.2. Equations of motion

### Continuity equation

From the governing equations of motion, the continuity equation (8.1) is given by

$$(u, v) \cdot \nabla\rho + \rho\nabla \cdot (u, v) = 0.$$

Using the gradient and divergence operators defined above,

$$v\frac{\partial\rho}{\partial z} + \rho\frac{u}{r} - r\rho^2 v^2 \frac{\partial}{\partial\psi}\left(\frac{u}{v}\right) + \rho\frac{\partial v}{\partial z} = 0.$$

Dividing by $-\rho^2 v^2$ gives

$$-\frac{1}{\rho^2 v}\frac{\partial\rho}{\partial z} - \frac{1}{\rho v^2}\frac{\partial v}{\partial z} - \frac{u}{rv^2} + r\frac{\partial}{\partial\psi}\left(\frac{u}{v}\right) = 0,$$

so that,

$$\frac{\partial}{\partial z}\left(\frac{1}{\rho v}\right) + r\frac{\partial}{\partial\psi}\left(\frac{u}{v}\right) - \frac{u}{\rho r v^2} = 0. \tag{8.13}$$

### Conservation of momentum

From the governing equations of motion, the conservation of momentum (8.2) is given by

$$\begin{aligned} \rho\left(\mathbf{u}\cdot\nabla\right)\mathbf{u} + \nabla p = 0, \\ \rho v\frac{\partial\mathbf{u}}{\partial z} + \left(-r\rho v\frac{\partial}{\partial\psi}, \frac{\partial}{\partial z} + r\rho u\frac{\partial}{\partial\psi}\right) p = 0. \end{aligned}$$

The radial momentum is then given by

$$\rho v\frac{\partial u}{\partial z} - r\rho v\frac{\partial p}{\partial\psi} = 0. \tag{8.14}$$

The axial momentum is then given by

$$\rho v\frac{\partial v}{\partial z} + r\rho u\frac{\partial p}{\partial\psi} + \frac{\partial p}{\partial z} = 0. \tag{8.15}$$

### Conservation of energy

From the governing equations of motion, the conservation of energy (8.3) is given by

$$\begin{aligned} v\frac{\partial e}{\partial z} - \frac{pv}{\rho^2}\frac{\partial\rho}{\partial z} = 0, \\ \frac{\partial e}{\partial z} - \frac{p}{\rho^2}\frac{\partial\rho}{\partial z} = 0. \end{aligned} \tag{8.16}$$

**Rate equation**

The final equation needed is the rate equation (8.4). This is given by

$$v\frac{\partial \lambda}{\partial z} = W. \tag{8.17}$$

### 8.1.3. Master equation

In the straight streamline approach, the equations of motion derived above are simplified into a single 'master equation'. This section outlines how this equation is obtained.

Given that the internal energy is assumed to be of Mie-Grüneisen form,

$$e = e(p, \rho, \lambda) \tag{8.18}$$

$$= e_{\text{ref}} + \frac{p - p_{\text{ref}}(\rho)}{\Gamma(\rho)\rho} - Q\lambda, \tag{8.19}$$

the conservation of energy (8.3) can be rewritten as

$$\frac{\partial e}{\partial p}\frac{\partial p}{\partial z} + \frac{\partial e}{\partial \rho}\frac{\partial \rho}{\partial z} - \frac{p}{\rho^2}\frac{\partial \rho}{\partial z} - Q\frac{\partial \lambda}{\partial z} = 0.$$

Noting that the sound speed is defined as $c^2 = \dfrac{\frac{p}{\rho^2} - \left(\frac{\partial e}{\partial \rho}\right)_p}{\left(\frac{\partial e}{\partial p}\right)_\rho}$ and $\dfrac{\partial e}{\partial p} = \dfrac{1}{\rho\Gamma(\rho)}$ and then multiplying by $v\Gamma$,

$$\begin{aligned}
0 &= -\frac{\partial \rho}{\partial z}\left(\frac{p}{\rho^2} - \frac{\partial e}{\partial \rho}\right) + \frac{1}{\rho\Gamma}\frac{\partial p}{\partial z} - Q\frac{\partial \lambda}{\partial z} \\
&= v\Gamma\frac{\partial \rho}{\partial z}\left(\frac{p}{\rho^2} - \frac{\partial e}{\partial \rho}\right) - \frac{v}{\rho}\frac{\partial p}{\partial z} + v\Gamma Q\frac{\partial \lambda}{\partial z} \\
&= \frac{v}{\rho}\frac{\frac{\partial \rho}{\partial z}\left(\frac{p}{\rho^2} - \frac{\partial e}{\partial \rho}\right)}{\frac{\partial e}{\partial p}} - \frac{v}{\rho}\frac{\partial p}{\partial z} + v\Gamma Q\frac{\partial \lambda}{\partial z} \\
&= \frac{vc^2}{\rho}\frac{\partial \rho}{\partial z} - \frac{v}{\rho}\frac{\partial p}{\partial z} + \Gamma Q\frac{d\lambda}{dt}.
\end{aligned} \tag{8.20}$$

Using the two components of conservation of momentum equations (8.14)-(8.15), note that

$$\begin{aligned}
\frac{v}{\rho}\frac{\partial p}{\partial z} &= \frac{v}{\rho}\left(-\rho u r\frac{\partial p}{\partial \psi} - \rho v\frac{\partial v}{\partial z}\right) \\
&= -uvr\frac{\partial p}{\partial \psi} - v^2\frac{\partial v}{\partial z} \\
&= -u^2\frac{\partial v}{\partial z} - v^3\frac{\partial r}{\partial z}\frac{\partial^2 r}{\partial z^2} - v^2\frac{\partial v}{\partial z},
\end{aligned} \tag{8.21}$$

since $\dfrac{\partial^2 r}{\partial z^2} = \dfrac{\partial}{\partial z}\left(\dfrac{u}{v}\right)$. Substituting (8.21) back into (8.20) gives

$$\frac{vc^2}{\rho}\frac{\partial \rho}{\partial z} + u^2\frac{\partial v}{\partial z} + v^3\frac{\partial r}{\partial z}\frac{\partial^2 r}{\partial z^2} + v^2\frac{\partial v}{\partial z} + \Gamma Q\frac{d\lambda}{dt} = 0.$$

Substituting in the conservation of mass (8.13) gives

$$-c^2\frac{\partial v}{\partial z} - \frac{\partial \psi}{\partial r}c^2 v\frac{\partial^2 r}{\partial z \partial \psi} + u^2\frac{\partial v}{\partial z} + v^3\frac{\partial r}{\partial z}\frac{\partial^2 r}{\partial z^2} + v^2\frac{\partial v}{\partial z} + \Gamma Q\frac{d\lambda}{dt} = 0.$$

Rearranging gives the master equation,

$$\frac{\partial v}{\partial z}\left(\left(u^2+v^2\right) - c^2\right) = \frac{\partial \psi}{\partial r}c^2 v\frac{\partial^2 r}{\partial z \partial \psi} - v^3\frac{\partial r}{\partial z}\frac{\partial^2 r}{\partial z^2} - \Gamma Q\frac{d\lambda}{dt},$$

so that

$$\frac{\partial v}{\partial z}\left(v^2\left(1+\left(\frac{\partial r}{\partial z}\right)^2\right) - c^2\right) = \frac{\partial \psi}{\partial r}c^2 v\frac{\partial^2 r}{\partial z \partial \psi} - v^3\frac{\partial r}{\partial z}\frac{\partial^2 r}{\partial z^2} - \Gamma Q\frac{d\lambda}{dt}. \quad (8.22)$$

The master equation also describes the first and second CJ conditions:

$$\text{1st CJ condition}: \quad v^2\left(1+\left(\frac{\partial r}{\partial z}\right)^2\right) - c^2 = 0, \quad (8.23)$$

$$\text{2nd CJ condition}: \quad \frac{\partial \psi}{\partial r}c^2 v\frac{\partial^2 r}{\partial z \partial \psi} - v^3\frac{\partial r}{\partial z}\frac{\partial^2 r}{\partial z^2} - \Gamma Q\frac{d\lambda}{dt} = 0. \quad (8.24)$$

The equations for the conservation of momentum (8.14)-(8.15) can be integrated to obtain an algebraic expression for the pressure via Bernoulli's equation. This is needed to calculate $c^2$ in the Master equation, since $c = c(\rho, p)$.

Rearranging (8.14) and substituting it into (8.15), the equation

$$\rho v\frac{\partial v}{\partial z} + \rho u\frac{\partial u}{\partial z} + \frac{\partial p}{\partial z} = 0 \quad (8.25)$$

can be integrated to obtain Bernoulli's equation,

$$e + \frac{p}{\rho} + \frac{1}{2}\left(u^2+v^2\right) = \frac{1}{2}D_0^2 + e_0 + \frac{p_0}{\rho_0}, \quad (8.26)$$

which can then be rearranged into an expression for $p$,

$$p = \rho\left(\frac{1}{2}D_0^2 + e_0 + \frac{p_0}{\rho_0} - \frac{1}{2}\left(u^2+v^2\right) - e(\rho,p)\right). \quad (8.27)$$

However, note that the right hand side of this equation involves the internal energy, $e = e(\rho, p)$, which is also a function of pressure. For a simple equation

of state, like the polytropic equation of state, it is straightforward to obtain an expression for $p$ algebraically. For a general equation of state, a numerical root finder can be used to find $p$.

The governing equations are therefore reduced to a single equation that, coupled to the rate law (8.4), describes the evolution of the the axial velocity, $v$. This evolution is a function of the slope of the streamline, $\dfrac{\partial r}{\partial z}$, as well as the divergence and curvature of the streamlines, of which $\dfrac{\partial r}{\partial \psi}$ and $\dfrac{\partial^2 r}{\partial z \partial \psi}$ and then $\dfrac{\partial^2 r}{\partial z^2}$ are related, respectively. To evaluate these terms, information is needed about both the shape of the shock front and the shape of the streamline. Since the shape of the shock front and streamlines are not known a priori, an optimisation algorithm is needed to determine the shapes. If both the shock front and streamline shapes need to be determined then this would create a multivariate optimisation problem that would be costly to solve.

To simplify the optimisation problem as far as possible, the streamlines are assumed to be straight but diverging. This means that no parameters are needed to describe the streamline shape, reducing the optimisation problem to one unknown. The straight streamlines also imply that $\dfrac{\partial^2 r}{\partial z^2} = 0$ thus simplifying the master equation.

The next section looks at how the straight streamline approximation allows for the determination of the remaining variables.

### 8.1.4. Straight streamline approximation

In the straight streamline approach,

$$\frac{\partial^2 r}{\partial z^2} = 0. \tag{8.28}$$

The shape of the shock front is determined from the curvature on each streamline via a shooting method on each streamline. Therefore, the values for the streamline slope and $\partial r/\partial \psi$ are known for each calculation. Coupled with the axial velocity, these expressions form the algebraic expressions used to calculate all other variables.

To calculate the radial velocity, (8.7) and (8.8) can be combined to give the ratio of the radial and axial velocities as a function of the slope of a streamline only:

$$\frac{\partial r}{\partial z} = \frac{u}{v}. \tag{8.29}$$

Since the left-hand side of this equation is constant along each streamline and $v$ is calculated via the master equation, $u$ can be determined from (8.29).

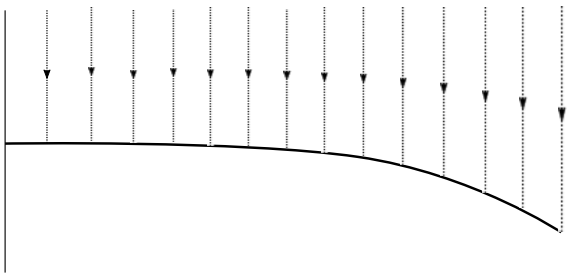

Figure 8.2.: Ahead of the shock front, despite the curvature, all streamlines are parallel to the direction of flow.

Assuming that the streamlines are straight, along a streamline the radial position can be recovered via the equation

$$r = r_f + F(\psi)(z - z_f), \tag{8.30}$$

where $(r_f, z_f)$ is the radial coordinate of the streamline at the shock front.

The function, $F(\psi)$, describes the material surface of the fluid. More generally, specifying that

$$F(\mathbf{x}, t) = \text{constant}$$

implies that $F$ is a quantity which is invariant for a fluid particle on the surface so that

$$\frac{DF}{Dt} = 0,$$

for all points on the fluid's surface. All equations describing the bounding of the fluid must satisfy this equation.

In context of the straight streamline approach, $F$ is taken to be the ratio of radial velocity to axial velocity at the shock front,

$$F(\psi) = \frac{u_f}{v_f}. \tag{8.31}$$

The expressions for $u_f$ and $v_f$ are the velocity components of the Rankine-Hugoniot shock jump conditions. The shock jump conditions are well-known, and are easily derived, for the ideal gas equation of state. For more complex equations of state, and for material mixtures, the jump conditions cannot be derived analytically. The $dF/d\psi$ term is instead found using a simple numerical derivative. Comparisons with the results in [78] for a single-phase, ideal gas illustrate that using a numerical derivative, with an appropriately chosen step size, is sufficiently accurate.

The shape of the shock front is unknown, but the incoming streamline intersects the shock at $(r_f, z_f)$. Ahead of the shock, all streamlines are parallel to the flow direction, as shown in Figure 8.2. This implies that,

ahead of the shock, $\rho$ and $v$ are independent of $r$:

$$\left(\frac{\partial\psi}{\partial r}\right)_z = -r\rho v, \tag{8.32}$$

so that

$$\psi = \int -r\rho v dr = -\rho v \int r dr,$$

and hence

$$\psi = -\frac{1}{2}r^2\rho v. \tag{8.33}$$

Ahead of the shock it is known that $\rho = \rho_0$, where $\rho_0$ is the initial density of the unreacted material; $v = -D$, where $D$ is the steady detonation velocity; and $r = r_f$, where $r_f$ is the radial coordinate of the shock front, so that

$$\psi = \frac{1}{2}\rho_0 D r_f^2,$$

so that

$$\frac{\partial\psi}{\partial r_f} = \rho_0 D r_f,$$

and hence

$$\frac{\partial r_f}{\partial\psi} = \frac{1}{\rho_0 D r_f}. \tag{8.34}$$

The final variable to be determined is the density. The density is calculated via (8.8), so the derivative $\dfrac{\partial r}{\partial\psi}$ needs to be determined. This derivative also forms part of the master equation and is related to the streamline divergence:

$$\begin{aligned}
\frac{\partial r}{\partial\psi} &= \frac{\partial}{\partial\psi}\left(r_f + F(\psi)(z - z_f)\right) \\
&= \frac{dr_f}{d\psi} + \frac{dF}{d\psi}(z - z_f) + F\frac{d(z - z_f)}{d\psi} \\
&= \frac{1}{\rho_0 D r_f} + \frac{dF}{d\psi}(z - z_f) + F\frac{dz}{d\psi} - F\frac{dz_f}{d\psi} \\
&= \frac{1}{\rho_0 D r_f} + \frac{dF}{d\psi}(z - z_f) + F\left(\frac{\partial z}{\partial z}\frac{\partial z}{\partial\psi} + \frac{\partial z}{\partial r}\frac{\partial r}{\partial\psi}\right) - F\frac{\partial z_f}{\partial r_f}\frac{\partial r_f}{\partial\psi} \\
&= \frac{1}{\rho_0 D r_f} + \frac{dF}{d\psi}(z - z_f) + F\left(\frac{1}{r\rho u} - \frac{v}{u}\frac{1}{r\rho v}\right) - \frac{F}{\rho_0 D r_r}z'_f \\
&= \frac{1}{\rho_0 D r_f} + \frac{dF}{d\psi}(z - z_f) - \frac{F}{\rho_0 D r_f}z'f \\
&= \frac{1}{\rho_0 D r_f}\left(1 - F z'_f\right) + \frac{dF}{d\psi}(z - z_f),
\end{aligned}$$

where $z'_f = \dfrac{\partial z_f}{\partial r_f}$.

### 8.1.5. Solving the model

To solve the SSA model, each streamline must be solved separately, finding a value for the unknown a priori shock front curvature via a shooting method that uses the oblique shock conditions and the first and second CJ conditions as boundary conditions, much like the Chan-Kirby approach. To find a complete 2D solution with a finite number of streamlines, the curvature and slope at the shock front of the current streamline must be integrated to find slope and position of the next streamline.

To solve for a single streamline, the master equation and reaction rate are integrated. The radius, $r_f$, the slope of the shock front, $\frac{dz_f}{dr_f}$, and the curvature of the shock front, $\frac{d^2z_f}{dr_f^2}$ need to be known. The integration starts at the shock front, where the oblique shock conditions apply, and goes to the sonic locus where the 1st and 2nd CJ conditions, given by (8.23)-(8.24), apply.

As the curvature of the shock front is unknown a priori, an optimisation package, Minpack [36], is used to solve the shooting problem with the given boundary conditions and a given $r_f$ and $\frac{dz_f}{dr_f}$. The optimisation algorithm minimises the difference between the 1st and 2nd CJ conditions to determine a solution for $\frac{d^2z_f}{dr_f^2}$.

### 8.1.6. Validation

To validate the derivation of the SSA for a general equation of state, the polytropic equation of state with $\gamma = 3$ and $Q = \frac{1}{2(\gamma^2-1)}$ is used and comparisons are made with results from [78]. The shock front slope at the edge, $\frac{\partial y_f}{\partial x_f}$, is taken to be $-\sqrt{\frac{\gamma-1}{\gamma+1}}$ which results from shock polar theory.

The reaction rate is given by a simple, pressure-dependent expression,

$$\frac{\partial \lambda}{\partial t} = \frac{1}{\tau_h} p^n (1-\lambda)^m , \tag{8.35}$$

where $\tau_h$ is a rate constant and $n$ and $m$ are fitted parameters. A range of parameters are explored for the comparisons and these are given in Table 8.1.

The results should be identical to those in [78] excepting any minor differences resulting from differences in numerical techniques and tolerances. The comparisons for the diameter effect curve (VoD curve) in slab geometry are shown in Figure 8.3 and for cylindrical geometry in Figure 8.4. Diameter effect comparisons between this implementation with a general equation

| $n$ | 0 | 1 | 1.7 | 2 |
|---|---|---|---|---|
| $1/\tau_h$ | 0.31434 | 0.680991 | 1.17138 | 1.47839 |

Table 8.1.: Reaction rate parameters (see (8.35)) used for slab and cylindrical geometry simulations with $m = 1/2$. The variables are non-dimensionalised so that $\rho_0 = 1$ and $D_{\text{CJ}} = 1$.

of state and the results in [78] show a good match for a variety of rate parameters, detonation velocities and for both slab and cylindrical geometry. However, there is some discrepancy in the curves, particularly for cylindrical geometry for higher $n$. Possible reasons for this are suggested below.

Interestingly, for $n = 0$, shown in the top of Figure 8.3, the results for this implementation extend to much lower detonation velocities than in [78]. It is unknown why there are no DNS or SSA results for the lower detonation velocities in [78] but it is pleasing that this implementation extends to lower detonation velocities and appears to carry on with the general trend.

Figure 8.5 shows a DDZ profile from the DNS and SSA results from [78] and from this implementation. There is a substantial discrepancy between the length of the DDZ on axis between the SSA and DNS. Furthermore, there is a difference between the two implementations of SSA with this implementation being shorter in both the axial and radial directions. This is most likely due to the use of the coordinate transformation to avoid the singularity at the sonic locus. This was not used in [78] so it is unclear if the differences are due to numerical problems Watt et al. would have to have overcome at the sonic locus.

Convergence of the solution for this implementation, when the number of streamlines is increased, shows that the numerical result is a faithful approximation of the underlying model. Convergence is demonstrated in Figure 8.6 as the streamlines step is decreased from $dr = 1.0$ to $dr = 0.2$ and then $dr = 0.1$. It is clear from these results that a step size of $dr = 1.0$ is not enough. Since there was no convergence study provided in [78] it is difficult to determine whether the published result represents an accurate solution of the SSA model. However, these results were also replicated by Cartwright in [25] who also found that for n = 1.7,2.0 the detonation velocity was slighter larger than in Watt et al. Cartwright then showed that using a larger step in $z_f$ between streamlines shifted both diameter effect curves towards the DNS results and the results of Watt et al were recovered. Therefore, it can be argued that the results published in [78] are somewhat misleading as they quickly converge to a solution away from the DNS results when fewer streamlines are used.

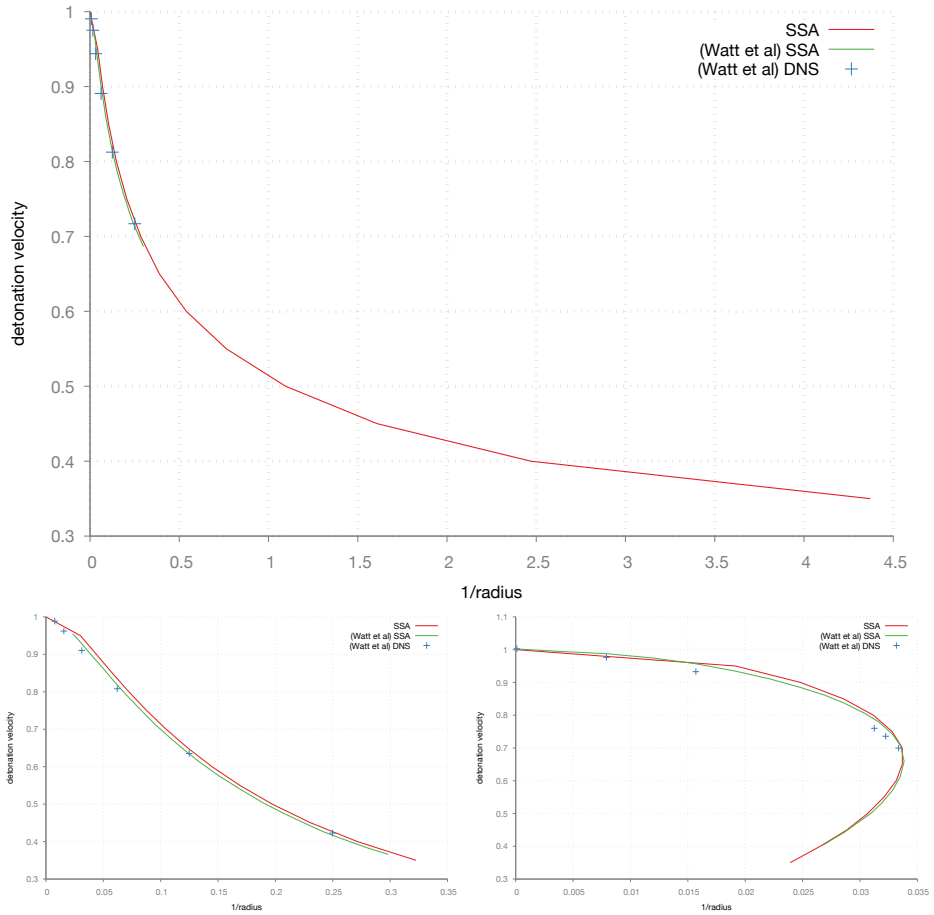


Figure 8.3.: Diameter effects in slab geometry for $m = 1/2$ and $n = 0$ (top), $n = 1$ (bottom left) and $n = 2$ (bottom right). Results from the SSA and DNS simulations from [78] are shown with the results from this implementation.

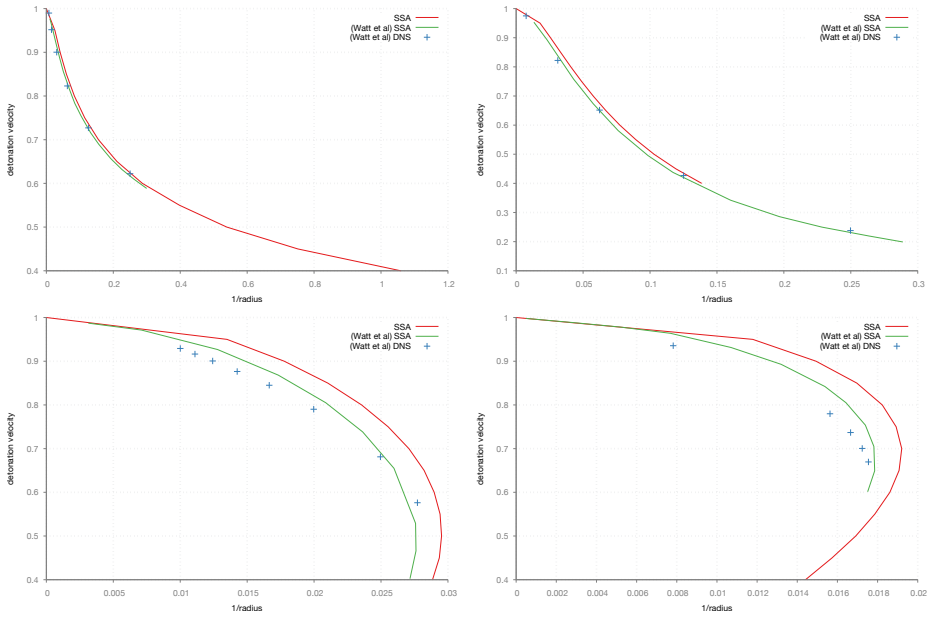


Figure 8.4.: Diameter effects in cylindrical geometry for $m = 1/2$ and $n = 0$ (top left), $n = 1$ (top right), $n = 1.7$ (bottom left) and $n = 2$ (bottom right). Results from the SSA and DNS simulations from [78] are shown with the results from this implementation.

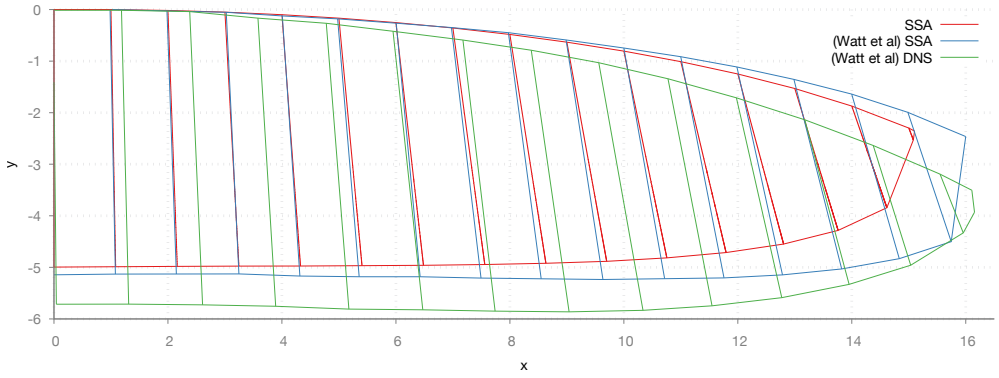


Figure 8.5.: The detonation driving zone from the SSA theory (blue) and DNS results (green) in [78] with this work's implementation of the SSA (red) for $D = 0.8D_{\mathrm{CJ}}$, $n = 1$ and $m = 1/2$ in slab geometry.

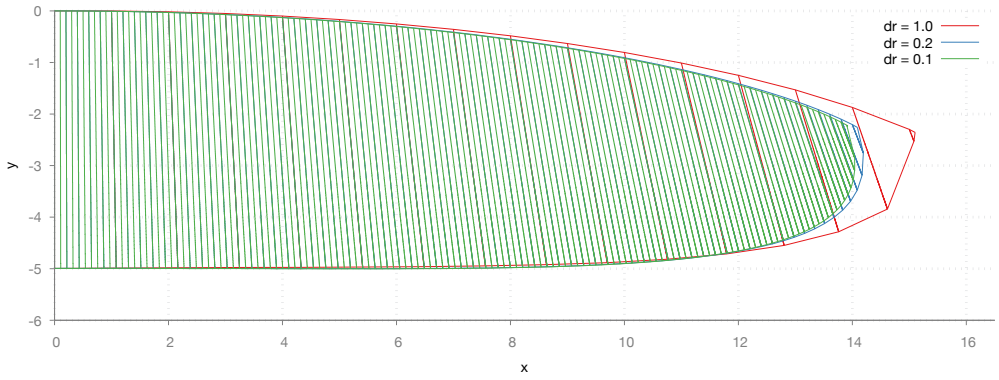


Figure 8.6.: The detonation driving zone with step sizes of $dr = 1.0$ (red), $dr = 0.2$ (blue) and $dr = 0.1$ (green). Convergence of the DDZ illustrates faithful representation of the SSA model.

## 8.2. Multiphase mechanical equilibrium extension

As outlined in Chapter 6, using a single phase to model a non-ideal explosive fails to take into account the multiphase nature of non-ideal condensed explosives or the effect of the transition to the reacted gaseous products. Furthermore, while using a polytropic equation of state to model a non-ideal explosive does make the equations and calculations simpler, it fails to capture the nature of a porous explosive.

As an extension to the SSA theory for an ideal gas proposed by Watt et al., this section describes the adaptation of this theory to a multiphase mechanical equilibrium straight streamline approach (MMESSA) that uses more suitable equations of state and reaction rates for non-ideal explosives.

The next section will outline the derivation of the master equation for the MMESSA and will illustrate the differences in the other relevant equations compared to the single-phase SSA. The final section, §8.2.4, looks at comparisons between the MMESSA and DNS solutions of the same unconfined, non-ideal detonation problems.

### 8.2.1. Multiphase mechanical equilibrium model

To incorporate the multiphase nature of non-ideal explosives, the underlying system of equations for the SSA is changed to that of the multiphase mechanical equilibrium model, outlined in §7.1. The governing equations,

(7.1)-(7.4), are repeated below:

$$\frac{\partial \alpha_k}{\partial t} + \mathbf{u} \cdot \nabla \alpha_k - \alpha_k \left( \frac{\rho c^2}{\rho_k c_k^2} - 1 \right) \nabla \cdot \mathbf{u} = \dot{\alpha}_k, \tag{8.36}$$

$$\frac{\partial \alpha_k \rho_k}{\partial t} + \nabla \cdot \alpha_k \rho_k \mathbf{u} = \rho \dot{\lambda}_k, \tag{8.37}$$

$$\frac{\partial \rho \mathbf{u}}{\partial t} + \nabla \cdot (\rho \mathbf{u} \otimes \mathbf{u}) + \nabla p = 0, \tag{8.38}$$

$$\frac{\partial \rho E}{\partial t} + \nabla \cdot ((\rho E + p)\, \mathbf{u}) = 0. \tag{8.39}$$

The multiphase mechanical equilibrium model in this form has $k$ continuity equations. To make use of the streamline function $\psi$, as in (8.7) and (8.8), we need just one continuity equation. To obtain this, the $k$ equations for $\rho_k$ are summed to give a single mixture density via (7.5):

$$\rho = \sum_k \alpha_k \rho_k. \tag{8.40}$$

This implies that the streamline function has the same definition as given in the case of the Euler equations so the operators and derivatives remain unchanged to those outlined in §8.1.1. The densities are then calculated via a rearrangement of (7.6),

$$\alpha_k = \frac{\lambda_k \rho}{\rho_k}. \tag{8.41}$$

This implies that $\alpha_k$ and $\lambda_k$ are known. In the single-phase SSA, $\lambda$ was evolved along the streamline via the rate equation. For the multiphase approach, each $\lambda_k$ is evolved in a similar way via each rate equation for each material.

Similarly, an ODE needs to be added to the integration to evolve the volume fraction, $\alpha_k$. The differential equation for this conservation of species mass density,

$$\cancelto{0}{\frac{\partial \alpha_k}{\partial t}} + \mathbf{u} \cdot \nabla \alpha_k - K_k \nabla \cdot \mathbf{u} - (M_k + H_k) = 0,$$

is specialised to the streamline coordinate system,

$$v \frac{\partial \alpha_k}{\partial z} - K_k \left( \frac{u}{r} - r \rho v^2 \frac{\partial r^2}{\partial \psi \partial z} + \frac{v^3}{u} \frac{\partial r}{\partial z} \frac{\partial^2 r}{\partial z^2} + \frac{\partial v}{\partial z} \right) = M_k + H_k,$$

to give an ODE for volume fraction,

$$\boxed{\frac{\partial \alpha_k}{\partial z} = \frac{1}{v} \left( K_k \left( \frac{u}{r} - r \rho v^2 \frac{\partial^2 r}{\partial \psi \partial z} + \frac{v^3}{u} \frac{\partial r}{\partial z} \frac{\partial^2 r}{\partial z^2} + \frac{\partial v}{\partial z} \right) + M_k + H_k \right).} \tag{8.42}$$

The final ODE to obtain is the master equation. Starting again from the conservation of energy with the definition of internal energy,

$$e = \sum_k \lambda_k e_k \left(\rho_k, p\right), \tag{8.43}$$

as shown in §7.1, (8.39) can be written as

$$\begin{aligned} 0 = \rho \sum_k \left(h_k - \frac{c_k^2}{\Gamma_k}\right) \dot{\lambda}_k - \frac{\rho}{\Gamma} \mathbf{u} \cdot \left(\mathbf{u} \cdot \nabla\right) \mathbf{u} \\ + \sum_k \frac{c_k^2 \rho_k}{\Gamma_k} \left[K_k \left(\nabla \cdot \mathbf{u}\right) + H_k + M_k\right] + \sum_k \frac{\alpha_k \rho_k c_k^2}{\Gamma_k} \left(\nabla \cdot \mathbf{u}\right). \end{aligned} \tag{8.44}$$

This is identical to (7.25). However, note that

$$\begin{aligned} &\sum_k \frac{c_k^2 \rho_k}{\Gamma_k} K_k \left(\nabla \cdot \mathbf{u}\right) + \sum_k \frac{\alpha_k \rho_k c_k^2}{\Gamma_k} \left(\nabla \cdot \mathbf{u}\right) \\ &\quad = \sum_k \frac{\alpha_k \rho_k c_k^2}{\Gamma_k} \left(\frac{\rho c^2}{\rho_k c_k^2} - 1\right) \nabla \cdot \mathbf{u} + \sum_k \frac{\alpha_k \rho_k c_k^2}{\Gamma_k} \left(\nabla \cdot \mathbf{u}\right) \\ &\quad = \sum_k \frac{\alpha_k \rho c^2}{\Gamma_k} \nabla \cdot \mathbf{u} - \frac{\alpha_k c_k^2 \rho_k}{\Gamma_k} \nabla \cdot \mathbf{u} + \frac{\alpha_k \rho_k c_k^2}{\Gamma_k} \nabla \cdot \mathbf{u} \\ &\quad = \frac{\rho c^2}{\Gamma} \nabla \cdot \mathbf{u}, \end{aligned}$$

so that (8.44) becomes

$$\begin{aligned} 0 = \rho \sum_k \left(h_k - \frac{c_k^2}{\Gamma_k}\right) \dot{\lambda}_k - \frac{\rho}{\Gamma} \mathbf{u} \cdot \left(\mathbf{u} \cdot \nabla\right) \mathbf{u} \\ + \sum_k \frac{c_k^2 \rho_k}{\Gamma_k} \left(H_k + M_k\right) + \frac{\rho c^2}{\Gamma} \nabla \cdot \mathbf{u}. \end{aligned} \tag{8.45}$$

In axisymmetric streamline coordinates this becomes

$$
\begin{aligned}
0 &= \rho \sum_k \left( h_k - \frac{c_k^2}{\Gamma_k} \right) \dot{\lambda}_k + \sum_k \frac{c_k^2 \rho_k}{\Gamma_k} \left( H_k + M_k \right) \\
&\quad + \frac{\rho}{\Gamma} \left( -uv \frac{\partial u}{\partial z} - v^2 \frac{\partial v}{\partial z} + c^2 \left( \frac{u}{r} - r\rho v^2 \frac{\partial}{\partial \psi} \left( \frac{u}{v} \right) + \frac{\partial v}{\partial z} \right) \right) \\
&= \rho \sum_k \left( h_k - \frac{c_k^2}{\Gamma_k} \right) \dot{\lambda}_k + \sum_k \frac{c_k^2 \rho_k}{\Gamma_k} \left( H_k + M_k \right) \\
&\quad + \frac{\rho}{\Gamma} \left( -uv \frac{\partial}{\partial z} \left( v \frac{\partial r}{\partial z} \right) - v^2 \frac{\partial v}{\partial z} + c^2 v \left( \frac{\partial r}{\partial z} \frac{1}{r} + \left( \frac{\partial r}{\partial \psi} \right)^{-1} \frac{\partial^2 r}{\partial z \partial \psi} \right) + c^2 \frac{\partial v}{\partial z} \right) \\
&= \rho \sum_k \left( h_k - \frac{c_k^2}{\Gamma_k} \right) \dot{\lambda}_k + \sum_k \frac{c_k^2 \rho_k}{\Gamma_k} \left( H_k + M_k \right) \\
&\quad + \frac{\rho}{\Gamma} \left( -uv^2 \frac{\partial^2 r}{\partial z^2} - uv \frac{\partial r}{\partial z} \frac{\partial v}{\partial z} - v^2 \frac{\partial v}{\partial z} + c^2 v \left( \frac{\partial r}{\partial z} \frac{1}{r} + \left( \frac{\partial r}{\partial \psi} \right)^{-1} \frac{\partial^2 r}{\partial z \partial \psi} \right) + c^2 \frac{\partial v}{\partial z} \right) \\
&= \rho \sum_k \left( h_k - \frac{c_k^2}{\Gamma_k} \right) \dot{\lambda}_k + \sum_k \frac{c_k^2 \rho_k}{\Gamma_k} \left( H_k + M_k \right) \\
&\quad + \frac{\rho}{\Gamma} \left( -v^3 \frac{\partial r}{\partial z} \frac{\partial^2 r}{\partial z^2} - u^2 \frac{\partial v}{\partial z} - v^2 \frac{\partial v}{\partial z} + c^2 v \left( \frac{\partial r}{\partial z} \frac{1}{r} + \left( \frac{\partial r}{\partial \psi} \right)^{-1} \frac{\partial^2 r}{\partial z \partial \psi} \right) + c^2 \frac{\partial v}{\partial z} \right).
\end{aligned}
$$

Therefore, the coefficients of the $\dfrac{\partial v}{\partial z}$ terms are

$$
\begin{aligned}
-\frac{\rho}{\Gamma} \left( v^2 + u^2 - c^2 \right) &= -\frac{\rho}{\Gamma} v^2 \left( 1 + \frac{u^2}{v^2} - c^2 \right) \\
&= -\frac{\rho}{\Gamma} \left[ v^2 \left( 1 + \left( \frac{\partial r}{\partial z} \right)^2 - c^2 \right) \right].
\end{aligned}
$$

When the equation is rearranged for $\dfrac{\partial v}{\partial z}$, both sides are multiplied by $\dfrac{\Gamma}{\rho}$ and the $-\dfrac{\rho}{\Gamma}$ at the front of the brackets disappears. The non-$\dfrac{\partial v}{\partial z}$ terms and are

$$
\begin{aligned}
&\Gamma \sum_k \left( h_k - \frac{c_k^2}{\Gamma_k} \right) \dot{\lambda}_k - v^3 \frac{\partial r}{\partial z} \frac{\partial^2 r}{\partial z^2} \\
&\quad + \frac{\Gamma}{\rho} \sum_k \frac{c_k^2 \rho_k}{\Gamma_k} \left( H_k + M_k \right) + c^2 v \left( \frac{1}{r} \frac{\partial r}{\partial z} + \frac{\partial^2 r}{\partial \psi \partial z} \left( \frac{\partial r}{\partial \psi} \right)^{-1} \right).
\end{aligned}
$$

The master equation is then:

$$\boxed{\frac{\partial v}{\partial z}\left[v^2\left(1+\left(\frac{\partial r}{\partial z}\right)^2\right)-c^2\right]=\Gamma\sum_k\left(h_k-\frac{c_k^2}{\Gamma_k}\right)\dot{\lambda}_k-v^3\frac{\partial r}{\partial z}\frac{\partial^2 r}{\partial z^2}+\frac{\Gamma}{\rho}\sum_k\frac{c_k^2\rho_k}{\Gamma_k}\left(H_k+M_k\right)+c^2v\left(\frac{1}{r}\frac{\partial r}{\partial z}+\frac{\partial^2 r}{\partial\psi\partial z}\left(\frac{\partial r}{\partial\psi}\right)^{-1}\right).} \tag{8.46}$$

To avoid the singularity at the sonic locus, another coordinate transformation is made, as outlined in §6.1.1. The integrated variable becomes $\bar{z}$ so all ODEs are multiplied by

$$\frac{\partial z}{\partial\bar{z}}=\frac{c-\mathbf{u}}{c}. \tag{8.47}$$

To be able to calculate the sound speed, each material sound speed must be known. This means that the pressure must also be calculated. As before, Bernoulli's equation is used to calculate the pressure. Note that the mechanical equilibrium model implies pressure and velocity equilibrium between the materials so that pressure is the same for both materials. The pressure is given by

$$p=\frac{\frac{D^2-\mathbf{u}^2}{2}-\sum_k\lambda_k\left(e_{\mathrm{ref},k}-\frac{p_{\mathrm{ref},k}}{\Gamma_k\rho_k}\right)+\frac{p_0}{\rho_0}+e_0}{\frac{1}{\rho}+\sum_k\frac{\lambda_k}{\Gamma_k\rho_k}}. \tag{8.48}$$

## 8.2.2. Solving the model

To solve the model, the same algorithms to solve the SSA model are utilised, as outlined in §8.1.5. The only exception is that to determine the slope at the charge edge for the multiphase solution, Afanasenkov theory is used, as outlined for the Chan-Kirby model in §7.4.3.

## 8.2.3. Validation

To validate the multiphase implementation of the SSA, two polytropic tests are undertaken. Firstly, the same polytropic material in both materials is simulated to test that the multiphase equations reduce to the single-phase equations. Secondly, an example taken from Fickett [40] is simulated with $\gamma_u = 3.0$ and $\gamma_r = 1.4$ and results are compared to a DNS solution. The results of these validation tests are outlined below.

### Multiphase reduced to single phase

An initial test for the MMESSA is a two-material simulation with the same material in both phases. The multiphase mechanical equilibrium equations reduce to the single-phase equations when the same material is used in all

phases. This means that any multiphase implementation should produce similar results to a single-phase implementation if the materials are identical.

A multiphase material with a polytropic equation of state in both phases with $\gamma = 3.0$, and with $m = 1/2$ in (8.35) with the other rate parameters shown in Table 8.1, is modelled with the MMESSA and is compared to the single-phase results for the same parameters. A comparison of the DDZ and pseudocolour plots for pressure, density and reaction progress for $D = 0.8D_{\text{CJ}}$ is shown in Figure 8.7. The diameter effect curves are also compared in Figure 8.8. The comparison shows very minor, if any, difference between the implementation of the MMESSA and the single-phase SSA when the same material is used in both the unreacted phase and the reacted phase.

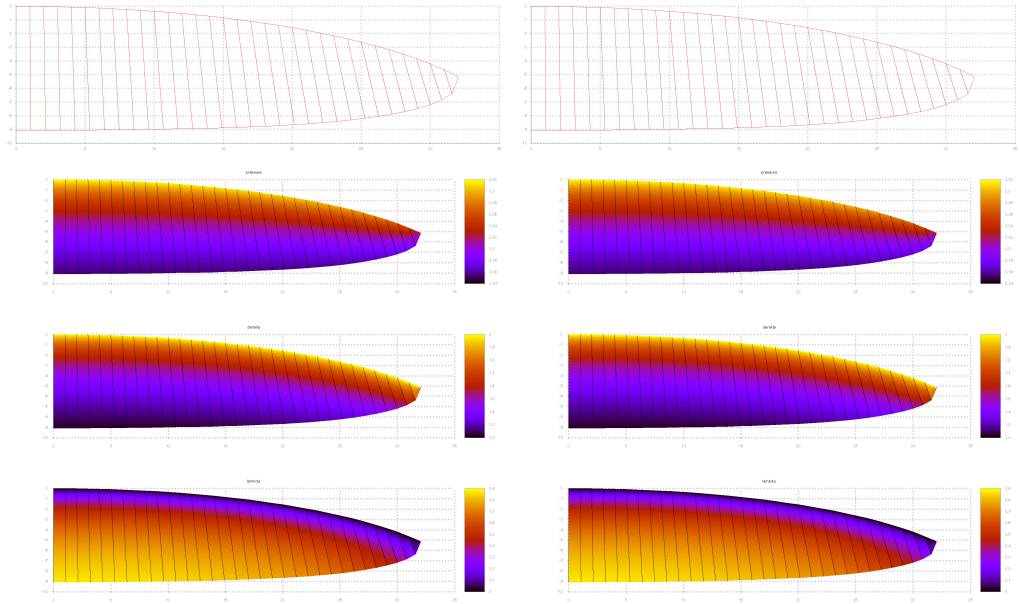

Figure 8.7.: Comparison between the single-phase SSA approach and the multiphase SSA approach with a polytropic equation of state with $\gamma = 3.0$ (in both phases for the multiphase simulation) in slab geometry $(x, y)$. The reaction rate parameters are $m = 1/2$ and $n = 2$ .The single-phase results are on the left and the multiphase results are on the right. The DDZ for the single-phase SSA (top left) and the multiphase DDZ (top right) are shown for $D = 0.8D_{\text{CJ}}$ as well as pseudocolour plots for pressure, density and reaction progress. In the limit that the materials are the same, the multiphase equations reduce to the single-phase equations. These results illustrate that the multiphase implementation reduces to the single-phase implementation and so we can be confident that the multiphase implementation is correct.

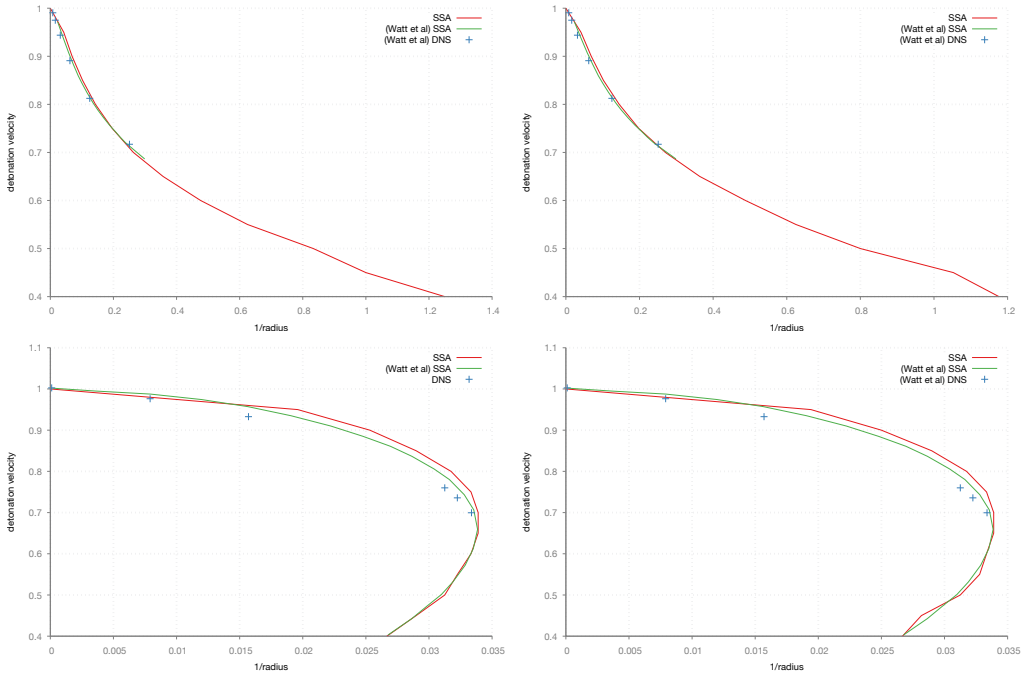


Figure 8.8.: Diameter effect comparisons between the single-phase SSA approach (left) and the multiphase SSA approach (right) with a polytropic equation of state with $\gamma = 3.0$ (in both phases for the multiphase simulation) in slab geometry. The reaction rate parameters are $m = \frac{1}{2}$ and $n = 0$ (top) and $n = 2$ (bottom). The results are very similar and again illustrate that the multiphase implementation is correct.

### Simple polytropic example

Figure 8.9 shows the diameter curve effect for MMESSA compared to the multiphase DNS for two polytropic materials with $\gamma_u = 3.0$ and $\gamma_r = 1.4$ and with reaction rate parameters $m = 1/2$, $n = 0$, $\tau_h = 5 \times 10^{-7}$. There is a surprisingly good match between the two results for the diameter effect curve, as shown in Figure 8.9. However, there is a better match for the smaller radii. There are two possible reasons for this. Firstly, these are very small numbers so any difference is smaller. Secondly, the DNS was not designed for modelling ideal gases, particularly at large, close-to-ideal radii, and so it is possible that the DNS results for the larger radii are incorrect. As mentioned in §6.2.3, the DNS cannot find stable solutions near the limit of $1/r = 0$ for the ideal gas example.

A closer inspection of one of these points is shown in Figure 8.10. At $D = 1400\text{ms}^{-1}$, the solution from the MMESSA (bottom half of image) is compared to DNS results (top half of the image). The black curves for the shock front and sonic locus are taken from the DNS results.

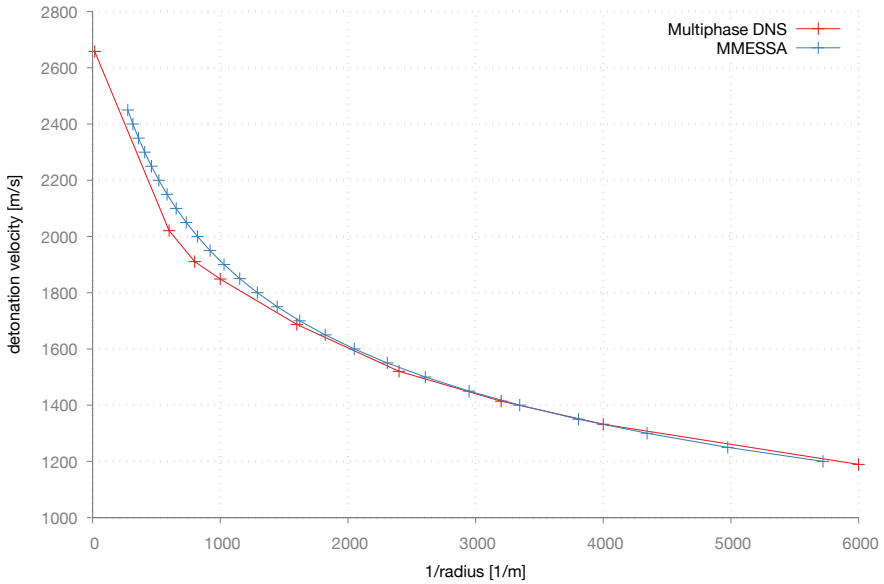


Figure 8.9.: The diameter effect curve for the MMESSA (blue) and DNS (red) with a polytropic equation of state in two phases with $\gamma_u = 3.0$ for the unreacted phase and $\gamma_r = 1.4$ for the reacted phase. The reaction rate is given by Equation (8.35) with $m = 1/2$, $n = 0$ and $\tau_H = 5 \times 10^{-7}$.

A good match between shock shape and radius is seen with a comparable match of pressure throughout the DDZ (compare the colours along the streamlines in the bottom half of the image with the flooded contours in the top half). There is an underestimation of the length of the DDZ on-axis and the edge of the charge is flatter than expected. Both of these discrepancies were also seen in the results of Watt et al. [78] and are surmised to be the result of the straight streamline approximation. The possible effects of this approximation will be discussed in §9.1.1. However, the DNS solution shows that the streamlines, plotted in black in Figure 8.10, are only very slightly curved and so the straight streamline approximation seems appropriate. The change in gradient of the streamlines is comparable to the change in gradient of the streamlines in MMESSA. There is, however, a slight kink in the streamlines just after the shock and the inclusion of this in the straight streamline approach could be beneficial.

Contour plots of the solutions on these streamlines for pressure, density and mass fraction are shown in Figure 8.11. A smooth solution for the DDZ is found, which can be more clearly seen in Figure 8.12.

One note to make is that in the contour plots it appears that the on-axis solution starts slightly set back from $(r, z) = (0, 0)$. As seen in the plot of the DDZ in Figure 8.12, this is not the case but is in fact an artefact of the interpolation used to produce the contour plots. This artificial offset is seen

throughout this work in the contour plots.

It is also shown in Figure 8.12 that the MMESSA has been implemented so that there are a greater number of streamlines at the charge edge. The streamlines are equally spaced in shock front gradient so that the region where there is most change in the curvature of the shock front, the charge edge, had a small enough step in $r$ to accurately determine a solution. This provides a more efficient way to calculate a more accurate solution.

In this polytropic example, due to the large range of diameters, the step in $r$ needed to be adjusted for ranges of detonation velocities so that each simulation would be efficient but accurate. There is also a large difference in the length of the DDZ for each detonation velocity and so the integration step, $dz$, along the streamline also needed to be adjusted for a trade-off between efficiency and accuracy for ranges of detonation velocity. It was found that a more accurate numerical integrator (8th-order Adams-Bashforth-Moulton method) with larger steps was more efficient and accurate than a greater number of steps in lower order numerical integrators (Runge-Kutta-Fehlberg, Runge-Kutta-Cash-Karp, Bulirsch-Stoer). With guidance on the step in $r$ and $z$, the entire diameter effect curve for a two-phase polytropic material, running different detonation velocities in parallel on four cores of a contemporary CPU, took under twelve seconds.

Given that in non-ideal explosives the diameter ranges are much narrower, the discrepancies discussed in this section do not cause any concern. Multiphase results for actual materials with realistic equations of state, that naturally have a narrower range of diameters, are shown in the following section.

### 8.2.4. Unconfined results

As for the results of the multiphase Chan-Kirby model in §7.3.3 and §7.4.4, the ammonium nitrate–based, non-ideal explosives EM120D and ANFO are simulated to compare the results of MMESSA with its parent PDE model. Full DNS calculations are used to highlight changes to the solution with the introduction of the straight streamline approach for unconfined detonations.

For the DNS and MMESSA comparisons below, only the variable values along the streamlines for the MMESSA solution are shown. The visualisation of these comparisons is limited by the type of output from the DNS and the visualisation software used to view this output. Interpolation between streamlines is particularly difficult with certain pieces of software and can often distort the solution with numerical smearing. It is also instructive to see the streamline nature of the MMESSA solutions.

Interpolation of the MMESSA results, using a different visualisation application, can be seen separately. However, this interpolation is also not without its problems and a slight offset on axis is seen at the shock front. This is due purely to the interpolation and the solution does indeed start

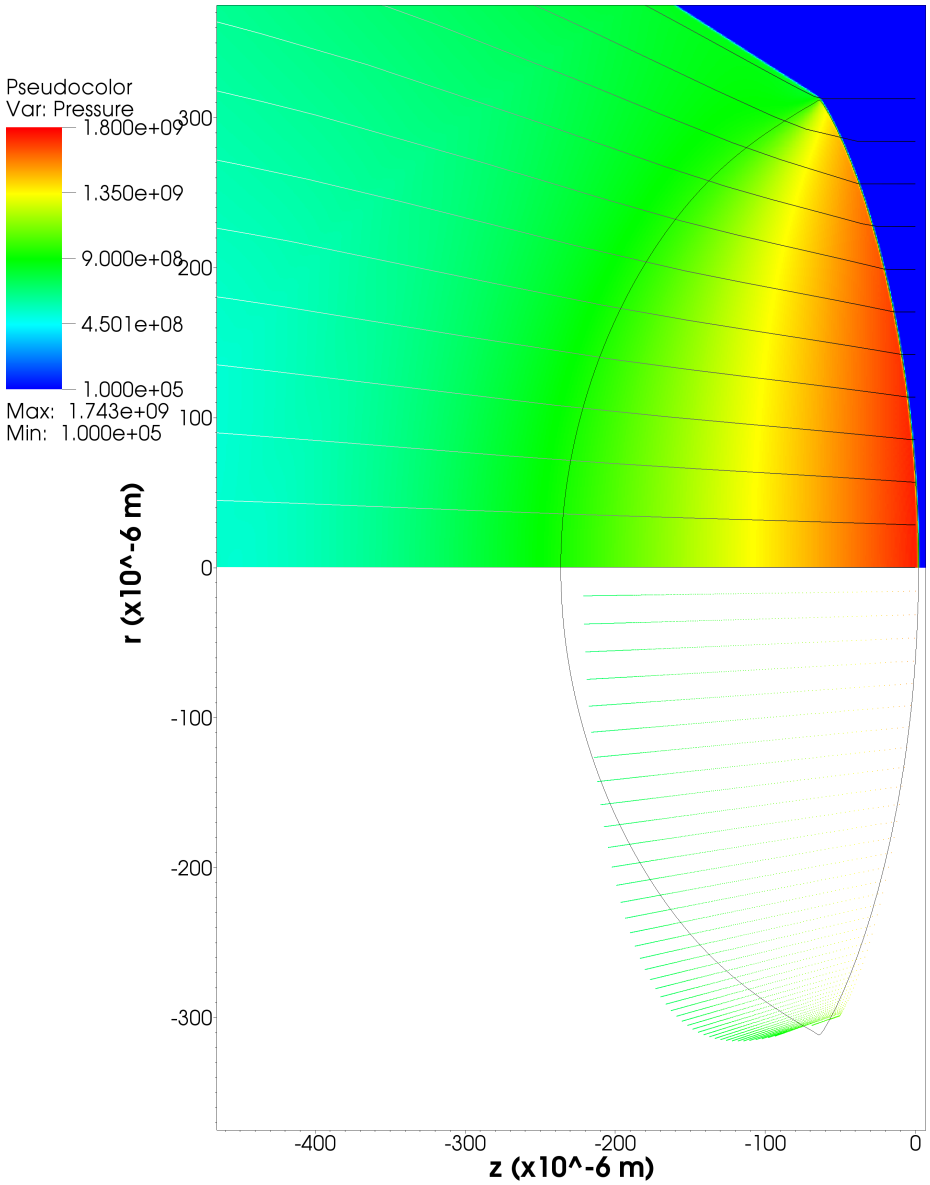


Figure 8.10.: Comparison between the DNS (top) and the MMESSA (bottom streamlines) for $D = 1400$ ms$^{-1}$ for the two material polytropic example. The straight black lines are the DNS streamlines and the curved black lines show the shock front and sonic locus of the DNS. A good match between shock shape and radius is seen with a comparable match of pressure [Pa] throughout the DDZ. There is an underestimation of the DDZ on-axis and the edge of the charge is flatter than expected.

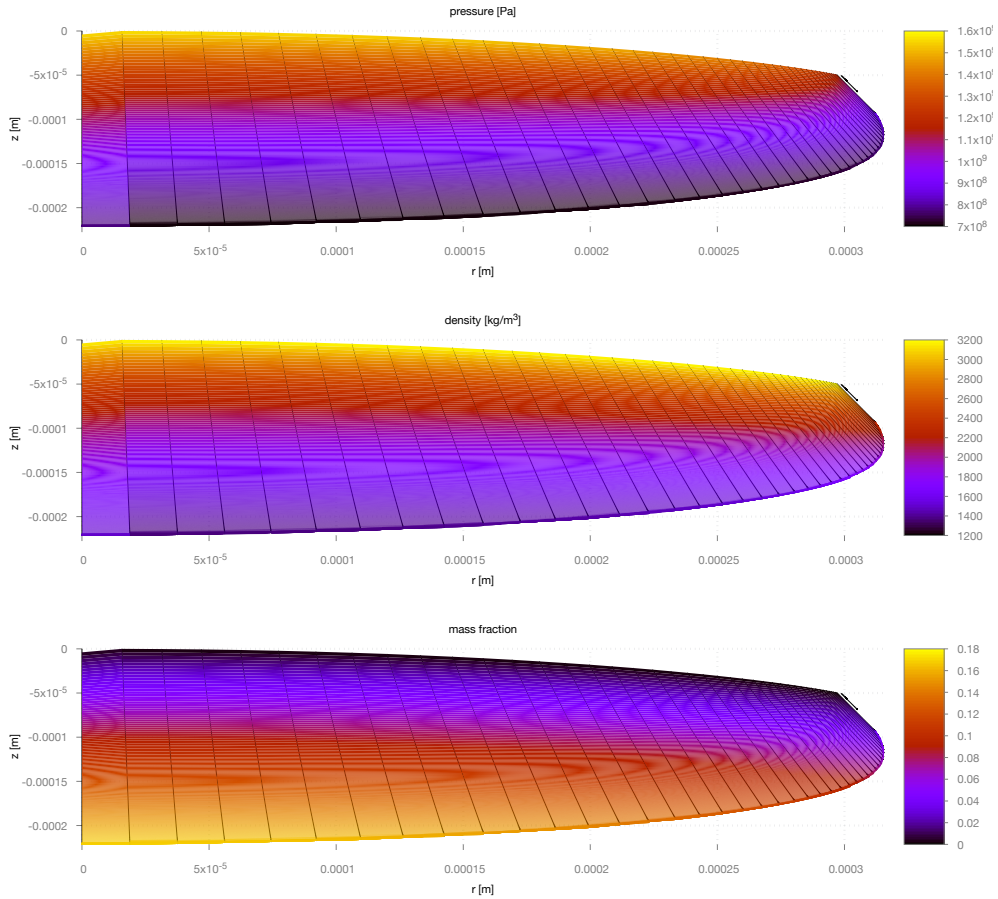


Figure 8.11.: Contour plots of pressure (top), density (middle) and reaction progress (bottom) calculated with MMESSA for a polytropic equation of state in two phases with $\gamma = 3.0$ for the unreacted phase and $\gamma = 1.4$ for the reacted phase, travelling at $D = 1400\ \mathrm{ms}^{-1}$. The reaction rate is given by Equation (8.35) with $m = 1/2$, $n = 0$, $\tau_h = 5 \times 10^{-7}$. As discussed in the text, the solution does start at $(r, z) = (0, 0)$, as shown in Figure 8.12, and the offset seen is a product of the interpolation used for the flooded contour plots.

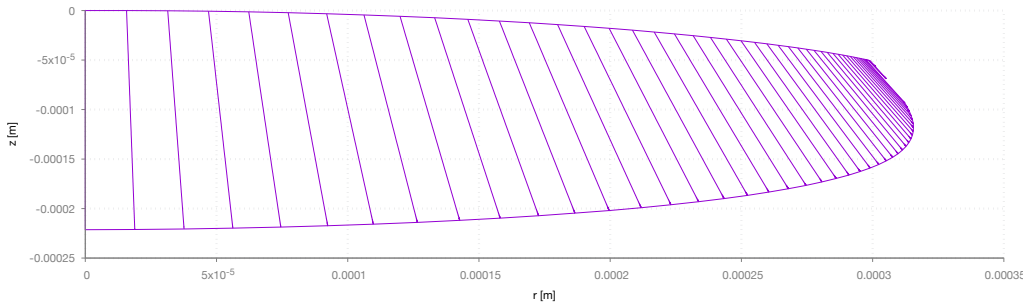


Figure 8.12.: Outline of the DDZ for the MMESSA for the two material polytropic example.

at $(r, z) = (0, 0)$. This in turn affects the position of the end of the on-axis solution and there is a visible positive gradient in the sonic locus from the on-axis solution to the first off-axis solution. However, not all of this is due to the interpolation problem and this will be discussed in §9.2.1.

The following sections illustrate the unconfined results for EM120D and ANFO in comparison to DNS and experimental results. Note that all variables are measured in standard units.

### EM120D

Figure 8.13 shows the diameter effect curve for unconfined EM120D for the MMESSA compared to a multiphase DNS simulation of the same materials and experimental results. The MMESSA underestimates the size of the radius but the shape of the diameter effect curves match well with some slight divergence at the lower detonation velocities where the radii are much smaller and similar relative errors have a bigger impact on the curve. The pressure and density pseudocolour plots, shown in Figures 8.14 and 8.15 for a lower and higher detonation velocity, respectively, further illustrate this. There appears to be a good match for the radius for $D = 4000\text{ms}^{-1}$ and a poor match for $D = 5400\text{ms}^{-1}$ but this is just due to the larger relative error in the larger inverse radius than the smaller inverse radius.

In both examples, the streamline solutions for the MMESSA are projected onto the pseudocolour plots from the DNS solutions. Despite the differences in radii, there is a good match of pressure and density along the streamlines throughout the DDZ, particularly near the axis and for the lower detonation velocity. Equivalent pseudocolour plots of pressure, density and mass fraction from the MMESSA simulations are are shown in Figures 8.16 and 8.17 to illustrate the full solution.

There is a distinct difference in the shape of the DDZ, particularly at the sonic locus at the charge edge. This squaring of the DDZ was also seen in the results of Watt et al. [78] and it is surmised that this is a result of the straight streamline approximation.

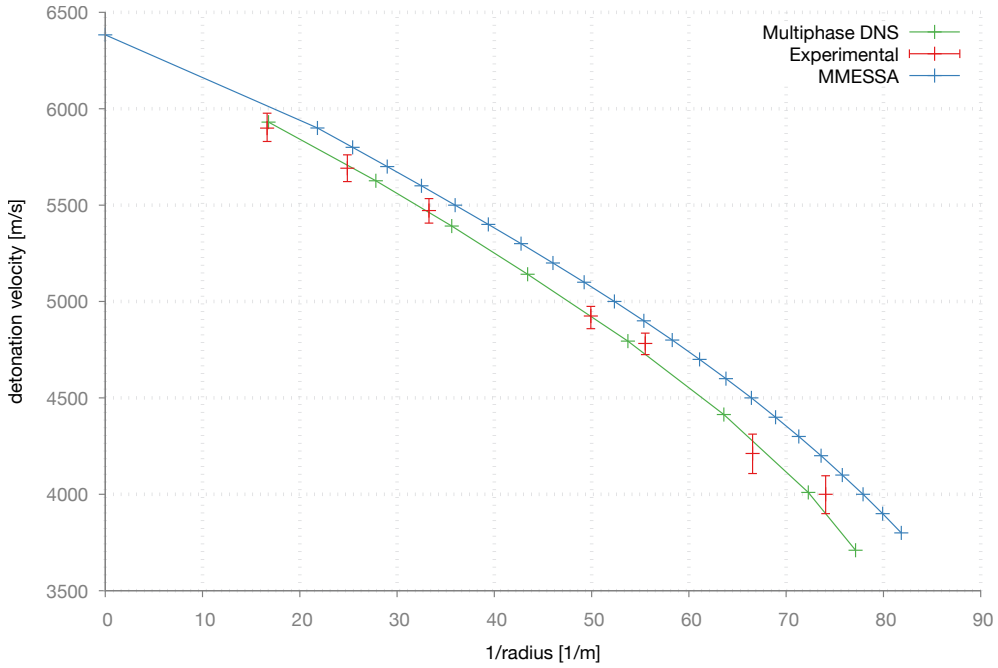


Figure 8.13.: Diameter effect for EM120D for the MMESSA (blue) and the multiphase DNS (green). Experimental points are also shown (red). Although MMESSA slightly underestimates the radius, there is a good match in shape with some slight divergence at the lower detonation velocities.

There is also a discrepancy in the length of the DDZ. For EM120D, the DDZ is in general longer than the DNS solutions. The polytropic examples in §8.2.3 (multiphase) and in [78] (single-phase) showed instead an underestimation of the DDZ. Again, the inconsistency and discrepancy in the length of the DDZ is surmised to be due to the straight streamline approximation and this will be discussed further in §9.1.1.

#### ANFO

The MMESSA is also used to simulate unconfined ANFO and the results are similarly compared to DNS solutions and experimental data. As shown in Figure 8.18, the MMESSA give a surprisingly good fit to both the experimental data and the DNS results. In fact, the MMESSA gives a better fit to the experimental results than the DNS for the lowest detonation velocities.

The pressure and density pseudocolour plots, shown in Figures 8.19 and 8.20 for a lower and higher detonation velocity, respectively, also show a good match between the MMESSA and the DNS with again some difference in the shape of the DDZ, particularly at the sonic locus at the charge edge.

Equivalent pseudocolour plots of pressure, density and mass fraction from

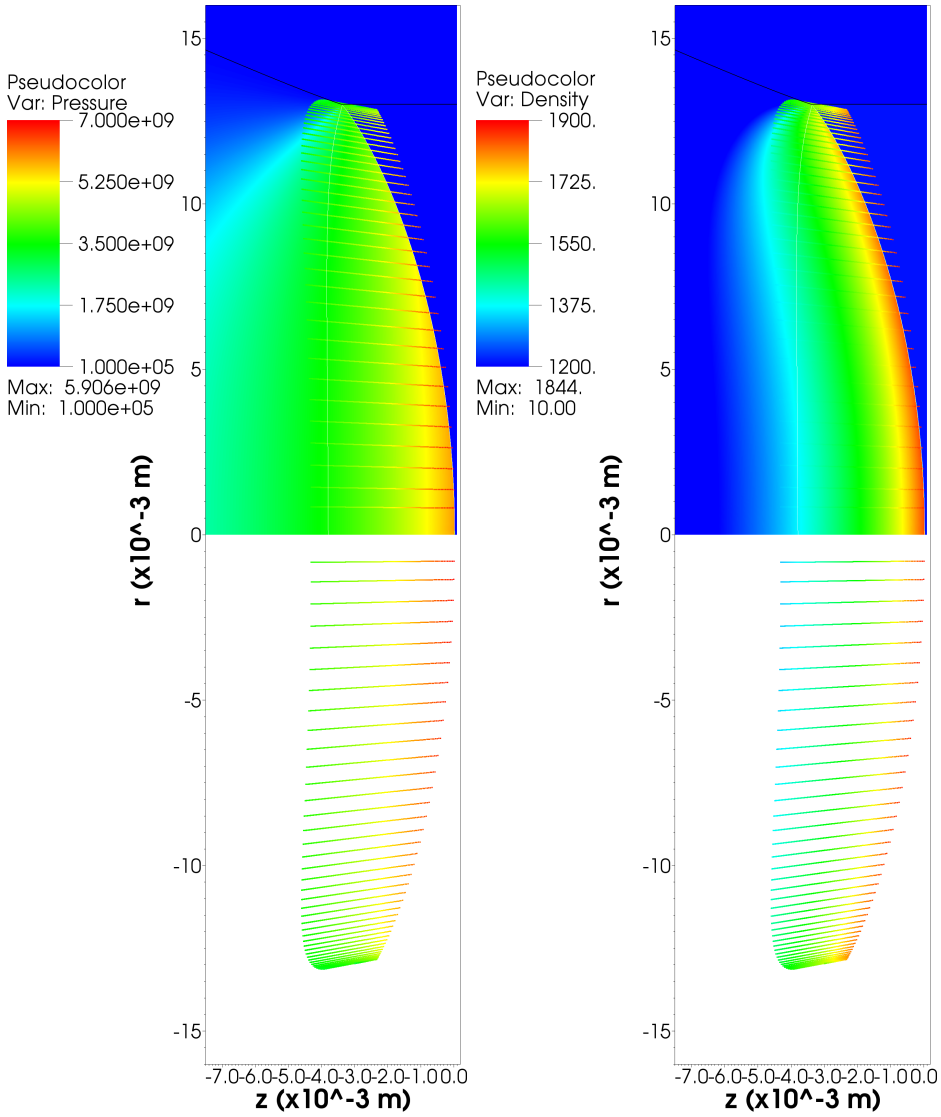


Figure 8.14.: Pseudocolour plots showing the DNS results (top) compared to the MMESSA results (overlayed on top and shown on bottom) for both pressure [Pa] (left) and density [kgm$^{-3}$] (left) for unconfined EM120D at $D = 4000$ ms$^{-1}$. The white line on the DNS results shows the sonic locus. The MMESSA results show overestimation of DDZ length but a good match for the radius for this lower detonation velocity.

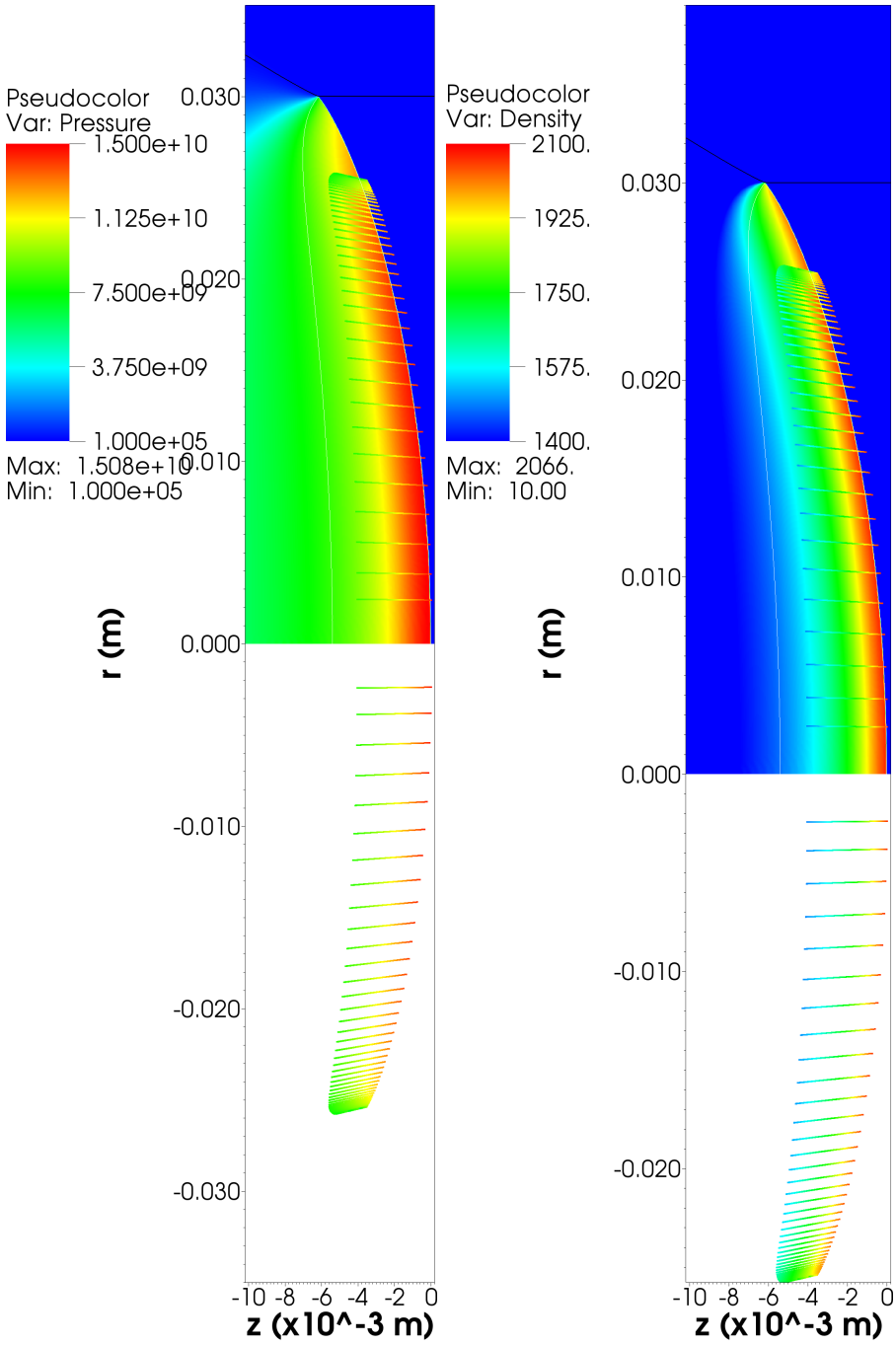


Figure 8.15.: Pseudocolour plots showing the DNS results (top) compared to the MMESSA results (overlayed on top and shown on bottom) for both pressure [Pa] (left) and density [kgm$^{-3}$] (right) for unconfined EM120D at $D = 5400$ ms$^{-1}$. The white line on the DNS results shows the sonic locus. The MMESSA results show underestimation of both DDZ length and radius for this higher detonation velocity.

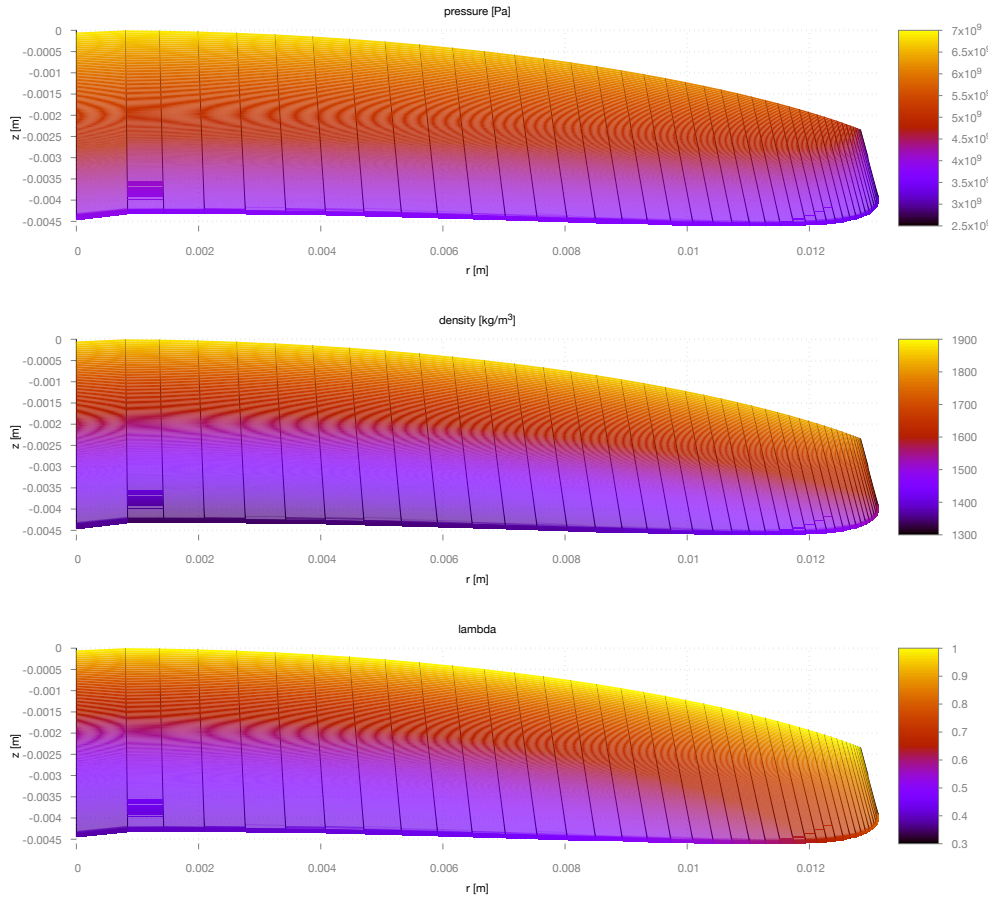


Figure 8.16.: Contour plots of pressure (top), density (middle) and reaction progress (bottom) for EM120D, travelling at $D = 4000$ ms$^{-1}$ in axisymmetric geometry $(r, z)$ for the MMESSA. These are equivalent to the results in Figure 8.14.

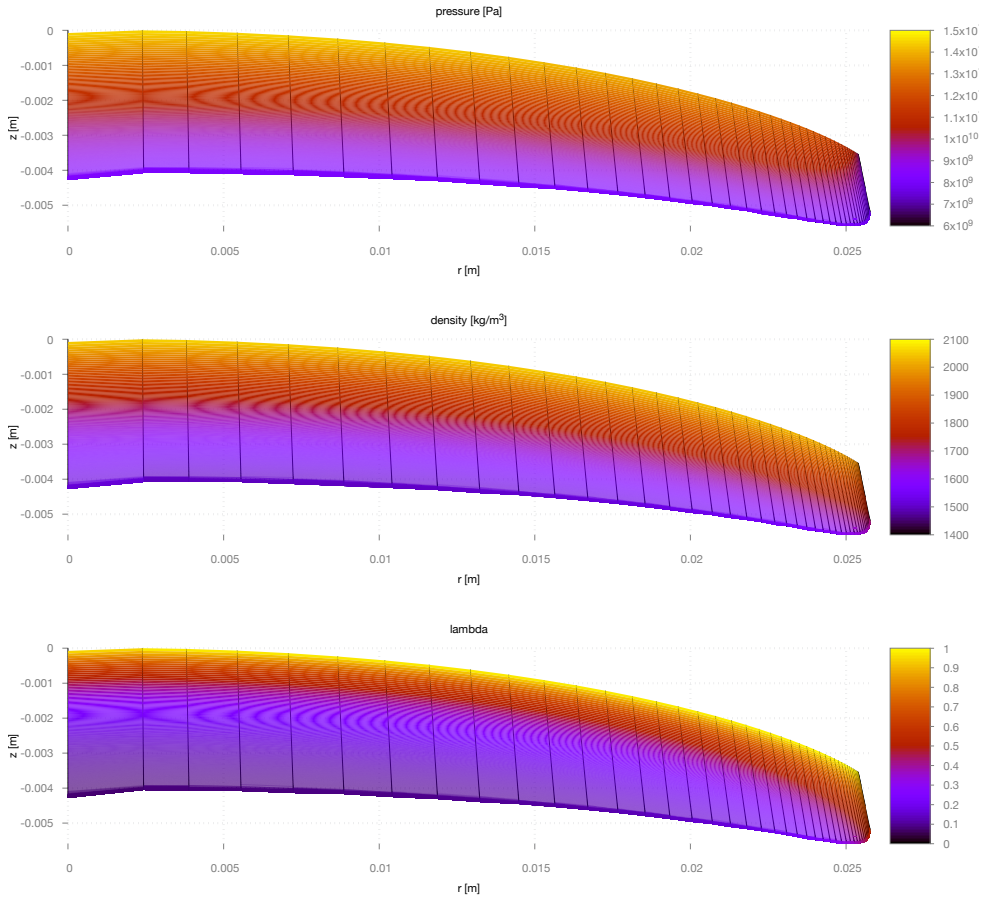


Figure 8.17.: Contour plots of pressure (top), density (middle) and reaction progress (bottom) for EM120D, travelling at $D = 5400$ ms$^{-1}$ in axisymmetric geometry $(r, z)$ for the MMESSA. These are equivalent to the results in Figure 8.15.

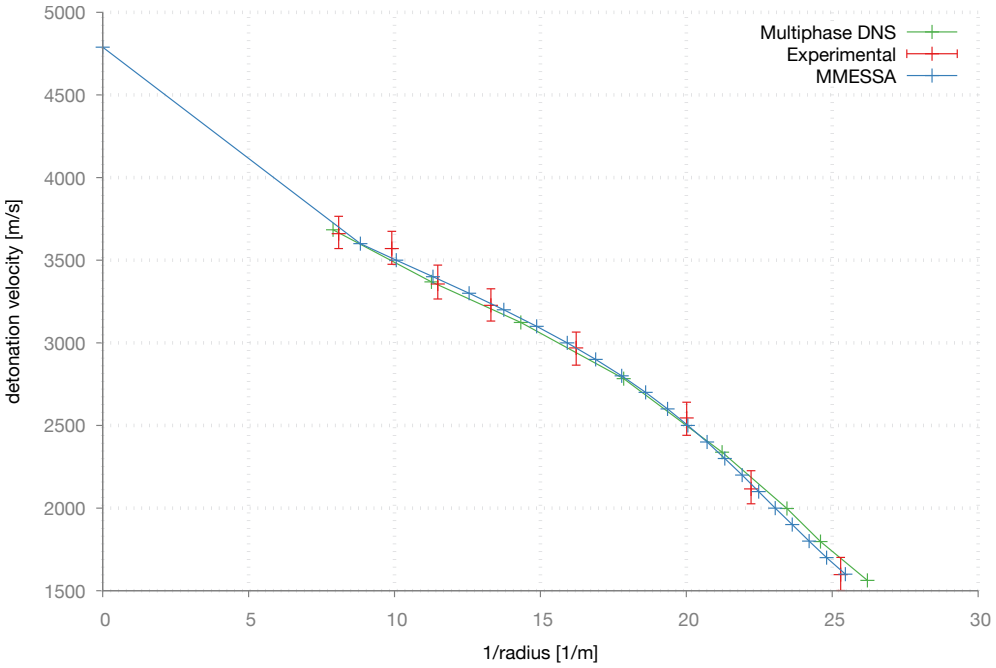


Figure 8.18.: Diameter effect for ANFO for MMESSA (blue) and the multiphase DNS (green). Experimental points are also shown (red).

the MMESSA simulations are are shown in Figures 8.21 and 8.22 to illustrate the full solution. Note that the sonic locus is concave at the charge axis. The possible reasons for this are discussed in §9.2.1.

Given the high porosity and non-ideal nature of ANFO, the close fit of the MMESSA to the experimental data and DNS solutions is promising for the use of the MMESSA in modelling non-ideal detonation. To further test capabilities of this approach, the next section looks at extending the theory to the same non-ideal explosives in confinement.

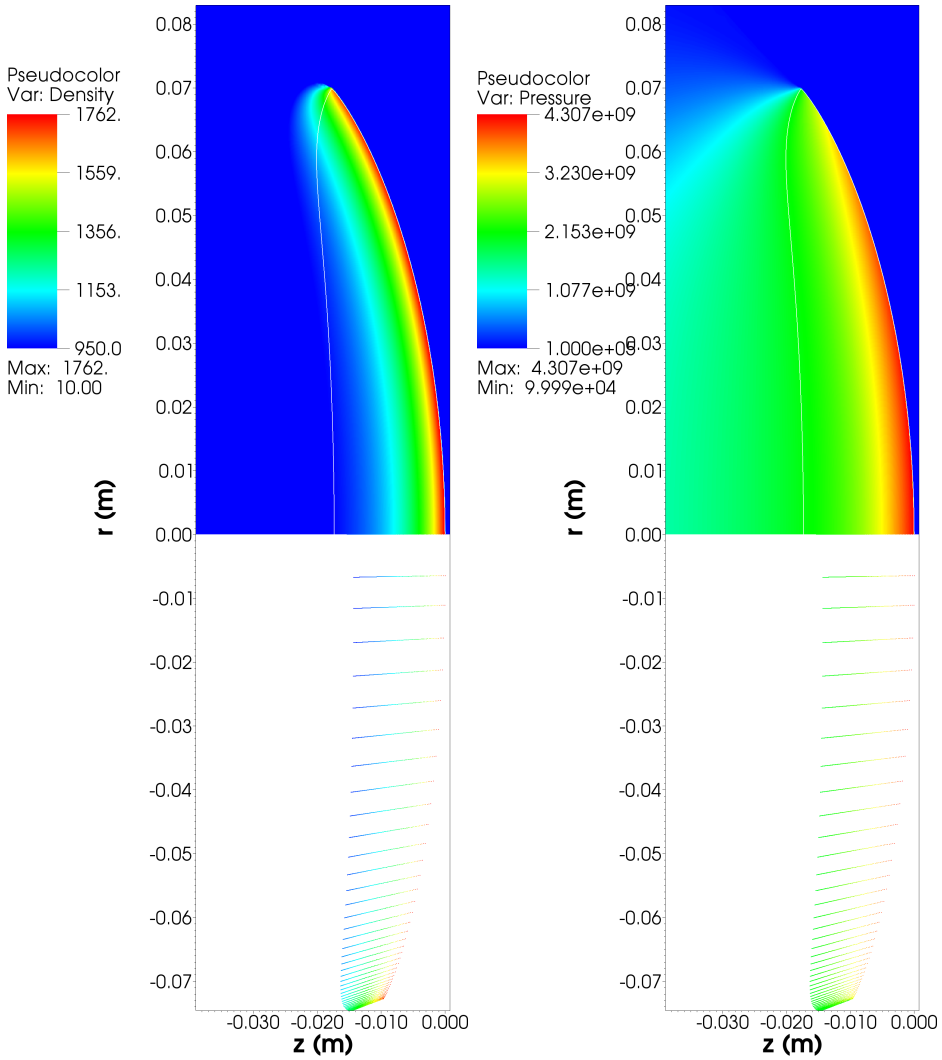


Figure 8.19.: Pseudocolour plots showing the DNS results (top) compared to the MMESSA results (bottom) for both density [kgm$^{-3}$] (left) and pressure [Pa] (right) for unconfined ANFO at $D = 3200$ ms$^{-1}$. The white line on the DNS results shows the sonic locus.

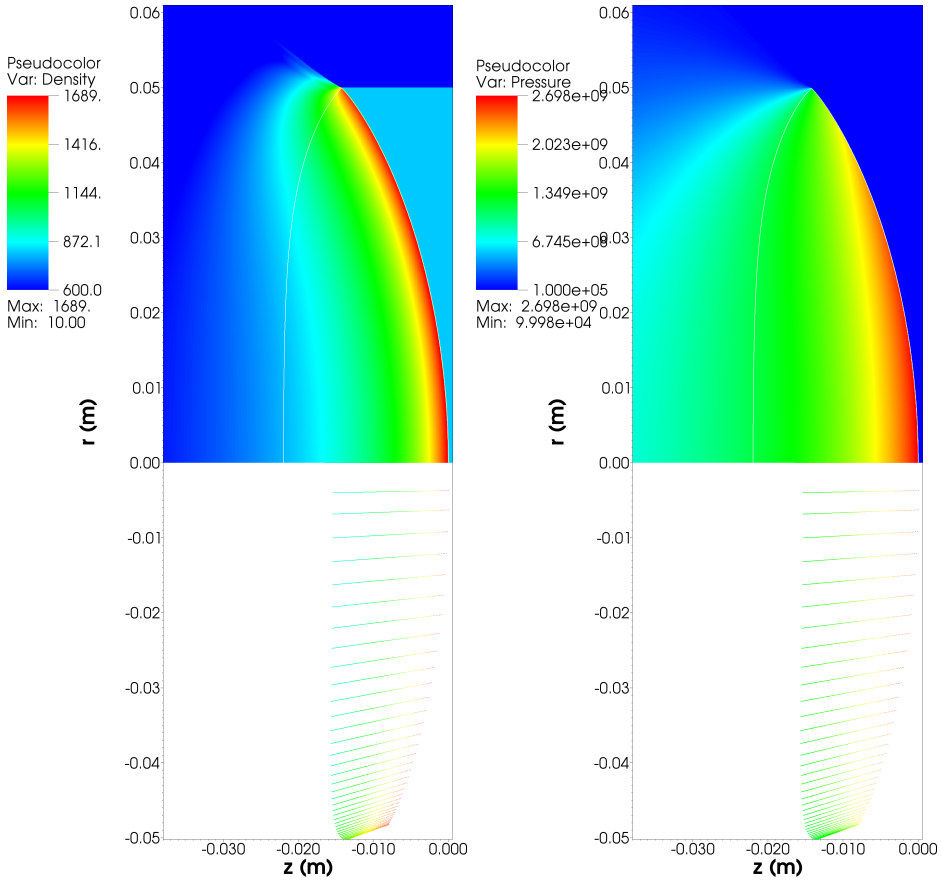


Figure 8.20.: Pseudocolour plots showing the DNS results (top) compared to the MMESSA results (bottom) for both density [kgm$^{-3}$] (left) and pressure [Pa] (right) for unconfined ANFO at $D = 2400$ ms$^{-1}$. The white line on the DNS results shows the sonic locus.

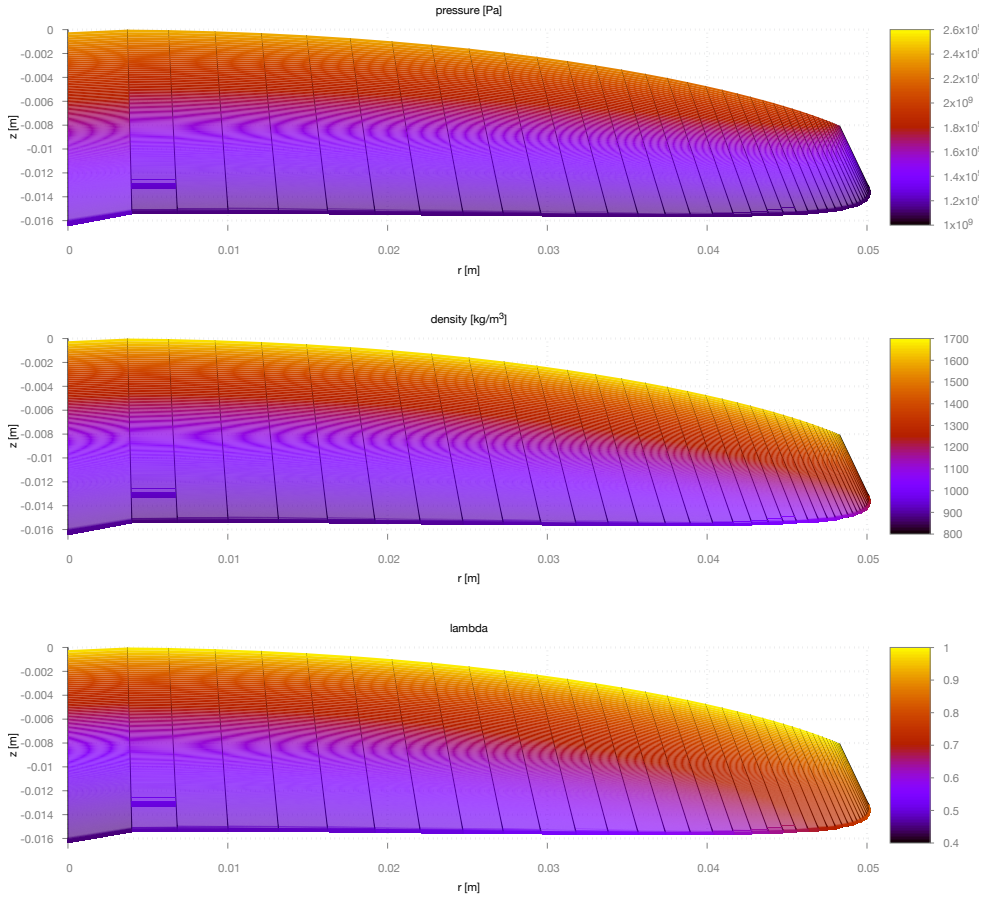


Figure 8.21.: Contour plots of pressure (top), density (middle) and reaction progress (bottom) for a ANFO, travelling at $D = 2400$ ms$^{-1}$ in axisymmetric geometry $(r, z)$ for the MMESSA.

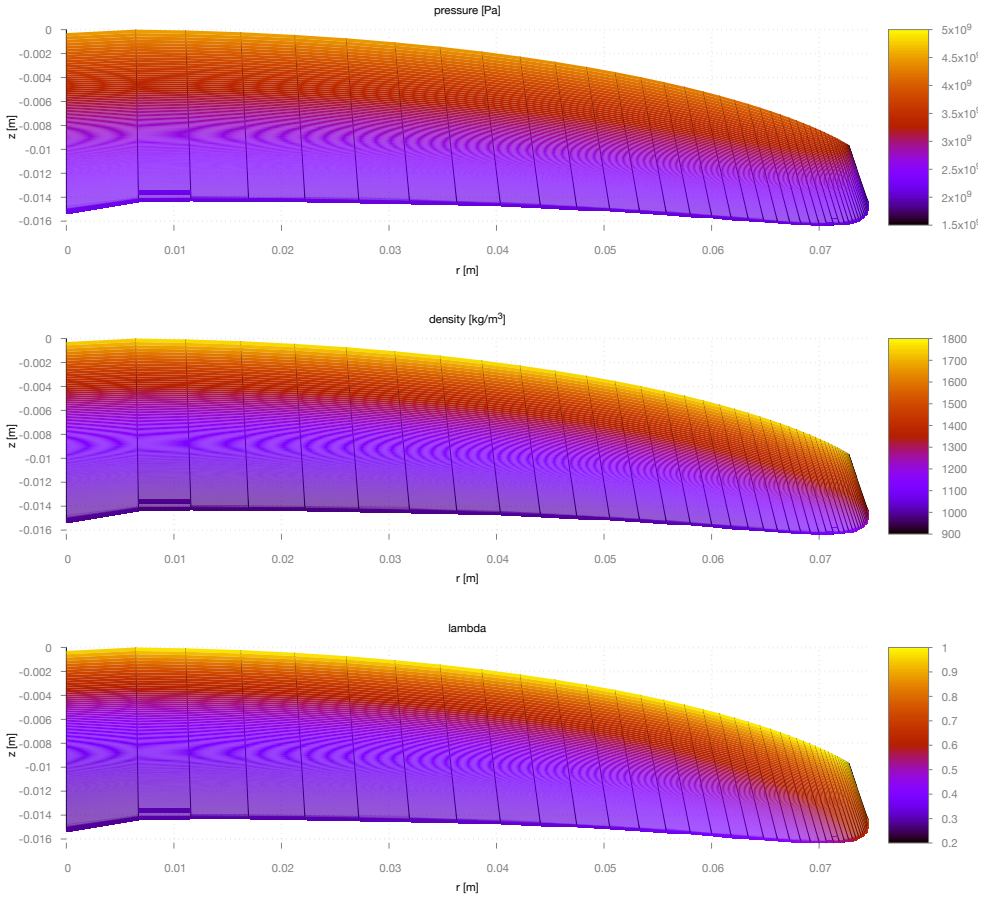


Figure 8.22.: Contour plots of pressure (top), density (middle) and reaction progress (bottom) for a ANFO, travelling at $D = 3200$ ms$^{-1}$ in axisymmetric geometry $(r, z)$ for the MMESSA.

## 8.3. Confined detonations

The MMESSA can be extended to confined detonation with further use of shock polar analysis. Like the unconfined simulations, the shock polar plot describes a match point in the pressure–shock deflection plane that is parametrised by the incoming shock angle. This incoming shock angle can be used to determine the slope of the shock front at the charge edge. However, for unconfined simulations this match point was the sonic point on the explosive shock polar (see the black line on the red curves in Figures 8.23 and 8.24) as this is the point where an intervening Prandtl-Meyer fan would be centred to further extend the deflection angle and low pressure seen in weakly confined or unconfined detonations. For strongly confined detonations, the match point instead takes place at the intersection of the subsonic branch of the explosive's shock polar with the supersonic branch of the confiner's shock polar (see the black line on the green and blue curves in Figures 8.23 and 8.24).

Of course, as mentioned in §7.4, strong and weak/no confinement are not the only types of confinement that occur. However, they are the only types investigated in this work and more of the discussion on the limitations of this follows.

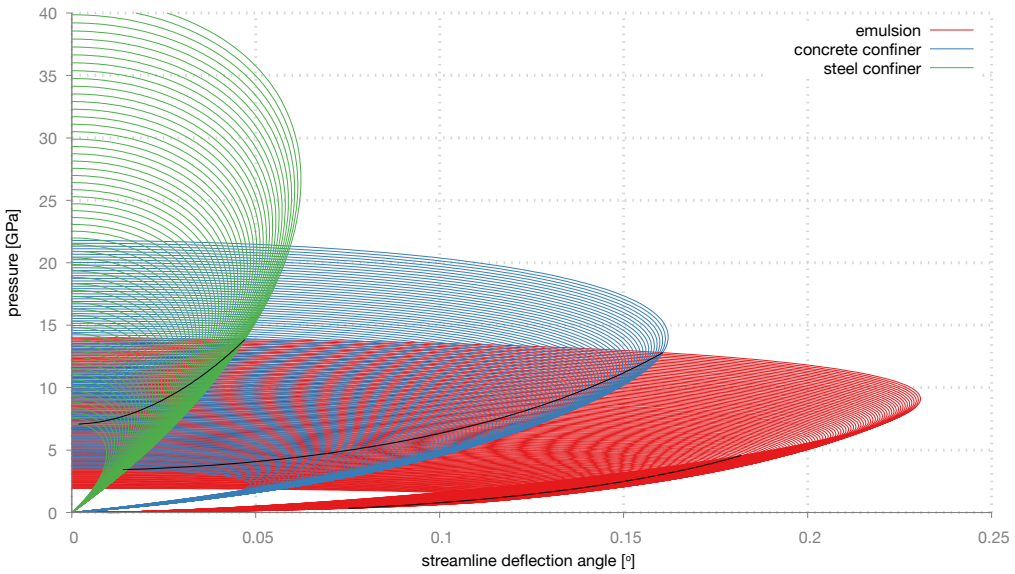


Figure 8.23.: Shock polars for EM120D (red), steel (green) and concrete (blue). The intersection point between EM120D and its confiner (black line on green and blue) defines the incoming shock angle, and hence the shock front slope, at the charge edge. The black line on red illustrates the sonic points of the unreacted EM120D explosive.

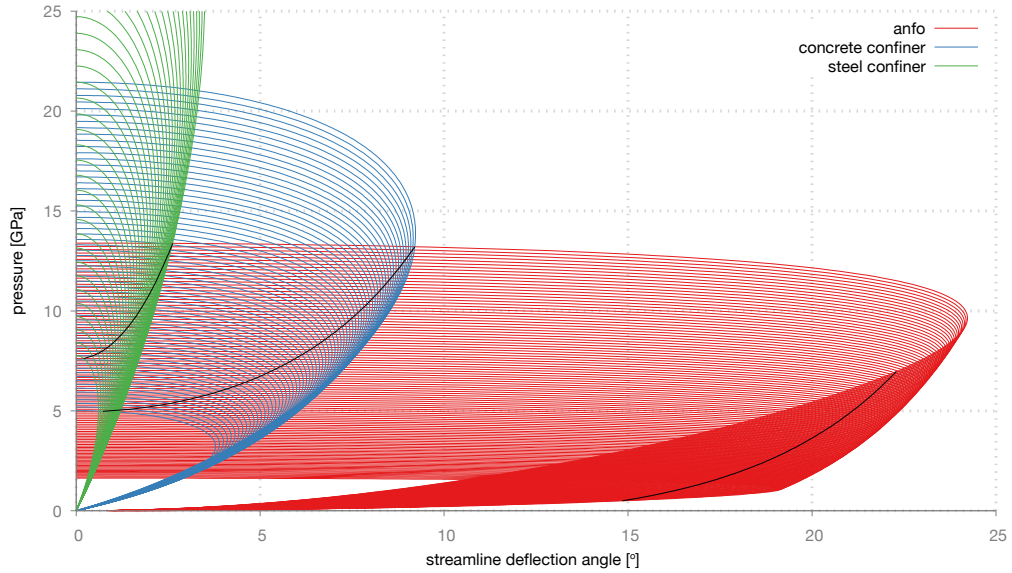


Figure 8.24.: Shock polars for ANFO (red), steel (green) and concrete (blue). The intersection point between ANFO and its confiner (black line on green and blue) defines the incoming shock angle, and hence the shock front slope, at the charge edge. The black line on red illustrates the sonic points of the unreacted ANFO explosive.

### 8.3.1. Confined results

Both EM120D and ANFO are simulated in both steel and concrete confinement and the diameter effect curves compared to DNS and experimental results are shown in Figures 8.25 and 8.26, respectively.

Despite the fact that the MMESSA consistently underestimated the radius for unconfined EM120D, the confined simulations give a good match to DNS results for both concrete and steel, as shown in the diameter effect curve in Figure 8.25. There is some discrepancy in the values taken by both the DNS and the MMESSA for low detonation velocities in steel and this was explored in [65] and was hypothesised to be due to a different type of steel used in the experiments for the last two points on the diameter effect curve (see §3.3.1 for more details). The two different DNS results for steel represent infinite confinement and 3 mm confinement and illustrate the limitations of the use of shock polar analysis, which will be discussed further below. Contour plots for pressure, density and mass fraction are shown in Figures 8.27 and 8.28.

The confined results for ANFO in Figure 8.26 illustrate the opposite effect to that seen in EM120D: despite a good match to the unconfined DNS and experimental results, the confined results diverge from the DNS results. For higher detonation velocities in both concrete and steel the results show a good match. However, for lower detonation velocities the results diverge.

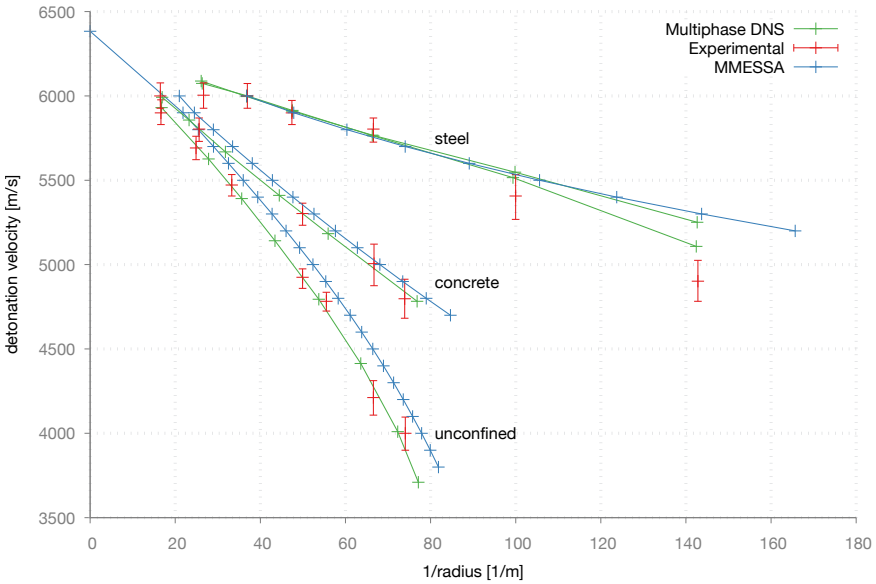


Figure 8.25.: Diameter effect for EM120D for MMESSA (blue) and the multiphase DNS (green) in steel (infinite thickness on upper branch and 3 mm thickness on lower branch) and concrete confinement. Experimental points are also shown (red). Experimental points and DNS results are taken from [65].

This could be due to the limitations of shock polar theory in this range of detonation velocities but this is most likely due to the fact that the shock front is very flat for both concrete and steel confinement, as shown in Figures 8.29 and 8.30.

The MMESSA finds a solution for the curvature of the shock front at each streamline by using the slope at the axis and integrating to the charge edge. If the shock front at the charge edge has a similar gradient to the shock front on the axis then any error found in determining the curvature can have a large impact on when the gradient at the charge edge will be reached. As the radius gets smaller, this error becomes more obvious, especially when the inverse radius is plotted. To overcome this problem, different integrators or lower tolerances could be considered.

Compared to the DNS results, Figure 8.31 shows that for the lower detonation velocities, the estimated shock front is too flat, the length of the DDZ is too short and consequently the distribution of the pressure and density is inaccurate. However, for the higher detonation velocities, Figure 8.32 illustrates that the MMESSA is not only able to give a good match to the radius but also to the variable distribution throughout the DDZ and the shape and size of the DDZ. Therefore, if the problems with the very strong confinement for lower detonation velocities for ANFO can be overcome, MMESSA could be a useful predictive tool for confined detonation.

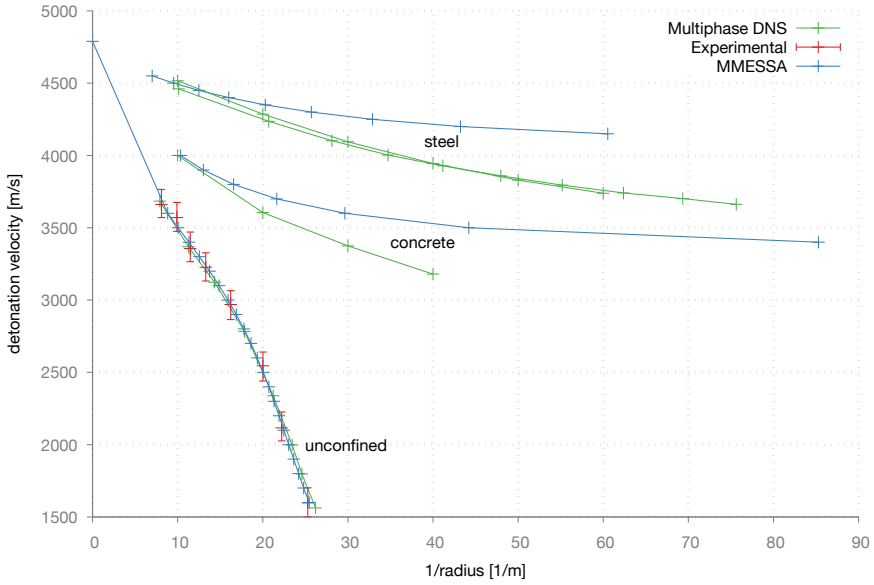


Figure 8.26.: Diameter effect for ANFO for MMESSA (blue) and the multiphase DNS (green) in steel (30 mm for the lower branch and infinite for the upper branch) and concrete confinement. Experimental points are also shown (red) were only available for unconfined (1 mm paper) detonations. DNS results are taken from [65].

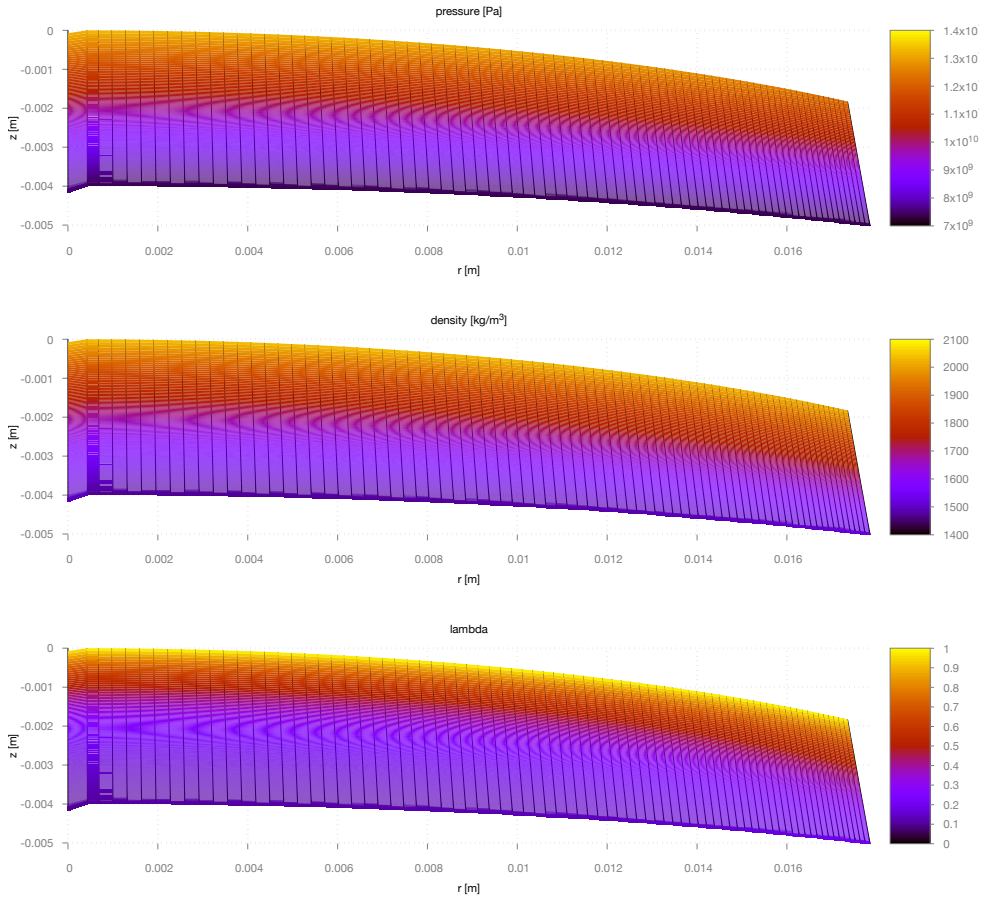


Figure 8.27.: Contour plots of pressure (top), density (middle) and reaction progress (bottom) for EM120D, travelling at $D = 5200$ ms$^{-1}$ in concrete confinement in axisymmetric geometry $(r, z)$ for the MMESSA.

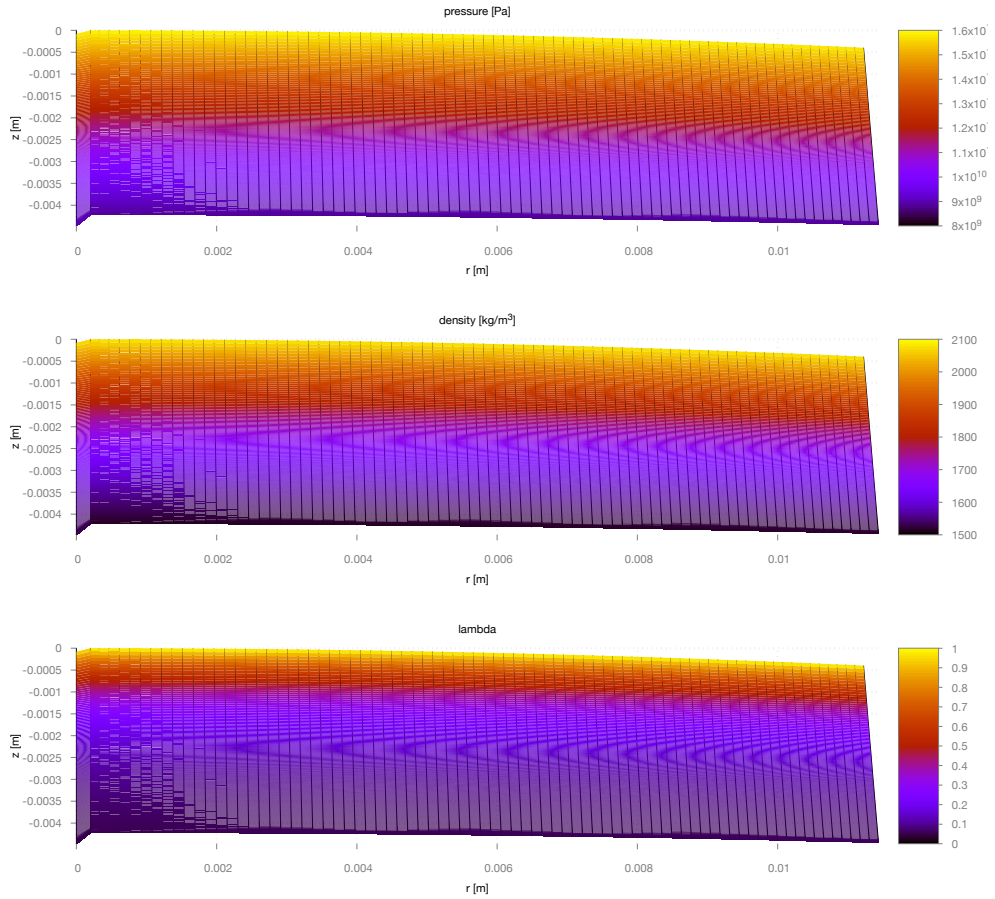


Figure 8.28.: Contour plots of pressure (top), density (middle) and reaction progress (bottom) for EM120D, travelling at $D = 5600$ ms$^{-1}$ in steel confinement in axisymmetric geometry $(r, z)$ for the MMESSA.

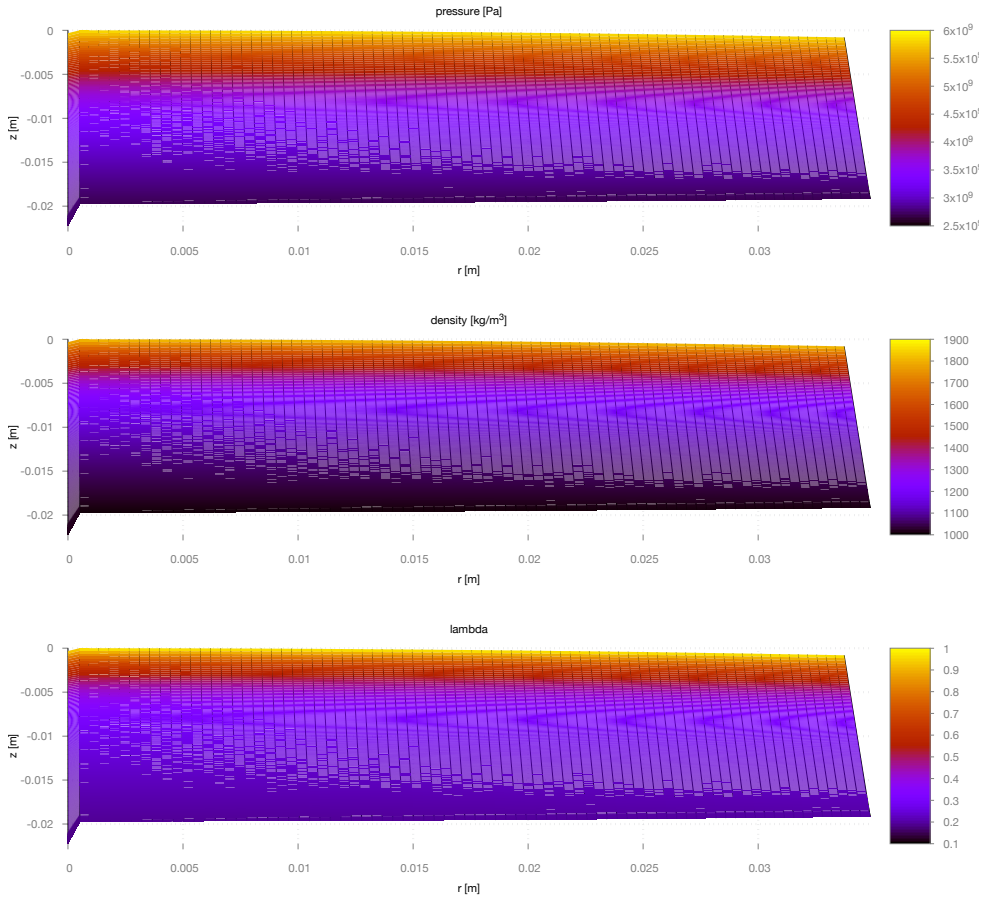


Figure 8.29.: Contour plots of pressure (top), density (middle) and mass fraction (bottom) for ANFO, travelling at $D = 3600$ ms$^{-1}$ in concrete confinement in axisymmetric geometry $(r, z)$ for the MMESSA.

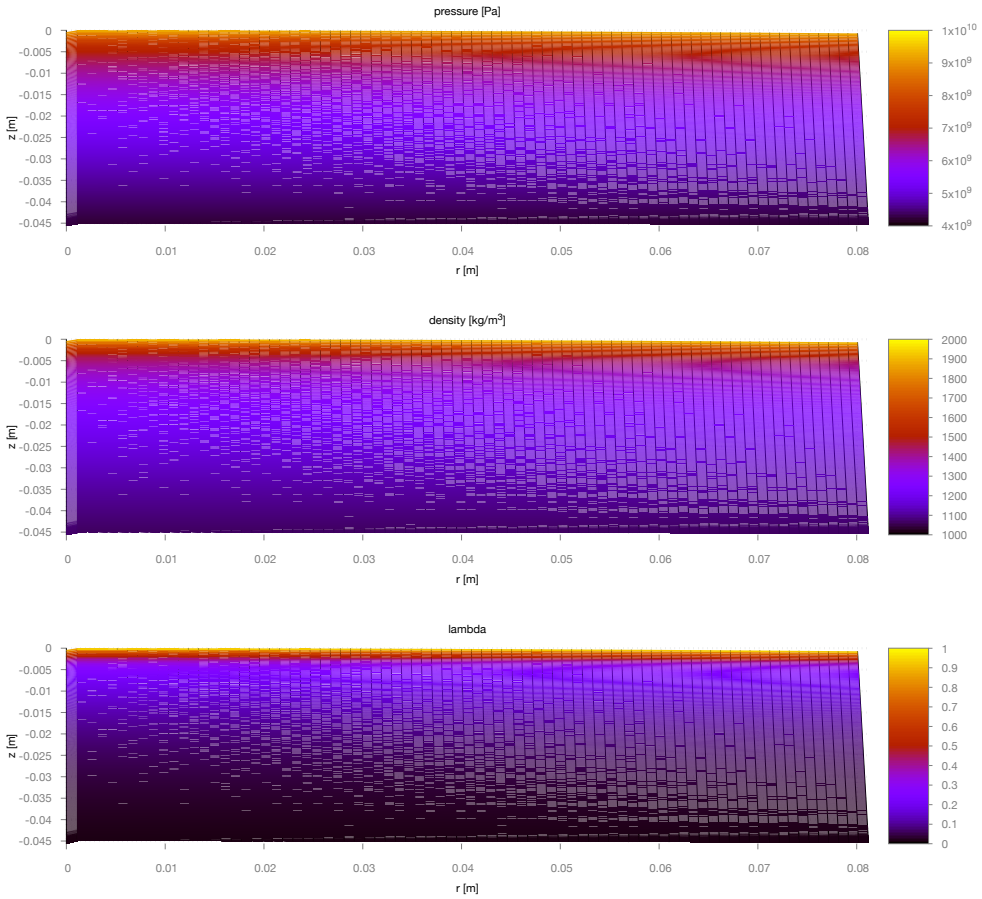


Figure 8.30.: Contour plots of pressure (top), density (middle) and mass fraction (bottom) for ANFO, travelling at $D = 4450\ \mathrm{ms}^{-1}$ in steel confinement in axisymmetric geometry $(r, z)$ for the MMESSA.

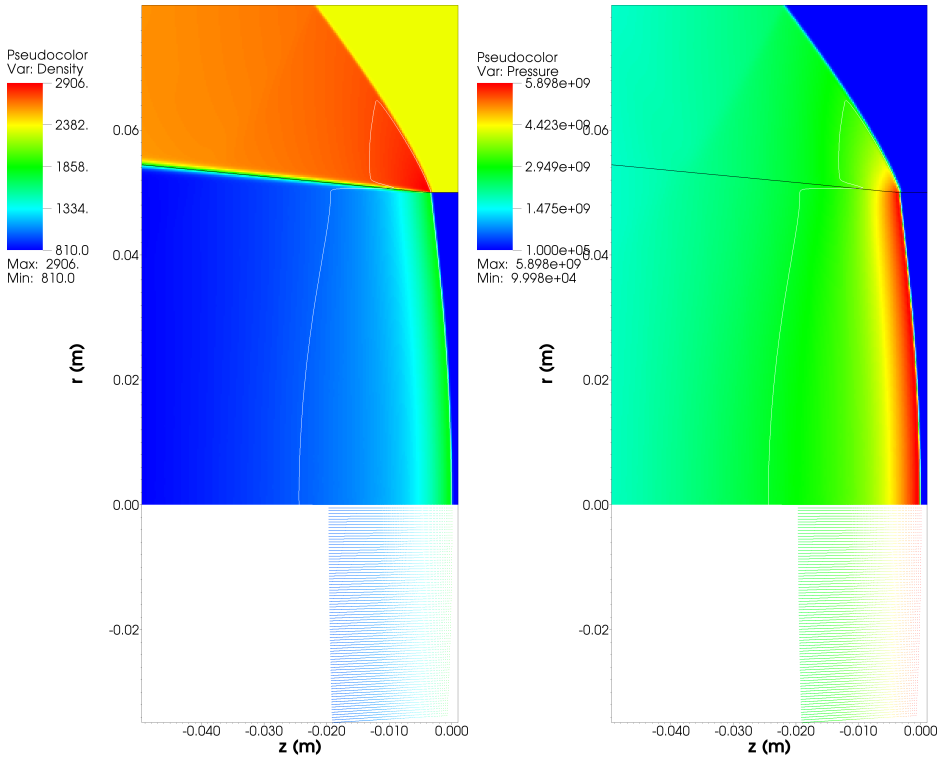


Figure 8.31.: Pseudocolour plots showing the DNS results (top) compared to the MMESSA results (bottom) for both density [kgm$^{-3}$] (left) and pressure [Pa] (right) for concrete confined ANFO at $D = 3600$ ms$^{-1}$. The white line on the DNS results shows the sonic locus and the black line shows the confiner-explosive interface.

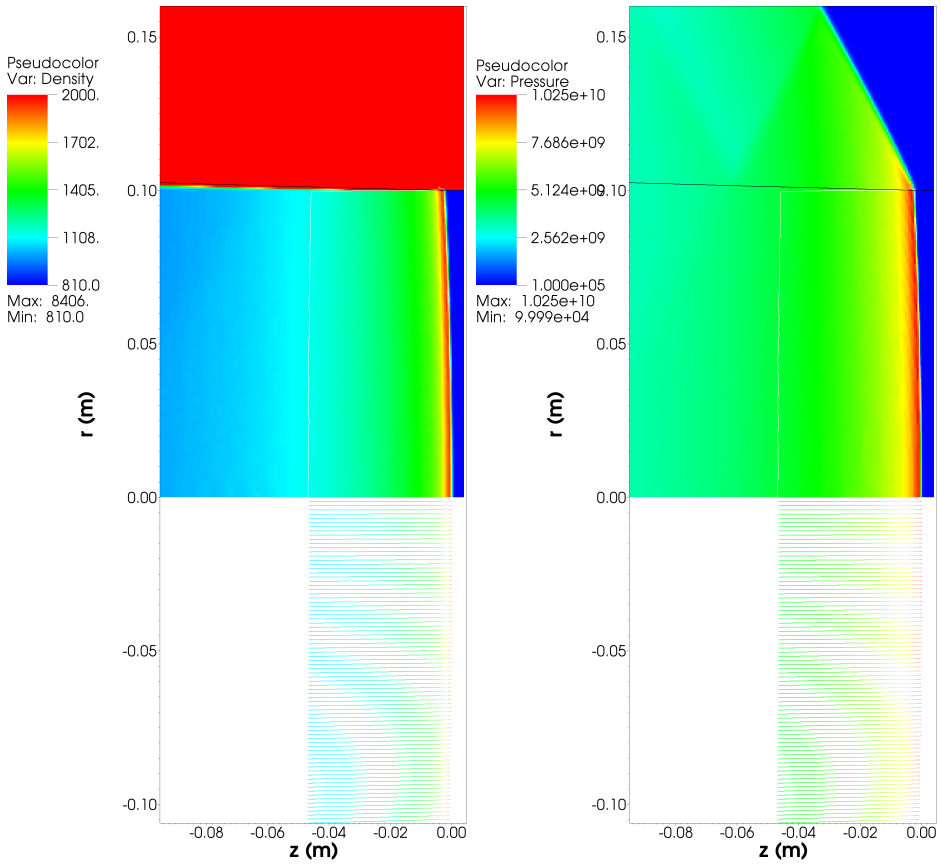


Figure 8.32.: Pseudocolour plots showing the DNS results (top) compared to the MMESSA results (bottom) for both density [kgm$^{-3}$] (left) and pressure [Pa] (right) for steel confined ANFO at $D = 4500$ ms$^{-1}$. The white line on the DNS results shows the sonic locus and the black line shows the confiner-explosive interface.

### 8.3.2. Limitations

For the MMESSA, the interaction between the explosive and confining materials is defined via a match between the explosive and confiner shock polars in the shock deflection – pressure plane. It is assumed that the match will take place on the subsonic (strong) branch of the explosive. However, as shown in §7.4 and following from the discussion in [9], a much wider range of explosive-confiner interactions is possible.

Figure 8.33 illustrates the limitations of shock polar analysis. A DNS of ANFO confined in steel is undertaken with the confining material simulated at three different thicknesses: 5 mm, 30 mm and infinite thickness. While the 30 mm and infinitely thick confinements are very similar, the 5 mm confinement shows drastic reduction in the performance of the explosive. This cannot be replicated by the MMESSA using shock polar analysis.

Using DNS of ANFO in steel confiners of differing thicknesses, Schoch [66] showed that in the case of the 5 mm steel confiner, acoustic waves in the confiner travel faster than the detonation speed in the explosive. This happens because the ambient sound speed in the confiner, $c_0 = 3670$ ms$^{-1}$ for steel, is greater than the detonation velocity of the explosive for smaller radii in thinner confinement and so the pressure wave, or flow, from the explosive to the confiner becomes subsonic and shockless. This phenomenon, referred to as unsteady confinement in [6, 66], means that information can move ahead of the detonation front through the confiner and so shock polar analysis, which relies on information being passed via a shock, cannot be used.

The MMESSA uses shock polar analysis to determine the explosive-confiner edge. However, these types of unsteady confinement solutions do exist in both mining and military applications of detonations but are particularly relevant for the lower detonation velocities and failure diameters of mining explosives. Therefore, unsteady confinement is a type of solution that the MMESSA will be unable to address without further development.

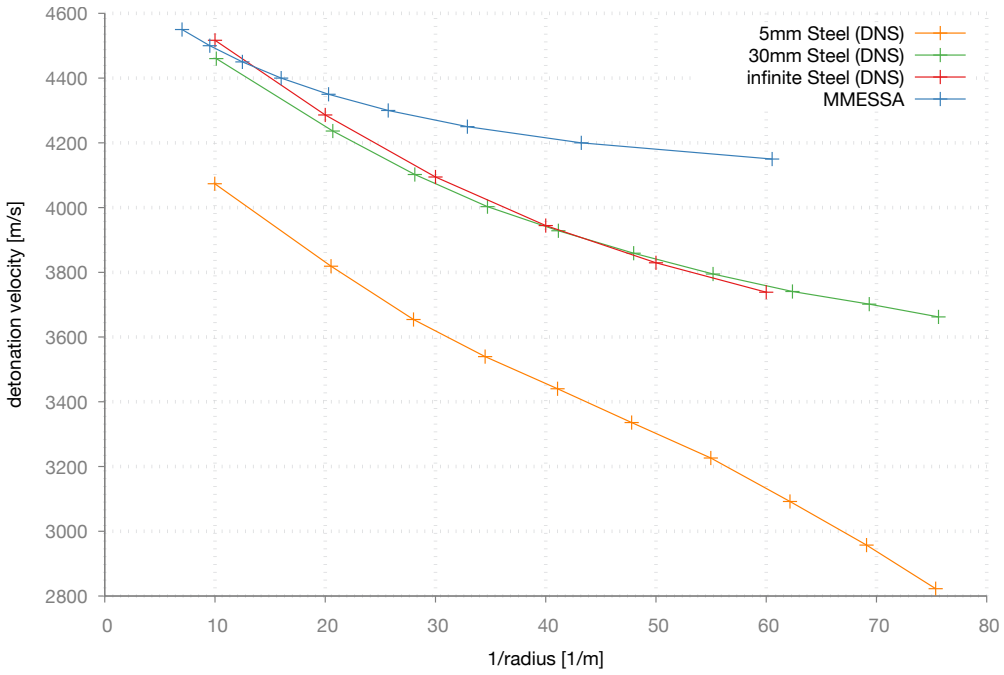


Figure 8.33.: ANFO confined in steel of varying thickness. Using shock polar analysis, only the higher detonation velocities for the thickest confinement are able to be replicated. The DNS solution of [66] is able to represent a whole range of thicknesses.

# Part III.

# Discussion & Conclusion

# 9. Comparison of the approaches

The aim of this work is to investigate current streamline ODE models for modelling non-ideal detonation and to extend any existing models to a multiphase system that is more likely to capture to the porous, heterogeneous nature and behaviour of non-ideal mining explosives.

Two different models are considered: a multiphase extension of the Chan-Kirby model [30] and a multiphase extension of the SSA [78]. Both models are validated with multiphase polytropic examples and then used on two non-ideal explosives: the emulsion EM120D and the highly porous ANFO.

A comparison of the unconfined diameter effect curves for both models, also compared with the DNS and experimental results, is shown in Figure 9.1. In both cases, the MMESSA gives a better fit to DNS and experimental results although the Chan-Kirby model does give comparable results for EM120D. In these simulations, the Chan-Kirby model is simulated with the new elliptical expression and using shock polar analysis to determine the edge of the charge.

For one point on each of these diameter effect curves, Figure 9.2 shows a comparison of the DDZ and the pressure distribution for both ANFO and EM120D. Interestingly, it appears that both the MMESSA and multiphase Chan-Kirby models recover similar on-axis solutions for both ANFO and EM120D, although this was shown to be incorrect for most simulations compared to the DNS solutions, being either too long or too short.

The errors in the determined curvature at each streamline in the multiphase Chan-Kirby model is illustrated by the different streamline lengths obtained and hence the jagged sonic locus. The MMESSA, on the other hand, calculates a smooth sonic locus excepting the jump from on-axis to off-axis solutions, discussed below.

This comparison indicates that the MMESSA provides a better approximation than the multiphase Chan-Kirby approach for unconfined, non-ideal explosives. The reasons for this have been suggested throughout as part of the investigation and extension of the two models. This investigation can be split into two parts: development of the underlying multiphase ODE models and then implementation of these models. The following section, §9.1, discusses this further by looking at the differences, approximations and limitations in the underlying models and how this might affect the solution. Then, in §9.2, the differences, problems and future work for the numerical implementation of these models is discussed.

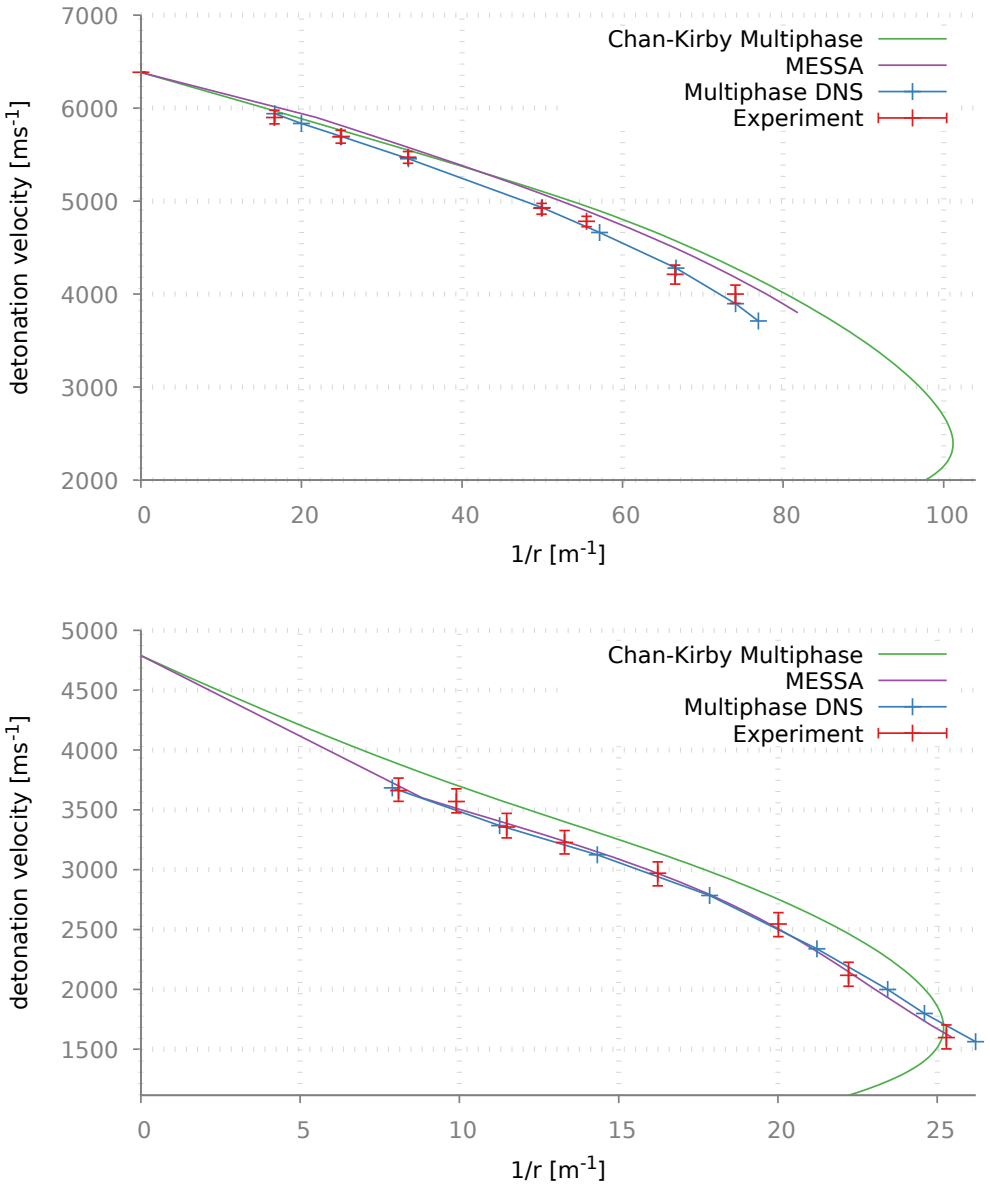


Figure 9.1.: Diameter effect curve for EM120D (top) and ANFO (bottom) show the comparison between the multiphase Chan-Kirby model with elliptical isobar expression and shock polar analysis for the edge angle (green), the MMESSA approach (purple), multiphase DNS results and extrapolated solution (blue) and experimental results (red). The MMESSA gives a better match for both these non-ideal explosives.

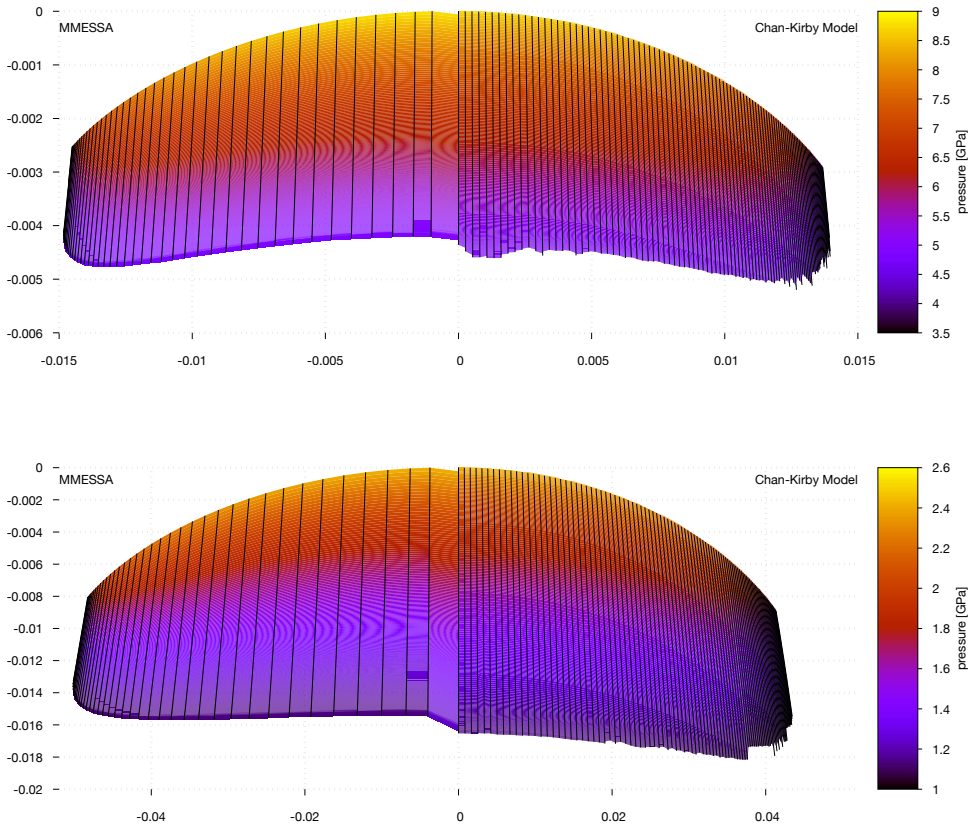


Figure 9.2.: The DDZ and pressure distribution for the MMESSA (left) with 80 streamlines and the multiphase Chan-Kirby model (right) with 100 streamlines for both EM120D (top) and ANFO (bottom) at $D = 4400$ ms$^{-1}$ and $D = 2400$ ms$^{-1}$, respectively. The MMESSA gives a smoother sonic locus indicating smaller errors in the determined curvature at the shock front.

# 9.1. Model development

As mentioned in Part II, both models rely on approximations for reduction to the required form or for efficiency. The models also involve assumptions that are theoretically sound but limit the applicability of the models. This section compares these approximations and assumptions.

## 9.1.1. Approximations

Both models investigated in this work are streamline ODE models that have been derived from a full set of PDEs that govern the motion and reaction of a reactive multiphase fluid and these derivations include approximations. This section will look at the validity of these approximations for the two non-ideal explosives of interest: EM120D and ANFO.

To reduce the multiphase mechanical equilibrium equations to ODEs, the Chan-Kirby model assumes that any terms in the PDEs multiplied by $u/v$, where $u$ is the radial velocity and $v$ is the axial velocity, are negligible. Figure 9.3 illustrates DNS solutions showing the values of this ratio throughout the DDZ for both EM120D and ANFO. A low detonation velocity for EM120D and a mid-range detonation velocity for ANFO are chosen as these are a good representation of the curved shock fronts of non-ideal explosives.

Near the axis, for both types of explosive, this ratio is zero. In fact, for approximately the first half of the charge closest to the axis, this ratio is negligible. After this point, towards the edge of the charge, the ratio increases and for the second half of the charge the radial velocity dominates the ratio to the point where the axial velocity is negligible. This means that this ratio is actually of vital importance, particularly at the charge edge where the shock front is becoming more curved and where determining an accurate solution on the streamline implies an accurate solution for the radius.

The other terms that are neglected from the PDEs in the Chan-Kirby model are those that are multiplied by the square of the radial velocity. Figure 9.4 again shows DNS solutions for EM120D and ANFO but only for radial velocity. Focussing only on the DDZ, the radial velocity is negligible near the charge axis but increases in magnitude near the charge edge. For most of the DDZ the radial velocity is non-zero and for about a third of it it is of a significant magnitude. Any terms multiplied by the radial velocity squared will have a significant impact on the solution for at least the third of the area closest to the charge edge for both EM120D and ANFO. Although EM120D and ANFO may not be representative of all non-ideal explosives, it is clear that these neglected radial terms near the axis are important for modelling non-ideal behaviour.

The MMESSA has comparatively few approximations. The most prominent approximation is that the streamlines are assumed to be straight and so any

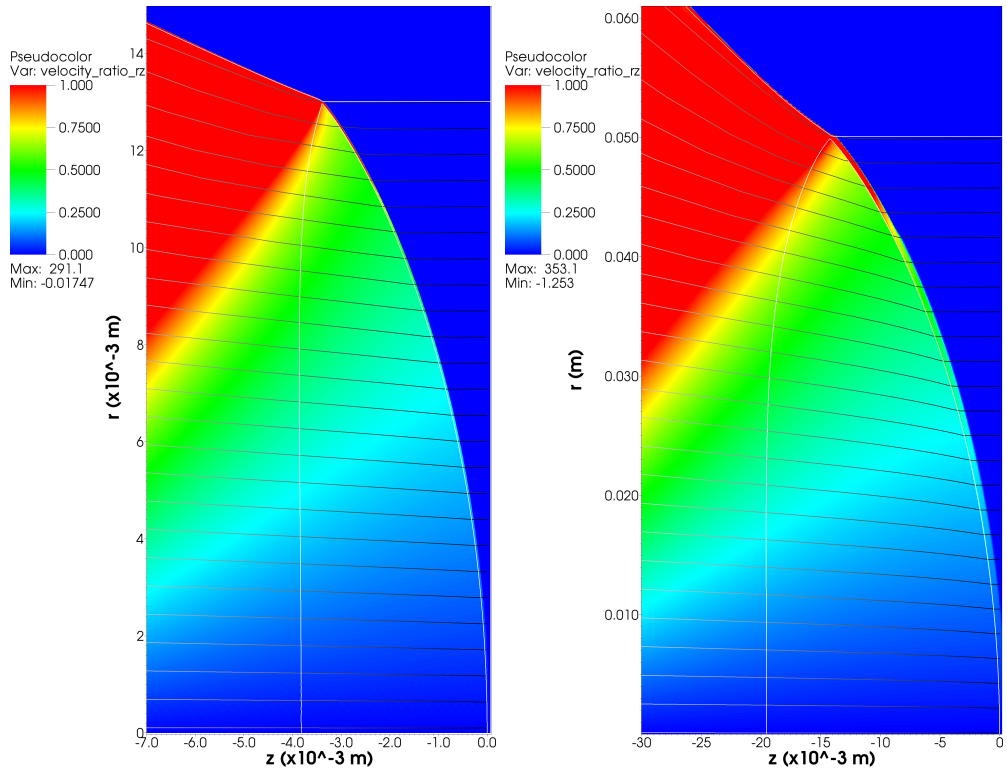


Figure 9.3.: The ratio of radial velocity to axial velocity from DNS for unconfined EM120D (left) at $D = 4000$ ms$^{-1}$ and ANFO (right) at $D = 2500$ ms$^{-1}$. The white lines indicated the sonic locus and explosive-confiner interface. Close to the axis, the ratio is negligible but near the charge edge this ratio is large, particularly for ANFO. The straight streamline approximation of MMESSA assumes that this ratio is constant along the streamlines which can be seen as a valid approximation. The Chan-Kirby model assumes that this ratio is always much less than one which is not a valid approximation near the charge edge.

streamline curvature term is assumed to be negligible. This assumption has two parts: firstly, it is equivalent to stating that the ratio between axial velocity and radial velocity is constant along a streamline, not negligible as assumed in the Chan-Kirby model. Referring again to Figure 9.3, it is clear that the ratio of the two velocities is not constant along the streamlines but it could be argued that this value is approximately constant.

The second part of the assumption is that the streamlines are not curved. For more non-ideal explosives, it is expected that the streamlines will be more curved and that the straight streamline approximation will be less valid. However, as shown in Figure 9.5, the 'straightness' of the streamlines is well approximated by the MMESSA for both the non-ideal explosives simulated, particularly for EM120D. The DNS results for ANFO show slightly more

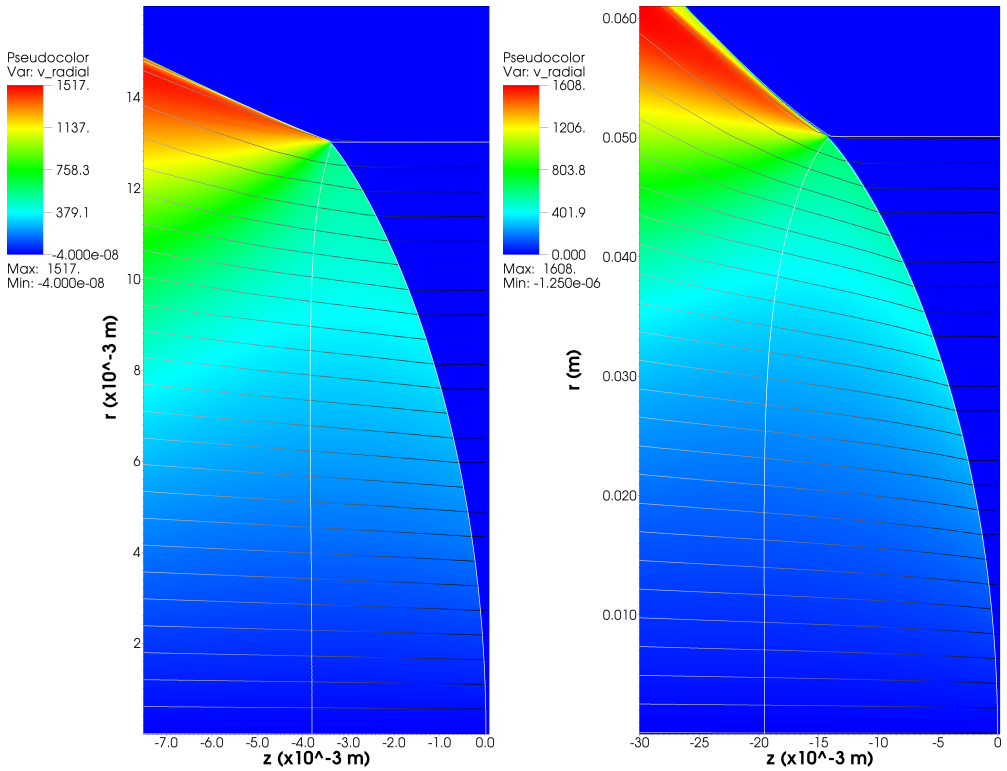


Figure 9.4.: The radial velocity from a DNS for unconfined EM120D (left) at $D = 4000$ ms$^{-1}$ and ANFO (right) at $D = 2500$ ms$^{-1}$. The white lines indicate the sonic locus and explosive-confiner interface. The Chan-Kirby model assumes that any terms involving the radial velocity squared can be neglected. This assumption is only valid close to the axis, particularly for ANFO where the streamlines are more curved and have greater slope.

curved streamlines but the MMESSA still approximates these curves well with similarly sloped straight lines.

Interestingly, most of the curving of the streamlines happens close to the shock front, as shown in the ANFO part of Figure 9.4. This occurs because most of the changes in variables happen just behind the shock front as most of the reaction takes place, particularly for porous ANFO. If including the curvature of the streamlines proves to be too numerically costly, these results suggest that a piecewise linear solution might also be an effective solution for including some non-linear streamline behaviour for porous, non-ideal explosives.

### 9.1.2. Empirical expressions

As well as approximations to neglect terms in the underlying equations, the Chan-Kirby model also uses empirical expressions to close the system of

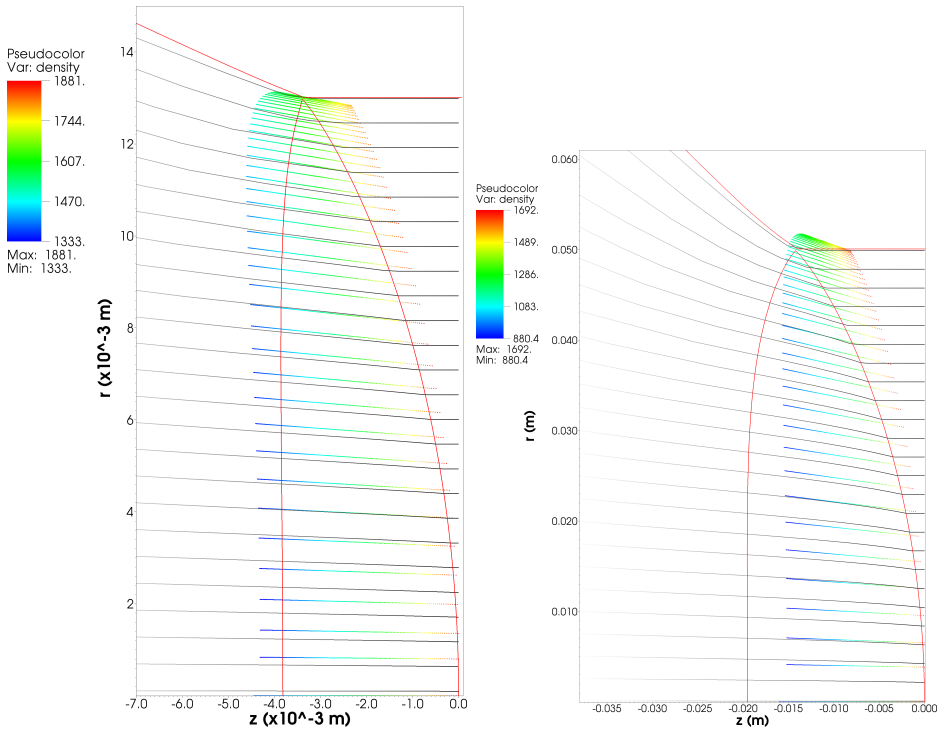


Figure 9.5.: Comparison of the streamline shape between the DNS results and the MMESSA results for unconfined EM120D (left) at $D = 4000$ ms$^{-1}$ and ANFO (right) at $D = 2500$ ms$^{-1}$. The red lines indicate the sonic locus and explosive-confiner interface. For EM120D, the streamlines from the DNS appear straight with gradients comparable to those from the MMESSA solution. For ANFO, the streamlines are slightly more curved but the straight approximation also gives lines with gradients that are comparable. Interestingly, the ANFO solutions give a better approximation of the diameter curve effect than the EM120D despite the streamlines being more curved.

equations.

One of these empirical assumptions is that the ratio between the radial velocity divided by the radius and the change in radial velocity with respect to the radius is constant,

$$\frac{du}{dr} = k\frac{u}{r}, \tag{9.1}$$

where $k$ is some constant. This implies that the radial velocity is a function of the radius only,

$$u = Ar^k, \tag{9.2}$$

where A is another constant.

Figure 9.6 shows a sample of the radial velocity in the radial direction for a single axial value for EM120D at $D = 3710$ms$^{-1}$ and from Figure 9.4

it can be seen that a similar graph would apply for ANFO. Although the polynomial $u = Ar^k$ would not represent the best fit for the curve, with two free parameters a good fit could be found and this is assessed as a reasonable assumption excepting that the radial velocity is actually coupled to the other flow variables.

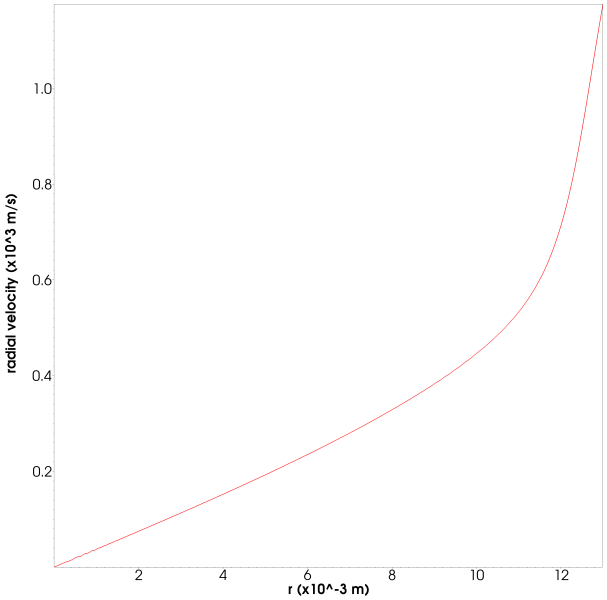


Figure 9.6.: Radial velocity profile, along the radius, for EM120D at $D = 3710\text{ms}^{-1}$. The Chan-Kirby models assumes that the radial velocity is a function of the radius only in the form of $u = Ar^k$ where $A$ and $k$ are constants.

Section 7.3 explored the use of the empirical isobar expression in the original Chan-Kirby theory and a new theory was developed, based on the assumption that the detonation front could be approximated by an ellipse. Although this expression eliminated an empirical parameter, the elliptical assumption is still an approximation. If the shock shape changed dramatically, for example with strong or unsteady confinement, then this elliptical assumption would no longer be valid. It is also only an approximation for the shape of an unconfined charge and it would be preferable not to have to have approximated the isobar behaviour at all.

### 9.1.3. Limitations

#### Edge of charge

This work has extended the previous models to allow the multiphase Chan-Kirby model and MMESSA to accurately locate the edge of the charge using shock polar analysis coupled with multiphase material modelling. This

means that both approaches use the same theory to locate the charge edge, although use this theory in different ways.

For unconfined modelling, multiphase shock polar theory is relatively straightforward as the interaction between the explosive and the weakly confining air is described by the sonic point on the unreacted shock polar. However, as noted by Stewart and Bdzil [74], there can be many types of explosive-inert interactions and as different types of confinement are introduced, these interactions can become more complex. To simulate explosives in confinement accurately, it is critical to understand appropriate boundary conditions for propagating detonation shocks [9]. Some of these interactions are able to be simulated using shock polar theory such as strong or classic confinement, as shown in §7.4 and §8.3, but some interactions are poorly described by shock polar theory such as unsteady, stiff and finite confined, as discussed in §7.4 and shown in Figure 8.33. Further discussion of the advantage of DNS solutions for these problems is discussed in detail in [66].

## 9.2. Numerical implementation

The main advantage of an ODE model compared to a PDE model is that ODE models can be faster and easier to solve. The implementation of an ODE solver needs to achieve a balance between accuracy and speed while still overcoming any numerical issues presented by the model, such as singularities.

### 9.2.1. Singularities in axisymmetric solutions

Axisymmetric equations to describe fluid dynamics can have problems with singularities caused by the addition of $u/r$, where $u$ is the radial velocity, introduced by the divergence operator in axisymmetric coordinates. This term, of course, is singular when $r = 0$.

Depending on the application, there are different ways to avoid this singularity. In axisymmetric detonation modelling, the on-axis solution is important in validating the implementation. For streamline models it is even more important as an accurate on-axis solution helps to determine more accurate off-axis solutions if the streamline solutions are determined from the axis outwards.

Both the multiphase Chan-Kirby model and MMESSA need to overcome this problem. The Chan-Kirby model does this by treating $u/r$ as a single variable which is proportional to the radial divergence. On the axis, the constant of proportionality is taken to be zero which is superfluous because the radial divergence is zero. As shown in Figure 7.24 for EM120D and ANFO, there is still a problem with the on-axis solution for the multiphase Chan-Kirby model and it does not always match the DNS solution well.

The on-axis singularity in MMESSA is overcome via a simple application of l'Hôpital's rule. This worked well for the polytropic validation case, as shown in Figure 8.11, as there is no visible difference between the on-axis solution and the off-axis solution although the length of the solution still does not match the DNS, as shown in Figure 8.10. However, for the non-ideal explosives EM120D and ANFO, with complex equations of state, there is an unexpected positive gradient in the sonic locus between the on-axis solution and the off-axis solution, as shown in Figures 8.16 - 8.17 and Figures 8.21 - 8.22 for unconfined solutions and Figures 8.27 - 8.29 and Figures 8.28 - 8.30 for confined solutions. This could imply that the on-axis assumption is incorrect, incorrect for complex equations of state or that additional considerations need to be accounted for. This is an area for further investigation in the future.

### 9.2.2. Time to solution

The results for the MMESSA were run using task-based parallelisation. The MMESSA is a suitable candidate for parallelisation as each detonation velocity for the same material has no dependence on any other detonation velocity; points on the diameter effect curve can be calculated in parallel. In the past, parallelisation was reserved for high performance computing but given that the average modern desktop computer or laptop has at least four cores, the use of parallelisation appears to be the most effective option for this type of modelling.

On a single core, simulation of a smooth diameter effect curve for the MMESSA takes less than two minutes. On a typical laptop or desktop with four cores, this is reduced by a factor of four to approximately thirty seconds. This kind of efficient but surprisingly accurate multiphase simulation with realistic equations of state has, to the author's knowledge, not been shown before. The short time to solution enables new research with mutliphase models including parameter studies and parameter fitting for DNS codes.

# 10. Conclusion

In this work, two streamline ODE models for detonation, the Chan-Kirby model [30] and the SSA [78], are extended to a multiphase system of equations with realistic equations of state. This extension is made to better capture the heterogeneities present in non-ideal explosives. Comparisons with multiphase DNS and experiments are made to investigate the effect of approximations and assumptions used in the reduction of the ODEs from the parent PDEs.

Using the same parameters as the DNS, both models produce comparable diameter effect curves for two different non-ideal explosives, EM120D and ANFO, in unconfined conditions. However, investigation shows that the MMESSA involves less approximations and no empiricism, compared with the Chan-Kirby model. The MMESSA is also extended to model confined detonations and predicts strong confinement in EM120D well but does not predict the correct radii for lower detonation velocities of ANFO in strong confinement.

Independent derivation of both the Chan-Kirby and SSA models for single-phase detonation in axisymmetric geometry are presented. These techniques are then applied to multiphase mechanical equilibrium equations and a multiphase ODE streamline model is produced for both approaches. To the author's knowledge, the application of these types of techniques to a multiphase model to obtain a comparable reduced ODE model has not been previously reported.

Some of the existing techniques used to reduce the models to ODEs have been improved. The Chan-Kirby model includes empirical values for the curvature of isobars in the DDZ and this is improved with a more general elliptical expression. Furthermore, in previous schemes, the angle at the charge edge for both models needed to be known. In this study, this prerequisite has been avoided by coupling shock polar theory with work on multiphase models and experiments. Thus, a technique has been developed to determine the angle of the incoming streamline at the charge edge for a porous explosive in different confinement conditions, using realistic equations of state.

The new models and techniques that have been developed here extend the available options for fast non-ideal, multiphase detonation modelling. This provides industry with a tool for quick calculations and provides a tool for performing academic research on detonation modelling such as fast parametric studies that can be used to fit parameters for larger codes.

Despite reasonable prediction of the diameter curve and DDZ, the models do

have limitations. The Chan-Kirby model involves too many fitted parameters to be considered for confined studies. It is also shown that its approximations are not appropriate. Confined studies would be possible but would involve further investigation of the isobar curvature. For this reason, the MMESSA is the preferred approach but this too has its drawbacks. Although it is able to model confinement well for EM120D and high ANFO velocities, these are examples of strong confinement only. Any other types of confinement, such as unsteady, stiff or finite confinement, cannot currently be modelled using shock polar theory. Investigating how shock polar theory can be extended to include these different cases of confinement is an option for further investigation.

The MMESSA also assumes that the streamlines in the DDZ are straight. Although this was shown to be a suitable approximation for EM120D and ANFO, it might be a problem for other non-ideal explosives. It is considered that introducing curvature would create an optimisation problem that would be significantly slower. Since most curvature is seen just behind the shock front, reducing this curve to a piecewise-linear curve could be an option. This is an area for further investigation.

One question this work does not answer is whether or not the reduced ODE models predict the failure diameter. More experimental and DNS data for a greater range of non-ideal explosives would be needed to investigate this.

Furthermore, the singularity in the axisymmetric flow equations needs further investigation and any improvements for this could enhance both the Chan-Kirby model and the MMESSA.

Finally, the parameters for all of the non-ideal comparisons in this work were taken from the DNS implementation. If the ODE models are to be used for parametric studies, they would need to be fitted to the unconfined data to then predict the confined behaviour. Whether or not this improves the confined results for MMESSA is another area for future investigation.

# Part IV.

# Bibliography

# Bibliography


[1] A. N. Afanasenkov, V. M. Bogomolov, and I. M. Voskoboinikov. "Generalized shock hugoniot of condensed substances". In: *Journal of Applied Mechanics and Technical Physics* 10 (4 1969), pp. 660–664. ISSN: 0021-8944. DOI: 10.1007/BF00916231. URL: http://dx.doi.org/10.1007/BF00916231.

[2] A.N. Afanasenkov, V.M. Bogomolov, and I.M. Voskoboinikov. "Calculation of the detonation wave parameters of mixtures of explosives and inert additives". In: *Combustion, Explosion and Shock Waves* 6.2 (1970), pp. 163–166. ISSN: 0010-5082. DOI: 10.1007/BF00742923. URL: http://dx.doi.org/10.1007/BF00742923.

[3] John D. Anderson. *Fundamentals of Aerodynamics*. 3rd edition. McGraw Hill, 2001.

[4] John D. Anderson. *Modern Compressible Flow*. Series in Mechanical Engineering. McGraw Hill, 2003.

[5] M. Arienti, E. Morano, and J. E. Shepherd. *Shock and detonation modeling with the Mie-Grüneisen equation of state*. Tech. rep. FM99-8. Graduate Aeronautical Laboratories, MS 205-45, California Institute of Technology, 2004.

[6] T. D. Aslam and J. B. Bdzil. "Numerical and theoretical investigations on detonation confinement sandwich test". In: *13th International Detonation Symposium*. 2006.

[7] T. D. Aslam, J. B. Bdzil, and L. G. Hill. *Extensions to DSD theory: analysis of PBX9502 rate stick data*. Tech. rep. Los Alamos National Lab, Dec. 1998. URL: public.lanl.gov/aslam/AslamDetSymp.pdf.

[8] Tariq Aslam. Private communication. 2011.

[9] Tariq D. Aslam and John B. Bdzil. "Numerical and theoretical investigations on detonation inert confinement interactions." In: *12th International Detonation Symposium*. 2002.

[10] G. K. Batchelor. *An introduction to fluid dynamics*. Cambridge University Press, 2000.

[11] S M Baturin, A N Dremin, and K K Shvedov. *Final Report on Research Contract with Imperial Chemical Industries PLC*. Tech. rep. MT-97/01-07F. Institute of Chemical Physics in Chernogolovka Russian Academy of Sciences, 1996.

[12] J. B. Bdzil. "Perturbation methods applied to problems in detonation physics". In: *6th International Detonation Symposium*. 1976.

[13] J. B. Bdzil. "Steady-state two-dimensional detonation". In: *J. Fluid Mech.* 108 (1981), pp. 195–226. URL: http://dx.doi.org/10.1017/S0022112081002085.

[14] John B. Bdzil, Tariq D. Aslam, and Mark Short. "DSD front models: nonideal explosive detonation in ANFO". In: *12th International Detonation Symposium*. 2002. URL: http://www.intdetsymp.org/detsymp2002/PaperSubmit/FinalManuscript/pdf/Bdzil-185.pdf.

[15] John B. Bdzil and D. Scott Stewart. "The dynamics of detonation in explosive systems". In: *Annu. Rev. Fluid Mech.* 39 (2007), pp. 263–292. URL: http://www.annualreviews.org/doi/pdf/10.1146/annurev.fluid.38.050304.092049.

[16] M Braithwaite and G J Sharpe. "Reduced, Chemistry Implicit, Equations of State for Explosion and Detonation Products". In: *Proc. 15th International Detonation Symposium*. 2014.

[17] M. Braithwaite et al. "A detonation problem posed as a differential/algebraic boundary value problem". In: *Math. Engng. Ind.* 3.1 (1990), pp. 44–57.

[18] W Byers Brown and A Amaee. *Review of Equations of State of Fluids Valid to High Density*. Tech. rep. Health & Safety Executive, 1992.

[19] W. Byers Brown and M. Braithwaite. "Williamsburg equation of state for detonation product fluid". In: *AIP Conference Proceedings* 309.1 (1994). Ed. by S. C. Schmidt et al., pp. 73–76. DOI: 10.1063/1.46205. URL: http://link.aip.org/link/?APC/309/73/1.

[20] W Byers Brown and M Braithwaite. "Analytical Representation of the Adiabatic Equation for Detonation Products based on Statistical Mechanics and Intermolecular Forces". In: *Shock Compression of Condensed Matter*. 1991.

[21] W Byers Brown and M Braithwaite. "Development of the Williamsburg Equation of State to model Non-ideal Detonation". In: *15th International Detonation Symposium*. 2014.

[22] W Byers Brown and M Braithwaite. "Williamsburg Equation of State for Detonation Product Fluid". In: *Shock Compression of Condensed Matter*. 1993.

[23] W. Byers Brown, Z. Feng, and M. Braithwaite. "Williamsburg Equation of State for Modelling Non-Ideal Detonation". In: *Journal de Physique IV Colloque* 05.C4 (1995), pp. 209–214. DOI: 10.1051/jp4:1995418. URL: https://hal.archives-ouvertes.fr/jpa-00253717.

[24] C. Campbell and D. W. Woodhead. "The ignition of gases by an explosion wave. Part I. Carbon monoxide and hydrogen mixtures". In: *J. Chem. Soc.* 1927 (1927), pp. 1572–1578.

[25] Malcolm Cartright. "Modelling of non-ideal steady detonations". PhD thesis. University of Leeds, 2016.

[26] S. K. Chan. Private communication. 2011.

[27] S. K. Chan. *CPeX-2D Modifications*. Tech. rep. Orica Mining Services, Mar. 2008.

[28] S. K. Chan. *Mathcad CPeX*. Tech. rep. 58639. Orica Mining Services, Mar. 2004.

[29] S. K. Chan. "Prediction of confinement effects on detonation with an analytical two-dimensional model". In: *13th International Detonation Symposium*. Office of Naval Research, 2007, pp. 224–232.

[30] S. K. Chan and I. J. Kirby. "Analysis of VOD-Diameter Data Using an Analytical Two-Dimensional Non-Ideal Detonation Model". In: *Shock Compression of Condensed Matter*. Ed. by M. D. Furnish, M. Elert, T. P. Russell, & C. T. White. Vol. 845. American Institute of Physics Conference Series. July 2006, pp. 453–456. DOI: 10.1063/1.2263358. URL: http://adsabs.harvard.edu/abs/2006AIPC..845..453K.

[31] D. L. Chapman. "On the rate of explosion in gases". In: *Philos. Mag.* 47 (1899), pp. 90–104.

[32] R. Courant and K. O. Friedrichs. *Supersonic Flow and Shock Waves*. Interscience Publishers, 1948.

[33] E. Croft. *Investigation of a reduced model using parametric studies of a 2-dimensional compliant confinement model*. Cambridge University MPhil Dissertation. M.Phil. Thesis. 2011.

[34] E. Croft. *Modelling two-dimensional detonation with reduced models*. Cambridge University CPGS Report. CPGS Report. 2012.

[35] E.M. Croft et al. "Modelling multiphase detonation with streamline models". In: *Proc. 15th International Detonation Symposium*. (Grand Hyatt San Francisco, July 13–18, 2014). Office of Naval Research, Arlington, Virginia, 2014, pp. 1096–1106.

[36] Frédéric Devernay. *C/C++ Minpack*. http://devernay.free.fr/hacks/cminpack/. 2007.

[37] W. Döering. "On detonation processes in gases". In: *Ann. Phys.* 43 (1943), pp. 421–436.

[38] A. N. Dremin. *Results from detonic research contract II*. Tech. rep. High Dynamics Pressure Department Institute of Chemical Physics Russian Academy of Sciences Chernogolovka Russia, 1999.

[39] A.N. Dremin. *Toward Detonation Theory*. Shock Wave and High Pressure Phenomena. Springer New York, 1999. ISBN: 9780387986722. URL: https://books.google.co.uk/books?id=pZLdfT-NZ-wC.

[40] Wildon Fickett and William C. Davis. *Detonation: Theory and Experiment*. Dover, 2000.

[41] Firsthuman. *ammonium nitrate/fuel oil (ANFO)*. Use of this image is licensed under the Creative Commons Attribution-Share Alike 3.0 Unported license http://creativecommons.org/licenses/by-sa/2.5/. This image has been cropped. 2009. URL: https://en.wikipedia.org/wiki/ANFO%5C#/media/File:Ammonium%5C_nitrate-fuel%5C_oil%5C_(ANFO)%5C_explosive.jpg.

[42] R.A. Granger. *Fluid Mechanics*. Dover Books on Physics. Dover Publications, 2012. ISBN: 9780486135052.

[43] Timo Halén. *Charging with anfo*. Use of this image is licensed under the Creative Commons Attribution-Share Alike 3.0 Unported license. http://creativecommons.org/licenses/by-sa/2.5/. 2004. URL: https://commons.wikimedia.org/wiki/File:Charging%5C_with%5C_anfo.jpg.

[44] A. K. Henrick. "Shock-fitted numerical solutions of one- and two-dimensional detonation". PhD thesis. University of Notre Dame, 2008.

[45] Scott I Jackson, Charles B Klyanda, and Mark Short. "Experimental observations of detonation in ammonium-nitrate-fuel-oil (ANFO) surrounded by a high-sound speed, shockless, aluminum confiner". In: (Jan. 2010). URL: http://www.osti.gov/scitech/servlets/purl/983227.

[46] H. R. James and B. D. Lambourn. "On the systematics of particle velocity histories in the shock-to-detonation transition regime". In: *Journal of Applied Physics* 100.8, 084906 (2006). DOI: http://dx.doi.org/10.1063/1.2354416. URL: http://scitation.aip.org/content/aip/journal/jap/100/8/10.1063/1.2354416.

[47] E. Jouguet. *Mécanique des explosifs*. Octave Doin et Fils, 1917.

[48] E. Jouguet. "Sur la propagation des réactions chimiques dans les gaz". In: *J. de Mathematiques Pure et Appliques* 1 (1905), pp. 347–425.

[49] E. Jouguet. "Sur la propagation des réactions chimiques dans les gaz". In: *J. de Mathematiques Pure et Appliques* 2 (1906), pp. 5–85.

[50] A. K. Kapila, J. B. Bdzil, and D. S. Stewart. "On the Structure and Accuracy of Programmed-Burn". In: *Combustion Theory and Modelling* 10 (2006), pp. 289–321. DOI: 10.1080/13647830500436540.

[51] A. K. Kapila et al. "Two-phase modeling of deflagration-to-detonation transition in granular materials: Reduced equations". In: *Physics of Fluids* 13 (2001), pp. 3002–3024.

[52] D. L. Kennedy. "The challenge of non-ideal detonaion". In: *Le Journal de Physique IV* 5(C4) (1995), pp. 191–207.

[53] I. J. Kirby and G. A. Leiper. "Small divergent detonation theory for intermolecular explosives". In: *Proc. 8th Intl. Symp. on Detonation*. 1985, pp. 176–186. URL: http://www.lsc.phy.cam.ac.uk/people/emc68/papers/kirby85.pdf.

[54] "Course of theoretical physics". In: *Fluid Mechanics*. Ed. by L. D. Landau and E. M. Lifshitz. First Edition. Pergamon Press, 1975.

[55] Charles L. Mader. *Numerical modeling of explosives and propellants*. 3rd. CRC Press, 2008.

[56] J. von Neumann. "Theory of detonation waves". In: *John von Neumann, collected works, Vol. 6*. Ed. by A. J. Taub. Macmillan, 1942.

[57] P. A. Persson, R. Holmberg, and J. Lee. *Rock Blasting and Explosives Engineering*. CRC Press, 1993.

[58] Fabien Petitpas et al. "Diffuse interface model for high speed cavitating underwater systems". In: *International Journal of Multiphase Flow* 35.8 (Aug. 2009), pp. 747–759. ISSN: 03019322. DOI: 10.1016/j.ijmultiphaseflow.2009.03.011. URL: http://linkinghub.elsevier.com/retrieve/pii/S0301932209000688.

[59] William H. Press et al. *Numerical recipes: The art of scientific computing*. 3rd. Cambridge UP, 2007.

[60] Christopher M. Romick and Tariq D. Aslam. "Two-dimensional detonation propagation using shock-fitting". In: *Proc. 15th International Detonation Symposium*. 2014.

[61] Jeffrey Salmond and Nikos Nikiforakis. "Characterisation of Reaction Waves in the Initiation of Detonation". In: *15th International Detonation Symposium*. 2014.

[62] Richard Saurel and Rémi Abgrall. "A Multiphase Godunov Method for Compressible Multifluid and Multiphase Flows". In: *Journal of Computational Physics* 150 (1999), pp. 425–467.

[63] Richard Saurel et al. "Modelling dynamic and irreversible powder compaction". In: *J. Fluid Mech.* 664 (2010), pp. 348–396.

[64] R. Saurel et al. "Shock jump relations for multiphase mixtures with stiff mechanical relaxation". English. In: *Shock Waves* 16.3 (2007), pp. 209–232. ISSN: 0938-1287. DOI: 10.1007/s00193-006-0065-7. URL: http://dx.doi.org/10.1007/s00193-006-0065-7.

[65] Stefan Schoch. "Multi-phase detonations in elastic-plastic confinement". PhD thesis. University of Cambridge, 2012.

[66] Stefan Schoch and Nikolaos Nikiforakis. "Propagation of detonation waves in ANFO confined by high sound-speed materials". In: *15th International Detonation Symposium*. 2014.

[67] Stefan Schoch, Nikolaos Nikiforakis, and Bok Jik Lee. "The propagation of detonation waves in non-ideal condensed-phase explosives confined by high sound-speed materials". In: *Physics of Fluids* 25.8, 086102 (2013). DOI: http://dx.doi.org/10.1063/1.4817069. URL: http://scitation.aip.org/content/aip/journal/pof2/25/8/10.1063/1.4817069.

[68] S. Schoch et al. "Multi-phase simulation of ammonium nitrate emulsion detonations". In: *Combustion and Flame* 160 (9 2013), pp. 1883–1899.

[69] G. J. Sharpe and M. Braithwaite. "Steady non-ideal detonations in cylindrical sticks of explosives". In: *J. Enging Math* 53 (2005), pp. 39–58. URL: http://link.springer.com/content/pdf/10.1007%2Fs10665-005-5570-7.pdf.

[70] Gary J. Sharpe. Private communication. 2011.

[71] Gary J. Sharpe et al. "Steady non-ideal detonation". In: *Shock Compression of Condensed Matter* (2009).

[72] G.J. Sharpe and J.B. Bdzil. "Interactions of inert confiners with explosives". In: *J. Enging Math* 54 (2006), pp. 273–298.

[73] Mark Short et al. "Simulation Of Detonation Of Ammonium Nitrate Fuel Oil Mixture Confined By Aluminum: Edge Angles For DSD". In: *14th International Detonation Symposium*. 2010. URL: http://public.lanl.gov/sjackson/papers/2010-Short-ANFO-det_symp10-91862.pdf.

[74] D. Scott Stewart and John B. Bdzil. "Examples of detonation shock dynamics for detonation wave spread applications". In: *9th International Detonation Symposium*. 1989.

[75] Eleuterio F. Toro. *Riemann Solvers and Numerical Methods for Fluid Dynamics: A Practical Introduction*. 3rd. Springer, 2009.

[76] I. M. Voskoboinikov, A. N. Afanasenkov, and V. M. Bogomolov. "Generalized shock adiabat for organic liquids". In: *Combustion, Explosion, and Shock Waves* 3 (4 1967), pp. 359–364. ISSN: 0010-5082. DOI: 10.1007/BF00741687. URL: http://dx.doi.org/10.1007/BF00741687.

[77] B. D. Lambourn W. Byers Brown. "Analytical Representation of the Adiabatic Equation for Detonation Products Based on Statistical Mechanics and Intermolecular Forces [and Discussion]". In: *Philosophical Transactions: Physical Sciences and Engineering* 339.1654 (1992), pp. 345–353. ISSN: 09628428. URL: http://www.jstor.org/stable/53951.

[78] Simon Watt et al. "A streamline approach to two-dimensional steady non-ideal detonation: the straight streamline approximation". In: *Journal of Engineering Mathematics* (2011), pp. 1–14. ISSN: 0022-0833. DOI: 10.1007/s10665-011-9506-0. URL: http://dx.doi.org/10.1007/s10665-011-9506-0.

[79] William W. Wood and John G. Kirkwood. "Diameter Effect in Condensed explosives. The relation between velocity and radius of curvature of the detonation wave." In: *Journal of Chem. Phys.* 22 (1954), pp. 1920–4. URL: http://dx.doi.org/10.1063/1.1739940.

[80] Ya. B. Zeldovich. "On the theory of propagation of detonation in gaseous systems". In: *Zh. Eksp. Teor. Fiz.* 10 (1940), pp. 542–568.

# Part V.

# Appendices

# A. Derivation of single-phase Chan-Kirby model

## A.1. Conservation of momentum

The steady state version of the conservation of momentum equation (1.2) is

$$(\mathbf{u}\cdot\nabla)\,\mathbf{u}+\frac{1}{\rho}\nabla p=0,$$

where $\mathbf{u}=(u,\omega)$ is the velocity vector in cylindrical coordinates, $p$ is the pressure and $\rho$ is the density. Expanding the left hand side gives

$$\begin{aligned}((u,\omega)\cdot\nabla)\,(u,\omega)+\frac{1}{\rho}\nabla\,(u,\omega) &= \left((u,\omega)\cdot\left(\frac{\partial}{\partial z},\frac{\partial}{\partial r}\right)\right)(u,\omega)+\frac{1}{\rho}\left(\frac{\partial}{\partial z},\frac{\partial}{\partial r}\right)p,\\ &=\left(\omega\frac{\partial\omega}{\partial r}+u\frac{\partial\omega}{\partial z}\right)\hat{r}+\left(\omega\frac{\partial u}{\partial r}+u\frac{\partial u}{\partial z}\right)\hat{z}+\frac{1}{\rho}\frac{\partial p}{\partial r}\hat{r}+\frac{1}{\rho}\frac{\partial p}{\partial z}\hat{z},\\ &=\left(\omega\frac{\partial\omega}{\partial r}+u\frac{\partial\omega}{\partial z}+\frac{1}{\rho}\frac{\partial p}{\partial r}\right)\hat{r}+\left(\omega\frac{\partial u}{\partial r}+u\frac{\partial u}{\partial z}+\frac{1}{\rho}\frac{\partial p}{\partial z}\right)\hat{z},\end{aligned}\tag{A.1}$$

where $\hat{r}$ and $\hat{z}$ are unit vectors in the radial and axial directions.

## A.2. Axial momentum

From the $\hat{z}$ component of (A.1),

$$\omega\frac{\partial u}{\partial r}+u\frac{\partial u}{\partial z}+\frac{1}{\rho}\frac{\partial p}{\partial z}=0.$$

Hence,

$$\frac{1}{u}\frac{\partial p}{\partial z}=-\rho\frac{\partial u}{\partial z}-\frac{\rho\omega}{u}\frac{\partial u}{\partial r}.$$

Neglecting the term $\dfrac{\rho\omega}{u}\dfrac{\partial u}{\partial r}$, since $\dfrac{\omega}{u}$ is assumed to be negligible in Chan-Kirby theory, gives

$$\begin{aligned}\frac{1}{u}\frac{\partial p}{\partial z} &\approx -\rho\frac{du}{dz}-\cancel{\frac{\rho\omega}{u}\frac{\partial u}{\partial r}}\\ \frac{dp}{dz} &= -u\rho\frac{du}{dz}\end{aligned}$$

## A.3. Radial momentum

From the $\hat{r}$ component of (A.1),

$$\omega\frac{\partial\omega}{\partial r}+u\frac{\partial\omega}{\partial z}+\frac{1}{\rho}\frac{\partial p}{\partial r}=0$$

The shape of the streamlines is determined by the incoming shock angle at the shock front, $\theta$, and the angle the isobars make with the horizontal, $\epsilon$, (see Figure 6.2). Hence, these angles are related to the change in pressure:

$$\epsilon=\theta-\left(\frac{dp}{dr}\right)_s\left(\frac{dz}{dp}\right). \tag{A.2}$$

Using the small angle (first order) approximation,

$$\frac{\partial p}{\partial r}=-\epsilon\frac{\partial p}{\partial z},$$

the radial momentum equation the becomes

$$\omega\frac{\partial\omega}{\partial r}+u\frac{\partial\omega}{\partial z}-\frac{\epsilon}{\rho}\frac{\partial p}{\partial z}=0. \tag{A.3}$$

Using the expression for axial momentum,

$$\omega\frac{\partial\omega}{\partial r}+u\frac{\partial\omega}{\partial z}+u\epsilon\frac{\partial u}{\partial z}=0.$$

Taking the partial derivative of the left hand side with respect to $r$ gives

$$\begin{aligned}
&\frac{\partial}{\partial r}\left(\omega\frac{\partial\omega}{\partial r}+u\frac{\partial\omega}{\partial z}+u\epsilon\frac{\partial u}{\partial z}\right)\\
&=\left(\frac{\partial\omega}{\partial r}\right)^2+\omega\frac{\partial^2\omega}{\partial r^2}+\frac{\partial u}{\partial r}\frac{\partial\omega}{\partial z}+u\frac{\partial^2\omega}{\partial r\partial z}+u\frac{\partial\epsilon}{\partial r}\frac{\partial u}{\partial z}+u\epsilon\frac{\partial^2 u}{\partial z\partial r}+\epsilon\frac{\partial u}{\partial z}\frac{\partial u}{\partial r},\\
&\approx\left(\frac{\partial\omega}{\partial r}\right)^2+\cancel{\omega\frac{\partial^2\omega}{\partial r^2}}+\cancel{\frac{\partial u}{\partial r}\frac{\partial\omega}{\partial z}}+u\frac{\partial^2\omega}{\partial r\partial z}+u\frac{\partial\epsilon}{\partial r}\frac{\partial u}{\partial z}+\cancel{u\epsilon\frac{\partial^2 u}{\partial z\partial r}}+\cancel{\epsilon\frac{\partial u}{\partial z}\frac{\partial u}{\partial r}},
\end{aligned}$$

where $\omega\frac{\partial^2\omega}{\partial r^2}$, $\frac{\partial u}{\partial r}\frac{\partial\omega}{\partial z}$, $u\epsilon\frac{\partial^2 u}{\partial z\partial r}$ and $\epsilon\frac{\partial u}{\partial z}\frac{\partial u}{\partial r}$ are assumed to be small and are therefore neglected. Hence,

$$\begin{aligned}
u\frac{\partial^2\omega}{\partial r\partial z}&\approx-\left(\frac{\partial\omega}{\partial r}\right)^2-u\frac{\partial\epsilon}{\partial r}\frac{\partial u}{\partial z},\\
\frac{\partial}{\partial z}\frac{\partial\omega}{\partial r}&\approx-\frac{1}{u}\left(\frac{\partial\omega}{\partial r}\right)^2-\frac{\partial\epsilon}{\partial r}\frac{\partial u}{\partial z}.
\end{aligned}$$

The isobar curvature is approximated as $C = \dfrac{\partial \epsilon}{\partial r}$ (see 'Isobar Curvature' in §6.1). Further, it is assumed that $\omega_r$ and $u$ are functions of $z$ only (that is, they are independent of $r$) so that $\dfrac{\partial \omega_r}{\partial z} = \dfrac{d\omega_r}{dz}$ and $\dfrac{\partial u}{\partial z} = \dfrac{du}{dz}$. Hence,

$$\boxed{\frac{d\omega_r}{dz} = -\frac{\omega_r^2}{u} - C\frac{du}{dz}.} \tag{A.4}$$

## A.4. Conservation of mass

The steady state, axisymmetric version of the conservation of mass equation (1.1) is

$$(\mathbf{u} \cdot \nabla)\,\rho + \rho \nabla \cdot \mathbf{u} = 0 \tag{A.5}$$

Expanding the left hand side gives

$$\begin{aligned}
&((u,\omega) \cdot \nabla)\,\rho + \rho \nabla \cdot (u,\omega)\,, \\
&= \left((u,\omega) \cdot \left(\frac{\partial}{\partial z}, \frac{\partial}{\partial r}\right)\right)\rho + \rho\left(\frac{1}{r}\frac{\partial\,(r\omega)}{\partial r} + \frac{\partial u}{\partial z}\right), \\
&= \left(u\frac{\partial}{\partial z} + \omega\frac{\partial}{\partial r}\right)\rho + \rho\left(\frac{\partial \omega}{\partial r} + \frac{\omega}{r} + \frac{\partial u}{\partial z}\right).
\end{aligned}$$

Hence,

$$\begin{aligned}
\frac{\partial \rho}{\partial z} &= \frac{-\rho}{u}\left(\frac{\partial \omega}{\partial r} + \frac{\omega}{r} + \frac{\partial u}{\partial z}\right) - \frac{\omega}{u}\frac{\partial \rho}{\partial r}, \\
&\approx \frac{-\rho}{u}\left(\frac{\partial \omega}{\partial r} + \frac{\omega}{r} + \frac{\partial u}{\partial z}\right) \cancel{- \frac{\omega}{u}\frac{\partial \rho}{\partial r}}, \\
\boxed{\frac{d\rho}{dz} &= \frac{-\rho}{u}\left(\omega_r + \frac{\omega}{r} + \frac{du}{dz}\right).}
\end{aligned} \tag{A.6}$$

The value of $C$ still needs to be determined. Currently this is done with an empirical expression that relates the isobar curvature along the streamline to the isobar curvature at the shock front, $C_s$,

$$C = C_s - \frac{2z}{(\beta R)^2}, \tag{A.7}$$

where $\beta$ is an empirical value taken to be 0.5 and $R$ is the radius of curvature at that point.

## A.5. Conservation of internal energy

The steady state, axisymmetric version of the conservation of internal energy equation (1.3) is

$$\mathbf{u}\cdot\nabla e - \frac{p}{\rho^2}\mathbf{u}\cdot\nabla\rho = 0.$$

Since

$$\nabla e = \frac{\partial e}{\partial p}\nabla p + \frac{\partial e}{\partial \rho}\nabla\rho + \frac{\partial e}{\partial \lambda}\nabla\lambda,$$

it follows that

$$\frac{p}{\rho^2}\mathbf{u}\cdot\nabla\rho = \mathbf{u}\cdot\left(\frac{\partial e}{\partial p}\nabla p + \frac{\partial e}{\partial \rho}\nabla\rho + \frac{\partial e}{\partial \lambda}\nabla\lambda\right)$$

The steady state conservation of momentum (A.1),

$$\rho\mathbf{u}\cdot\nabla\mathbf{u} + \nabla p = 0 \quad \Rightarrow \quad \nabla p = -\rho\mathbf{u}\cdot\nabla\mathbf{u},$$

can be used with the steady state conservation of mass (A.5),

$$(\mathbf{u}\cdot\nabla)\,\rho = -\rho\nabla\cdot\mathbf{u},$$

to obtain

$$\frac{p}{\rho^2}\mathbf{u}\cdot\nabla\rho = \mathbf{u}\cdot\left(-\frac{\partial e}{\partial p}\rho\,(\mathbf{u}\cdot\nabla)\,\mathbf{u} + \frac{\partial e}{\partial \rho}\nabla\rho + \frac{\partial e}{\partial \lambda}\nabla\lambda\right)$$

$$\frac{\partial e}{\partial p}\rho\,(\mathbf{u}\cdot(\mathbf{u}\cdot\nabla)\,\mathbf{u}) - \left(\frac{p}{\rho^2} - \frac{\partial e}{\partial \rho}\right)\rho\nabla\cdot\mathbf{u} = \frac{\partial e}{\partial \lambda}\mathbf{u}\cdot\nabla\lambda$$

$$\rho\,(\mathbf{u}\cdot(\mathbf{u}\cdot\nabla)\,\mathbf{u}) - \frac{\left(\frac{p}{\rho^2} - \frac{\partial e}{\partial \rho}\right)}{\frac{\partial e}{\partial p}}\rho\nabla\cdot\mathbf{u} = \frac{\frac{\partial e}{\partial \lambda}}{\frac{\partial e}{\partial p}}\mathbf{u}\cdot\nabla\lambda$$

$$\mathbf{u}\cdot(\mathbf{u}\cdot\nabla\mathbf{u}) - \frac{\left(\frac{p}{\rho^2} - \frac{\partial e}{\partial \rho}\right)}{\frac{\partial e}{\partial p}}\frac{\rho\nabla\cdot\mathbf{u}}{\rho} = \frac{\frac{\partial e}{\partial \lambda}}{\frac{\partial e}{\partial p}}\frac{\mathbf{u}\cdot\nabla\lambda}{\rho}$$

Recalling the expression for sound speed, $c^2 = \dfrac{\frac{p}{\rho^2} - \left(\frac{\partial e}{\partial \rho}\right)_p}{\left(\frac{\partial e}{\partial p}\right)_\rho}$, and thermicity, $\sigma = -\dfrac{1}{\rho c^2}\dfrac{\frac{\partial e}{\partial \lambda}}{\frac{\partial e}{\partial p}}$, and noting that $\dot\lambda = \dfrac{d\lambda}{dt} = \dfrac{\partial\lambda}{\partial t} + \mathbf{u}\cdot\nabla\lambda = \mathbf{u}\cdot\nabla\lambda$, the equation simplifies to

$$\mathbf{u}\cdot(\mathbf{u}\cdot\nabla\mathbf{u}) - c^2\cdot\nabla\mathbf{u} = -c^2\sigma\dot\lambda.$$

Expanding in axisymmetric coordinates with $\mathbf{u} = (u_z, u_r) = (u, \omega)$ gives

$$u^2\left(\frac{\partial u}{\partial z}\right) + \omega^2\left(\frac{\partial \omega}{\partial r}\right) + u\omega\left(\frac{\partial u}{\partial r} + \frac{\partial \omega}{\partial z}\right) - c^2\left(\frac{\partial u}{\partial z} + \frac{\partial \omega}{\partial r} + \frac{\omega}{r}\right) = -c^2\sigma\dot\lambda.$$

This can be further simplified as follows:

$$\left(c^2-u^2\right)\frac{\partial u}{\partial z}=c^2\left(\sigma\dot{\lambda}-\frac{\partial\omega}{\partial r}-\frac{\omega}{r}\right)+\omega^2\left(\frac{\partial\omega}{\partial r}\right)+u\omega\left(\frac{\partial u}{\partial r}+\frac{\partial\omega}{\partial z}\right),$$

$$\frac{\partial u}{\partial z}=\frac{1}{(c^2-u^2)}\left(c^2\left(\sigma\dot{\lambda}-\frac{\partial\omega}{\partial r}-\frac{\omega}{r}\right)+\omega^2\left(\frac{\partial\omega}{\partial r}\right)+u\omega\left(\frac{\partial u}{\partial r}+\frac{\partial\omega}{\partial z}\right)\right),$$

$$\frac{\partial u}{\partial z}\approx\frac{1}{(c^2-u^2)}\left(c^2\left(\sigma\dot{\lambda}-\frac{\partial\omega}{\partial r}-\frac{\omega}{r}\right)\cancel{+\omega^2\left(\frac{\partial\omega}{\partial r}\right)+u\omega\left(\frac{\partial u}{\partial r}+\frac{\partial\omega}{\partial z}\right)}\right),$$

$$\boxed{\frac{du}{dz}=\frac{\left(\sigma\dot{\lambda}-\frac{\partial\omega}{\partial r}-\frac{\omega}{r}\right)}{\left(1-\frac{u^2}{c^2}\right)}=\frac{\psi}{\eta},} \tag{A.8}$$

under the assumption that $u$ is a function of $z$ only and that terms in $\omega^2$ and $\omega$ multiplied by a derivative are small. This $\dfrac{du}{dz}$ equation is referred to the 'master' equation.

## A.6. Particle velocity, space and time

The ODEs for the particle velocity, space and time need to be specified when the integral is taken over $\lambda$ and not space or time.

The ODE for time is found using the axial velocity:

$$\boxed{\frac{dt}{dz}=\frac{1}{u}.} \tag{A.9}$$

# B. Shock Polar Theory

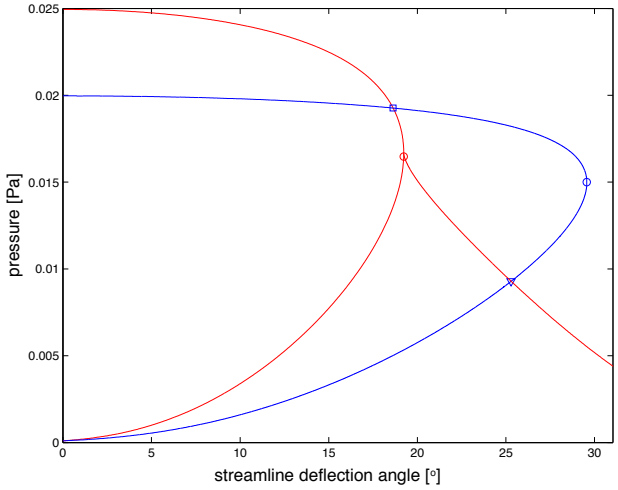


Figure B.1.: Two shock polar curves with an intervening Prandtl-Meyer expansion fan in the explosive (red). The red curve represents the explosive and the blue curve represents the inert confiner. The circles denote the sonic point on each shock polar. The square and triangle denote two different match points between the two materials. The square is a match point on the subsonic, strong branch of both the confiner and the explosive. The triangle shows a match point between the pressure expansion at the edge of the explosive and the supersonic branch of the inert confiner.

A shock polar relates the postshock pressure $p$ of a material with the streamline deflection $\phi$ caused by an oblique shock, parameterised by the incoming shock angle $\mu$. Oblique shock theory is used to determine the flow conditions immediately behind the leading shock [9].

Note that in this appendix, $u$ denotes the velocity of fluid which is then split into its tangential $u_t$ and normal components $u_n$.

## B.1. Oblique shock theory

The downstream flow conditions from an oblique shock can be readily determined using a combination of the Rankine-Hugoniot shock conditions,

an equation of state and simple trigonometry. For general equations of state these conditions need to be determined numerically using root finding algorithms. A special case is for the ideal gas (polytropic) equation of state when the expressions can be conveniently simplified. This theory is widely explored in many texts but the discussion presented in this appendix follows from [4, 32, 42, 54] and the reader is referred to these sources for further information.

The intersection of the explosive shock polar with the confinement shock polar gives the pressure and flow deflection matching conditions for the given upstream Mach number or detonation velocity, as shown in Figure B.1. The turning point on a shock polar is the maximum deflection angle for that material. The sonic point represents the value of $p$ and $\phi$ for which the upstream flow is sonic, $M_0 = 1$ where $M_0$ is the Mach number of the upstream flow, and this is shown as the circle on both shock polars in Figure B.1. Note that this is not necessarily the maximum deflection angle.

The solutions above the sonic point represent a strong oblique shock and subsonic downstream flow. The solutions below the sonic point represent the weak oblique shock and supersonic downstream flow. The following sections outline how to obtain the equations for the downstream flow and deflection angle that are used to construct the shock polars, beginning with a brief outline of how shock waves and Mach numbers are related and the role of the Mach angle. The equations given are for general equations of state.

**Mach angle**

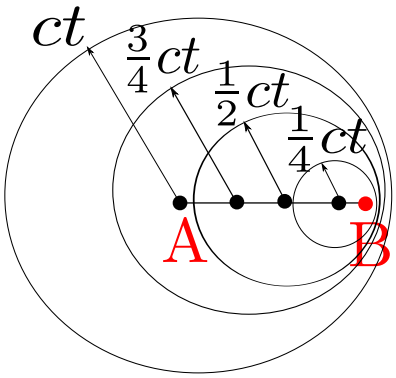


Figure B.2.: At $t = 0$ the body is at A. At $t > 0$, waves that originated from A have grown to a sphere with $r = ct$ and the body will have moved $AB = ut$. Since $u < c$, pressure waves move ahead of the body so that B is inside the sphere. The pressure waves travel ahead of the body, informing the fluid of the body's approach.

In a Mach cone, small elastic waves are the means by which information is transmitted from one point in the fluid to another. Information can be

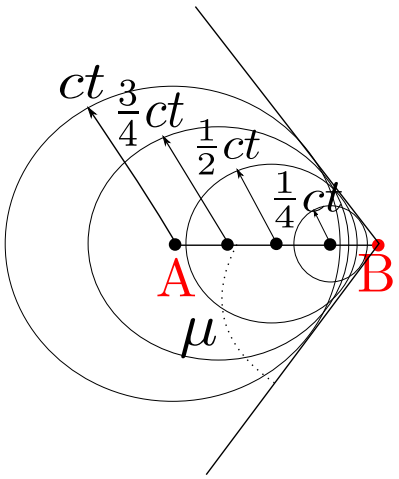


Figure B.3.: At $t = 0$ the body is at A. At $t > 0$ the body has travelled $ut > ct$ and is therefore outside the sphere formed by the pressure waves that were sent out at $t = 0$. The body travels faster than the information about the body and so the unprepared fluid forms a shock wave. B is the instantaneous position of the body and the cone formed has a semi-vertex angle, called the Mach angle, of $\mu$.

sent in a particular direction only if the velocity of the fluid in the opposite direction is less than the sonic velocity $c$.

For example, consider a small, solid body moving in a straight line through a stationary fluid. If $u < c$, where $u$ is the body velocity in the direction of the straight line and $c$ is the speed of sound in the fluid, then the movement of the body generates pressure waves in the fluid which are transmitted radially with velocity $c$, as shown in Figure B.2. Since $u < c$ the pressure waves in the forward direction are able to move ahead of the body; the waves travelling ahead of the body inform the fluid of the body's approach.

If, however, $u > c$, then the body travels faster than the sphere formed by the pressure waves, as shown in Figure B.3. The unprepared fluid has to move suddenly producing sharp discontinuities or shock waves. This means that a cone that advances with the body into the undisturbed fluid is generated with an axis in the direction of the body motion. The semi-vertex angle of this cone is

$$\sin \mu = \frac{ct}{ut} = \frac{c}{u} = \frac{1}{M}, \tag{B.1}$$

where $\mu$ is the Mach angle made between the axis and the edge of the Mach cone.

### Oblique shock conditions

The oblique shock conditions describe the postshock state of a material and the deflection angle $\phi$ across an oblique shock given initial state parameters and the incoming shock angle $\mu$. These expressions can then be used to obtain a relationship between the postshock pressure $p_s$ and the deflection angle via a parametrisation in the incoming shock angle $\mu$.

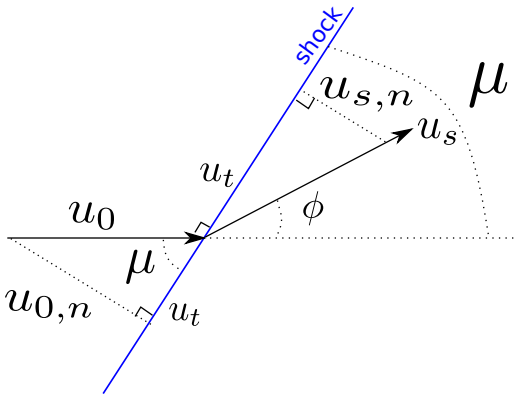


Figure B.4.: Schematic of an incoming velocity vector at an incoming shock angle $\mu$ passing through an oblique shock. The flow is deflected through an angle $\phi$ by the oblique shock. The upstream and downstream velocity vector is split into its normal and tangential components, with respect to the shock, and conservation laws across the shock are used to determine expressions for the downstream flow variables and the deflection angle in terms of the upstream flow variables and the incoming shock angle.

To do this, first note that the upstream Mach number is given by

$$M_0 = \frac{u_0}{c} \Rightarrow u_0 = M_0 c, \tag{B.2}$$

and that the conservation of mass states that

$$\rho_0 u_0 = \rho_s u_s \Rightarrow u_s = \frac{\rho_0 u_0}{\rho_s}$$

As shown in Figure B.4, conservation of momentum in the tangential direction dictates that

$$\cos\mu = \frac{u_t}{u_0}, \quad \cos(\mu - \phi) = \frac{u_t}{u_s}.$$

Conservation of mass in the tangential direction implies

$$\begin{aligned} \rho_0 u_t \tan\mu &= \rho_s u_t \tan(\mu - \phi) \\ \Rightarrow \frac{\rho_0}{\rho_s} &= \frac{\tan(\mu - \phi)}{\tan\mu}. \end{aligned}$$

This is an important relation as it allows us to determine the deflection angle $\phi$ from the incoming flow angle $\mu$ and the other flow variables.

The postshock density and pressure can be obtained as a function of the incoming shock angle $\mu$ by using the conservation of momentum and the conservation of energy. Note that the enthalpy is unaffected by the shock because the shock does no work and there is no heat transfer across it.

Normal to the shock, the conservation of momentum is used to obtain an expression for the postshock pressure:

$$\begin{aligned} p_0 + \rho_0 u_{0,n}^2 &= p_s + \rho_0 u_{s,n}^2, \\ \Rightarrow p_0 + \rho_0 u_0^2 \sin^2\mu &= p_s + \rho_0 \frac{\rho_0^2 u_0^2}{\rho_s^2} \sin^2\mu, \\ \Rightarrow p_0 + \rho_0 M_0^2 c^2 \sin^2\mu &= p_s + \rho_0 \frac{\rho_0^2 M_0^2 c^2}{\rho_s^2} \sin^2\mu, \\ \Rightarrow p_s &= p_0 + \rho_0 M_0^2 c_0^2 \sin^2\mu \left(1 - \frac{\rho_0^2}{\rho_s^2}\right). \end{aligned}$$

Using the expression for enthalpy,

$$h = e + pv,$$

the conservation of momentum becomes

$$\begin{aligned} h_s + \frac{u_{s,n}^2}{2} &= h_0 + \frac{u_{0,n}^2}{2} \\ \Rightarrow e(p_s,\rho_s) + \frac{p_s}{\rho_s} + \frac{u_{s,n}^2}{2} &= e(p_0,\rho_0) + \frac{p_0}{\rho_0} + \frac{u_{0,n}^2}{2} \\ \Rightarrow e(p_s,\rho_s) + \frac{p_s}{\rho_s} + \frac{u_s^2 \sin^2\mu}{2} &= e(p_0,\rho_0) + \frac{p_0}{\rho_0} + \frac{u_0^2 \sin^2\mu}{2} \\ \Rightarrow e(p_s,\rho_s) + \frac{p_s}{\rho_s} &= e(p_0,\rho_0) + \frac{p_0}{\rho_0} + \frac{1}{2} M_0^2 c_0^2 \left(1 - \frac{\rho_0^2}{\rho_s^2}\right) \sin^2\mu \end{aligned}$$

Within the frame of reference of the shock, $u_s' = u_s - D$, where $D$ is the detonation velocity of the material, and $u_0' = u_0 - D = -D$.

These equations are then used to construct the shock polar curve for each material, an example of which is shown in Figure B.5a. The intersection points of these curves gives the match point conditions for the streamline deflection angle, from which the maximum incoming shock angle can be calculated. An example of this is shown in Figure B.1. However, as shown in Figure B.5c, the curves often do not intersect on an appropriate branch of the explosive or confiner, the conditions of which will be explored in a later section, then the only solution may be via a pressure expansion fan in the explosive that then intersects the other shock polar. This expansion fan is called a Prandtl-Meyer expansion fan and the next section outlines its derivation for general equations of state.

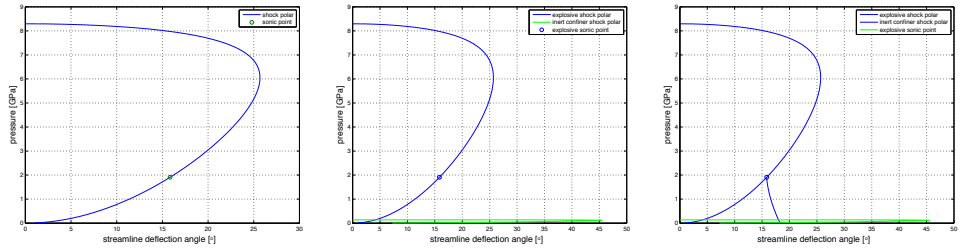


(a) (b) (c)

Figure B.5.: (a) Shock polar curve with the sonic point shown by the circle. (b) Two shock polar curves for explosive (blue) and confiner (green) with the only intersection at very low pressures on the supersonic, weak branch of the explosive (blue). An intervening pressure expansion from the sonic point is needed. (c) An intervening Prandtl-Meyer expansion fan gives a valid match point between the explosive and confiner.

### B.1.1. Prandtl-Meyer expansion

The use of intersecting shock polars to determine the pressure and flow deflection match conditions at the material interface assumes that the confinement is of a type for which it is guaranteed that there is an appropriate match of the two shock polars.

In general there are several types of interactions between the explosive and the confining material. The two main types of interactions are for strong confinement and weak confinement.

For typical strong confinement there is a lead shock in the explosive that is transmitted into the inert confiner. Behind the detonation front in the explosive there is a subsonic region so we expect that the intersection of the two shock polars will occur on the subsonic (upper) branch of the explosive's shock polar. For the inert confiner, the region behind the transmitted shock could be either subsonic or supersonic and so the intersection could take place on either branch of the inert's shock polar. For the case of typically strong confinement, both cases are valid as long as the subsonic branch of the explosive intersects part of the inert shock polar, as in Figure B.1.

For the case of typical weak confinement, there is again a lead shock in the explosive that is transmitted to the inert confiner. However, due to the weak nature of the confiner, this transmitted shock is at a much lower pressure than the shock in the explosive. This implies that there will be a pressure expansion in the explosive at the edge of the charge as in Figure B.5b. This intervening pressure expansion is in the form of a Prandtl-Meyer expansion fan that begins at the sonic point on the explosive's shock polar where $M_0 = 1$. The intersection then takes place in the expansion between the explosive and the shock in the inert material.

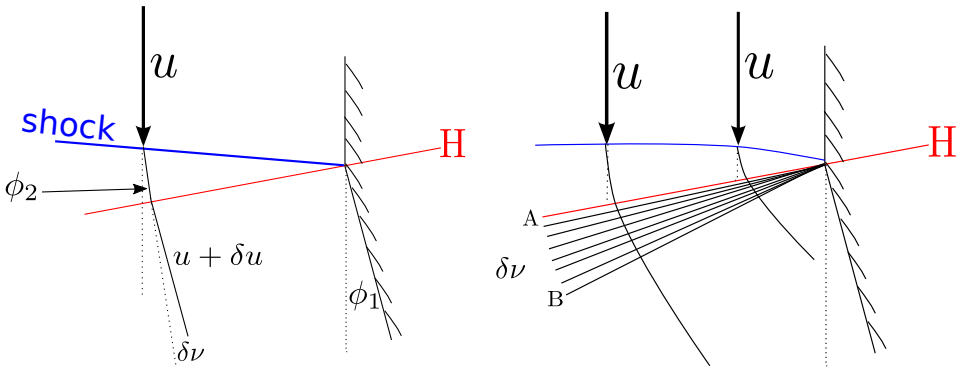


Figure B.6.: (a) Flow approaching a convex corner undergoes an expansion through an infinitesimal Mach wave, $H$. After being deflected by the shock front through an angle $\phi_2$, the flow is further deflected through $\delta\nu$ by the Mach wave $H$ so the downstream flow is $u + \delta u$. (b) Individual Mach waves intersect a common point. The flow is unaffected until A and between A and B the gas expands gradually and isentropically. After B, by the action of both the shock and the expansion in the explosive, the flow has been turned through an angle of $\phi_1$ so that it is now parallel to the flow in the confiner.

In an interaction between an explosive and weak confinement, the expanding explosive behind the sonic locus will create a convex corner at the edge of the charge where the shock front and the sonic locus intersect. This corner turns the flow with an angle of $\phi_1 - \phi_2$, which is the difference between the deflection angle of the shock in the explosive and the shock in the confiner, as shown in Figure B.6a. The supersonic, incoming flow at the edge then creates a centered expansion fan as it turns around the convex corner, as shown in Figure B.6b. The fan consists of an infinite number of Mach waves that diverge from the convex corner, each turning the flow by an angle, $\delta\nu$.

There is no pressure gradient along the Mach wave so the velocity parallel to the wave is unaltered,

$$u \cos\nu = (u + \delta u)\cos(\nu + \phi),$$

as shown in Figure B.6a.

Using trigonometric identities and assuming that $\phi$ is small enough so that $\cos\phi \approx 1$ and $\sin\phi \approx \phi$,

$$\begin{aligned} u\cos\nu &= (u + \delta u)(\cos\nu\cos\phi - \sin\nu\sin\phi), \\ &= (u + \delta u)(\cos\nu - \phi\sin\nu). \end{aligned}$$

Rearranging this becomes

$$(u+\delta u)\phi\sin\nu = (u+\delta u-u)\cos\nu,$$
$$(u+\delta u)\phi = (u+\delta u-u)\frac{\cos\nu}{\sin\nu},$$
$$\phi = \frac{\delta u}{u+\delta u}\cot\nu.$$

Assuming that $u \gg \delta u$,

$$\phi \approx \frac{\delta u}{u}\cot\nu.$$

Using (B.1) this becomes

$$= \frac{\delta u}{u}(M^2-1)^{\frac{1}{2}}.$$

Finally,

$$\delta u = u\phi(M^2-1)^{-\frac{1}{2}} > 0, \tag{B.3}$$

which implies that the velocity increases around a convex corner.

If initially uniform flow makes a succession of small turns there will be a number of regions of uniform flow separated by Mach waves emanating from the corners. If the straight portions between these small turns is indefinitely decreased, a continuously curved surface is obtained and an infinite number of Mach waves is generated. Heat transfer is neglected due to the high velocities and infinitesimal waves.

From (B.3), the deflection angle can be written as

$$\phi = \int_u \frac{(M^2-1)^{\frac{1}{2}}}{u}du.$$

The parallel component of the velocity remains unchanged so the normal component to the Mach wave must increase, therefore the density must decrease. The change in $M$, from upstream to downstream, associated with an angular deflection $\phi$ can be calculated from the Prandtl-Meyer function which describes the angle through which a flow can turn isentropically from a given initial and final Mach number.

The Prandtl-Meyer function is obtained by recognising that,

$$\frac{du}{u} = \frac{dM}{M} + \frac{dc}{c}.$$

The second term on the right hand side, $\frac{dc}{c}$, needs to be expressed as a function of $dM$ with use of an equation of state and the oblique shock conditions. For example, the ideal gas equation of state gives the following condition at the oblique shock:

$$\frac{c}{c_0} = \left(1+\frac{\gamma-1}{2}M^2\right)^{-\frac{1}{2}}.$$

Differentiating this gives,

$$\frac{dc}{c} = -\frac{\gamma - 1}{2} M \left(1 + \frac{\gamma - 1}{2} M^2\right)^{-1} dM.$$

Hence,

$$\phi = \phi_{\text{ref}} - \int_{M_1}^{M_2} \frac{\sqrt{M^2 - 1}}{1 + \frac{\gamma - 1}{2} M^2}. \tag{B.4}$$

This discussion follows from [3].

# C. Characteristic curves

It is instructive to investigate the flow at the edge of an explosive in terms of characteristic curves (characteristics). Studying characteristics is illustrative when investigating the nature of the solution of systems of hyperbolic differential equations, such as those that govern the flow of variables in the propagation of a detonation wave. A characteristic is a curve in the dependent-variable space (for example, $x - t$ space) along which one of the equations of the system becomes an ODE. This means that for a system of $n$ equations there are $n$ families of characteristics and these characteristics describe how information is transferred from one region in the domain to another. This information does not travel at a constant speed but instead moves as a function of the local speed of sound.

There are two types of characteristics within each family: forward characteristics, $C_+$, and backward characteristics, $C_-$. A simple example of a propagating disturbance is shown in Figure C.1. At $t = 0$, a finite section of the $x$-axis between points $A$ and $B$ is disturbed while the rest of the axis remains undisturbed. The characteristics illustrate how this disturbance propagates in time ahead and behind the initial disturbance in the subsequent motion. The slope of the characteristic curves will depend on how the local speed of sound and any relevant flow variables change. The region to the left of $C_-^A$ and to the right of $C_+^B$ remain unaffected by the disturbance. After some time $t_1$, $C_-^B$ intersects with $C_+^A$ at the point marked by a green circle. The two propagating waves then become coupled. In Riemann's initial-value problem, this is the point where the disturbance that was initially confined to AB becomes disentangled into a pair of simple waves propagating in opposite directions. For other systems, such as the Euler equations, the results are far more complicated.

In terms of the detonation problem, we are interested in the area near the intersection of the charge edge and the leading shock in the explosive. The same assumption in [74] is made so that the flow at the intersection of the shock and edge boundary is assumed to be exactly sonic. This is the point at which the Prandtl-Meyer singularity is located and the pressure at the intersection is reduced discontinuously from the value of the pressure in the explosive to the value of the pressure in the inert. It is from this point that the intervening Prandtl-Meyer pressure expansion in the explosive takes place; an infinite number of Mach lines fan to match the higher pressure in the explosive's shock to the lower pressure in the transmitted shock in the inert confiner. These Mach lines are just characteristic curves.

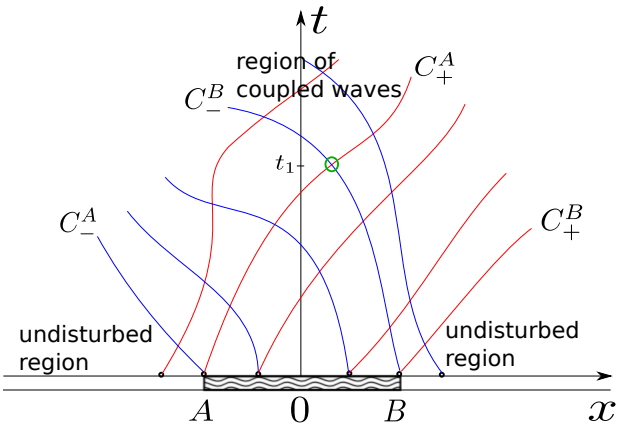


Figure C.1.: Characteristics from a disturbed region. The region to the left of $C_-^A$ and to the right of $C_+^B$ remain unaffected by the disturbance. After some time $t_1$, $C_-^B$ intersects with $C_+^A$ at the point marked by a green circle and the two waves then become coupled.

Information about the edge travels along the $C_+$ characteristics from this point of intersection and is transferred to the subsonic region of flow behind the detonation front via the sonic locus, as shown in Figure C.2. This information then influences the subsonic region of flow between the detonation front and sonic locus. Furthermore, there is a limiting characteristic which is exactly tangent to the sonic locus that splits the flow into regions that are unaffected and affected by the information from the edge [13].

All of the $C_+$ characteristics to the right of this limiting characteristic do not come into contact with the sonic locus and therefore do not transfer information from the edge to the subsonic region. Any $C_+$ characteristics to the left of the limiting characteristics will influence the subsonic region; that is, the areas of the subsonic region closest to the charge edge will be greater influenced by the information than those further away.

In the supersonic region below the sonic locus both the $C_+$ and $C_-$ characteristics transfer information downward. The $C_-$ characteristics (not shown in Figure C.2) transfer information from this supersonic region below the sonic locus to the inert.

If the charge is unconfined, as shown in Figure C.3a, no information from the edge is transferred to the subsonic region. If the charge is weakly confined, as shown in Figure C.3b, the limiting characteristic is now tangential to the sonic locus and there is therefore at least one point of contact between the characteristics and the sonic locus. This means that information from the edge can now be transferred to the subsonic region and influence the structure of the detonation shock.

As the strength of confinement is increased, the sonic locus detaches from the shock as shown in Figure C.4, and the whole region between explosive

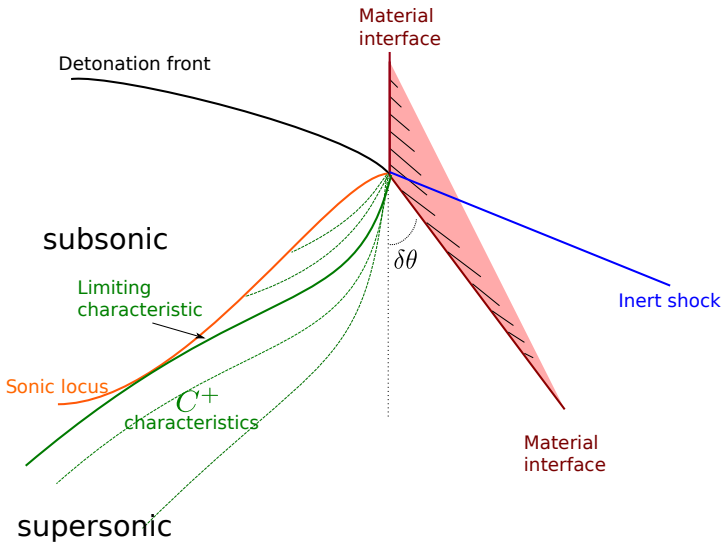


Figure C.2.: A schematic for the characteristics for the detonation problem, based on [74]. The solid green line is the limiting $C_+$ characteristic and the dashed green lines are some other $C_+$ characteristics.

and material interface is now subsonic. The pressure in the inert will be equal to or greater than the pressure at the detonation front which implies that the P-M expansion fan is no longer needed. Figure C.4 shows the case where the flow in the inert confiner is supersonic. Both the $C_+$ and $C_-$ characteristics are downward-going with the $C_+$ characteristics transferring information from the explosive to the inert material and vice versa for the $C_-$ characteristics [74]. This appendix was based mostly on the work of Bdzil et al in [9, 6, 12, 13, 74] and the reader is referred to these works for further information.

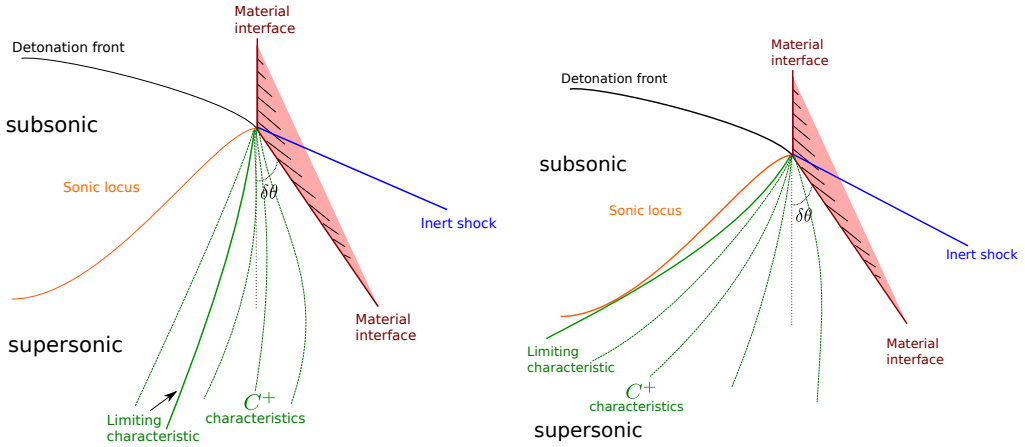


(a) No confinement. (b) Weak confinement.

Figure C.3.: Schematics for the typical characteristics for the detonation problem in no confinement and weak confinement based on [13, 74]. The solid green line is the limiting $C_+$ characteristic and the dashed green lines are some other $C_+$ characteristics.

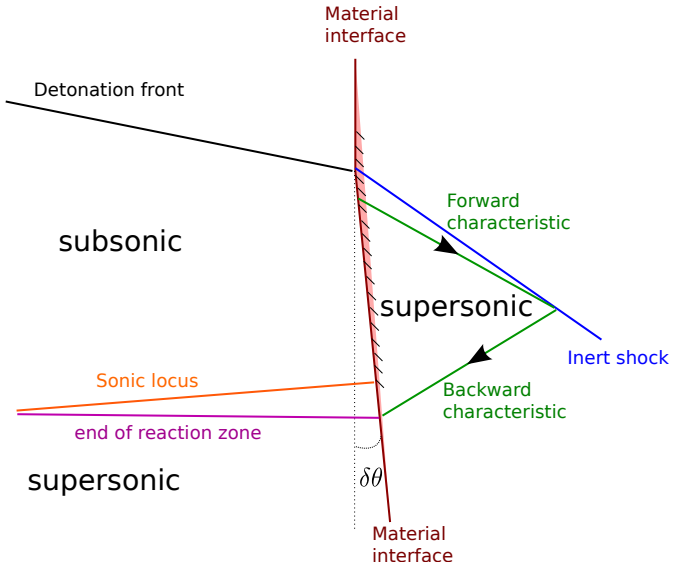


Figure C.4.: A schematic for the characteristics for the detonation problem in strong confinement based on [9, 74].